

Technische Universität München  
TUM School of Engineering and Design

# **A Consistent Helmholtz Framework for the Accurate Prediction of Linear and Nonlinear Thermoacoustic Stability in Gas Turbine Combustors**

**Gerrit Heilmann**

Vollständiger Abdruck der von der TUM School of Engineering and Design der Technischen Universität München zur Erlangung eines

DOKTORS DER INGENIEURWISSENSCHAFTEN (DR.–ING.)

genehmigten Dissertation.

Vorsitz:

Prof. Dr.–Ing. Chiara Manfletti

Prüfer\*innen der Dissertation:

1. Prof. Dr.–Ing. Thomas Sattelmayer
2. Prof. Aimee Morgans, Ph.D.
3. Prof. Timothy Charles Lieuwen, Ph.D.

Die Dissertation wurde am 16.01.2023 bei der Technischen Universität München eingereicht und durch die TUM School of Engineering and Design am 15.05.2023 angenommen.



---

## Acknowledgements

This dissertation emerged from the work I conducted as research assistant from 2016 to 2022 at the Chair of Thermodynamics, Technical University of Munich. It was funded by the German Federal Ministry of Economic Affairs and Energy (BMWi) and the working group AG Turbo in the framework of the joint research project “ECOFlex-turbo”.

Foremost, I would like to express my sincere gratitude to my supervisor Prof. Dr.–Ing. Thomas Sattelmayer for his reliable support at all times and the numerous discussions, which were both critical and constructive. Still, with his trust he gave me the scientific freedom to conduct the research leading to the present thesis. Also the collaboration in the course of the lecture Thermodynamics 2 was quite fruitful, particularly regarding the challenges during the Covid-19 pandemic. Thank you also to Prof. Aimee S. Morgans (Ph.D.) for her interest in my research and taking on the role as the second examiner as well as to Prof. Dr.–Ing. Chiara Manfletti for chairing the examination committee.

Writing such a thesis is not feasible without the helping hands of many people. Specifically, I want to thank Dr.–Ing Christoph Hirsch for his scientific support and for always having a sympathetic ear for the doctoral students. The administrative support of Helga Bassett and Sigrid Schulz-Reichwald is highly appreciated. A special thank you to Dr.–Ing. Thomas Hofmeister for meticulously proof-reading this thesis. And let me not forget about the other fellow doctoral students that can not all be explicitly mentioned here: we suffered together and we celebrated together. Thank you so much for the countless scientific and personal discussions, sporting activities, field trips and parties, making my doctorate a wild ride.

I am very thankful for the productive collaboration with Dr.–Ing. Michael Huth, Dr.–Ing. Lukasz Panek and Patrick Flohr of SIEMENS ENERGY and their inputs to the joint project and thus to this thesis.

The excellent work of my students Alexander Mages, Ángel Brito Gadeschi, Simon Wenzler, Dominik König, Joachim Ottinger and Tong Liu remarkably contributed to this thesis, which is gratefully acknowledged.

---

Dear Franziska, without your unconditional backing in the final stage of the thesis, I would not have managed to finish it. Also, you always helped me finding the work-life balance I needed. I want to wholeheartedly thank you for that.

Finally, I can't thank my parents enough for paving the way to do my doctorate. Thank you for your loving support and parental advice at all times.

München, im Januar 2023

Gerrit Heilmann

# Abstract

A sequential computational procedure for the efficient and reliable prediction of combustion instabilities in future gas turbine generations is developed in the present thesis. Special focus is put on the accurate inclusion of damping mechanisms. Essentially, the procedure consists of the creation of a linear computational model, a subsequent linear stability analysis and finally an investigation of nonlinear saturation mechanisms. A particularly efficient linear computational approach is the combination of spatially resolved finite element method approaches based on the Helmholtz equation with one-dimensional network models to account for acoustic losses. To increase the accuracy of the Helmholtz approach, a methodology to include the advection of sound waves in arbitrary mean flow fields is developed. Similar to the regular Helmholtz equation, this approach requires the development of a transformation procedure for the combination with network models to avoid energetic errors at the coupling interfaces. Using this linear computational model for a modal stability analysis with established flame driving models allows to identify potentially unstable oscillation states. The corresponding modal results can subsequently be exploited to investigate nonlinear damping mechanisms by means of reduced order models. Therefore, a universal methodology coupled with nonlinear resonator models is developed. Finally, the efficiency of the approach and thus its applicability to industrial setups is demonstrated on the basis of a geometrically complex configuration representative for a commercial gas turbine combustor. This highlights the significance of nonlinear damping mechanisms for limit-cycle oscillations.



# Kurzfassung

Zur effizienten und zuverlässigen Vorhersage von Verbrennungsinstabilitäten zukünftiger Gasturbinengenerationen wird in der vorliegenden Arbeit ein sequentielles Berechnungsverfahren entwickelt. Besonderes Augenmerk wird dabei auf die akkurate Erfassung von Dämpfungsmechanismen gelegt. Die Prozedur besteht im Wesentlichen aus der Erstellung eines linearen Berechnungsmodells, der nachfolgenden linearen Stabilitätsanalyse sowie einer abschließenden Untersuchung nichtlinearer Sättigungsmechanismen. Ein besonders effizienter linearer Berechnungsansatz ergibt sich aus der Kombination der räumlich mittels Finite Elemente Methoden aufgelösten Helmholtz-Gleichung mit eindimensionalen Netzwerkmodellen zur Integration akustischer Verluste. Zur Verbesserung der Genauigkeit bei gleichbleibender Effizienz wird der Helmholtz-Ansatz erweitert, um die Advektion akustischer Wellen durch beliebige zeitgemittelte Strömungsfelder abzubilden. Wie auch bei der herkömmlichen Helmholtzgleichung erfordert dies die Entwicklung einer Transformation des angekoppelten Netzwerkansatzes, um energetische Fehler an den Schnittstellen der beiden Methoden zu vermeiden. Mittels des so erstellten linearen Modells inklusive etablierter Flammenantriebsmodelle können potentiell instabile Schwingungszustände durch eine modale Stabilitätsanalyse bestimmt werden. Die Ergebnisse können anschließend zur Untersuchung nichtlinearer Dämpfungsmechanismen in Modellen reduzierter Ordnung genutzt werden. Hierfür wird eine universelle Methode zur Kopplung mit nichtlinearen Resonatormodellen entwickelt. Die Effizienz und damit die Anwendbarkeit der Prozedur auf industrielle Anwendungen sowie die Signifikanz nichtlinearer Dämpfungsmechanismen für den Grenzzyklus wird anhand einer für kommerzielle Gasturbinen-Brennkammern repräsentativen komplexen Konfiguration demonstriert.



# Contents

<b>List of Figures</b>	<b>xiv</b>
<b>List of Tables</b>	<b>xix</b>
<b>Nomenclature</b>	<b>xxi</b>
<b>1 Introduction</b>	<b>1</b>
1.1 Thermoacoustics in Gas Turbines . . . . .	2
1.2 Control Strategies and Damping Devices . . . . .	5
1.2.1 Active Control . . . . .	5
1.2.2 Passive Control . . . . .	6
1.3 Thermoacoustic Modeling Classification . . . . .	7
1.4 Scope and Structure of the Thesis . . . . .	11
<b>2 Thermoacoustic Fundamentals</b>	<b>15</b>
2.1 Governing Reactive Flow Equations . . . . .	15
2.2 Perturbed Equations . . . . .	17
2.2.1 Decomposition Approach . . . . .	17
2.2.2 PENNE and LEE . . . . .	18
2.2.3 APE . . . . .	20
2.2.4 Convective Wave Equation . . . . .	21
2.2.5 Wave Equation . . . . .	22
2.3 Acoustic Analogies . . . . .	23
2.3.1 Lighthill's Analogy . . . . .	24
2.3.2 Moehring's Analogy . . . . .	25
2.4 Frequency-Domain Analysis . . . . .	26
2.5 Acoustic Energy . . . . .	27
2.6 Boundary Conditions . . . . .	29

2.6.1	Open End Boundary . . . . .	30
2.6.2	Slip Wall Boundary . . . . .	30
2.6.3	Impedance Boundary . . . . .	30
2.6.4	Energetically Neutral Boundaries . . . . .	31
2.7	Green's Function of the Sturm-Liouville Problem . . . . .	33
2.8	Flame Dynamics . . . . .	36
2.8.1	Fluctuating Heat Release Contributions . . . . .	36
2.8.2	Linear Acoustics-Flame Interactions . . . . .	37
<b>3</b>	<b>One-Dimensional Network Models</b>	<b>43</b>
3.1	Network Modeling Concept . . . . .	44
3.2	Network Elements . . . . .	46
3.2.1	Duct with Constant Cross Section . . . . .	46
3.2.2	Sudden Area Change . . . . .	46
3.3	Acoustic Liner Models . . . . .	49
3.3.1	Mass-Spring-Damper Model . . . . .	51
3.3.2	Howe Model . . . . .	53
3.3.3	Jing and Sun Model . . . . .	54
3.3.4	Bellucci Model . . . . .	54
<b>4</b>	<b>Linear Hybrid Numerical Strategy</b>	<b>59</b>
4.1	General Modeling Procedure . . . . .	59
4.2	Exact Convective Wave Equation . . . . .	62
4.3	Finite Element Methodology . . . . .	63
4.3.1	Weak Form Equation . . . . .	64
4.3.2	Volume Source Treatment . . . . .	65
4.3.3	Acoustic Boundary Conditions for the Weak Form . . . . .	69
4.4	Energetical Consistency . . . . .	71
4.4.1	Impedance Transformation for Zero Mach Number Domains . . . . .	71
4.4.2	Transfer Matrix Transformation for Zero Mach Number Domains . . . . .	74
4.5	Linearization of the Nonlinear Eigenvalue Problem . . . . .	77
4.5.1	Linearization of Frequency-Dependent Boundary Conditions . . . . .	78
4.5.2	Linearization of Flame Driving . . . . .	80

4.6	Simple Test Case . . . . .	82
4.6.1	Numerical Model . . . . .	83
4.6.2	Investigated Configurations . . . . .	84
4.6.3	Results . . . . .	86
<b>5</b>	<b>Modal Model Order Reduction Methods</b>	<b>91</b>
5.1	Direct Modal Reduction . . . . .	92
5.2	Modal Amplitude Equations . . . . .	95
5.3	Comparison of the Two Modal Reduction Approaches . . . . .	99
5.4	ROM Coupling with Source Models . . . . .	102
5.4.1	Flame Source . . . . .	103
5.4.2	Nonlinear Resonator Patches . . . . .	104
<b>6</b>	<b>Industrial-Scale Combustor</b>	<b>109</b>
6.1	Platform Combustion System . . . . .	109
6.2	Hybrid Model of the Industrial-Scale Combustor . . . . .	111
6.2.1	Domain Split and FEM setup . . . . .	111
6.2.2	Resonator Model . . . . .	114
6.2.3	Burner Transfer Matrices . . . . .	118
6.3	Modal Analysis Results . . . . .	120
6.4	Nonlinear ROM Simulations of the Large-Scale Combustor . . . . .	124
6.4.1	ROM Creation . . . . .	125
6.4.2	Time-Domain Results . . . . .	128
6.4.3	Classification of the Time-Domain Results . . . . .	136
<b>7</b>	<b>Concluding Remarks and Future Work</b>	<b>137</b>
	<b>Previous Publications</b>	<b>143</b>
	<b>Supervised Student Theses</b>	<b>145</b>
	<b>References</b>	<b>147</b>
	<b>Appendix</b>	<b>171</b>
<b>A</b>	<b>Acoustic Source Term Filtering for LEE</b>	<b>172</b>
<b>B</b>	<b>Partial Integration for the Weak Form of the Convective Helmholtz</b>	

<b>Equation</b>	<b>177</b>
<b>C Natural Neumann Boundary Condition for the Convective Helmholtz Equation</b>	<b>180</b>
<b>D Linear Framework of the Convective Helmholtz Equation in Weak Form</b>	<b>183</b>
<b>E Simplification of the Projected Input Matrix</b>	<b>186</b>
<b>F Construction of the Input Matrices for the Generalized Discrete MAE</b>	<b>187</b>
<b>G Scattering Matrix Coefficients of the PCS Burners</b>	<b>189</b>



# List of Figures

1.1	Signal flow diagram of a closed-loop thermoacoustic system. . .	2
1.2	Schematic pressure trace (black curve) of a linearly unstable system with exponential growth at low amplitudes (red dashed curve) and nonlinear amplitude saturation (blue curve). . . . .	4
1.3	Modeling Cascade of suitable computational approaches to predict thermoacoustic instabilities with decreasing computational cost and increasing degree of modeling. . . . .	9
1.4	Workflow of the proposed sequential linear and nonlinear thermoacoustic stability analysis. . . . .	12
3.1	Schematic network representation of a series of ducts with different cross-sections and solid termination on both ends. . . . .	44
3.2	Schematic of a scattering matrix two-port. (a) Superposed scattering of incident waves. (b) Exclusive reflection of the incident wave at the downstream port. (c) Exclusive transmission of the incident wave at the upstream port. . . . .	45
3.3	Sketch of the procedure to characterize a multi-layer perforated resonator. . . . .	50
3.4	Sketch of a damped mechanical oscillator. . . . .	52
3.5	Reflection coefficient over normalized forcing frequency for different normalized damping factors $d/(m \omega_0)$ . . . . .	53

4.1	Workflow to model a gas turbine. (a) The complete gas turbine is characterized regarding the local Helmholtz number $He$ . (b) The compressor, the burner and swirler as well as the turbine are characterized by 1D networks. (c) The plenum and combustion chamber are resolved with 3D-CA using the boundary conditions and transfer matrix from the 1D networks as termination and coupling of the disconnected resolved domains, respectively.	60
4.2	Left: full iCHE with flux $\mathbf{F}$ and sources $S_{iCHE}$ . Center: hCHE (without sources) and reduced flux $\mathbf{F}^{M=0}$ . Right: resulting overall volumetric source $S_{iCHE}^{M=0}$ from erroneous fluxes $\epsilon_F^{M=0}$ and dropped sources $S_{iCHE}$ .	67
4.3	Schematic of a scattering matrix element connecting two low Mach number domains. (a) Complete scattering of characteristics. (b) Exclusive reflection of incident wave at downstream port. (c) Exclusive transmission of incident wave at upstream port.	75
4.4	Schematic of different approaches for the extrapolation of transfer functions $F$ specified for real valued frequencies $f$ to the complex plane with growth rate $\alpha$ following Schmid et al. [1]: extrusion (left) and filter (right).	79
4.5	Cross-sectional sketch of the simple test case.	82
4.6	Network model of the sudden area change connected to ducts of constant cross-sectional areas on both sides.	83
4.7	Mesh, axial Mach number field and coupled surfaces (grey) of the FEM setup.	84
4.8	Mode shapes in terms of velocity fluctuations of the first (a), second (b) and sixth (c) eigenmode of setup I for $M = 0.1$ , $\beta = 0.02$ .	86
4.9	Frequency and damping rate of the first eigenfrequency over the Mach number for $\beta = 0$ (cf. Tab. 4.2 for the legend).	87
4.10	Frequency and damping rate of the first eigenfrequency over the Mach number for $\beta = 0.02$ .	88
4.11	Frequency and damping rate of the second eigenfrequency over the Mach number for $\beta = 0$ .	88
4.12	Frequency and damping rate of the second eigenfrequency over the Mach number for $\beta = 0.02$ .	89

---

4.13	Frequency and damping rate of the third eigenfrequency over the Mach number for $\beta = 0.02$ . . . . .	89
4.14	Frequency and damping rate of the sixth eigenfrequency over the Mach number for $\beta = 0.02$ . . . . .	90
5.1	Schematic of the Generalized Discrete MAE coupled with the volumetric flame source model and the two boundary sources representing the damper models. . . . .	103
5.2	Ratio of the linear viscous ( $R_\mu$ ) and nonlinear vortical ( $R_\nu$ ) part of Bellucci's resistance at ambient conditions ( $p = 1$ bar, $T = 300$ K). Left: $r = 1$ mm, Center: $r = 2$ mm, Right: $r = 3$ mm. . . . .	107
5.3	Signal flow diagram of the nonlinear damper model and its coupling with the ROM of the combustor. . . . .	108
6.1	Sketch of a SIEMENS ENERGY H-Class can-annular combustion chamber based on Sattelmayer et al. [2]. . . . .	110
6.2	Disconnected FEM domains including the unstructured tetrahedral mesh of the investigated complex configuration. The burners connecting the two domains in terms of transfer matrices are indicated by double arrows. Top: Top view with the inlet, outlet and perforated liner patches highlighted in blue. Bottom left: View on the basket's face plate with the downstream coupling surfaces of the burners highlighted in blue. Bottom right: View on the plenum's face plate with the upstream coupling surfaces of the burners highlighted in blue. . . . .	112
6.3	Mean temperature (left) and mean volumetric heat release rate (right) fields interpolated on the FEM mesh of the investigated complex configuration. The excluded burner geometries are indicated by double arrows. . . . .	113
6.4	Schematic of a dual-layer resonator employed in the PCS. . . . .	115
6.5	Comparison of the resonator's reflection coefficients obtained from the original Bellucci model (black) and the state-space model based on a rational function fit of the ND Bellucci curve (red) at different acoustic amplitude levels (ND and OD). . . . .	117
6.6	1D network model of the PCS burners. . . . .	118

6.7	Energetically transformed scattering matrix coefficients of a single main burner obtained from a 1D network. . . . .	120
6.8	Stability map of eigenmodes computed in the vicinity of the target frequency $f_{0,PCS}$ . . . . .	122
6.9	Mode shapes of the PCS without resonators in the vicinity of the target frequency $f_{0,PCS}$ with the symbols in parentheses referring to the stability map in Fig. 6.8. . . . .	123
6.10	Eigenvector Gram matrices of the setup ‘ND Dampers’. Left: Inner product of right eigenvectors $\mathbf{V}$ . Center: Inner product of left eigenvectors $\mathbf{W}$ . Right: Inner product of left and right eigenvectors.	126
6.11	Compact subdomains with non-negligible heat release rate. . . . .	128
6.12	Temporal pressure evolution at four neighboring resonators including detailed views with corresponding FFTs. . . . .	130
6.13	Temporal evolution of the modal amplitude’s magnitudes $ \xi_n(t) $ over time. . . . .	131
6.14	Temporal evolution of the modal amplitude’s phase $\angle \xi(t)$ over time with detailed views of the unsynchronized and the synchronized state. . . . .	132
6.15	Comparison of the magnitude of boundary sources $S1$ and $S2$ for the linearly unstable eigenmode 1 (left) as well as the linearly stable eigenmodes 2 (center) and 7 (right). . . . .	133
6.16	Comparison of the period-averaged sources $\langle \xi \cdot \mathbf{B}_S \mathbf{u}_S \rangle_{t,n}$ for the linearly unstable eigenmode 1 (left) as well as the linearly stable eigenmodes 2 (center) and 7 (right). Top row: linear scale. Bottom row: logarithmic scale. . . . .	135
G.1	Energetically transformed scattering matrix coefficients of the pilot burner obtained from a 1D network. . . . .	189
G.2	Original scattering matrix coefficients of a single main burner obtained from a 1D network. . . . .	190
G.3	Original scattering matrix coefficients of the pilot burner obtained from a 1D network. . . . .	191



# List of Tables

- 4.1 Geometric and thermodynamic properties of the simple test case. 82
- 4.2 Setups for eigenfrequency computations of the simple test case. 85
  
- 5.1 Comparison of the Direct Modal Reduction (DMR), the Modal Amplitude Equations (MAE) and the combined Generalized Discrete MAE. . . . . 99
  
- 6.1 Operating conditions of the industrial-scale configuration. . . . 111
- 6.2 Geometric and thermodynamic properties of the dual-layer perforated resonators. . . . . 116
- 6.3 Acoustic velocity amplitudes for optimal damping of the dual-layer resonator using the multi-layer characterization and the fitted state-space model. . . . . 118
- 6.4 Parameters of the 1D network to acoustically describe the pilot and main burners of the PCS. The naming is in accordance with Fig. 6.6. . . . . 119
- 6.5 Configurations for the modal stability analysis of the PCS. . . . . 121



# Nomenclature

## Latin Letters

$A$	[m <sup>2</sup> ]	Area
$\mathbf{A}$	[ ]	System Matrix
$B$	[J/kg]	Non-Chemical Stagnation Enthalpy
$\mathbf{B}$	[ ]	Input Matrix
$c$	[m/s]	Speed of Sound
$\mathbf{C}$	[ ]	Output Matrix
$c_p$	[J/(kg·K)]	Specific Heat at Constant Pressure
$c_v$	[J/(kg·K)]	Specific Heat at Constant Volume
$C_d$	[ ]	Discharge Coefficient
$C_R$	[1/m]	Rayleigh Conductivity
$d$	[kg/s]	Damping Factor
$d$	[m]	Diameter
$D$	[m <sup>2</sup> /s]	Diffusion Coefficient
$D$	[ ]	Dissipation Coefficient
$\mathbf{D}$	[ ]	Feedthrough Matrix
$e$	[ ]	Exponential Function
$E$	[J/m <sup>3</sup> ]	System Energy Content
$\mathbf{E}$	[ ]	Descriptor Matrix
$E_n$	VU	Inner Product of the $n$ -th Left and Right Eigenfunction
$f$	[Hz]	Frequency
$f, g$	[m/s]	Characteristic Waves
$F$	[N]	External Force
$\mathbf{F}$	[J/(m <sup>2</sup> ·s)]	Flux Vector
$G$	[ ]	Green's Function
$h_s$	[J/kg]	Sensible Enthalpy
$i$	[ ]	Imaginary Unit

$\mathbf{I}$	[ ]	Identity Matrix
$I$	[J/m <sup>2</sup> ]	Intensity
$I_m$	[ ]	Modified Bessel Function of order $m$
$J_m$	[ ]	Bessel Function of the first Kind of order $m$
$k$	[rad/m]	Wave Number
$k$	[kg/s <sup>2</sup> ]	Spring Constant
$K_m$	[ ]	Modified Bessel Function of order $m$
$l$	[m]	Length
$m$	[kg]	Mass
$\mathbf{n}$	[ ]	Normal Vector
$n$	[ ]	Interaction Index
$\mathbf{N}$	[ ]	Nonlinearity Matrix
$p$	[Pa]	Pressure
$\dot{q}$	[J/(m <sup>3</sup> ·s)]	Volumetric Heat Release Rate
$r$	[m]	Radius
$R$	[J/(kg·K)]	Specific Gas Constant
$R$	[ ]	Reflection Coefficient
$R$	[kg/(m <sup>2</sup> ·s)]	Resistance
$s$	[rad/s]	Laplace Variable
$s$	[J/(kg·K)]	Entropy
$S$	VU	Volume Source
$t$	[s]	Time
$t$	[m]	Liner Thickness
$T$	[K]	Temperature
$T$	[ ]	Transmission Coefficient
$T_s$	[s]	Oscillation Period
$u/\mathbf{u}$	[m/s]	Velocity (Vector)
$\mathbf{u}$	VU	Input Vector
$V$	[m <sup>3</sup> ]	Volume
$\mathbf{V}$	VU	Right Eigenvector Matrix
$\mathbf{W}$	VU	Left Eigenvector Matrix
$\mathbf{x}$	[m]	Spatial Coordinates
$\mathbf{x}$	VU	State Vector
$X$	[kg/(m <sup>2</sup> ·s)]	Reactance
$y$	[ ]	Specific Admittance

<b>y</b>	VU	Output Vector
<b>Y</b>	[ ]	Mass Fraction
<b>z</b>	[ ]	Specific Impedance
<b>Z</b>	[kg/(m <sup>2</sup> ·s)]	Impedance

### Greek Letters

<b><math>\alpha</math></b>	[rad/s]	Growth Rate
<b><math>\beta</math></b>	[ ]	Total pressure loss coefficient
<b><math>\gamma</math></b>	[1/m]	Real Part of Howe's Conductivity
<b><math>\Gamma</math></b>	[ ]	Propagation Constant
<b><math>\delta</math></b>	[1/m]	Imaginary Part of Howe's Conductivity
<b><math>\delta</math></b>	[rad/s]	Damping Rate
<b><math>\delta</math></b>	[ ]	Dirac Delta
<b><math>\Delta</math></b>	[1/m <sup>2</sup> ]	Laplace Operator
<b><math>\Delta</math></b>	[m]	Field Displacement
<b><math>\epsilon</math></b>	VU	Erroneous Flux
<b><math>\zeta</math></b>	[ ]	Loss Coefficient
<b><math>\eta</math></b>	[ ]	Amplitudes of Green's Expansion Series
<b><math>\kappa</math></b>	[ ]	Ratio of Specific Heats
<b><math>\lambda</math></b>	[W/(m·K)]	Thermal Conductivity
<b><math>\Lambda</math></b>	[rad/s]	Eigenvalue Matrix
<b><math>\nu</math></b>	[m <sup>2</sup> /s]	Kinematic Viscosity
<b><math>\xi</math></b>	[ ]	Modal Amplitude
<b><math>\rho</math></b>	[kg/m <sup>3</sup> ]	Density
<b><math>\sigma</math></b>	[ ]	Porosity
<b><math>\tau</math></b>	[Pa]	Time-Lag
<b><math>\tau</math></b>	[Pa]	Viscous Stress Tensor
<b><math>\phi</math></b>	[ ]	Arbitrary Transport Variable
<b><math>\phi</math></b>	[ ]	Equivalence Ratio
<b><math>\varphi</math></b>	[m <sup>2</sup> /s]	Velocity Potential
<b><math>\varphi</math></b>	VU	Substitution Variable
<b><math>\chi</math></b>	VU	Left Eigenfunction
<b><math>\chi</math></b>	VU	Left Eigenvector
<b><b>X</b></b>	VU	Left Eigenvector Matrix

$\psi$	VU	Right Eigenfunction
$\Psi$	VU	Right Eigenvector
$\Psi$	VU	Right Eigenvector Matrix
$\omega$	[rad/s]	Real Valued Angular Frequency
$\omega_0$	[rad/s]	Angular Eigenfrequency of an Undamped Oscillator
$\omega_c$	[rad/s]	Complex Valued Angular Frequency
$\Omega$	[1/s]	Vorticity Vector

### Superscripts

$(\cdot)'$	Temporal Perturbation
$(\bar{\cdot})$	Temporally Averaged Field Quantity
$(\hat{\cdot})$	Fourier-/Laplace-Transformed Quantity
$(\overline{\cdot})$	Complex Conjugate
$(\check{\cdot})$	Identifier for Implicit State-Space Matrices
$(\cdot)^*$	Adjoint
$(\check{\cdot})$	Test Function
$(\dot{\cdot})$	First Order Time Derivative
$(\ddot{\cdot})$	Second Order Time Derivative
$(\cdot)^{[j]}$	$j$ -th Order Time Derivative
$(\cdot)^T$	Transposed

### Indices

$(\cdot)_0$	Aperture Area Average
$(\cdot)_a$	Acoustic
$(\cdot)_B$	Burner
$(\cdot)_C$	Compressor
$(\cdot)_d$	Damper
$(\cdot)_d$	Downstream
$(\cdot)_e$	End
$(\cdot)_{eff}$	Effective
$(\cdot)_l$	Loss
$(\cdot)_{lin}$	Linear

$(\cdot)_{mech}$	Mechanical
$(\cdot)_{nl}$	Nonlinear
$(\cdot)_{qs}$	Quasi-Steady
$(\cdot)_r$	Reflected
$(\cdot)_{red}$	Reduced
$(\cdot)_{res}$	Resonator
$(\cdot)_s$	Entropic
$(\cdot)_{st}$	Stochastic
$(\cdot)_t$	Transmitted
$(\cdot)_T$	Turbine
$(\cdot)_{tot}$	Total
$(\cdot)_{tr}$	Transfer
$(\cdot)_u$	Upstream
$(\cdot)_v$	Vortical
$(\cdot)_\mu$	Viscous

## Operators

$\langle \cdot \rangle_t$	Period Average
$\langle \cdot, \cdot \rangle$	Inner Product
$\Im$	Imaginary Part
$\mathcal{O}$	Landau Operator (Order of Magnitude)
$\Re$	Real Part

## Dimensionless Numbers

He	Helmholtz Number
$M$	Mach number
Sh	Shear Number
Sr	Strouhal Number

## Abbreviations

APE	Acoustic Perturbation Equations
ALE	Arbitrary Lagrangian Eulerian
BC	Boundary Condition
BVP	Boundary Value Problem
CA	Computational Acoustics
CHE	Convective Helmholtz Equation
CFD	Computational Fluid Dynamics
DMR	Direct Modal Reduction
DNS	Direct Numeric Simulation
DOF	Degrees of Freedom
FD	Frequency-Domain
FDF	Flame Describing Function
FEM	Finite Element Method
FFT	Fast Fourier Transform
FRF	Flame Response Function
FTF	Flame Transfer Function
HE	Helmholtz Equation
HF	High-Frequency
LEE	Linearized Euler Equations
LES	Large Eddy Simulation
LF	Low-Frequency
LHS	Left-Hand Side
LNSE	Linearized Navier-Stokes Equations
LRF	Linearized Reactive Flow
MAE	Modal Amplitude Equations
MF-LEE	Moving Flame Linearized Euler Equations
ND	Normally Damped
NLDE	Nonlinear Disturbance Equations
NLRPE	Nonlinear Reactive Perturbation Equations
NLWE	Nonlinear Wave Equation
NSE	Navier-Stokes Equations
OD	Optimally Damped
PCS	Platform Combustion System
PDE	Partial Differential Equations

PENNE	Perturbed Nonlinear Nonconservative Euler
RHS	Right-Hand Side
ROM	Reduced Order Model
TD	Time-Domain
(U)RANS	(Unsteady) Reynolds-Averaged Navier-Stokes Equations
VU	Varying Units
WE	Wave Equation







# 1 Introduction

In a world with an expanding wealth of a simultaneously rapidly increasing population [3] also the demand of energy considerably increases [4–7]. Still in 2020, approximately 80% of the overall global energy was supplied in the form of fossil energy carriers [7]. Their chemical energy is transformed into heat via combustion to power the electricity production, transportation or industrial processes. A wide range of emissions and pollutants such as  $CO$ ,  $CO_2$  or  $NO_x$  are produced in the process. Not only does this air pollution have a negative health effect [8] but it is also considered the main driver of anthropogenic, irreversible climate change [9, 10]. Since the share of electricity in the overall energy demand is expected to grow from 20% in 2020 to 50% by 2050 [7], the production of electricity has the highest potential to reduce the emission of greenhouse gases. In the international effort of limiting the mean global temperature rise to  $1.5^\circ\text{C}$  relative to the pre-industrial time [11], the expansion of electric power generation based on renewable energies (mainly wind and solar technologies) thus came into focus [12, 13]. Major challenges of these technologies are their natural power output intermittency and uncertainty as well as their integration into existing electric power systems maintaining a stable grid [14, 15]. With their high operational flexibility [16] and reduced greenhouse gas emissions compared to coal-fired power plants [17], gas turbines play a crucial role to counterbalance those issues in the transition to a power grid solely driven by renewable energies. But even beyond that, gas turbines fueled with synthetic fuels produced from renewable energies might be a long-term supplement to a carbon-neutral and stable power production [16, 18, 19]. A key to further enhance the significance of gas turbines for the energy transition is to steadily increase their efficiency. Notable potential for an efficiency increase lies in the optimization of thermoacoustic damping concepts. By providing a numerical framework to reliably predict thermoacoustic instabilities, the present thesis aims to support the development of novel gas turbine combustion chambers with increased efficiency, further mitigating their climate impact already in the near future.

## 1.1 Thermoacoustics in Gas Turbines

To cap the emission of pollutants and greenhouse gases from gas turbines, numerous industrialized nations implemented strict emission regulations [20]. Particularly  $NO_x$  emissions with their detrimental environmental impact were put into focus by governmental limits [21]. In contrast to the production of  $CO_2$ , which is exclusively determined by the used fuel and the machine efficiency, the formation of  $NO_x$ ,  $CO$  and other pollutants is significantly impacted by the combustion process [20]. To comply with the strict regulations, gas turbine manufacturers established the lean premixed combustion, also reducing the emission of unburnt hydrocarbons and soot [22]. However, this lean premixed operation of modern gas turbine combustion chambers features an increased susceptibility to self-excited thermoacoustic instabilities [23–25]. These are a result of complex interactions between the chemical reactions in the flame region, acoustics, aerodynamics and the fuel feed system as schematically represented in Fig. 1.1. Herein, the stochastic turbulent mo-

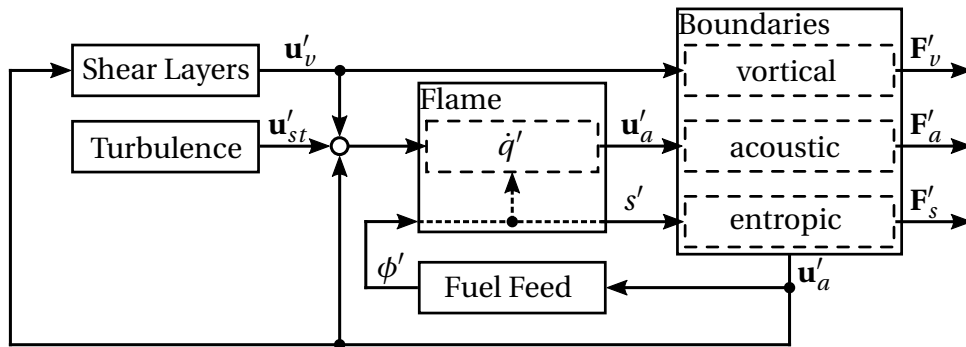


**Figure 1.1:** Signal flow diagram of a closed-loop thermoacoustic system.

tions of the fluid  $u'_{st}$  and an unsteady fuel feed causing equivalence ratio fluctuations  $\phi'$  lead to initially stochastic heat release fluctuations  $\dot{q}'$ . The instantaneous fluid expansion related to these perturbations of the flame causes the propagation of acoustic waves  $u'_a$ . At the system boundaries, large portions of the acoustic waves and the inherent acoustic energy are reflected. Apart from a direct impact of the reflected acoustic waves on the local rate of combustion, also an indirect impact is caused by the interaction with shear layers and the fuel feed system. The latter interaction may cause a modulation of the equivalence ratio fluctuations also being the root-cause of entropy fluctuations  $s'$ ,

mainly emerging within the heat release zone [26, 27]. These entropy waves manifest as temperature fluctuations and are therefore also referred to as hot-spots. Acoustic waves passing area discontinuities and interacting with shear layers lead to coherent vortical fluctuations  $\mathbf{u}'_v$  [28–32], which (when being created upstream of the flame) may impact the combustion processes. Similar to entropic fluctuations, also vortical fluctuations are transported convectively with the flow. When interacting with the system boundaries, the energy related to those fluctuations may be transformed back into acoustic energy. This is referred to as indirect combustion noise. Since the combustion chamber is not entirely confined by solid walls, considerable portions of the energy related to acoustic, vortical and entropic fluctuations may simply leave the combustor as fluctuating energy fluxes  $\mathbf{F}'$  at open boundaries such as the turbine inlet.

An essential prerequisite for the occurrence of thermoacoustic instabilities is a positive net energy gain fed into the pure acoustic part of the dynamic system. Assessing this net energy gain requires the balance of all driving and damping mechanisms included in the thermoacoustic system. Most conveniently, this is achieved by means of the generic integral energy conservation equation

$$\int_V \frac{\partial E}{\partial t} dV = \int_V S dV - \int_{\partial V} \mathbf{F} \cdot \mathbf{n} dA \begin{cases} > 0 & \text{unstable,} \\ < 0 & \text{stable.} \end{cases} \quad (1.1)$$

Equation (1.1) states that the rate of change of energy content  $E$  within the system of volume  $V$  is determined by volumetric sources and sinks  $S$  and the energy flux  $\mathbf{F}$  across the system boundaries  $\partial V$  with the outward pointing normal vector  $\mathbf{n}$ . If the energy content changes at a positive rate, the system is unstable, whereas it is labeled stable for negative rates of change. In a thermoacoustic system, the unsteady combustion is considered the primary supplier of acoustic energy, cf. Fig. 1.1. Already in the late 19th century, Lord Rayleigh [33] found that a flame may act as a heat engine generating acoustic energy, when adding heat at a state of increased pressure [34]. On the contrary, the flame is a heat pump, when the heat is added at decreased pressure levels. For periodic fluctuations of heat release and pressure, the instantaneous driving or damping is not very meaningful. Instead, it is more significant to evaluate the temporal average over an oscillation period  $T_s$ . Rayleigh's criterion may thus be formulated in terms of a time-averaged volumetric source

term as per

$$\langle S'_{\dot{q}} \rangle_t = \frac{1}{T_s} \int_{t-T_s}^t S'_{\dot{q}} dt \propto \frac{1}{T_s} \int_{t-T_s}^t p' \dot{q}' dt \begin{cases} |\angle p' - \angle \dot{q}'| < 90^\circ & \text{driving,} \\ \text{else} & \text{damping.} \end{cases} \quad (1.2)$$

A constructive interaction between the heat release of the flame and the combustion chamber acoustics is thus only obtained if the phase shift between the fluctuations of pressure and heat release rate is less than  $90^\circ$ . Further acoustic energy sources and sinks are founded on the interaction between acoustic, vortical and entropic fluctuations. For a comprehensive energy analysis, these sources and the corresponding energy fluxes across the boundaries must be accurately captured, which is a classic discipline of aeroacoustics.

An unstable thermoacoustic system typically exhibits a characteristic pressure trace as schematically shown in Fig. 1.2. At sufficiently low amplitudes, it fea-

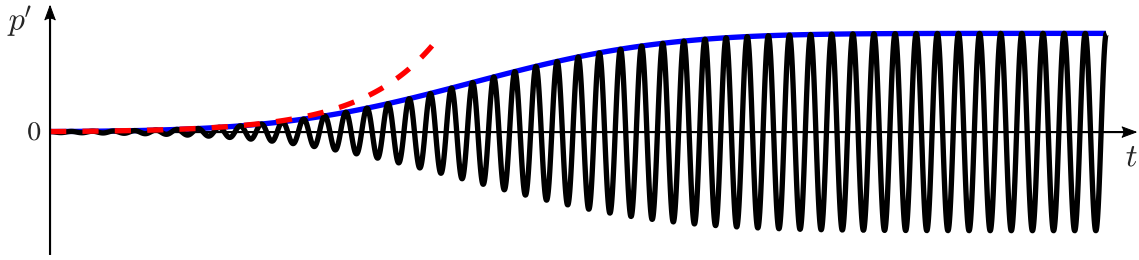


**Figure 1.2:** Schematic pressure trace (black curve) of a linearly unstable system with exponential growth at low amplitudes (red dashed curve) and nonlinear amplitude saturation (blue curve).

tures exponentially growing pressure amplitudes indicated by the red dashed curve. Like in any natural dynamic system, these amplitudes can not grow infinitely. Instead, the system is either destroyed or nonlinear mechanisms lead to an amplitude saturation (blue curve) before damage is inflicted on the system. To avoid the first scenario, it is crucial for manufacturers of gas turbines to identify potentially unstable oscillation states and the maximum pressure amplitudes they may reach. This implies two consecutive steps: first, the stability of the system must be evaluated at low amplitude levels. With the processes involved being of linear nature, this step is also referred to as linear stability analysis. Secondly, the mechanisms at elevated amplitudes must be investigated. These are predominantly nonlinear and lead to an equilibrium

of driving and damping effects. In turn, this results in oscillations at constant amplitude, also referred to as limit-cycle.

According to the universal energy conservation equation (1.1), an unstable system may be stabilized by either reducing the flame's driving or by increasing the acoustic damping within the system. Common stabilization methods are summarized in the following section.

## 1.2 Control Strategies and Damping Devices

Most generally, thermoacoustic control strategies may be classified into active and passive measures [35–38]. Since this work focuses on passive damping devices, these are reviewed in a little more detail after giving a coarse overview of the active counterpart.

### 1.2.1 Active Control

Actively controlling combustion dynamics requires an actuator, being an essential part of a controller in classic control theory. Depending on the input signal of the controller, one may distinguish between open-loop and closed-loop control.

Open-loop controllers impact a dynamic system independently of the system's response. An example of such open-loop control strategies in the field of thermoacoustics is the modulation of the fuel feed at specific operation points of the gas turbine prone to instabilities. With an active fuel staging concept, the equivalence ratio is spatially modulated to impact the flame response and thus its driving capabilities. Particularly an azimuthal staging concept has been shown to stabilize transversal thermoacoustic instabilities in annular combustion chambers [39–41]. Also the temporal modulation of the equivalence ratio has been observed to have a stabilizing effect on the combustion dynamics [42–44]. A commonality of both concepts is the potentially negative impact on the pollutant emissions, particularly  $NO_x$ .

A more versatile and efficient active control approach is to include the system's feedback into a closed-loop controller. In addition to actuators, this requires sensors to measure the system's response. Obviously, the open-loop concepts can also be used for closed-loop controllers. Additionally, active noise cancel-

lation techniques, which recently also gained increased popularity in the consumer audio market, have been investigated to control combustion dynamics [45, 46]. Depending on the measured pressure fluctuations, loudspeakers introduce ‘antisound’ to the system, being the anti-cyclic excitation of the dynamic system. Although this methodology requires an additional energy feed into the system, the anti-cyclic character of the energy actually contributes to the acoustic damping of the system. The greatest challenge of closed-loop concepts is the accurate measurement of the system’s state under the extreme thermodynamic conditions present in combustion systems.

For more detailed information regarding the active control of combustion dynamics the interested reader is referred to [37, 47–49].

### 1.2.2 Passive Control

Also the passive control strategies seek to either reduce the flame driving or to introduce further acoustic energy losses into the system. A notable procedure for the former approach involves design modifications of the burner, the fuel injector or the combustion chamber [50, 51]. In accordance with the Rayleigh integral, eq. (1.2), the acoustics-flame interactions may then be shifted from a constructive (i.e. driving) to a desctructive (i.e. damping) regime for certain unstable frequencies. However, such alleged design improvements may then destabilize other formerly stable oscillation states [34]. Furthermore, this procedure is impracticable for gas turbines with flexible fuel operation, since the fuel type was observed to have a strong impact on thermoacoustic instabilities [52, 53].

In practice, increasing the dissipation of acoustic energy is a more viable strategy. This may be achieved by installing passive damping devices<sup>1</sup> to the combustion chamber walls. A great overview of common damper designs and implementations in combustion systems is provided by Culick [54] and by Zhao et al. [55]. Baffles are frequently applied in rocket engines and will not be further addressed here. Instead, more emphasis is put on resonators and perforated liners, which are more commonly applied in gas turbine combustors.

All damping devices are based on the same working principle: acoustic energy is transformed either into internal energy via viscous dissipation or into coher-

---

<sup>1</sup>For brevity, such damping devices are henceforth also simply referred to as dampers.

ent vortical energy [29]. Both mechanisms are very pronounced close to the resonance frequency of resonators such as Helmholtz resonators or quarter-wave tubes [38, 56–60]. This is due to the considerable oscillation amplitudes observed in the resonator mouth at resonance [61], also leading to nonlinear damping mechanisms [62–64]. To avoid damage of the resonators from hot flue gases entering the resonators, they are usually purged with small mass flow rates of compressed air [65]. This bias flow and the associated shear layers are known to enhance the damping by means of an energy transfer from acoustic to vortical energy [66]. Similarly, perforated liners providing cooling air for the combustion chamber walls exhibit great acoustic damping capabilities [61]. Combining the benefits of resonators and perforated liners with bias flow lead to the development of honeycomb resonators [67, 68], single-layer perforated resonators [69] and multi-layer perforated resonators [70, 71]. With the transition from non-premixed to the cleaner lean premixed combustion, gas turbine manufacturers were forced to significantly increase the air mass flow in the burners. This was achieved at the expense of cooling air to still obtain sufficiently high turbine inlet temperatures [35]. This is a major criterion for a high machine efficiency [72] being desirable in the course of the energy transition. Therefore, optimized damping concepts must be tailored for future gas turbine generations with the goal of further reducing the purge air flow. This requires elaborate computational tools being capable of accurately capturing the linear and nonlinear mechanisms of damping devices to support the development process. An overview of some established computational approaches is provided subsequently.

### **1.3 Thermoacoustic Modeling Classification**

The occurrence of thermoacoustic instabilities is highly sensitive to geometric parameters as well as the operating conditions of the combustor and the attached components. As a consequence, a combustor's stability must ultimately be evaluated by testing in the final machine setup. At this stage, design modifications are normally unfeasible to implement. Also at earlier development stages, machine tests for the design iterations are highly expensive and hard to realize. Instead, reliable, accurate and robust numerical methods are required to aid throughout the entire design process.

Generally, computational approaches can be classified regarding their complexity [73]: High-order mathematical models come at high computational cost but are also expected to represent the underlying physics with high accuracy. The purpose of low-order approaches is to considerably reduce the computational complexity of the mathematical model. A common practice for an order reduction is to disaggregate the underlying physics into different mechanisms. Only one or few mechanisms are then resolved with an elevated accuracy, whereas the remaining mechanisms and their interaction are modeled and normally highly simplified. Consequently, the required spatial and temporal resolution reduces to the expected length and time scales inherent to the mechanisms considered in detail.

Thermoacoustic phenomena are governed by a wide range of physical mechanisms such as the propagation, refraction and scattering of acoustic waves, heat and mass diffusion, chemical reactions, vortex shedding or viscous dissipation. A mathematical model capturing all of these mechanisms is provided by the compressible *Navier-Stokes equations* (NSE) in conjunction with the conservation of mass and energy as well as one additional conservation equation for each species of a suitable reaction mechanism to account for chemical reactions. They form the origin of various numerical methods in the field of thermoacoustics. In the modeling cascade illustrated in Fig. 1.3 the most common methods are arranged according to their degree of modeling, which is normally inversely proportional to their computational cost.

Brute force approaches like *Direct Numeric Simulation* (DNS) and *Large Eddy Simulation* (LES) numerically solve the NSE without notable simplifications. The high spatio-temporal resolution associated with the various length and time scales of the individual flow phenomena come at high computational cost [74–80]. They are therefore reserved for academic purposes or as an alternative to late-stage testings.

Decomposing the instantaneous field quantities of the NSE into an a priori known time-averaged mean part and transient fluctuations around that mean field forms the basis of hybrid methods. The resulting *Nonlinear Reactive Perturbation Equations* (NLRPE) still include all physical mechanisms of the original equations and are thus of the same complexity as the brute force approaches. Therefore, to the author's best knowledge, such a set of equations has not been applied to study thermoacoustic phenomena (denoted by \* in

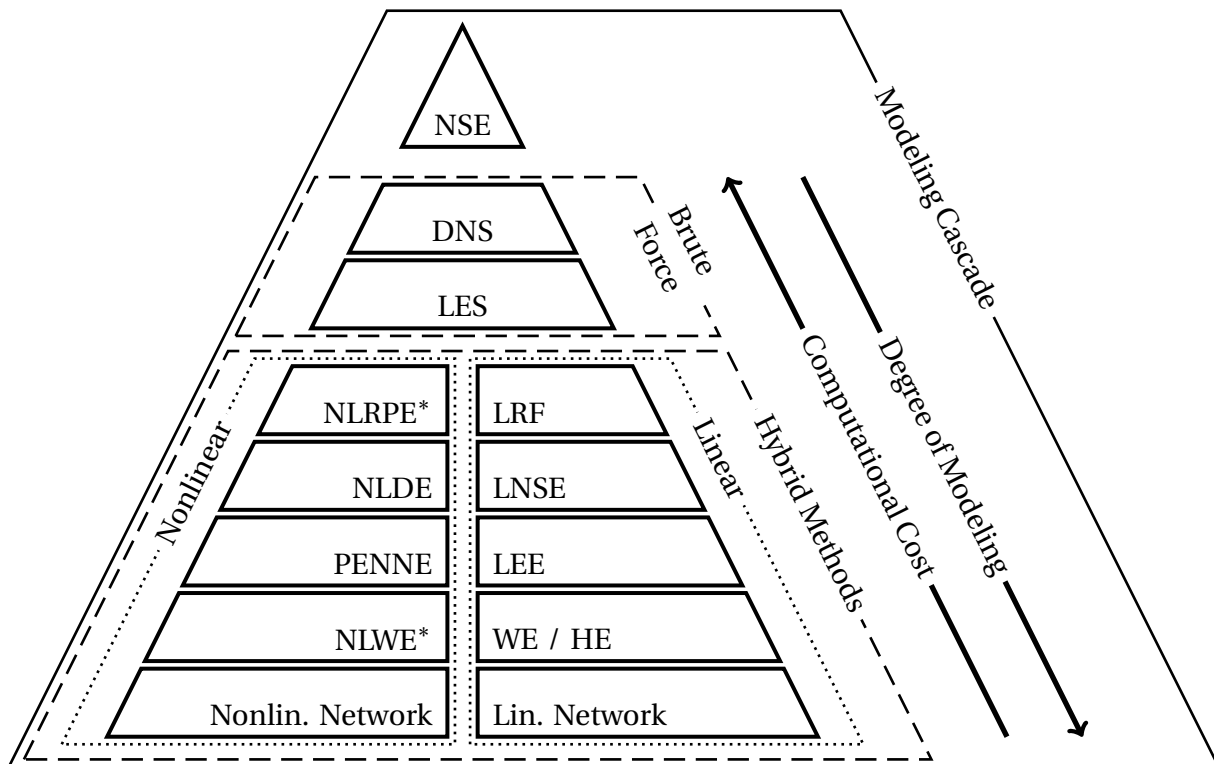


**Figure 1.3:** Modeling Cascade of suitable computational approaches to predict thermoacoustic instabilities with decreasing computational cost and increasing degree of modeling.

Fig. 1.3). However, the disturbance ansatz paves the way for the linearization of the equations, which reduces the computational complexity. The linear counterpart of the NLRPE is the *Linearized Reacting Flow* (LRF, cf. e.g. [81,82]). A significant reduction of the computational cost for both, linear and nonlinear hybrid approaches, can be achieved by introducing further simplifications and thus increasing the degree of modeling. Dropping the reaction mechanism yields the *Nonlinear Disturbance Equations* (NLDE, [83]) and its linear counterpart, the *Linearized Navier-Stokes Equations* (LNSE, cf. e.g. [84–86]). To still account for acoustics-flame interactions, it is common practice to employ a nonlinear *Flame Describing Function* (FDF) or a linear *Flame Response Function* (FRF), which may be obtained from experiments, numerical simulations or analytic models. Furthermore neglecting heat and mass diffusion as well as viscous dissipation yields the *Perturbed Nonconservative Nonlinear Euler* (PENNE) equations [87, 88] and after linearization the *Linearized Euler Equations* (LEE, cf. e.g. [89–91]). For low Mach-number flows it is reasonable

to assume a stagnant mean flow field. Then, the set of perturbation equations can be merged to a single wave equation. An application of a *Nonlinear Wave Equation* (NLWE) in the field of thermoacoustics is only known to the author in terms of an acoustic analogy: Here, the widely-used linear *Wave Equation* (WE) or its counterpart in the frequency-domain, the *Helmholtz Equation* (HE), are solved while the nonlinear terms are exclusively considered as sources or sinks for the linear wave propagation, cf. [92]. With the negligence of the mean flow velocity, the WE/HE describe pure irrotational acoustic wave propagation preventing the formation of vortical structures. While the acoustic wave propagation in complex three-dimensional geometries normally requires the numerical solution of the WE/HE, analytical solutions exist for simple geometries such as cylindrical ducts. Particularly in the low-frequency (LF) regime, the acoustic wave propagation in ducted geometries represented by this solution can virtually be considered as one-dimensional (1D). This paves the way for network models as similarly used to describe electric circuits. For this purpose, the real geometry under consideration is split and abstracted in terms of smaller acoustic network elements. The single elements are acoustically characterized either by analytic solutions of the WE/HE or by 1D perturbation equations. Depending on whether the selected equations to describe the individual elements are nonlinear or linearized, also the network methods can be classified as nonlinear or linear.

Each of the elements normally represents an acoustic two-port, which naturally enables the serial connection of multiple elements. Also the acoustics-flame interactions can be described by a two-port and can thus be included in the network. With fork elements, also the parallel connection of elements can be realized. This yields a modeling approach with very low computational cost, which allowed Bade [93] to model a lab-scale combustor. In conjunction with quasi 2D analytical solutions of the WE/HE, Evesque et al. [94, 95] even reproduced the transversal modes in annular combustors.

Still, this methodology is limited to simple geometries without local boundary conditions or distributed volume sources, e.g. as a result of non-compact flames (cf. chapter 3). For industrial combustors with complex geometries and local acoustic damping devices, these requirements are not satisfied in the high-frequency (HF) regime, which necessitates the employment of one of the more expensive and elaborate numerical approaches.

## 1.4 Scope and Structure of the Thesis

The thesis at hand targets the development of a numerical procedure for the investigation of thermoacoustic instabilities with the following specifications:

- **High efficiency:** A major objective is the applicability of the procedure to industrial systems. Fully resolving the corresponding complex, large-scale geometries is normally related to tremendous computational cost. Reducing this cost while still being capable of resolving complex three-dimensional processes requires a combination of suitable approaches.
- **Accuracy/Consistency:** Combining different approaches for an increased efficiency necessitates a careful assessment of the assumptions made within the individual approaches. Accurate results can only be obtained when ensuring consistent assumptions in the combined approaches.
- **Completeness:** Generally, there are two important aspects for the evaluation of thermoacoustic stability. Firstly, all potentially unstable oscillation states must be identified at low acoustic amplitudes. They are the origin of exponential amplitude growth dominated by linear processes. Secondly, the nonlinear saturation mechanisms need to be considered to evaluate the maximum pressure amplitudes expected at a specific operation point of the investigated configuration. A complete numerical framework comprises both aspects, i.e. the linear and the nonlinear stability.
- **Numerical robustness:** The aspired methodology should not be prone to numerical instabilities and spurious modes, independently of the investigated geometry and operation points.

A procedure complying with these requirements is proposed according to the workflow depicted in Fig. 1.4. The sequential character of the procedure stems from the individual computations that need to be performed consecutively with different tools. To keep the overall computational complexity low, the individual computational steps are limited to the lower end of the modeling cascade in Fig. 1.3.

Steps 1 to 3 represent the creation of a hybrid computational model. In the first step, the overall domain subject to the thermoacoustic investigation is

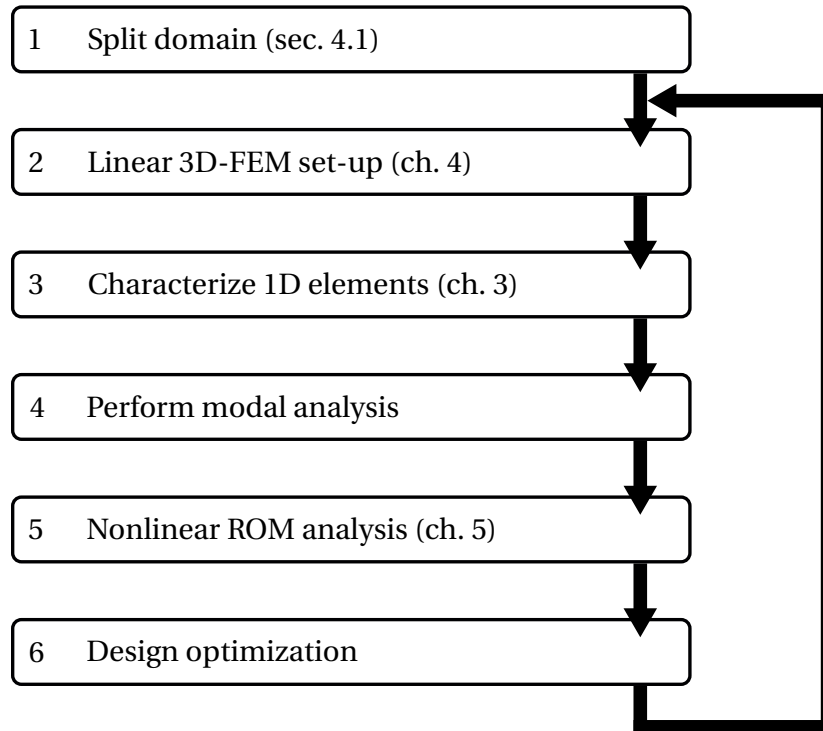


**Figure 1.4:** Workflow of the proposed sequential linear and nonlinear thermoacoustic stability analysis.

split into subdomains. Depending on the local thermodynamic and geometric parameters, only parts of the domain are resolved using three-dimensional *Finite Element Methods* (3D-FEM, step 2). Due to its numerical robustness, high availability in commercial solvers and low computational cost, the Helmholtz equation is predestined to describe the acoustic field in the 3D-FEM components. For an even further increased computational efficiency, the remaining components are characterized using 1D network models (step 3). These may, for instance, be used to couple spatially disconnected 3D-FEM domains or to include the damping mechanisms of resonators and perforated liners.

Such a 3D-Helmholtz approach coupled with 1D network elements is not a new concept: The group of Camporeale [96, 97] demonstrated this procedure for a simple annular combustion chamber. It was later similarly applied by Ni et al. [98, 99] to investigate the impact of flow-acoustic interactions on the thermoacoustic stability in an elaborate, industrial combustor. Discrepancies between the basic assumptions of the Helmholtz equation and 1D networks and their implications on the energy balance of the approach have not been

addressed in these works. This is investigated in-depth in the present work. Additionally, a methodology to include the mean flow advection of acoustic waves into the Helmholtz approach is developed. Ultimately, this yields an energetically consistent and highly accurate computational approach.

Steps 4 and 5 are the center core of the actual stability analysis. Using the afore developed model, a linear modal stability analysis is at first performed in step 4. The combined 3D-Helmholtz and 1D network approach including the major mechanisms contributing to the overall system's energy balance represents a nonlinear eigenvalue problem. Accurate eigenvalues are obtained when implementing a suitable linearization procedure. Using the linear modal results, a modal model order reduction procedure for the efficient computation of nonlinear saturation mechanisms in the time-domain is conducted. This combination of linear modal analysis and nonlinear *reduced order models* (ROM) in the field of thermoacoustics has been implemented by Hummel et al. [100–102] and was later also used by Hofmeister [103]. In their studies, the nonlinear saturation mechanisms are exclusively ascribed to a nonlinear acoustics-flame interaction. To also account for nonlinear resonators and dampers, a novel modified model order reduction procedure is developed.

Based on the results obtained from steps 4 and 5, design iterations of the thermoacoustic system may be performed to improve its stability. This will not be further addressed within this work.

Roughly following the proposed sequential numerical procedure, this thesis is structured as follows: After reviewing the most relevant mathematical models to describe aeroacoustic and thermoacoustic phenomena in chapter 2, the employed 1D network modeling procedure is introduced in chapter 3. The development of the entire linear modeling procedure (steps 1 to 4 of Fig. 1.4) is subject to chapter 4. In chapter 5 the nonlinear ROM procedure including nonlinear damping mechanisms of resonators is derived. Ultimately, the entire procedure is deployed to a geometrically complex configuration similar to a commercial SIEMENS ENERGY gas turbine combustor in chapter 6. This chapter is also meant to proof the significance of nonlinear damping for the amplitude saturation observed in combustors and to demonstrate the capability of the developed methodology to predict the impact of nonlinear dampers.



## 2 Thermoacoustic Fundamentals

The mathematical and physical fundamentals of the theoretical and numerical analysis of combustion dynamics are presented in this chapter. In accordance with the modeling cascade of Fig. 1.3, this phenomenon is governed by reactive flow equations, which are discussed first in section 2.1. The derivation of some perturbation equations commonly used in the fields of aero- and thermoacoustics from the general reactive flow equations is subsequently presented in section 2.2. Some of these equations describe a superposition of acoustic, vortical and entropic fluctuations (cf. section 2.2.3) and their interaction with each other. When solving them numerically for specific setups, it might be difficult to distinguish between the three types of fluctuations. To facilitate a more theoretical analysis of the impact of different flow mechanisms (e.g. turbulence) on the pure acoustic wave propagation, acoustic analogies have been established. In section 2.3 two important acoustic analogies are derived from the general flow equations. Transforming the governing equations into the frequency-domain as presented in section 2.4 is beneficial for both, analytical and numerical analysis of combustion dynamics. This also allows for a more pragmatic determination of the acoustic energy contained in a system, being subject of section 2.5. The acoustic energy balance of a system according to eq. (1.1) is significantly impacted by the energy flux across the system's boundaries. It is thus vital to specify boundary conditions suitable to the considered problem. The most common boundary conditions in the frequency-domain are discussed in section 2.6. Finally, a review on common methodologies to model the acoustics-flame interactions is provided in section 2.8. A closer look is taken at the coherent movement of the flame under acoustic excitation and its impact on the thermoacoustic stability.

### 2.1 Governing Reactive Flow Equations

A mathematical model for the unsteady combustion being the root-cause of thermoacoustic phenomena is provided by the conservation principles of a

reactive gas mixture consisting of  $N$  species. More specifically, these are the conservation of mass, momentum, energy and species. In a non-conservative, lagrangian form without any volume sources, they may be written as (cf. e.g. [86, 104, 105])

$$\frac{D\rho}{Dt} = -\rho \nabla \cdot \mathbf{u}, \quad (2.1a)$$

$$\rho \frac{D\mathbf{u}}{Dt} = -\nabla p + \nabla \cdot \underline{\boldsymbol{\tau}}, \quad (2.1b)$$

$$\rho \frac{DB}{Dt} = \dot{q} + \nabla \cdot (\lambda \nabla T) + \frac{\partial p}{\partial t} + \dot{\mathcal{Q}} + \nabla \cdot (\mathbf{u} \cdot \underline{\boldsymbol{\tau}}) + \nabla \cdot \left( \rho \sum_{k=1}^N h_{s,k} D_k \nabla Y_k \right), \quad (2.1c)$$

$$\rho \frac{DY_k}{Dt} = \nabla \cdot (\rho D_k \nabla Y_k) + \dot{\Omega}_k, \quad (2.1d)$$

with the material derivative  $D/Dt = \partial/\partial t + \mathbf{u} \cdot \nabla$  containing the convective transport with the velocity  $\mathbf{u}$ . Although only the momentum conservation equations (2.1b) represent the Navier-Stokes Equations in classical fluid mechanics, the whole set of conservation equations (2.1) will be referred to as reactive Navier-Stokes Equations (reactive NSE) for the sake of simplicity. The density  $\rho$ , pressure  $p$  and temperature  $T$  are related via a thermodynamic equation of state, commonly the ideal gas law

$$p = \rho RT \quad (2.2)$$

employing the specific gas constant  $R$  of the mixture. Viscous, thermal and species diffusion are represented by the viscous stress tensor  $\underline{\boldsymbol{\tau}}$ , the thermal conductivity  $\lambda$  and the species diffusion coefficients  $D_k$ . The non-chemical stagnation enthalpy  $B = h_s + (\mathbf{u} \cdot \mathbf{u})/2$  is the sum of the sensible enthalpy  $h_s$  and the kinetic energy. Its rate of change is impacted by external volumetric heat sources or sinks  $\dot{\mathcal{Q}}$  (e.g. ignition sparks) and by the volumetric heat release rate due to chemical reactions  $\dot{q}$ . The latter term is determined according to

$$\dot{q} = - \sum_{k=1}^N h_{f,k}^0 \dot{\Omega}_k, \quad (2.3)$$

where  $h_{f,k}^0$  and  $\dot{\Omega}_k$  are the enthalpy of formation and the mass production rate of species  $k$  within the chemical reaction. This rate of species formation also determines the rate of change of the mass fraction of each species in the fluid

mixture  $Y_k$ . The number of considered species and their corresponding production rate is normally preset by a chemical kinetic mechanism suitable for the individual combustion parameters. For the closure of the system of equations, a caloric equation of state is required. For ideal gases, this equation may be stated as [106, 107]

$$dh_s(T) = c_p(T) dT = T ds + \frac{1}{\rho} dp \quad (2.4)$$

with the specific heat capacity at constant pressure  $c_p$ . It is related to the specific gas constant via the the specific heat capacity at constant volume  $c_v$  via  $R = c_p - c_v$ . All three quantities are determined from the mass average over the species, e.g.  $c_p = \sum_{k=1}^N Y_k c_{p,k}$ . The caloric equation of state (2.4) also allows to express the energy equation in terms of the temperature, the entropy  $s$  or the pressure. The latter representation can be simplified by assuming equal heat capacities for all species  $c_{p,k} = c_p$  yielding

$$\frac{Dp}{Dt} = -\kappa p \nabla \cdot \mathbf{u} + (\kappa - 1) (\dot{q} + \nabla \cdot (\lambda \nabla T) + \dot{\mathcal{Q}} + \underline{\boldsymbol{\tau}} : (\nabla \mathbf{u})) , \quad (2.5)$$

with the ratio of specific heats  $\kappa = c_p/c_v$ . Although the assumption of equal heat capacities is an oversimplification in the presence of combustion, it is still often used [104]. Furthermore, for the derivation of acoustic equations in the following section, this form of the energy equation is an excellent starting point.

## 2.2 Perturbed Equations

The formation, propagation and decay of sound waves is a major subject in the field of acoustics. Exploiting the characteristics of sound waves allows for the derivation of equations for the specific description of acoustic phenomena in compressible media, which is subject of the present section.

### 2.2.1 Decomposition Approach

To describe dynamic processes such as acoustic wave propagation, all state and process variables may be split into a time-averaged mean part ( $\bar{\cdot}$ ) and a

fluctuating part  $(\cdot)'$ . For a generic quantity  $\phi$  the local, instantaneous value can then be expressed via

$$\phi(\mathbf{x}, t) = \bar{\phi}(\mathbf{x}) + \phi'(\mathbf{x}, t). \quad (2.6)$$

Inserting eq. (2.6) into the compressible, reactive NSE (2.1) yields a set of non-linear, reactive perturbation equations (NLRPE). The perturbation approach (2.6) results in a duplication of unknown variables, making the resulting set of perturbed equations unclosed. To overcome this issue, solving for the transient quantities is performed in two steps, constituting the basis of hybrid approaches: The steady-state quantity is determined first using *Computational Fluid Dynamics* (CFD) simulations, measurements or analytically. The latter is limited to simple, academic applications and sets of equations, whereas the comprehensive measurement of various spatially resolved field quantities is not feasible for applications with practical relevance. With CFD simulations, on the other hand, various field sizes can be calculated also for complex geometries. With their low computational cost due to the modeling of turbulent eddies, *Reynolds-Averaged Navier-Stokes* (RANS) simulations are particularly suitable for the use in cost-effective hybrid approaches. After determining the required mean flow quantities with CFD, the perturbed equations can finally be solved for the transient fluctuations around the steady-state by means of *Computational Acoustics* (CA), constituting the hybrid CFD/CA approaches. Generally, the transient fluctuations resolved by the NLRPE still comprise the full spectrum of spatio-temporal scales. In fact, the perturbed equations do not constitute a simplification compared to the original reactive NSE. A separation of the fluctuations into stochastic turbulent or periodic and coherent (such as acoustic) disturbances as discussed by Hummel [102] can only be achieved by introducing further assumptions and simplifications. Some of those simplifications of the NLRPE and the resulting sets of equations as per Fig. 1.3 are discussed in the subsequent sections.

### 2.2.2 PENNE and LEE

In the broad spectrum of spatio-temporal scales covered by the NLRPE, acoustic waves may be assigned to the larger spatial scales for a wide range of frequencies and thus temporal scales. This is in contrast to the random turbulent motions. According to the energy cascade, the corresponding stochastic

motions may be found throughout the entire spectrum of length-scales. For the specific investigation of coherent acoustic waves it is therefore not sufficient to filter the overall fluctuations in the relevant spatial spectrum, as the acoustic waves would be superimposed by turbulent fluctuations. Instead, it is beneficial to distinguish between random turbulent and coherent disturbances. This may be achieved by making use of the diffusive character of turbulent motions. Neglecting any diffusion within the disturbed equations thus eliminates the turbulent part in the fluctuation quantities. Similarly, diffusion is also an essential feature of combustion processes: without the diffusion of reactive radicals and heat from the reaction zone into the cold flow of reactants, a flame can not propagate. Dropping any diffusion mechanisms thus also prevents the disturbed equations from the resolution of transient combustion processes. Therefore, also the reaction mechanism and the species transport equations become obsolete. Instead, the transient heat release rate fluctuations due to chemical reactions  $\dot{q}'$  must be modeled (cf. section 2.8). This yields the Perturbed Nonconservative Nonlinear Euler (PENNE) equations [87, 88]:

$$\frac{\partial \rho'}{\partial t} + (\bar{\mathbf{u}} + \mathbf{u}') \cdot \nabla \rho' + \mathbf{u}' \cdot \nabla \bar{\rho} + (\bar{\rho} + \rho') \nabla \cdot \mathbf{u}' + \rho' \nabla \cdot \bar{\mathbf{u}} = 0 \quad (2.7a)$$

$$\frac{\partial \mathbf{u}'}{\partial t} + (\bar{\mathbf{u}} + \mathbf{u}') \cdot \nabla \mathbf{u}' + \mathbf{u}' \cdot \nabla \bar{\mathbf{u}} + \frac{1}{\bar{\rho} + \rho'} \left( \nabla p' - \frac{\rho'}{\bar{\rho}} \nabla \bar{p} \right) = \mathbf{0} \quad (2.7b)$$

$$\frac{\partial p'}{\partial t} + (\bar{\mathbf{u}} + \mathbf{u}') \cdot \nabla p' + \mathbf{u}' \cdot \nabla \bar{p} + \kappa (\bar{p} + p') \nabla \cdot \mathbf{u}' + \kappa p' \nabla \cdot \bar{\mathbf{u}} = (\kappa - 1) \dot{q}' . \quad (2.7c)$$

Note that the ratio of specific heats  $\kappa$  has been assumed to be spatially uniform, which is a commonly applied oversimplification in the context of thermoacoustics. The nonlinearity in terms of the fluctuation quantities within the PENNE (2.7) reproduces amplitude-dependent saturation mechanisms that may ultimately lead to limit-cycle oscillations. However, for most applications, the amplitude levels of fluctuating quantities and their gradients are much smaller than their mean flow counterpart, i.e.  $|\phi'|, |\nabla \phi'| \ll \bar{\phi}$ .<sup>1</sup> This justifies the linearization of the perturbed equations by neglecting second order fluctua-

<sup>1</sup>Normally, the acoustic velocity fluctuations are compared to the speed of sound. The condition for small amplitude levels would then read  $|\mathbf{u}'|, |\nabla \cdot \mathbf{u}'| \ll \bar{c}$ . However, at this point, no assumption regarding the mean flow velocity is made at all. And while terms of order  $\mathcal{O}(\bar{\mathbf{u}}\phi')$  are considered whereas terms of order  $\mathcal{O}(\mathbf{u}'\phi')$  are dropped, it is implicitly also required, that the velocity fluctuations are much smaller than the mean flow velocity  $|\mathbf{u}'|, |\nabla \cdot \mathbf{u}'| \ll \bar{\mathbf{u}}$ , cf. chapter 4.

tion terms. Note that this step precludes the fluctuating quantities from capturing significant deviations from the mean flow field at small temporal scales such as a flame contraction induced by large amplitude acoustic waves observed by Hofmeister [103, 108].<sup>2</sup> In fact, the mean flow field must be regarded as an average in a temporal section not being impacted by the small amplitude fluctuations subject to the linearization. For the PENNE the linearization procedure gives the Linearized Euler Equations (LEE), which read

$$\frac{\partial \rho'}{\partial t} + \bar{\mathbf{u}} \cdot \nabla \rho' + \mathbf{u}' \cdot \nabla \bar{\rho} + \rho' \nabla \cdot \bar{\mathbf{u}} + \bar{\rho} \nabla \cdot \mathbf{u}' = 0, \quad (2.8a)$$

$$\frac{\partial \mathbf{u}'}{\partial t} + \bar{\mathbf{u}} \cdot \nabla \mathbf{u}' + \mathbf{u}' \cdot \nabla \bar{\mathbf{u}} + \frac{\rho'}{\bar{\rho}} \bar{\mathbf{u}} \cdot \nabla \bar{\mathbf{u}} + \frac{1}{\bar{\rho}} \nabla p' = \mathbf{0}, \quad (2.8b)$$

$$\frac{\partial p'}{\partial t} + \bar{\mathbf{u}} \cdot \nabla p' + \mathbf{u}' \cdot \nabla \bar{p} + \kappa p' \nabla \cdot \bar{\mathbf{u}} + \kappa \bar{p} \nabla \cdot \mathbf{u}' = (\kappa - 1) \dot{q}'. \quad (2.8c)$$

It must be highlighted that terms being pure functions of mean flow field quantities have been dropped in eqs. (2.7) and (2.8). This is a common step in the derivation of perturbed equations, which requires the mean flow field to satisfy the equivalent set of basic equations, i.e. the Euler equations in the case of the PENNE and the LEE. This constitutes an inconsistency when applying those sets of equations to mean flow fields with chemical reactions. This inconsistency is inherent to most hybrid approaches used for the investigation of thermoacoustic phenomena.<sup>3</sup> Still, hybrid methods are a standard tool for the prediction of thermoacoustic stability.

### 2.2.3 APE

It has been demonstrated that the LEE (2.8) inherently comprise acoustic, vortical and entropic oscillation states [109]. Those oscillation states may interact with each other and exchange energy. This energy transfer is considered a major acoustic damping mechanism. However, indirect combustion noise due to the acceleration of hot spots [110] or whistling due to vortices interacting with rotational mean flow fields may in turn cause acoustic excitation [111, 112]. Consequently, the impact of vortical and entropic fluctuations may be considered as sources and sinks of acoustics. This is the principle of the source

---

<sup>2</sup>In contrast to the NLRPE, also the nonlinear PENNE are not capable of reproducing this particular mechanism due to the neglected reaction mechanism.

<sup>3</sup>Exceptions are the NLRPE and LRF when using mean flow fields determined using consistent assumptions.

term filtering for the LEE (2.8) as introduced by Ewert and Schroeder [109] and demonstrated in Appendix A. By filtering out convectively transported vortical and entropic components, the *Acoustic Perturbation Equations* (APE, (A.11)) result. Therefore, the APE describe pure acoustic wave propagation in arbitrary mean flow fields, whereas the interactions with the convectively transported vorticity and entropy are represented by the sources  $S_i^{v,s}$ . The insignificant drop in mean pressure common to most technical combustion systems may be exploited to further simplify the APE: from the mean momentum conservation equation, a constant pressure gives  $\nabla \bar{p} / \bar{\rho} = \bar{\mathbf{u}} \cdot \nabla \bar{\mathbf{u}} = 0$ . Then, the continuity equation is decoupled from the momentum and energy conservation equations<sup>4</sup> and the closed set of the simplified APE read

$$\frac{\partial \mathbf{u}'}{\partial t} + \frac{1}{\bar{\rho}} \nabla p' + \nabla (\bar{\mathbf{u}} \cdot \mathbf{u}') = \mathbf{S}_{\mathbf{u}}^{v,s,\nabla \bar{p}=0}, \quad (2.9a)$$

$$\frac{\partial p'}{\partial t} + \kappa \bar{p} \nabla \cdot \mathbf{u}' + \bar{\mathbf{u}} \cdot \nabla p' + \kappa p' \nabla \cdot \bar{\mathbf{u}} = (\kappa - 1) \dot{q}'. \quad (2.9b)$$

The momentum source  $\mathbf{S}_{\mathbf{u}}^{v,s,\nabla \bar{p}=0}$  excites vortical and entropic modes for isobaric mean flow fields. Therefore, it is equivalent to the first two terms of eq. (A.12b). To accurately reproduce the interactions between acoustics and vorticity or entropy, it needs to be modeled or obtained from high-fidelity simulations. Simply dropping the source prohibits any interaction between the oscillation modes and the fluctuation quantities. Then, the acoustic waves represented by the fluctuation quantities are neither excited nor attenuated by those interactions. Regarding its computational cost, solving the APE (2.9) is advantageous over the LEE, since not resolving the rather small-scale vortical and entropic modes also allows for coarser meshes. However, this comes at the drawback of either the complex modeling of the interaction between the oscillation modes or the inaccuracy by dropping this mechanism.

## 2.2.4 Convective Wave Equation

A rather academic simplification of the governing acoustic equations is obtained from the assumption of a uniform mean flow velocity. This only applies to flows in straight ducts or channels without any diffusion or heat release,

<sup>4</sup>This does not only apply to the APE but also to the LEE.

which does not apply to technically relevant applications. Still, this simplification gives a good insight into the propagation of acoustic waves subject to mean flow and forms the basis for acoustic analogies (cf. section 2.3) or one-dimensional acoustic network models (cf. section 3.1).

A uniform mean flow velocity implies zero gradients of the mean density and pressure. Assuming pure acoustic fluctuations, the corresponding terms in the APE<sup>5</sup> including the momentum source  $\mathbf{S}_u^{v,s,\nabla\bar{p}=0}$  and the volumetric heat release rate fluctuations  $\dot{q}'$  thus vanish. This is a prerequisite to eliminate the velocity fluctuations by subtracting the divergence of eq. (2.9a) multiplied by  $\bar{\rho}\bar{c}^2 = \kappa\bar{p}$  from the material derivative  $\bar{D}/Dt = \partial/\partial t + \bar{\mathbf{u}} \cdot \nabla$  of eq. (2.9b). This yields the convective wave equation for uniform mean flow fields:

$$\frac{\partial^2 p'}{\partial t^2} + 2\bar{\mathbf{u}} \cdot \nabla \frac{\partial p'}{\partial t} + \bar{\mathbf{u}}(\bar{\mathbf{u}} \cdot \nabla) \cdot \nabla p' - \bar{c}^2 \nabla^2 p' = 0. \quad (2.10)$$

Reducing this convective wave equation to one dimension denoted by the  $x$ -coordinate, a solution can be found analytically using an exponential approach. The solution may be expressed as

$$p'(x, t) = \bar{\rho}\bar{c} \left( |f| e^{i(\omega t - k^+ x)} + |g| e^{i(\omega t + k^- x)} \right), \quad (2.11)$$

where  $\omega$  is the angular frequency and  $k$  is the wave number. It may be observed that the two components of this solution represent downstream and upstream traveling waves  $f$  and  $g$ , respectively. Those characteristics propagate at the mean speed of sound  $\bar{c}$  altered by the mean flow velocity  $\bar{u}$  becoming manifest in the individual wave numbers

$$k^\pm = \frac{\omega}{\bar{c} \pm \bar{u}}, \quad (2.12)$$

for the downstream ( $k^+$ ) and the upstream ( $k^-$ ) traveling waves. Making use of the linearized momentum equation for uniform mean flow velocities, a solution equivalent to eq. (2.11) may be found for the acoustic velocity:

$$u'(x, t) = |f| e^{i(\omega t - k^+ x)} - |g| e^{i(\omega t + k^- x)}. \quad (2.13)$$

### 2.2.5 Wave Equation

Describing the propagation of sound waves in stagnant fluids ( $\bar{\mathbf{u}} = \mathbf{0}$ ) is a typical discipline in classical acoustics. This simplification is also a widespread

---

<sup>5</sup>The derivation can equivalently be performed using the LEE.

approximation to describe the sound propagation in low Mach-number flows [104, 105]. A stagnant fluid is not limited to uniform mean flow densities and may thus comprise temperature gradients. In the context of combustion, the variable temperature field plays a crucial role for the propagation of acoustic waves [113, 114]. While the uniform mean flow assumption was required to eliminate the velocity fluctuations for the derivation of the convective wave equation, this can be equivalently achieved for stagnant fluids with variable mean temperature fields. The corresponding wave equation is then obtained from the stagnant APE by subtracting the divergence of eq. (2.9a) multiplied by  $\bar{\rho}\bar{c}^2$  from the time-derivative of eq. (2.9b):

$$\frac{\partial^2 p'}{\partial t^2} - \bar{\rho}\bar{c}^2 \nabla \cdot \left( \frac{1}{\bar{\rho}} \nabla p' \right) = (\kappa - 1) \frac{\partial \dot{q}'}{\partial t}. \quad (2.14)$$

As mean field temperature gradients are explicitly allowed, also a volumetric heat release rate  $\dot{q}'$  is included as acoustic source. This equation is similar to the one proposed by Cummings [114]. In contrast to his explication, eq. (2.14) is not homentropic ( $ds = 0$ ) and does include entropy fluctuations in regions with non-vanishing mean flow entropy gradients. However, as such entropy fluctuations may only propagate advectively, they remain at their point of creation for quiescent fluids. For uniform stagnant mean fields, the 1D solution of the convective wave equation (2.11) also applies to the wave equation. In this case the characteristics propagate at the speed of sound yielding an equal wave number  $k = \omega/\bar{c}$  for both characteristics.

## 2.3 Acoustic Analogies

For many technical systems with turbulent flow fields, the emergence of aerodynamically induced sound is of high relevance. This mechanism is subject to the field of aeroacoustics and is inherently included in the basic conservation principles of fluid mechanics, eqs. (2.1). However, the identification of aeroacoustic sources and the analysis of their impact on the sound field from these equations is not trivial. One possible approach to facilitate such an analysis is the source term filtering developed for the APE in section 2.2.3. However, with the negligence of diffusion mechanisms also the impact of turbulence on the emergence of sound waves is dropped in the APE. Furthermore, the

set of four equations does not allow for an intuitive analytic description of the sound propagation. This last drawback is in contrast to the (convective) wave equation discussed in sections 2.2.4 and 2.2.5. Therefore, transforming the NSE (2.1) into the form of the wave equation allows for a more intuitive analysis of aeroacoustic sources, including turbulence. This is the basic idea of acoustic analogies, first introduced by Lighthill [115]. Since then, further acoustic analogies have been derived. Delfs [116] gives a great overview on the most relevant ones. In the present thesis, the principle of acoustic analogies will be exploited in chapter 4 to derive an exact convective wave equation from the APE. For this purpose, it is sufficient to introduce the analogies of Lighthill as well as Moehring, which are summarized below.

### 2.3.1 Lighthill's Analogy

In 1952, Lighthill [115] derived an acoustic analogy from the exact equations of fluid mechanics. Similar to the derivation of the wave equation (2.14), Lighthill's analogy is based on a cross-differentiation of the conservation of mass and momentum according to  $\partial/\partial t$  (2.1a)  $-\nabla\cdot$  (2.1b). Subsequent introduction of the disturbance approach (2.6) and reshaping yields the following form:

$$\frac{\partial^2 \rho'}{\partial t^2} - \bar{c}^2 \Delta \rho' = \nabla \cdot \nabla \cdot (\rho \mathbf{u} \mathbf{u} + (p' - \bar{c}^2 \rho') \mathbf{I} - \underline{\boldsymbol{\tau}}) . \quad (2.15)$$

The left-hand side (LHS) of this equation equals the wave equation for stagnant fluids in terms of density fluctuations. In the fashion of an analogy, the right-hand side (RHS) constitutes sources of the turbulent flow field on sound waves virtually propagating in a quiescent environment. While the Reynolds stress  $\rho \mathbf{u} \mathbf{u}$  may be relevant in turbulent flow regimes, the viscous stresses  $\underline{\boldsymbol{\tau}}$  are normally completely neglected. The second source term represents entropy fluctuations, which can be demonstrated by transforming the caloric equation of state (2.4) into

$$\frac{\bar{\rho}}{c_p} \bar{c}^2 s' = p' - \bar{c}^2 \rho' . \quad (2.16)$$

Using this relation, eq. (2.15) can also be transformed into an analogy in terms of the pressure fluctuations. It has to be noted that Lighthill's analogy is limited to mean flow fields with a uniform speed of sound  $\bar{c}$  and is thus not immediately applicable to thermoacoustics. Furthermore, the convection and re-

fraction (e.g. in boundary layers or temperature gradients) of acoustic waves are considered part of the sources, although being an essential feature of the sound propagation. On the other hand, analytic solutions of the sound pressure field can be obtained for given aeroacoustic sources using the framework of Green's function (cf. section 2.7).

### 2.3.2 Moehring's Analogy

To overcome the issues of Lighthill's analogy, Moehring [117] derived an analogy for acoustic wave propagation in non-reacting, single-species potential flows. This is achieved by using the stagnation enthalpy  $B$ , which is the native transport quantity of the energy conservation (2.1c). To obtain a compatible form of the momentum equation (2.1b), it is first transformed into Crocco's form by using the vector identity  $\mathbf{u} \cdot \nabla \mathbf{u} = 1/2 \nabla (\mathbf{u} \cdot \mathbf{u}) + \boldsymbol{\Omega} \times \mathbf{u}$  and the caloric equation of state (2.4) to give

$$\rho \frac{\partial \mathbf{u}}{\partial t} + \rho \nabla B = \rho \mathbf{u} \times \boldsymbol{\Omega} + \nabla \cdot \underline{\boldsymbol{\tau}} - T \rho \nabla s. \quad (2.17)$$

Here,  $\boldsymbol{\Omega} = \nabla \times \mathbf{u}$  denotes the vorticity, i.e. the rotation of the velocity field. Equivalent to the derivation of the convective wave equation, an analogy for the stagnation enthalpy is now obtained via  $\rho \frac{D}{Dt} \frac{1}{\rho \bar{c}^2} (2.1c) - \nabla \cdot (2.17)$ . Further transformations exploiting the continuity equation (2.1a) and the caloric equation of state (2.4) ultimately leads to Moehring's analogy as per

$$\rho \frac{D}{Dt} \frac{1}{\bar{c}^2} \frac{DB}{Dt} - \nabla \cdot (\rho \nabla B) = \frac{\partial}{\partial t} \left( \frac{\rho}{\bar{c}^2} T \frac{Ds}{Dt} \right) \nabla \cdot \left( \mathbf{u} \frac{\rho}{\bar{c}^2} T \frac{Ds}{Dt} \right) - \nabla \cdot (\rho \mathbf{u} \times \boldsymbol{\Omega}). \quad (2.18)$$

This analogy does not contain any simplifications and is thus generally applicable to thermoacoustic analyses. Although the wave operator on the LHS is similar to the one of the convective wave equation (2.10), using the stagnation enthalpy results in an analogy for potential flows [29, 30, 118] instead of uniform flows. The RHS represents sources due to the unsteady transport of entropy and vorticity. Still, this equation is of minor practical use as Green's function (cf. section 2.7) can not be applied to obtain an analytical solution. Furthermore, the formulation in terms of the stagnation enthalpy  $B$  impedes the formulation of intuitive boundary conditions for numeric simulations (cf. section 2.6).

## 2.4 Frequency-Domain Analysis

The perturbed equations and analogies discussed in the previous sections 2.2 and 2.3 describe the evolution of disturbance quantities over time, which may be solved numerically for complex geometries. However, the computation in the time-domain (TD) comes at a number of drawbacks:

- Hybrid linear methods like the LRF, LNSE or LEE still include acoustic, vortical and entropic fluctuations comprising multiple time scales. Particularly their interaction may cause fast changes in the acoustic field [119]. To obtain reliable results, these scales must be resolved with sufficiently small time step sizes correlated with high computational cost.
- The LEE also include Kelvin-Helmholtz instabilities, which may grow infinitely due to the lack of nonlinear terms and dissipation mechanisms. Then, these instabilities may obliterate the solution of the acoustic wave propagation [120].
- Boundary conditions representing acoustic liners or resonators exhibit a frequency-dependent behavior [67, 119, 121, 122]. Similarly, the flame response to acoustic excitation strongly depends on the oscillation frequency, as can be seen from the low-pass filter characteristic of laminar flames (cf. e.g. [123]). Transforming this frequency-dependency into the TD is a very complex task (cf. e.g. [122, 124]).
- The solution in the TD prevents a comprehensive modal stability analysis as pursued in the present thesis.

All of the above issues may be overcome by transforming the equations under consideration into the frequency-domain (FD). A common hypothesis for the transformation is the time-periodic character of the fluctuation quantities. Then, exploiting the Fourier-series theory, the disturbances can be expressed as a series of time-harmonic oscillations with fixed frequencies [24, 125]. This is particularly advantageous for linear sets of equations, as the single harmonic frequencies can then be considered individually. Making use of the time-harmonic character, each disturbed quantity can be expressed as  $\Phi'(\mathbf{x}, t) = \hat{\Phi}(\mathbf{x})e^{i\omega t}$ . Here, the hat denotes the (complex-valued) spatial oscillation field and  $\omega$  is the angular frequency. This approach corresponds to a

Fourier-transformation of the equations under consideration, which is limited to real-valued angular frequencies. However, in the context of stability analysis in the linear regime, the oscillation signals are expected to exponentially grow or decay in time due to flame-acoustic interactions and dissipation mechanisms. Such quasi-harmonic oscillations require the transformation using the Laplace transform according to

$$\mathcal{L}\{\Phi'(t, \mathbf{x})\} = \int_0^{\infty} \Phi'(t, \mathbf{x}) e^{-st} dt = \hat{\Phi}(s, \mathbf{x}) . \quad (2.19)$$

This is equivalent to expressing each disturbed quantity as

$$\Phi'(\mathbf{x}, t) = \hat{\Phi}(\mathbf{x}) e^{st} . \quad (2.20)$$

Note that this procedure is limited to linear acoustic equations since non-linear terms are transformed into convolutions in the FD, which are unfeasible to resolve. The Laplace variable  $s$  is related to a commonly used complex angular frequency via  $s = i\omega_c = \alpha + i2\pi f$ , being a function of the growth rate  $\alpha$  and the oscillation frequency  $f$ . Important features of the Laplace transform are the differentiation property  $\mathcal{L}\left\{\frac{\partial}{\partial t}\Phi'(t)\right\} = s\hat{\Phi}(s)$  and the integration property  $\mathcal{L}\left\{\int_0^t \Phi'(t) dt\right\} = \frac{1}{s}\hat{\Phi}(s)$ . Exemplarily applying this transformation to the inhomogeneous wave equation (2.14) and making use of the assumption  $\kappa\bar{p} = \bar{\rho}\bar{c}^2 = \text{const.}$  suitable for stagnant media yields the inhomogeneous Helmholtz equation for variable mean temperature fields

$$s^2 \hat{p} - \nabla \cdot (\bar{c}^2 \nabla \hat{p}) = s (\kappa - 1) \hat{q} . \quad (2.21)$$

This equation is also referred to as *Sturm-Liouville Eigenvalue Problem*. As this name also indicates, the transformation into the FD paves the way for eigenvalue (or modal) analyses.

## 2.5 Acoustic Energy

The stability of any confined (thermo-) acoustic system may be determined by evaluating the rate of change of acoustic energy content  $E$  within the system according to the generic energy conservation eq. (1.1). Similar to the source term based on the Rayleigh criterion, eq. (1.2), it is also more meaningful to evaluate the acoustic energy content and the acoustic energy fluxes as a temporal average. Suitable expressions for these quantities can not be found on

the basis of linear energy correlations, since the integral over an oscillation period of the corresponding time-harmonic energy oscillations vanishes. To overcome this issue, Cantrell and Hart [126] first analyzed the acoustic energy using second order fluctuations, which are neglected when using linear disturbed equations. They ultimately arrive at formulations for the acoustic energy and the energy flux as a function of first order fluctuations according to

$$E^{v,s=0} = \frac{p'^2}{2\bar{\rho}\bar{c}^2} + \frac{1}{2}\bar{\rho}\mathbf{u}'^2 + \rho'\bar{\mathbf{u}} \cdot \mathbf{u}', \quad (2.22a)$$

$$\mathbf{F}^{v,s=0} = \underbrace{\left(\frac{p'}{\bar{\rho}} + \bar{\mathbf{u}} \cdot \mathbf{u}'\right)}_{=B'} \underbrace{\left(\bar{\rho}\mathbf{u}' + \frac{\bar{\mathbf{u}}}{\bar{c}^2}p'\right)}_{=\dot{\mathbf{m}}'}. \quad (2.22b)$$

The derivation of Cantrell and Hart [126] was limited to homentropic potential flows (no vorticity and entropy fluctuations, superscript  $v, s = 0$ ), which do not contain any volumetric acoustic sources or sinks  $S$ . Later, Morfey [127] introduced sink terms  $S$  accounting for energy losses resulting from viscosity and heat conduction. Myers [128] finally derived a general formulation for arbitrary mean flow fields. For the specific application to thermoacoustics, Brear et al. [129] expressed Myers' energy corollary as

$$E = \frac{p'^2}{2\bar{\rho}\bar{c}^2} + \frac{1}{2}\bar{\rho}\mathbf{u}'^2 + \rho'\bar{\mathbf{u}} \cdot \mathbf{u}' + \frac{\bar{\rho}\bar{T}}{2c_p} s', \quad (2.23a)$$

$$\mathbf{F} = \left(\frac{p'}{\bar{\rho}} + \bar{\mathbf{u}} \cdot \mathbf{u}'\right) \left(\bar{\rho}\mathbf{u}' + \frac{\bar{\mathbf{u}}}{\bar{c}^2}p'\right) + \bar{\rho}\bar{\mathbf{u}}T' s', \quad (2.23b)$$

$$D = \left(\bar{\rho}\mathbf{u}' + \frac{\bar{\mathbf{u}}}{\bar{c}^2}p'\right) \cdot (\boldsymbol{\Omega}' \times \bar{\mathbf{u}} + \bar{\boldsymbol{\Omega}} \times \mathbf{u}' - s'\nabla\bar{T}) + \bar{\rho}\bar{\mathbf{u}} \cdot (s'\nabla T') + \frac{\dot{q}'T'}{\bar{T}} - \frac{\bar{q}}{\bar{T}^2}T'^2. \quad (2.23c)$$

All of the terms in eqs. (2.22) and (2.23) are of second order in the fluctuation quantities. To obtain the more meaningful periodic average of the product of two quasi-harmonically quantities  $\Phi'_1$  and  $\Phi'_2$ , the following identity can be exploited

$$\langle \Phi'_1 \cdot \Phi'_2 \rangle_t = \frac{1}{T_s} \int_{t-T_s}^t \Phi'_1 \cdot \Phi'_2 dt \approx \frac{1}{2} \Re \left\{ \overline{\hat{\Phi}_1} \cdot \hat{\Phi}_2 \right\}, \quad |\alpha| \ll f, \quad (2.24)$$

where  $T_s$  is the oscillation period and  $\Re$  and  $\overline{(\cdot)}$  denote the real part and the complex conjugate of a complex valued quantity, respectively. This means that

the temporal average of quadratic fluctuation terms can be expressed in terms of their corresponding Laplace transforms. Note that eq. (2.24) is only valid for small absolute values of the growth rate  $\alpha$  in comparison to the oscillation frequency  $f$ .

## 2.6 Boundary Conditions

The acoustic equations discussed in section 2.2 are partial differential equations (PDE) with the solution functions depending on time and the three spatial coordinates. In order to obtain unique solutions, suitable initial and boundary conditions need to be specified. Therefore, such PDEs are also referred to as initial-boundary value problems. The initial values are not required for equations in the FD such as the Sturm-Liouville problem (2.21), making it a pure boundary value problem (BVP). The initial or boundary conditions of a partial differential equation of order  $n$  may be specified up to the order  $n - 1$ . Representative for a second order PDE, the inhomogeneous Sturm-Liouville problem may be written as a well-posed BVP according to

$$s^2 \hat{p} - \nabla (\bar{c}^2 \nabla \hat{p}) = s(\kappa - 1) \hat{q} \quad \text{in } V, \quad (2.25a)$$

$$a \hat{p} + b \nabla \hat{p} \cdot \mathbf{n} = h \quad \text{on } \partial V. \quad (2.25b)$$

If the overall boundary  $\partial V$  is split into multiple sub-boundaries, a boundary condition in the form of eq. (2.25b) must be specified for each sub-boundary. Depending on the parameters  $a$  and  $b$ , different types of boundary conditions may be realized [130]:

- $a \neq 0, b = 0$  is a *Dirichlet* boundary condition (first type),
- $a = 0, b \neq 0$  is a *Neumann* boundary condition (second type),
- $a \neq 0, b \neq 0$  is a *Robin* boundary condition (third type).

Common physical boundary conditions and their characterization with the above listed types are introduced subsequently.

### 2.6.1 Open End Boundary

An *open end* boundary is connecting the domain  $V$  to the atmosphere. Similar to *pressure outlet* boundary conditions commonly applied in CFD simulations, the atmospheric pressure is assumed to be constant. Therefore, for an ideal open end boundary condition, the pressure fluctuations must vanish, i.e.

$$\hat{p} = 0. \quad (2.26)$$

This corresponds to a frequency-independent, homogeneous ( $h = 0$ ) Dirichlet boundary condition.

### 2.6.2 Slip Wall Boundary

The *slip wall* boundary for acoustic equations can be formulated analogously to fluid mechanics. While tangential fluid motion is permitted, the normal velocity components must vanish at sound hard slip walls:

$$\hat{\mathbf{u}} \cdot \mathbf{n} = -\frac{1}{s\bar{\rho}} \nabla \hat{p} \cdot \mathbf{n} = 0. \quad (2.27)$$

The first equality is a consequence of the linearized momentum equation for quiescent media in the FD. It reveals that the slip wall is a homogeneous Neumann type boundary condition.

### 2.6.3 Impedance Boundary

The concept of the acoustic *impedance* was borrowed from electrical engineering. There, it relates the complex valued signals of voltage drop to current flowing through a circuit element. The acoustic counterpart is referred to as *transfer impedance*  $z_{tr}$  and relates the acoustic pressure difference across an acoustic element to the acoustic velocity (cf. chapter 3). It can also be expressed as a local quantity to describe the local acoustic field and may thus serve as a boundary condition as per

$$Z = \frac{\hat{p}}{\hat{\mathbf{u}} \cdot \mathbf{n}} = R + iX. \quad (2.28)$$

The real and imaginary parts of the complex valued impedance are referred to as *resistance*  $R$  and *reactance*  $X$ , respectively. A normalized representation may

be obtained by means of the characteristic impedance  $\bar{\rho}\bar{c}$  of a medium:

$$z = \frac{\hat{p}}{\bar{\rho}\bar{c}\hat{\mathbf{u}} \cdot \mathbf{n}}. \quad (2.29)$$

Using the relation between the boundary normal velocity and the pressure used for the wall boundary condition (2.27) and comparing the impedance to the general boundary condition representation (2.25b) discloses the homogeneous Robin type of the impedance boundary.

While the implementation of a slip wall boundary and an open end boundary may be equally achieved for acoustic equations in TD, this is not as straightforward for the general impedance as this would imply a temporally varying boundary condition (see e.g. [118, 131]). Further difficulties for the TD implementation are caused by the general frequency dependent behavior of the impedance (cf. the damper models in section 3.3), which was addressed by Morgenweck [124].

In the case of 1D sound propagation, the primitive variables  $\hat{p}$  and  $\hat{u}$  can be related to the characteristic waves found in the solution of the convective wave equation (2.11) and (2.13) as per

$$\begin{pmatrix} \frac{\hat{p}}{\bar{\rho}\bar{c}} \\ \hat{u} \end{pmatrix} = \begin{pmatrix} 1 & 1 \\ 1 & -1 \end{pmatrix} \begin{pmatrix} \hat{f} \\ \hat{g} \end{pmatrix}. \quad (2.30)$$

The complex valued characteristics  $\hat{f}$  and  $\hat{g}$  are also called *Riemann Invariants* [132]. They may be used to transform the specific impedance to

$$z = \frac{\hat{p}}{\bar{\rho}\bar{c}\hat{u}} = \frac{\hat{f} + \hat{g}}{\hat{f} - \hat{g}} = \frac{1 + R}{1 - R}, \quad (2.31)$$

$$R = \frac{\hat{g}}{\hat{f}} = -\frac{1 - z}{1 + z}. \quad (2.32)$$

The *reflection coefficient*  $R$  relates the complex amplitudes of a (normally scattered) upstream traveling wave  $\hat{g}$  and a (normally incident) downstream traveling wave  $\hat{f}$ .

#### 2.6.4 Energetically Neutral Boundaries

As shown in 2.5, the energy content of a system is significantly impacted by the energy fluxes at its boundaries. For the pure investigation of the driving or

damping potential of specific sources it might be useful to prohibit any energetic flux at the boundary. Such energetically neutral boundary conditions are specifically useful for systems, which are not restricted to quiescent fluids as the BVP (2.25). Assuming a homentropic acoustic field, energetical neutrality of the boundaries can be achieved according to eq. (2.22b) by two different requirements, which can be reformulated into impedance representations:

1. Zero stagnation enthalpy fluctuations ( $\hat{B} = 0$ ):

$$\hat{B} = \left( \frac{\hat{p}}{\bar{\rho}} + \bar{\mathbf{u}} \cdot \hat{\mathbf{u}} \right) \stackrel{!}{=} 0 \rightarrow z^{\hat{B}=0} = -\frac{\bar{\mathbf{u}} \cdot \mathbf{n}}{\bar{c}} = -\mathbf{M} \cdot \mathbf{n}. \quad (2.33)$$

Here,  $\mathbf{M} = \frac{\bar{\mathbf{u}}}{\bar{c}}$  is the mean flow Mach number vector representing the local relation between the mean flow velocity and the speed of sound. To obtain this simplified impedance formulation, the velocities of mean flow and fluctuating field are required to be parallel to the outward pointing normal vector  $\mathbf{n}$ . Otherwise, the velocity fluctuation vector cannot be eliminated from this expression. This assumption is reasonable, if the flow field downstream of the boundary can be assumed one-dimensional, which will be discussed in more detail in chapter 3. It may be noted that for vanishing mean flow velocities, the stagnation enthalpy reduces to the open end boundary. This corresponds to  $z^{\hat{B}, \mathbf{M}=0} = 0$  and  $R^{\hat{B}, \mathbf{M}=0} = 1$ , which is only energetically neutral for quiescent fluids.

2. Zero mass flow fluctuations ( $\hat{\mathbf{m}} = 0$ ):

$$\hat{\mathbf{m}} = \bar{\rho} \hat{\mathbf{u}} + \frac{\bar{\mathbf{u}}}{\bar{c}^2} \hat{p} \stackrel{!}{=} 0 \rightarrow z^{\hat{\mathbf{m}}=0} = -\frac{\bar{c}}{\bar{\mathbf{u}} \cdot \mathbf{n}} = -\frac{1}{\mathbf{M} \cdot \mathbf{n}}. \quad (2.34)$$

This impedance formulation is not subject to the restriction of one-dimensionality and is therefore more versatile. It reduces to the slip wall boundary condition when assuming a stagnant mean flow field, which corresponds to  $z^{\hat{\mathbf{m}}, \mathbf{M}=0} = -\infty$  and  $R^{\hat{\mathbf{m}}, \mathbf{M}=0} = -1$ .

A very useful quantity to assess the energy reflected at an arbitrary boundary with mean flow is the energetic reflection coefficient<sup>6</sup> [133], which will not be further addressed here.

---

<sup>6</sup>This is not to be confused with the 'classic' reflection coefficient of eq. (2.32) relating the complex amplitudes of reflected and incident waves.

## 2.7 Green's Function of the Sturm-Liouville Problem

For the analysis of a system's response to arbitrary volumetric or boundary sources, *Green's function* is of great use. It is a common methodology to investigate the influence of aerodynamic sources on the acoustic field (cf. e.g. [134–138]). Culick adapted the method for the investigation of thermoacoustic phenomena. A thorough description of his work is provided in [54]. In the course of the present thesis, Green's function approach will be exploited to derive a methodology for the coupling of unstable thermoacoustic systems with nonlinear damper models leading to limit-cycle oscillations (cf. chapter 5). To begin with, the general framework is presented in this section, roughly following the explications of Culick [54] and Schuermans [49].

Green's function  $G$  represents the unit impulse response of a system. Regarding the Sturm-Liouville BVP (2.25), it is defined as the solution of

$$s^2 \hat{G}(\mathbf{x}|\mathbf{x}_0) - \nabla (\bar{c}^2 \nabla \hat{G}(\mathbf{x}|\mathbf{x}_0)) = \delta(\mathbf{x} - \mathbf{x}_0) \quad \text{in } V, \quad (2.35a)$$

$$a \hat{G}(\mathbf{x}|\mathbf{x}_0) + b \nabla \hat{G}(\mathbf{x}|\mathbf{x}_0) \cdot \mathbf{n} = h \quad \text{on } \partial V. \quad (2.35b)$$

The argument of Green's function for an eigenvalue problem  $\hat{G}$  indicates the system's response in space  $\mathbf{x}$  as a result of a point source at the location  $\mathbf{x}_0$ . This point source is given by the Dirac delta with the important property

$$\langle \delta(\mathbf{x} - \mathbf{x}_0), \phi(\mathbf{x}) \rangle = \phi(\mathbf{x}_0), \quad (2.36)$$

where the chevrons  $\langle \cdot \rangle$  denote the inner product of two square-integrable, complex-valued functions  $\phi_1$  and  $\phi_2$ :

$$\langle \phi_1, \phi_2 \rangle = \iiint_V \overline{\phi_1(\mathbf{x})} \phi_2(\mathbf{x}) \, dV. \quad (2.37)$$

The complex conjugate of continuous functions represented by an overline is equivalent to the conjugate transpose required for dot products, which is the inner product for complex vector spaces (e.g. as a result of spatial discretization).

Before discussing how Green's function may be used to find a solution of the original BVP, an equation to describe Green's function is initially pursued. For this purpose, Green's function is expressed in terms of the series expansion

$$\hat{G}(\mathbf{x}|\mathbf{x}_0) = \sum_{n=0}^{\infty} \eta_n(\mathbf{x}_0) \hat{\psi}_n(\mathbf{x}), \quad (2.38)$$

with the entirety of  $\psi_n$  forming a basis of the solution space. They satisfy the homogeneous BVP as per

$$s_n^2 \hat{\psi}_n(\mathbf{x}) - \nabla (\bar{c}^2 \nabla \hat{\psi}_n(\mathbf{x})) = 0 \quad (2.39)$$

and are thus also referred to as eigenfunctions of the system. To find the coefficients of the series expansion  $\eta_n$ , the series expansion (2.38) is inserted into the partial differential equation (2.35a) resulting in

$$s^2 \sum_{n=0}^{\infty} \eta_n(\mathbf{x}_0) \hat{\psi}_n(\mathbf{x}) - \nabla \left( \bar{c}^2 \nabla \sum_{n=0}^{\infty} \eta_n(\mathbf{x}_0) \hat{\psi}_n(\mathbf{x}) \right) = \delta(\mathbf{x} - \mathbf{x}_0). \quad (2.40)$$

For converging series the order of summation and differentiation may be flipped. In addition, the coefficients  $\eta$  may be factored out since they are not subject to the spatial differentiation, which leads to

$$\sum_{n=0}^{\infty} \eta_n(\mathbf{x}_0) (s^2 \hat{\psi}_n(\mathbf{x}) - \nabla (\bar{c}^2 \nabla \hat{\psi}_n(\mathbf{x}))) = \delta(\mathbf{x} - \mathbf{x}_0). \quad (2.41)$$

Exploiting the definition of the system's eigenfunction (2.39) then gives

$$\sum_{n=0}^{\infty} \eta_n(\mathbf{x}_0) (s^2 - s_n^2) \hat{\psi}_n(\mathbf{x}) = \delta(\mathbf{x} - \mathbf{x}_0). \quad (2.42)$$

To determine the individual coefficients, the adjoint (or left) eigenfunctions  $\chi_m$  are required. These are related to the right eigenfunctions via

$$\langle \hat{\chi}_m, \hat{\psi}_n \rangle = \begin{cases} E_n, & m = n, \\ 0, & \text{otherwise,} \end{cases} \quad (2.43)$$

and are thus bi-orthogonal. Forming the inner product of the adjoint eigenfunction with eq. (2.42) yields

$$\sum_{n=0}^{\infty} \eta_n(\mathbf{x}_0) (s^2 - s_n^2) \langle \hat{\chi}_m, \hat{\psi}_n \rangle = \overline{\hat{\chi}_m(\mathbf{x}_0)}. \quad (2.44)$$

Here, the property of the Dirac distribution (2.36) and the convergence of the series to interchange the summation and the inner product have been exploited. Ultimately, making use of the bi-orthogonality according to eq. (2.43) gives a relation for the individual coefficients

$$\eta_n(\mathbf{x}_0) = \frac{\overline{\hat{\chi}_n(\mathbf{x}_0)}}{E_n (s^2 - s_n^2)}, \quad (2.45)$$

and thus for Green's function

$$\hat{G}(\mathbf{x}|\mathbf{x}_0) = \sum_{n=0}^{\infty} \frac{\overline{\hat{\chi}_n(\mathbf{x}_0)} \hat{\psi}_n(\mathbf{x})}{E_n (s^2 - s_n^2)}. \quad (2.46)$$

After obtaining a universal expression for Green's function, it may now be used to find a solution for the original BVP. Formally, this requires the use of the adjoint Green's function  $\hat{G}^*$  as elaborated by Bleistein [139]. It is the unit impulse response of the adjoint BVP and is related to the original Green's function via the reciprocity relation  $\hat{G}(\mathbf{x}|\mathbf{x}_0) = \hat{G}^*(\mathbf{x}_0|\mathbf{x})$ . However, since Green's PDE (2.35a) is self-adjoint, the original function  $\hat{G}$  could be used instead of its adjoint in this particular case. Multiplying eq. (2.35a) with  $\hat{p}$  and subtracting eq. (2.25a) multiplied by  $\hat{G}^*$  and then integrating over the domain volume yields

$$\begin{aligned} & \iiint_V \left\{ \hat{p}(\mathbf{x}) \left( s^2 \hat{G}^*(\mathbf{x}|\mathbf{x}_0) - \nabla (\bar{c}^2 \nabla \hat{G}^*(\mathbf{x}|\mathbf{x}_0)) \right) - \hat{G}^*(\mathbf{x}|\mathbf{x}_0) \left( s^2 \hat{p}(\mathbf{x}) - \nabla (\bar{c}^2 \nabla \hat{p}(\mathbf{x})) \right) \right\} dV \\ &= \iiint_V \left\{ \hat{p}(\mathbf{x}) \delta(\mathbf{x} - \mathbf{x}_0) - \hat{G}^*(\mathbf{x}|\mathbf{x}_0) s (\kappa - 1) \hat{q}(\mathbf{x}) \right\} dV \\ &= \hat{p}(\mathbf{x}_0) - \iiint_V \hat{G}^*(\mathbf{x}|\mathbf{x}_0) s (\kappa - 1) \hat{q}(\mathbf{x}) dV. \end{aligned} \quad (2.47)$$

Making use of some universal properties of inner products, the LHS can be simplified as some terms cancel out according to

$$\begin{aligned} & \iiint_V \left\{ \hat{p}(\mathbf{x}) \left( s^2 \hat{G}^*(\mathbf{x}|\mathbf{x}_0) \right) - \hat{G}^*(\mathbf{x}|\mathbf{x}_0) \left( s^2 \hat{p}(\mathbf{x}) \right) \right\} dV = \langle \bar{\hat{p}}, s^2 \hat{G}^* \rangle - \langle \overline{\hat{G}^*}, s^2 \hat{p} \rangle \\ &= s^2 \langle \bar{\hat{p}}, \hat{G}^* \rangle - s^2 \langle \bar{\hat{p}}, \hat{G}^* \rangle = 0. \end{aligned} \quad (2.48)$$

Finally, eq. (2.47) can be reshaped into a formulation for the pressure fluctuations. Additionally interchanging  $\mathbf{x}$  and  $\mathbf{x}_0$  as well as exploiting the reciprocity relation gives

$$\begin{aligned} \hat{p}(\mathbf{x}) &= \iiint_V \hat{G}(\mathbf{x}|\mathbf{x}_0) s (\kappa - 1) \hat{q}(\mathbf{x}_0) dV_0 \\ &+ \iiint_V \left\{ \hat{G}(\mathbf{x}|\mathbf{x}_0) \nabla_0 (\bar{c}^2 \nabla_0 \hat{p}(\mathbf{x}_0)) - \hat{p}(\mathbf{x}_0) \nabla_0 (\bar{c}^2 \nabla_0 \hat{G}(\mathbf{x}|\mathbf{x}_0)) \right\} dV_0. \end{aligned} \quad (2.49)$$

As a result of interchanging  $\mathbf{x}$  and  $\mathbf{x}_0$ , the integration and differentiation has to be performed regarding the source position  $\mathbf{x}_0$ , denoted by an additional index 0 for the nabla operator and the integration variable. This final equation

(2.49), just like eq. (2.48), also holds for general, non self-adjoint second order BVPs as may be concluded from [140]. A severe issue of eq. (2.49) is that the second integral on the RHS still depends on the solution variable, i.e. the pressure fluctuations. Independently of the self-adjointness of the problem, this integral is associated with the boundary conditions of the BVP [139]. For specific boundary conditions of the Sturm-Liouville problem, the corresponding transformation is addressed in section 5.2. Then, eq. (2.49) allows to include the effect of variable boundary impedances on the solution as required for the consideration of nonlinear damper patches.

## 2.8 Flame Dynamics

A fundamental difference between the fields of aeroacoustics and thermoacoustics lies in unsteady combustion. While heat release fluctuations are inherently included in the NLRPE and LRF, they are dropped together with the reaction mechanism and the species transport equations for all other perturbed equations discussed in 2.2. To still account for acoustic driving caused by a fluctuating chemical conversion, a source term representing the unsteady volumetric heat release rate must be provided for the energy equation. Although mainly dealing with damping mechanisms, the consideration of acoustics-flame interactions still plays a crucial role in the present thesis. Adequate models reproducing their driving potential are essential for a complete energy balance. This allows for the pursued identification of linearly unstable oscillation states and their evolution over time as well as a subsequent optimization of the system's damping capabilities. For this purpose, various mechanisms of unsteady combustion are presented within this section. Specific emphasis is put on the contributions to the linear stability behavior of acoustic modes together with their mathematical modeling.

### 2.8.1 Fluctuating Heat Release Contributions

In general, three individual contributions to the overall volumetric heat release fluctuations related to turbulent flames may be identified [102, 141]:

$$\dot{q}'(\mathbf{x}, t) = \dot{q}'_{st}(\mathbf{x}, t) + \dot{q}'_{lin}(\mathbf{x}, t) + \dot{q}'_{nl}(\mathbf{x}, t). \quad (2.50)$$

The stochastic part  $\dot{q}'_{st}$  stems from turbulent velocity fluctuations in the chemical reaction zone producing broadband combustion noise [26, 136]. Such a broadband acoustic radiation was also found for unbounded, turbulent flames [26, 136, 142, 143]. In confined geometries, these stochastic heat release fluctuations excite the acoustic modes of the combustor and can thus be considered the starting point of thermoacoustic instabilities. Assuming a negligible feedback from linear acoustic oscillations to turbulence (cf. Fig. 1.1), the related stochastic heat release fluctuations may be neglected for linear stability analyses of acoustics-flame couplings [141].

The linear coupling between the flame and the combustor acoustics is represented by the term  $\dot{q}'_{lin}$ . It constitutes a closed feedback loop between acoustics and combustion and is therefore often described in terms of a flame response function (FRF)<sup>7</sup> in the FD. Modeling of this linear part is subject of the next section 2.8.2.

Finally, a nonlinear contribution  $\dot{q}'_{nl}$  may become relevant at large acoustic oscillation amplitudes. This nonlinear term is commonly assumed to cause a saturation of the flame driving and therefore leading to limit-cycle oscillations. This has been analytically demonstrated using a time-lag flame model by Dowling et al. [144]. Since this type of model may be used to capture equivalence ratio fluctuations (cf. section 2.8.2), it is suitable to investigate nonlinear mechanisms inherent to non-premixed combustion [141]. However, the applicability of this concept to premixed combustion is limited to flame surface changes due to convectively transported disturbances like vortices. It is questionable though, whether this mechanism leads to the heat release saturation as investigated by Dowling et al. [144]. Instead, the potentially nonlinear acoustic damping mechanism related to vortex shedding is investigated as a main driver of limit-cycle oscillations in the present thesis.

## 2.8.2 Linear Acoustics-Flame Interactions

Linear interaction mechanisms between acoustics and combustion are highly dependent on the operating conditions (e.g. premixed or non-premixed combustion). Identifying and modeling the relevant mechanisms for a specific setup is thus very challenging. One of the first models to describe an exper-

<sup>7</sup>Although typically being computed or measured for purely real valued frequencies, the FRF is mostly referred to as flame transfer function (FTF) in literature.

imentally observed acoustics-flame coupling dates back to the early 1950's. From theoretical considerations, Crocco [145, 146] identified acoustically induced mixture inhomogeneities as a source of heat release fluctuations. Such mixture disturbances are essentially related to velocity fluctuations at the burner mouth. A major finding of Crocco's work is the time lag  $\tau$  associated with the convective transport of the mixture inhomogeneities into the flame, leading to the  $n$ - $\tau$  model [34, 147]. Time lags are also a feature of coherent flame wrinkling, i.e. acoustically induced fluctuations in the flame surface area [34, 148] also observed for premixed combustion. Due to their versatility, those time-delay models are often employed in analytic studies or within network models (cf. chapter 3) and 3D-Helmholtz solvers [97, 149–151]. In these applications, they can accurately reproduce acoustics-flame interactions of technical combustors when taking time-lag distributions into consideration [152].

A fundamental feature of the  $n$ - $\tau$  model is its limitation to the low-frequency (LF) regime. In this case, the flame can be assumed to be acoustically compact with length scales much smaller than the characteristic acoustic wave length. This allows for the use of the Rankine-Hugoniot description of discontinuities [153, 154]: Therein, the flame is considered a lumped element with concentrated heat release fluctuations equivalent to the volume-integrated acoustics-flame interactions of the real flame. The corresponding FRF is referred to as global FRF. Instead of using the  $n$ - $\tau$  model, global FRFs can also be identified from measurements or high-fidelity CFD. Being in line with the lumped element theory, the global FRF is commonly mapped onto the spatial mean heat release rate field without any spatial phase distribution for the usage in acoustics solvers. However, this methodology postulates a static flame (i.e. a flame sheet or flame brush at rest), which is deficient in the context of thermoacoustics. Neglecting flame movement in linearized approaches leads to a considerable production of entropy across perfectly premixed flames. This was first elaborated by Strobio Chen et al. [155] using one-dimensional jump conditions and later confirmed by Meindl et al. [82] who applied a global FRF to the LNSE. Since the lack of mixture inhomogeneity lacks a physical justification of significant temperature and corresponding entropy fluctuations downstream of the premixed flame, this is considered unphysical or spurious. Reconsidering Myers' energy corollary, eq. (2.23), spurious entropy may

severely falsify the results of a stability analysis (cf. [156, pp. 189-192]).

This issue may be overcome by using a locally resolved FRF, which incorporates the effect of flame movement via a spatial phase distribution [82]. Local FRFs were previously reserved for thermoacoustic analysis in the high-frequency (HF) regime. Here, the compactness assumption is not valid anymore. Analytical models like the  $n$ - $\tau$  model with distributed time lags account for the resulting local acoustics-flame interactions [34, 157]. However, this model normally requires some tuning regarding the interaction index  $n$ . Furthermore, it is generally not designed to incorporate an acoustically induced flame movement.

As proposed by Meindl et al. [82], a consistent local FRF may be obtained from NLRPE/LRF or high-fidelity reactive CFD simulations, which inherently include a consistent flame movement but come at tremendous computational effort. Also measurements with optical techniques allow for a local resolution of the FRF. However, optical access can normally not be provided in industrial applications. It may be concluded that there is no reliable and computationally efficient methodology available to account for flame movement in common hybrid models and thus prevent for errors due to spurious entropy generation. This also prevents the employment of global FRFs, independently of the considered frequency regime.

To overcome this issue for linear perturbed approaches, the author of this thesis developed a novel decomposition approach. Using the Arbitrary Lagrangian Eulerian (ALE) methodology [158, 159], Heilmann et al. [160] performed a transient coordinate transform of the Euler equations to establish an intrinsically consistent mean field movement of all flow variables. After perturbation, cf. eq. (2.6), and subsequent linearization, they arrive at ALE transformed LEE. These are equivalently obtained, when introducing a triple decomposition into the Euler equations according to

$$\phi(\mathbf{x}, t) = \bar{\phi}(\mathbf{x}) - \Delta' \cdot \nabla \bar{\phi} + \phi',$$

where  $\Delta' = \Delta'(\mathbf{x}, t)$  is the local and instantaneous field deflection. When this deflection is assumed to be exclusively driven by acoustic fluctuations, a simple kinematic relation to describe the mean field deflection can be used:

$$\Delta'(\mathbf{x}, t) = \int_0^t \mathbf{u}'(\mathbf{x}, \tilde{t}) d\tilde{t}; \quad \hat{\Delta} = \frac{\hat{\mathbf{u}}}{s}. \quad (2.51)$$

Integrating the acoustic velocity over time represents the acoustically induced particle displacement, which is more easily represented in the FD. This particle displacement (2.51) also constitutes a closure relation for the unclosed ALE transformed LEE, ultimately yielding the Moving Flame Linearized Euler Equations (MF-LEE). The quite complex form of these equations prevents for an intuitive interpretation of their actual significance. Such an intuitive interpretation is provided for stagnant flows, which yields the following set of linear equations in the FD [160]

$$s \hat{p} + \bar{\rho} \nabla \cdot \hat{\mathbf{u}} = 0, \quad (2.52a)$$

$$s \bar{\rho} \hat{\mathbf{u}} + \nabla \hat{p} = 0, \quad (2.52b)$$

$$s \hat{p} + \kappa \bar{p} \nabla \cdot \hat{\mathbf{u}} - (\kappa - 1) \hat{q} = (\kappa - 1) \frac{1}{s} \left[ \underbrace{\bar{q} \nabla \cdot \hat{\mathbf{u}}}_{\hat{q}_\rho} - \underbrace{\hat{\mathbf{u}} \cdot \nabla \bar{q}}_{\hat{q}_\Delta} \right]. \quad (2.52c)$$

While the linearized mass and momentum balance equations (2.52a) and (2.52b) equal those of the LEE (2.8) for quiescent fluids, the linearized energy balance (2.52c) contains two additional source terms. They stem from the generally inconsistent assumption of a stationary, stagnant mean flow field with heat release. Based on early experimental and analytical studies on HF driving mechanisms due to coherent flame movement from Schwing et al. [161, 162] and Zellhuber et al. [163], those source terms were referred to as flame deformation  $\hat{q}_\rho$  and displacement  $\hat{q}_\Delta$  by Hummel et al. [164]. It may be noted that Hummel et al. [164] further modified the deformation source assuming homentropicity, which is invalid in regions with heat release.

The mechanisms of displacement and deformation are in fact adequate to consistently account for flame movement in quiescent fluids. However, they do not solve the issue of spurious entropy generation when simply being added to approaches taking mean flow velocities into account, like the LEE [160]. In this case, a complex 3D distortion of the flame is expected, which can only be reproduced by the full set of MF-LEE.

To summarize, the MF-LEE solve the issues of spurious entropy of common hybrid approaches by establishing a consistent field movement. They inherently include the linear driving mechanisms associated with a complex distortion of the flame shape induced by acoustic and vortical fluctuations. Additional heat release oscillations (e.g. due to equivalence ratio fluctuations in non-premixed combustion) can still be included by means of an additional

source term  $\hat{q}$ . Being deduced from the MF-LEE, eqs. (2.52) illustrate that the mechanisms of flame deformation and displacement indeed represent the consistent driving associated with flame movement for quiescent fluids. Although originally derived as HF driving mechanisms, their identification on the basis of the MF-LEE also justifies their validity in the LF regime. Consequently, they are perfectly suitable for the universal 3D-Helmholtz framework pursued in the present thesis and presented in chapter 4.



### 3 One-Dimensional Network Models

Sound waves propagate in all three spatial dimensions, which is of particular interest for the analysis of the acoustic near and far field in unbounded media, i.e. in an acoustic free field.<sup>1</sup> Although not being subject to an acoustic free field, the three-dimensional character of the wave propagation also plays a crucial role in confined geometries at high frequencies. The framework for the analysis of the sound propagation in space is provided by the mathematical models discussed in section 2.2. Particularly for complex 3D system boundaries and mean flow fields, all of the corresponding BVPs lack an analytic solution. This is circumvented under the condition of purely 1D wave propagation. An indicator for the 1D propagation of acoustic waves in confined geometries is the Helmholtz number

$$\text{He} = \frac{l \omega}{\bar{c}} = l k . \quad (3.1)$$

For  $\text{He} \ll 1$ , the acoustic wave length is much larger than a characteristic length  $l$  of the considered geometry, which is then labeled as acoustically *compact*. If this criterion is satisfied for the hydraulic diameter of a duct or channel, the wave propagation is considered one-dimensional along the axial coordinate of the geometry. Acoustic compactness is a common assumption in the LF spectrum and forms the basis for the acoustic network modeling as discussed in section 3.1. Hereafter, some readily available acoustic network elements are presented in section 3.2. Since acoustic liners can normally be described using 1D models, they can also be integrated into network models, which will be subject of section 3.3. A methodology to combine the 1D models discussed in this chapter with 3D-CA tools is developed in chapter 4, yielding the highly efficient linear, hybrid numerical approach pursued in the present thesis.

---

<sup>1</sup>Since the distinction between an acoustic near and far field can normally not be transferred to confined geometries subject to the present thesis, these concepts are not further detailed here. Instead, the interested reader is referred to standard literature for acoustics such as [118, 134].

### 3.1 Network Modeling Concept

The simplified one-dimensional approach to describe acoustic propagation in compact elements facilitates the analysis of acoustic systems analogously to electrical as well as mechanical systems [165]. Particularly the basic theory regarding electrical networks pioneered by Helmholtz and Kirchhoff can be made use of to describe a sequence of compact elements [166]. A classic field of application is the sound propagation within a series of connected ducts with different cross-sections. Such a system may be represented by a network of lumped elements as sketched in Fig. 3.1. In accordance with elec-

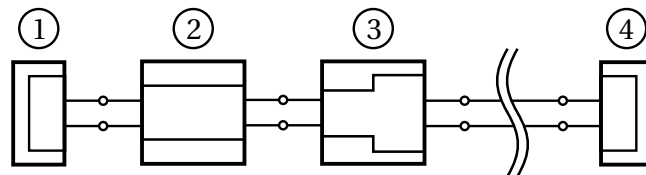


**Figure 3.1:** Schematic network representation of a series of ducts with different cross-sections and solid termination on both ends.

trical network theory, the acoustic elements may generally be characterized regarding their number of terminals connecting to neighboring elements. For the network of Fig. 3.1 these are one-ports (elements 1 and 4) and two-ports (elements 2 and 3). At each port, a complete set of state variables needs to be transferred. While this set of state variables is normally formed by the current and voltage for electrical systems, it may be represented by the velocity and the force applied to a mass point in mechanical systems (cf. [165]). Analogously, a complete characterization of the acoustic field is obtained by two state variables. These may be the acoustic pressure and velocity fluctuations or alternatively, making use of eq. (2.11) and (2.13), the Riemann Invariants. Depending on the selected set of acoustic state variables, acoustic one-ports may then be represented by an impedance (2.31) or a reflection coefficient (2.32). As these elements terminate a network, the boundary conditions as discussed in section 2.6 may be applied.

Similarly, different representations for two-ports may be specified. Fischer [167] gives a great overview over common acoustic two-port representations and their electrical counterparts. Of practical relevance is the classic transfer matrix  $\mathbf{TM}$ . It relates the primitive acoustic variables, i.e. pressure and velocity

fluctuations, downstream (index  $d$ ) of a lumped element to those upstream (index  $u$ ) according to

$$\begin{pmatrix} \frac{\hat{p}}{\hat{\rho}\hat{c}} \\ \hat{u} \end{pmatrix}_d = \mathbf{TM} \begin{pmatrix} \frac{\hat{p}}{\hat{\rho}\hat{c}} \\ \hat{u} \end{pmatrix}_u = \begin{pmatrix} \mathbf{TM}_{11} & \mathbf{TM}_{12} \\ \mathbf{TM}_{21} & \mathbf{TM}_{22} \end{pmatrix} \begin{pmatrix} \frac{\hat{p}}{\hat{\rho}\hat{c}} \\ \hat{u} \end{pmatrix}_u. \quad (3.2)$$

A more intuitive two-port representation in terms of system identification is provided by the scattering matrix  $\mathbf{SM}$  as it relates scattered waves ( $\hat{f}_d, \hat{g}_u$ ) to incident waves ( $\hat{f}_u, \hat{g}_d$ ):

$$\begin{pmatrix} \hat{f}_d \\ \hat{g}_u \end{pmatrix} = \mathbf{SM} \begin{pmatrix} \hat{f}_u \\ \hat{g}_d \end{pmatrix} = \begin{pmatrix} T_u & R_d \\ R_u & T_d \end{pmatrix} \begin{pmatrix} \hat{f}_u \\ \hat{g}_d \end{pmatrix}. \quad (3.3)$$

While the coefficients of the transfer matrix are not easy to interpret, the scattering matrix elements can be intuitively identified as reflection and transmission coefficients. This is illustrated in Fig. 3.2 where the characteristic  $\hat{f}_d$  leaving the two-port on the downstream side consists of the transmitted part  $\hat{f}_{d,t} = T_u \cdot \hat{f}_u$  and the reflected part  $\hat{f}_{d,r} = R_d \cdot \hat{g}_d$  of the incident waves. On the

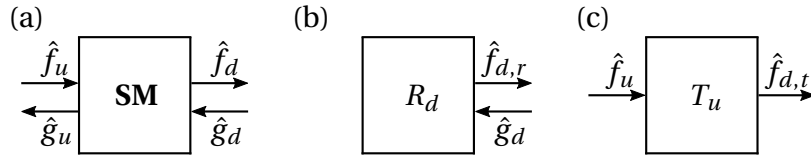


**Figure 3.2:** Schematic of a scattering matrix two-port. (a) Superposed scattering of incident waves. (b) Exclusive reflection of the incident wave at the downstream port. (c) Exclusive transmission of the incident wave at the upstream port.

other hand, the transfer matrix representation allows for a more straightforward interconnection of two-ports. For a serial network of  $N$  two-ports, an overall transfer matrix  $\mathbf{TM}_{tot}$  may then be obtained by matrix multiplication of the single element transfer matrices as per

$$\mathbf{TM}_{tot} = \mathbf{TM}_N \cdot \mathbf{TM}_{N-1} \cdot \dots \cdot \mathbf{TM}_1. \quad (3.4)$$

Exploiting the advantages of both representations requires mutual conversion rules, which are provided by Fischer et al. [168].

Finally, it may be noted that the network modeling framework also allows for more complex system analysis. For instance, parallel connections of elements

can be established by multi-port elements such as trijunctions [93, 132]. Furthermore, the network modeling framework is not necessarily limited to 1D acoustic analysis. It was also employed to investigate 3D modes in axisymmetric annular combustors [94, 169].

## 3.2 Network Elements

The networks considered in the course of this thesis will exclusively be of serial character. A large range of acoustically compact geometries may simply be abstracted by a series of interconnected ducts [135]. This requires only two types of network elements to reproduce the acoustic transfer behavior of the corresponding real geometries with reasonable accuracy. These are *ducts with constant cross sections* and *sudden area changes* to connect the individual ducts. A mathematical model for both elements will be discussed subsequently.

### 3.2.1 Duct with Constant Cross Section

Within a duct of constant cross-sectional area (graphically represented by element 2 in Fig. 3.1) the acoustic characteristics  $\hat{f}$  and  $\hat{g}$  propagate at the speed of sound modified by a constant mean flow velocity  $\bar{u}$ . Making use of the 1D solution of the convective wave equation (2.11), a duct of length  $l$  thus constitutes a time-lag of  $k^\pm l$  for the characteristics. In terms of the primitive variables, a corresponding transfer matrix may be written as [93]

$$\mathbf{TM}_{pu,duct} = \begin{pmatrix} e^{-ik^+l} + e^{ik^-l} & e^{-ik^+l} - e^{ik^-l} \\ e^{-ik^+l} - e^{ik^-l} & e^{-ik^+l} + e^{ik^-l} \end{pmatrix}. \quad (3.5)$$

### 3.2.2 Sudden Area Change

Ducts of different cross sections are connected via sudden area changes (graphically represented by element 3 in Fig. 3.1), also referred to as backward or forward facing steps. The three-dimensional processes at such area discontinuities are projected on an infinitesimally thin lumped element. A one-dimensional model was first derived by Gentemann et al. [170] and Schuermans [49]. While their derivation was limited to linear mechanisms, this section pursues the goal to highlight nonlinear mechanisms, in particular regarding acoustic damping. The basis to describe the nonlinear transfer behavior of

area discontinuities is formed by the continuity and the momentum conservation equations. The continuity equation in integral form reads

$$\frac{\partial}{\partial t} \int_V \rho \, dV + \int_{\partial V} \rho \mathbf{u} \cdot \mathbf{n} \, dA = 0. \quad (3.6)$$

Introducing the perturbation ansatz (2.6) and exploiting the one-dimensionality of the flow as well as the compactness of the element ( $\text{He} \ll 1$ ), the perturbed nonlinear continuity equation is obtained:

$$\frac{\partial \rho'_u}{\partial t} \int_{x_u}^{x_d} A(x) \, dx + [(\rho' \bar{u} + \bar{\rho} u' + \rho' u') A]_u^d = \mathcal{O}(\text{He})^2. \quad (3.7)$$

The integration of the cross-sectional area along the infinite length of the sudden area change is mathematically not easy to justify. From a physical point of view, however, the integral is related to a compression capacity in the vicinity of the sudden area change. The control volume corresponding to the capacitance of the compact element may be expressed by defining a reduced length  $l_{red} = \int_{x_u}^{x_d} \frac{A(x)}{A_d} \, dx$ . This quantity may be determined experimentally or numerically to fit the model to the specific setup. Assuming small Mach number mean flows with constant mean density along the streamlines and isentropic perturbations, the nonlinear mass conservation yields

$$\begin{aligned} \frac{A_d}{\bar{\rho} \bar{c}^2} l_{red} \frac{\partial p'_u}{\partial t} + \left( A_d \left( \frac{p'_d}{\bar{\rho} \bar{c}} M_d + u'_d \right) - A_u \left( \frac{p'_u}{\bar{\rho} \bar{c}} M_u + u'_u \right) \right) \\ + \left( A_d \frac{p'_d}{\bar{\rho} \bar{c}^2} u'_d - A_u \frac{p'_u}{\bar{\rho} \bar{c}^2} u'_u \right) = \mathcal{O}(\text{He})^2. \end{aligned} \quad (3.8)$$

This equation may be further simplified by also neglecting mixed terms of higher order in the Helmholtz and Mach number, which ultimately gives

$$\frac{A_d}{\bar{\rho} \bar{c}^2} l_{red} \frac{\partial p'_u}{\partial t} + (A_d u'_d - A_u u'_u) + \left( A_d \frac{p'_d}{\bar{\rho} \bar{c}^2} u'_d - A_u \frac{p'_u}{\bar{\rho} \bar{c}^2} u'_u \right) = \mathcal{O}(\text{He})^2. \quad (3.9)$$

The momentum conservation is described in detail by the Navier-Stokes equations. For pure acoustic investigations at low Mach numbers, dissipation due to viscosity, heat conduction and acoustic-vortex interaction may be neglected. This leads to the incompressible Bernoulli equation for homentropic, irrotational flow. In the case of area discontinuities, these assumptions fail as the flow irrotationality leads to infinitely large flow velocities at the rim of the

sudden area change. In these regions, vortices are formed, which are advected by the mean flow and are ultimately dissipated. Due to these complex dissipation mechanisms, which are described by the full Navier-Stokes equations, an irreversible drop in the total pressure is observed. For low Mach numbers, this total pressure drop may simply be added to the Bernoulli equation, which then reads

$$\frac{\partial \nabla \varphi}{\partial t} + \frac{1}{2} \nabla (\mathbf{u} \cdot \mathbf{u}) + \frac{1}{\rho} \nabla p = \frac{1}{\rho} \nabla p_l, \quad (3.10)$$

with the irrotational velocity being replaced by the gradient of the scalar potential field  $\varphi$ . Considering this equation along a streamline yields a one dimensional formulation. Introducing the perturbation ansatz (2.6) and integrating along the streamline gives

$$\frac{\partial}{\partial t} \int_{x_u}^{x_d} \nabla \varphi' dx + \left[ \bar{u} u' + \frac{1}{2} u'^2 \right]_{x_u}^{x_d} + \frac{1}{\bar{\rho}} [p']_{x_u}^{x_d} = \frac{1}{\bar{\rho}} [p'_l]_{x_u}^{x_d}. \quad (3.11)$$

The total pressure loss on the RHS is usually expressed as  $[p_l]_{x_u}^{x_d} = -\frac{1}{2} \rho \zeta |u_u| u_u$  with the pressure loss coefficient  $\zeta$  and the upstream velocity  $u_u$ . The corresponding perturbed term reads  $[p'_l]_{x_u}^{x_d} = -\frac{1}{2} \bar{\rho} \zeta (|\bar{u}_u + u'_u| (\bar{u}_u + u'_u) - |\bar{u}_u| \bar{u}_u)$ . The velocity potential may be transformed by exploiting the incompressibility with regard to the mass conservation  $u(x) = \frac{A_u}{A(x)} u_u$ . In conjunction with the compactness of the element, the first term on the LHS of eq. (3.11) thus becomes

$$\frac{\partial}{\partial t} \int_{x_u}^{x_d} \nabla \varphi' dx = \frac{\partial}{\partial t} \int_{x_u}^{x_d} u' dx = \frac{\partial u'_u}{\partial t} \int_{x_u}^{x_d} \frac{A_u}{A(x)} dx = \frac{\partial u'_u}{\partial t} l_{eff}. \quad (3.12)$$

Similar to the reduced length, the effective length  $l_{eff} = \int_{x_u}^{x_d} \frac{A_u}{A(x)} dx$  was introduced to circumvent the mathematical issues regarding the integration of the cross sectional area. It corresponds to the volume related to the inertial mass oscillating within the compact element. Finally, the momentum conservation equation becomes

$$\begin{aligned} \frac{\partial u'_u}{\partial t} l_{eff} + \bar{u}_u u'_u \left( \left( \frac{A_u}{A_d} \right)^2 - 1 \right) + \frac{1}{\bar{\rho}} (p'_d - p'_u) + \frac{1}{2} (u'_d{}^2 - u'_u{}^2) \\ + \frac{1}{2} \bar{\rho} \zeta (|\bar{u}_u + u'_u| (\bar{u}_u + u'_u) - |\bar{u}_u| \bar{u}_u) = 0. \end{aligned} \quad (3.13)$$

The nonlinear loss term particularly becomes relevant when the acoustic velocity fluctuations take values greater than the mean flow velocity (cf. chapter

5). Below that limit, the acoustic processes are assumed to behave in a linear manner and the equations simplify to the ones proposed by Gentemann et al. [170], which ultimately yields the linear transfer matrix of a sudden area change

$$\mathbf{TM}_{pu,AC} = \begin{pmatrix} 1 & -i \frac{\omega}{c} l_{eff} - M_u \left[ \left( \frac{A_u}{A_d} \right)^2 + \zeta - 1 \right] \\ -i \frac{\omega}{c} l_{red} & \frac{A_u}{A_d} \end{pmatrix}. \quad (3.14)$$

Note that the  $T_{21}$  element slightly deviates from the formulation of Gentemann et al. [170], which may be ascribed to their inconsistent transformation step of the continuity eqs. (3.8) and (3.9).

Generally, a nonlinear counterpart of this linear transfer matrix representation can be included into the nonlinear framework developed in chapter 5 analogously to the nonlinear resonator models. However, since the geometrically complex configuration investigated in chapter 6 is not expected to be significantly impacted by nonlinear damping mechanisms of transfer matrix couplings, the present thesis is limited to the application of eq. (3.14).

### 3.3 Acoustic Liner Models

As already outlined in section 1.2, all common passive damping devices rely on the principle of the energy transfer from acoustics to vorticity. This is mostly observed at sudden area changes. Since the acoustic velocity is commonly assumed to be a potential field (cf. section 2.3.2 and [29,30,118,171]), it would become infinitely large at the edges of such area discontinuities. In this case, viscous diffusion creates rotational components constituting the energy transfer between acoustics and vorticity [49].

In the presence of mean flow, the coherent formation of vortices is even enhanced due to the interaction of the acoustic fluctuations with the mean flow shear layer. This mechanism has been investigated by Howe in 1979 [28] and forms the basis for the Howe model discussed in section 3.3.2. While he assumed a single aperture of infinitesimal thickness for his analysis, his results can also be applied to perforated plates or liners. Normally, the thickness  $t$  of such liners or apertures is acoustically compact. As a consequence, the acoustic velocity is considered constant across the plate thickness, whereas only the

pressure may exhibit remarkable changes. This promotes the introduction of a transfer impedance  $z_{tr}$  relating the difference in acoustic pressure on both sides of the plate to the normal velocity

$$z_{tr} = \frac{\hat{p}_u - \hat{p}_d}{\bar{\rho} \bar{c} \hat{u}}, \quad (3.15)$$

which in fact represents the difference of the local impedances upstream and downstream of the compact element. The transfer impedance and its application to perforated liners is explicated by Hua [172]. It can be reformulated in terms of a transfer matrix according to:

$$\begin{pmatrix} \frac{\hat{p}}{\bar{\rho} \bar{c}} \\ \hat{u} \end{pmatrix}_d = \underbrace{\begin{pmatrix} 1 & -z_{tr} \\ 0 & 1 \end{pmatrix}}_{\mathbf{TM}_{tr}} \begin{pmatrix} \frac{\hat{p}}{\bar{\rho} \bar{c}} \\ \hat{u} \end{pmatrix}_u. \quad (3.16)$$

Multi-layer perforated resonators as sketched in Fig. 3.3 may then be characterized by using the network framework of section 3.1. The cavities separating

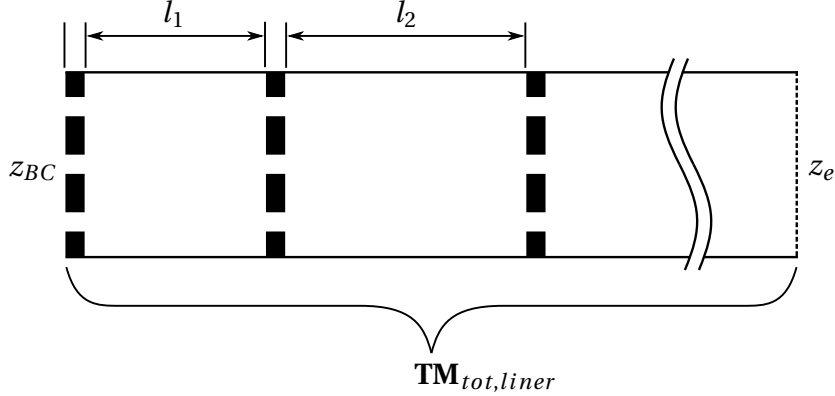


**Figure 3.3:** Sketch of the procedure to characterize a multi-layer perforated resonator.

the single compact perforated plates may be represented by the duct transfer matrix (3.5). Since the purge mass flow is normally quite low, the mean flow velocities can be neglected in the cavities, simplifying the wave numbers to  $k^{+, \bar{u}=0} = k^{-, \bar{u}=0} = k$ . Alternately multiplying the transfer matrices of the duct elements and the still unknown transfer impedances according to (3.4) then gives an overall transfer matrix of the multi-layer resonator  $\mathbf{TM}_{tot,liner}$ . Depending on the termination boundary impedance  $z_{BC}$ , the overall impedance

$z_e$  at one end of the resonator can be expressed as

$$z_e = \frac{\hat{p}_e}{\bar{\rho} \hat{c} \hat{u}_e} = \frac{\text{TM}_{tot,liner,11} z_{BC} + \text{TM}_{tot,liner,12}}{\text{TM}_{tot,liner,21} z_{BC} + \text{TM}_{tot,liner,22}} . \quad (3.17)$$

This procedure can be exemplified by means of a resonator with a solid termination ( $z_{BC} = \infty$ ), a cavity of length  $l$  and a perforated liner with the transfer impedance  $z_{tr}$  flush mounted to the combustion chamber. This yields the end impedance of the resonator at the combustion chamber wall

$$z_{e,res} = i \cot(kl) - z_{tr} . \quad (3.18)$$

With suitable models for the transfer impedances of perforated liners, this framework allows for the 1D characterization of technically relevant resonators. They may then be included as impedance boundary conditions in a linear 3D-CA concept (cf. chapters 4 and 6). The impedance is then even further evolved into a nonlinear resonator model for the use in reduced order models in section 5.4.2. To do so, the mechanical analogy of a damped system by means of a mass-spring-damper model as discussed subsequently is of great use. The remainder of the present section is then used to summarize selected acoustic models to describe the transfer impedance of perforated liners. For a more comprehensive and sound overview over the broad range of models available in literature, the interested reader is referred to Lahiri et al. [121, 173].

### 3.3.1 Mass-Spring-Damper Model

An analogy to gain useful insight into the damping capabilities of acoustic dampers is the rectilinear damped mechanical oscillator (cf. e.g. [165, 174]). With reference to Fig. 3.4, this mass-spring-damper model consists of a mass  $m$  with a rectilinear motion in the  $x$ -direction. It is connected to a solid, stationary wall via a spring with the spring constant  $k$  and a damper with the damping factor  $d$ . Additionally, a transient external force  $F(t)$  may be applied. The dynamics of such a system with a single degree of freedom can be converted into the ordinary differential equation

$$m\ddot{x} + d\dot{x} + kx = F(t) . \quad (3.19)$$

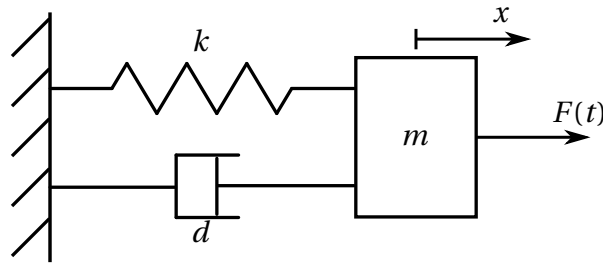


**Figure 3.4:** Sketch of a damped mechanical oscillator.

Here, the movement of the mass is assumed to be damped proportional to its velocity  $\dot{x}$ . The properties of this system can be analyzed using the definition of the mechanical impedance

$$Z_{mech} = \frac{\hat{F}}{\hat{u}} = \frac{s^2 m + sd + k}{s} = sm + d + \frac{k}{s}. \quad (3.20)$$

For a purely harmonic force ( $s = i\omega_F$ ), the real and imaginary part representing the resistance and reactance, respectively, can be identified according to

$$R_{mech} = d; \quad X_{mech} = \omega_F m - \frac{k}{\omega_F}. \quad (3.21)$$

While the mass and the spring constant both contribute to the reactance, the resistance is exclusively formed by the damping factor. The mechanical impedance (3.20) can be normalized with the mass and the angular eigenfrequency of the undamped system  $\omega_0 = \sqrt{k/m}$ . Depending on the values of the normalized damping factor  $d/(m\omega_0)$ , one can distinguish between three damping regimes [175]: normally damped ( $d/(m\omega_0) < 1$ ), optimally damped ( $d/(m\omega_0) = 1$ ) and overdamped ( $d/(m\omega_0) > 1$ ). Making use of eq. (2.32), these three regimes are plotted in Fig. 3.5 by means of the mechanical reflection coefficient  $R_{mech}$  over the normalized forcing frequency  $\omega_f/\omega_0$ . At the eigenfrequencies of the undamped system  $\omega_0$ , the absolute value of the reflection coefficient takes smallest values, indicating maximum energy dissipation. It can be observed that the damping capabilities of a normally damped system increases with increasing damping factor until reaching an optimally damped state. Further increasing the damping factor results in a more broadband damping characteristic with decreasing energy dissipation in the vicinity of the undamped eigenfrequency  $\omega_0$ . This attribute will be exploited when designing resonators for an industrial-scale combustor in section 6.2.2.

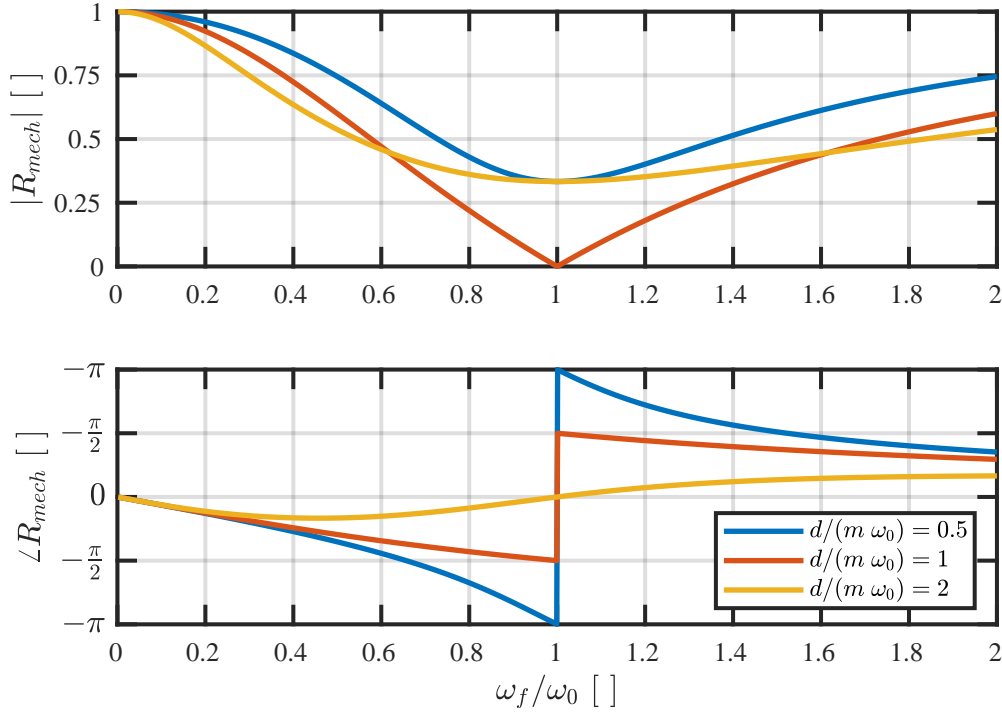


**Figure 3.5:** Reflection coefficient over normalized forcing frequency for different normalized damping factors  $d/(m\omega_0)$ .

### 3.3.2 Howe Model

A major mechanism for the attenuation of acoustic energy in compact apertures subject to bias flow is the interaction of the acoustic fluctuations with the shear layer of the steady jet flow. Howe [28] derived a model for the Rayleigh conductivity  $C_R$  of an infinitesimal thin aperture with a low Mach number mean flow for small Helmholtz numbers  $\text{He} = \frac{\omega}{c}r \ll 1$ . The Rayleigh conductivity can be expressed as

$$C_{R,a} = i\omega\bar{\rho}A \frac{\hat{u}_0}{\hat{p}_u - \hat{p}_d} = iA \frac{k}{z_{tr,a}}, \quad (3.22)$$

with the index 0 denoting area-averaged velocities through the cross-sectional area  $A$  of the aperture. With the assumption of circular apertures, Howe arrives at

$$C_{R,a,Howe} = 2r(\gamma + i\delta), \quad (3.23)$$

with the real and imaginary components  $\gamma$ ,  $\delta$

$$\gamma = \frac{I_1(\text{Sr})^2 \left(1 + \frac{1}{\text{Sr}}\right) + \left(\frac{2}{\pi}\right)^2 e^{2\text{Sr}} \cosh(\text{Sr}) K_1(\text{Sr})^2 \left(\cosh(\text{Sr}) - \frac{\sinh(\text{Sr})}{\text{Sr}}\right)}{I_1(\text{Sr})^2 + \left(\frac{2}{\pi}\right)^2 e^{2\text{Sr}} \cosh(\text{Sr})^2 K_1(\text{Sr})^2}$$

$$\delta = \frac{\text{Sr} \frac{2}{\pi} I_1(\text{Sr}) K_1(\text{Sr}) e^{2\text{Sr}}}{I_1(\text{Sr})^2 + \left(\frac{2}{\pi}\right)^2 e^{2\text{Sr}} \cosh(\text{Sr})^2 K_1(\text{Sr})^2}.$$

The modified Bessel functions of order  $m$ ,  $I_m$  and  $K_m$  are characteristic for the assumption of a cylindrical coordinate system. Howe's solution is mainly depending on the Strouhal number  $\text{Sr} = \omega r / \bar{u}_0$  with the radius of the aperture  $r$  and the area-averaged bulk velocity across the aperture  $\bar{u}_0$ .

### 3.3.3 Jing and Sun Model

A major drawback of Howe's model is the assumption of the infinitesimal thickness of the apertures leading to a lack of oscillating inertia within the aperture. Such an inertia creates an additional phase shift between pressure and velocity oscillations and does thus alter Rayleigh's conductivity. Jing and Sun [176, 177] experimentally investigated the impact of the thickness of perforated plates on their acoustic characteristics with low Mach-number mean flows. They used Howe's model to analytically reproduce their findings in terms of a specific transfer impedance  $z_{tr}$ . To account for the impact of the inertia within a plate of finite thickness  $t$ , Jing and Sun added a reactance term to the formalism of Howe, which resembles the reactance of a single duct of length  $t$ . Consequently, they obtain a modified Howe model in terms of the transfer impedance in the form

$$z_{tr,a,Jing} = \frac{\pi r k \delta}{2(\gamma^2 + \delta^2)} - i \left[ \frac{\pi r k \gamma}{2(\gamma^2 + \delta^2)} + k t \right]. \quad (3.24)$$

### 3.3.4 Bellucci Model

Bellucci et al. [56, 178, 179] merge different effects into a single transfer impedance model to characterize Helmholtz resonators and perforated liners. The overall transfer impedance derived by Bellucci essentially takes the following form:

$$z_{tr,Bellucci} = \frac{1}{\bar{\rho} \bar{c} \sigma} \left[ \frac{\hat{\Phi}}{\hat{u}_0} + i \omega \bar{\rho} (t \Gamma + t') \right]. \quad (3.25)$$

Note that this equation is applicable to perforated plates and not only to single apertures. This is indicated by the porosity  $\sigma$  in the denominator of eq. (3.25). The three terms in the bracket may be interpreted as follows:

- The first term represents the external flow resistance due to pressure losses in the vicinity of the apertures. The losses are caused by the transformation of acoustic energy into rotational vortical energy at the sharp aperture edge.
- The second term comprises inertia effects and viscous losses in the single apertures, which are based on acoustic wave propagation in a cylindrical duct at low Helmholtz numbers.
- The last term comprises semi-empirical correction factors. Especially the inertia of the air mass in the apertures is not limited to the thickness of the plate and requires thus a correction.

In the following, these three terms are discussed in more detail and the corresponding constitutive equations are provided.

In the TD, the external flow resistance may simply be described by the perturbed, nonlinear pressure drop of a single aperture

$$\Phi' = \frac{1}{2} \bar{\rho} \zeta \left( |\bar{u}_0 + u'_0| (\bar{u}_0 + u'_0) - |\bar{u}_0| \bar{u}_0 \right), \quad (3.26)$$

with the pressure loss coefficient  $\zeta$ . Note that this nonlinear expression is equivalent to the pressure drop in the momentum equation (3.13) to describe the sudden area change. Transforming eq. (3.26) into the FD yields

$$\hat{\Phi} = \bar{\rho} \zeta g \left( \frac{\bar{u}_0}{\hat{u}_0} \right) |\hat{u}_0| \hat{u}_0. \quad (3.27)$$

The function  $g(\phi)$  is the result of the transformation of the nonlinearity in the pressure drop equation. It is defined as

$$g(\phi) = \begin{cases} \frac{2}{\pi} \left[ \phi \sin^{-1}(\phi) + \left( \frac{\sqrt{1-\phi^2}}{3} \right) (2 + \phi^2) \right], & |\phi| \leq 1 \\ |\phi|, & |\phi| > 1, \end{cases} \quad (3.28)$$

and reveals a nonlinear flow resistance once the acoustic velocity  $\hat{u}_0$  exceeds the mean flow velocity  $\bar{u}_0$ . For the calculation of the pressure loss coefficient,

Bellucci introduces a distinction of cases for the values of the mean flow velocity and the acoustic Strouhal number  $Sr_a = \omega r / |\hat{u}_0|$ :

$$\zeta = \begin{cases} \frac{1}{C_d^2} = \frac{1}{2} (1 - \sigma) + (1 - \sigma)^2 := \zeta_{0,1}, & \text{for } \bar{u}_0 = 0, Sr_a \leq (Sr_a)_{qs} & (3.29a) \\ \frac{1}{2} \frac{3\pi}{4} Sr_a^{1/3} := \zeta_{0,2}, & \text{for } \bar{u}_0 = 0, Sr_{ac} > (Sr_a)_{qs} & (3.29b) \\ \frac{\pi}{2} \frac{\delta \cdot Sr}{\gamma^2 + \delta^2} := \zeta_{lin}, & \text{for } \bar{u}_0 \geq |\hat{u}_0| & (3.29c) \\ \frac{\zeta_0(1 - g) + \zeta_{lin}(g - \frac{4}{3\pi})}{1 - \frac{4}{3\pi}}, & \text{for } 0 \leq \bar{u}_0 \leq |\hat{u}_0|. & (3.29d) \end{cases}$$

The Strouhal number threshold for quiescent mean flow fields, eq. (3.29a) and (3.29b), is given by the quasi-steady Strouhal number  $(Sr_a)_{qs} = \frac{0.61}{C_D^6}$  with the discharge coefficient  $C_D$ . Due to the stagnant mean flow, the corresponding losses are a result of nonlinear processes. In the linear regime, the acoustic flow velocity does not exceed the mean flow velocity. This is covered by Howe's model of the Rayleigh conductivity (3.23) with the coefficients  $\gamma$  and  $\delta$ , which is adopted by Bellucci in eq. (3.29c). Nonlinear losses are again expected, once the acoustic velocity exceeds the non-vanishing mean flow velocity. This is represented by eq. (3.29d), which can be interpreted as an intermediate regime between the stagnant mean flow and the linear regime.

The inner pressure loss due to viscous effects inside an aperture and the related inertial mass represents the second term in eq. (3.25). A suitable expression for this pressure loss is found from simplifications of the incompressible Navier-Stokes equations in polar coordinates yielding the following expression [179]

$$\Delta p_{inner} = \frac{\Delta \hat{p}}{\hat{u}_0} = i \bar{\rho} \omega t \Gamma(\text{Sh}), \quad (3.30)$$

where the propagation constant  $\Gamma$  is a function of the Shear number  $\text{Sh} = \sqrt{-\frac{i\omega}{\nu}} \cdot r$  according to

$$\Gamma = 1 - \frac{2J_1(\text{Sh})}{\text{Sh} J_0(\text{Sh})}. \quad (3.31)$$

It uses the Bessel functions of the first kind  $J_m$  of order  $m$  and is directly applied to the transfer impedance of eq. (3.25).

The modeling of  $\Delta p_{inner}$  exclusively incorporates viscous effects of the medium inside an aperture of thickness  $t$ . However, the oscillating mass within an aperture also accelerates an additional portion of mass outside of the aperture. This additional inertial mass alters the reactance of the perforated plate. This effect is accounted for by Bellucci using an end-correction term  $t'$  in the form

$$t' = \varphi_1(\text{He}) \varphi_2(\sigma) \varphi_3(\text{Sr}) \varphi_4(\text{Sr}_a) . \quad (3.32)$$

The individual semi-empirical terms of this end-correction term are given by

$$\begin{aligned} \varphi_1(\text{He}) &= 2 \cdot 0.8216 r \left[ 1 + \frac{(0.77 \text{He})^2}{1 + 0.77 \text{He}} \right]^{-1} ; \quad \varphi_2(\sigma) = 1 - \sqrt{\frac{\sigma}{2}} \\ \varphi_3(\text{Sr}) &= \frac{0.3(6/\text{Sr}^2) + 1}{6/\text{Sr}^2 + 1} ; \quad \varphi_4(\text{Sr}_a) = 1 - 0.3/\text{Sr}_a^{0.6} . \end{aligned}$$

Inserting Bellucci's transfer impedance model of eq. (3.25) into the end impedance of a single-layer perforated resonator (3.18) gives insight into the contributions of the individual terms to the transfer resistance and reactance:

$$\mathbf{R}_{e,Bellucci} = -\frac{1}{\sigma} \left[ \frac{\hat{\Phi}}{\hat{u}_0} - \omega \bar{\rho} t \mathfrak{I}(\Gamma) \right] , \quad (3.33)$$

$$\mathbf{X}_{e,Bellucci} = \bar{\rho} \bar{c} \cot(kl) - \frac{i\omega \bar{\rho}}{\sigma} (t \mathfrak{R}(\Gamma) + t') . \quad (3.34)$$

Particularly the resistance formulation of eq. (3.33) will be exploited to derive a nonlinear damper model in the TD in section 5.4.2, whereas the original Bellucci model in the FD is used to model the resonators of the geometrically complex test configuration in section 6.2.2.



## 4 Linear Hybrid Numerical Strategy

The development of a linear hybrid numerical strategy with low computational complexity while still assuring a high degree of accuracy is subject of this chapter. It is based on prior publications of the author [180, 181]. Note that the term *hybrid* is henceforth no longer limited to a combined CFD/CA approach. Instead, the 3D-CA part is expanded to additionally incorporate 1D network models. The general procedure to set up such a hybrid methodology is discussed in section 4.1. For an accurate and yet efficient modeling of the 3D-CA part, section 4.2 provides an exact formulation of the convective wave equation. Its discretization with finite element methods (FEM) is elaborated in section 4.3. It will be demonstrated that the correct use of this equation for arbitrary mean flow fields requires the energetically consistent boundary conditions of the regular Helmholtz equation, being subject of section 4.4. Section 4.5 deals with the linearization of the resulting nonlinear eigenvalue problem. Finally, the accuracy and efficiency of the developed methodology is demonstrated in section 4.6 using a simple test case.

### 4.1 General Modeling Procedure

The computational cost of a linear hybrid numerical approach is mainly determined by the spatial resolution of the 3D-CA part. In order to keep costs low, the computational domain needs to be limited to the geometric entities, which substantially impact the system's thermoacoustic stability. It is additionally desirable to not resolve components of small dimensions with high degrees of geometric detail. Such components are normally characterized by low Helmholtz numbers and might thus be characterized by adequate network models, cf. chapter 3. To identify the components to be resolved with 3D-CA, the thermoacoustic system is split into subdomains. Each subdomain is characterized by its geometry, the flow regime within the confined geometry as well as the targeted frequencies. The procedure will be discussed by means of the gas turbine as sketched in Fig. 4.1.

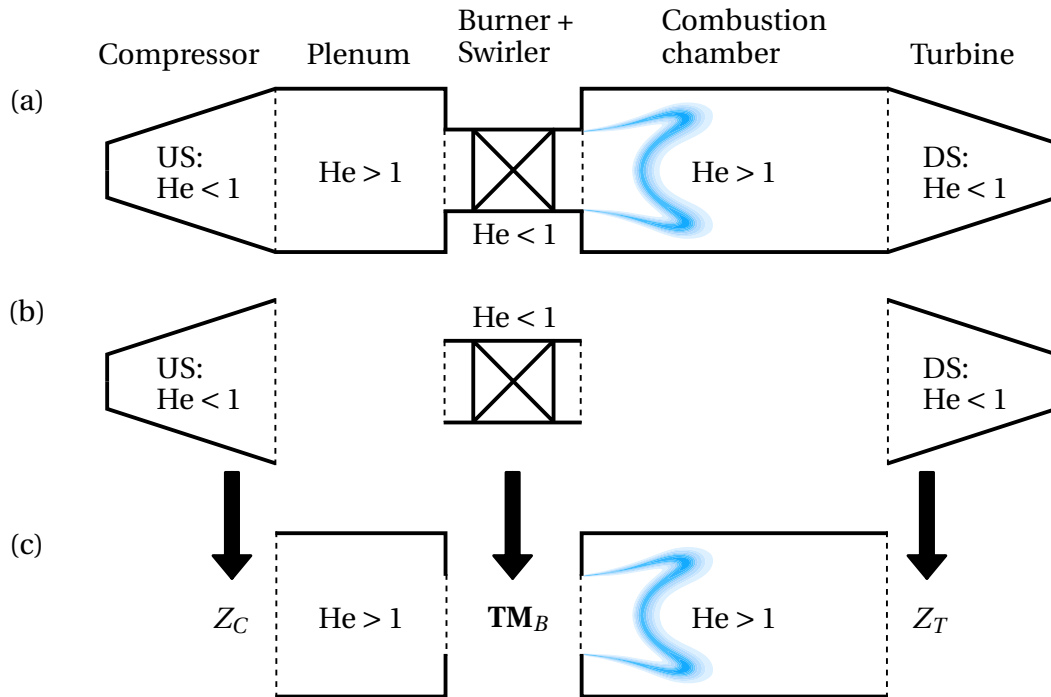


**Figure 4.1:** Workflow to model a gas turbine. (a) The complete gas turbine is characterized regarding the local Helmholtz number  $He$ . (b) The compressor, the burner and swirler as well as the turbine are characterized by 1D networks. (c) The plenum and combustion chamber are resolved with 3D-CA using the boundary conditions and transfer matrix from the 1D networks as termination and coupling of the disconnected resolved domains, respectively.

The combustion chamber enclosing the flame, cf. Fig. 4.1 (a), is the focal point for the thermoacoustic stability analysis. Also the burners including the swirlers play a crucial role: the interaction of sound waves with the highly turbulent flow in these components as well as the sudden area change connecting the burner and the combustion chamber constitute losses of acoustic energy. Accurately capturing these losses is crucial for a reliable stability analysis and is thus of major interest for the present thesis. The complex and small-scale geometry of the swirlers normally requires high spatial resolution. However, the acoustically compact diameter of the burner yielding a small Helmholtz number ( $He < 1$ ) allows for an acoustic characterization as two-port (e.g. a *burner transfer matrix*  $TM_B$ ) using 1D networks. Via the burner, the adjacent plenum can acoustically couple with the combustion chamber

and therefore impact its potentially unstable oscillation states. Being located far upstream (US) of the combustion chamber, the compressor is expected to be only weakly coupled with the thermoacoustic oscillations originating from the combustor. Similarly, the turbine section can be assumed to be virtually uncoupled from the combustor on the downstream (DS) end due to the acceleration of the hot gases in the high-pressure turbine stage.<sup>1</sup> Both, the compressor and the turbine sections do thus not need to be resolved in great detail. Instead, they can be cut off at the plenum inlet (i.e. the compressor outlet) and the combustor outlet (i.e. the turbine inlet), respectively. These interfaces are usually compact ( $He < 1$ ), which allows to describe the compressor and the turbine sections in terms of end impedances  $Z$ , again using 1D networks.<sup>2</sup> The components subject to 1D network modeling are highlighted in Fig. 4.1 (b). The large volume of the remaining plenum and combustion chamber in conjunction with a lack of symmetry common to many industrial combustors limits the 1D network methodology to the LF regime. In the HF regime, the Helmholtz number takes large values ( $He > 1$ ) requiring a resolution with 3D-CA. The disconnected resolved plenum and combustion chamber are finally coupled with the 1D networks as visualized in Fig. 4.1 (c).

The local Helmholtz number being the main indicator for this modeling procedure also gives a rough idea on the flow regimes in the individual components: large Helmholtz numbers correspond to large cross-sectional areas, which in turn imply small Mach numbers and vice versa. Therefore, the plenum and the combustion chamber are often modeled using the zero Mach number assumption for stagnant fluids. This simplification may be justified globally but fails locally in regions with non-negligible Mach numbers like in the vicinity of the turbine inlet. Here, the advection of the characteristic waves has significant impact on the eigenfrequencies of the system. Therefore, a modification of the well-established Helmholtz equation including the wave advection is highly desirable for the 3D-CA part, which will be discussed in the next section.

---

<sup>1</sup>At locations with Mach numbers exceeding unity, no sound waves created or reflected downstream of this location can travel upstream. In the case of the turbine section, this also means that aerodynamically induced sound of the turbine can not enter the combustor via the supersonic flow regime in the rotor blades.

<sup>2</sup>Most notably for deriving a 1D model for the acoustic response of accelerated acoustic and entropy waves (e.g. in the first turbine guide vane row) is the work of Marble and Candel [110]. More recent works to model the acoustic response of the compressor and turbine section were presented by Leyko et al. [182], Duran and Moreau [183] and Silva et al. [184], just to mention some.

## 4.2 Exact Convective Wave Equation

Apart from the domain size resolved with 3D-CA, the complexity of the mathematical model representing the sound propagation, amplification and dissipation has significant impact on the computational cost. Solving multiple coupled equations like the APE, LEE or LNSE is in general computationally more demanding than solving a single equation. The acoustic analogies discussed in section 2.3 are exact formulations to describe acoustic propagation. The mechanisms, which are not intrinsically included on the LHS are shifted to the RHS as sources. The equation most suitable to include the advection of acoustic waves in arbitrary mean flow fields is Moehring's equation (2.18). However, being a function of the stagnation enthalpy, this equation is highly impractical. Therefore, an exact convective wave equation in terms of the acoustic pressure is derived and discussed in this section.

Since the APE (2.9) represent pure acoustic wave propagation in arbitrary, isobaric mean flow fields, they form an ideal basis for the derivation of a universal convective wave equation. Following the procedure of Kotake [185] and Candel et al. [186] the divergence of eq. (2.9a) multiplied by  $\bar{\rho}\bar{c}^2 = \kappa\bar{p}$  is subtracted from the material derivative of eq. (2.9b). This leads to the acoustically consistent, inhomogeneous convective wave equation:

$$\begin{aligned}
& \frac{\partial^2 p'}{\partial t^2} + 2\bar{\mathbf{u}} \cdot \nabla \frac{\partial p'}{\partial t} + \bar{\mathbf{u}} \cdot \nabla (\bar{\mathbf{u}} \cdot \nabla p') - \bar{\rho}\bar{c}^2 \nabla \cdot \left( \frac{1}{\bar{\rho}} \nabla p' \right) \\
& = -\kappa \frac{\partial p'}{\partial t} \nabla \cdot \bar{\mathbf{u}} - \bar{\mathbf{u}} \cdot \nabla (\kappa p' \nabla \cdot \bar{\mathbf{u}}) - \kappa \bar{p} (\bar{\mathbf{u}} \cdot \nabla) (\nabla \cdot \mathbf{u}') + \kappa \bar{p} \Delta (\bar{\mathbf{u}} \cdot \mathbf{u}') \\
& \quad - \kappa \bar{p} \nabla \cdot \mathbf{S}_{\mathbf{u}}^{\nu, s, \nabla \bar{p}=0} + (\kappa - 1) \frac{\partial \dot{q}'}{\partial t} + (\kappa - 1) \bar{\mathbf{u}} \cdot \nabla \dot{q}' .
\end{aligned} \tag{4.1}$$

Here, the LHS is reshaped into that of eq. (2.10), whereas the RHS contains all remaining terms. These terms are considered as sources and sinks for acoustic waves advected by the flow velocity  $\bar{\mathbf{u}}$  and only take nonzero values in regions with flow inhomogeneities. This is easily proven by assuming a uniform mean flow field leading to a vanishing RHS of eq. (4.1). Then, the homogeneous convective wave equation (2.10) is obtained. Recall that with the assumption of a uniform mean flow velocity in eq. (2.10) mean density gradients and thus also combustion processes are precluded. Equation (4.1) further reduces to the inhomogeneous wave equation (2.14) for stagnant fluids with unsteady heat re-

lease.

Laplace transforming eq. (4.1) yields its counterpart in the FD

$$\begin{aligned}
 & s^2 \hat{p} + 2s\bar{\mathbf{u}} \cdot \nabla \hat{p} + \bar{\mathbf{u}} \cdot \nabla (\bar{\mathbf{u}} \cdot \nabla \hat{p}) - \bar{\rho} \bar{c}^2 \nabla \cdot \left( \frac{1}{\bar{\rho}} \nabla \hat{p} \right) \\
 = & -s\kappa \hat{p} \nabla \cdot \bar{\mathbf{u}} - \bar{\mathbf{u}} \cdot \nabla (\kappa \hat{p} \nabla \cdot \bar{\mathbf{u}}) - \kappa \bar{p} (\bar{\mathbf{u}} \cdot \nabla) (\nabla \cdot \hat{\mathbf{u}}) + \kappa \bar{p} \Delta (\bar{\mathbf{u}} \cdot \hat{\mathbf{u}}) \\
 & - \kappa \bar{p} \nabla \cdot \hat{\mathbf{S}}_{\mathbf{u}}^{v,s,\nabla \bar{p}=0} + s(\kappa - 1) \hat{q} + (\kappa - 1) \bar{\mathbf{u}} \cdot \nabla \hat{q}.
 \end{aligned} \tag{4.2}$$

For uniform mean flow fields, a homogeneous convective wave equation in the FD results

$$s^2 \hat{p} + 2s\bar{\mathbf{u}} \cdot \nabla \hat{p} + \bar{\mathbf{u}} \cdot \nabla (\bar{\mathbf{u}} \cdot \nabla \hat{p}) - \bar{c}^2 \nabla^2 \hat{p} = 0, \tag{4.3}$$

whereas the inhomogeneous Helmholtz equation (2.21) is obtained for stagnant fluids with unsteady heat release. In order to attain an intelligible nomenclature, the convective wave equation in the FD will henceforth be referred to as convective Helmholtz equation despite being well aware that it does not satisfy the classic definition of the Helmholtz equation.

The acoustically consistent equations (4.1) and (4.2) are unclosed due to the terms depending on the velocity fluctuations on the RHS. Instead of modeling these terms, a procedure to account for the volumetric sources with modified boundary conditions is developed. This requires the consideration of the equations in a volume-integrated sense, which is also an essential feature of FEM discretization. The corresponding procedure including the transformation of the equations for the use with FEM is presented in the following section.

### 4.3 Finite Element Methodology

The basic idea of FEM is to satisfy the employed BVP multiplied by a weighting function within the entire computational domain in an integral sense. Spatial discretization is obtained by introducing a weighting function for each node of the finite element mesh, also referred to as test functions. These test functions only take nonzero values in the immediate vicinity of their corresponding node locations. For further information on the spatial discretization in FEM, the reader is referred to Donea and Huerta [187].

It is easy to prove that the convective Helmholtz equation, similar to the Helmholtz equation for stagnant flows, is of elliptic type for subsonic mean

flow fields. Particularly these types of partial differential equations are robustly solved by the widespread Galerkin FEM discretization scheme and offer a great advantage over mixed-type PDEs like the LNSE or LEE: while the latter require numerical diffusion in order to give stable results (cf. e.g. [156, 187]), the Helmholtz equations of elliptic type are not prone to numerical instabilities and do thus not require any stabilization schemes.

For the discretization with FEM, the equations need to be provided in the weak formulation. This form intrinsically requires the specification of boundary fluxes, which may be exploited for the formulation of adequate boundary conditions. The derivation of the weak form and suitable boundary conditions will be discussed subsequently.

#### 4.3.1 Weak Form Equation

Finding a solution to the exact convective Helmholtz equation (4.2) requires the specification of suitable boundary conditions. The equation including the boundary conditions is thus a boundary value problem, whereas the corresponding wave equation (4.1) additionally requires initial values for the problem closure. Due to their natural frequency-dependency, acoustic boundary conditions are more straightforward to implement in the FD than in the TD. Therefore, the following derivation is performed for the inhomogeneous convective Helmholtz equation (4.2). It may be noted that the derivations can be performed equivalently for the TD equations.

First, eq. (4.2) is multiplied by the weighting function  $\tilde{p}$  and then integrated over the domain volume  $V$ . Subsequently, terms subject to second order spatial derivatives are integrated by parts. The detailed procedure is demonstrated in Appendix B, which ultimately yields the weak form of the inhomogeneous convective Helmholtz equation (iCHE)

$$\begin{aligned} & \iiint_V \left\{ s^2 \hat{p} \tilde{p} + s (\bar{\mathbf{u}} \cdot \nabla \hat{p}) \tilde{p} - s \hat{p} \bar{\mathbf{u}} \cdot \nabla \tilde{p} - (\bar{\mathbf{u}} \cdot \nabla \hat{p}) \bar{\mathbf{u}} \cdot \nabla \tilde{p} + \bar{c}^2 \nabla \hat{p} \cdot \nabla \tilde{p} \right\} dV \\ & + \iint_{\partial V} \mathbf{F} \cdot \mathbf{n} \tilde{p} dA = \iiint_V S_{iCHE} \tilde{p} dV . \end{aligned} \quad (4.4)$$

This weak form resembles the acoustically consistent inhomogeneous Helmholtz equation's (4.2) character of an acoustic analogy: the entire LHS describes the propagation of acoustic waves in a uniform mean flow field and

equals thus the weak formulation of the homogeneous convective Helmholtz equation. This also includes the flux  $\mathbf{F}$  across the boundary  $\partial V$ , which reads

$$\mathbf{F} = s\bar{\mathbf{u}}\hat{p} + \bar{\mathbf{u}}(\bar{\mathbf{u}} \cdot \nabla \hat{p}) - \bar{c}^2 \nabla \hat{p}. \quad (4.5)$$

It is important to highlight that this weak form flux is a result of the partial integration performed in Appendix B and is not to be confused with the acoustic energy flux of eq. (1.1). Interactions of the advected waves with mean flow inhomogeneities are described by the RHS volume sources  $S_{iCHE}$  in eq. (4.4):

$$\begin{aligned} S_{iCHE} = & -s(\kappa - 1)\hat{p}\nabla \cdot \bar{\mathbf{u}} - \kappa\hat{p}(\bar{\mathbf{u}} \cdot \nabla)(\nabla \cdot \bar{\mathbf{u}}) - (\kappa - 1)(\bar{\mathbf{u}} \cdot \nabla \hat{p})(\nabla \cdot \bar{\mathbf{u}}) \\ & + \kappa\bar{p}\Delta(\bar{\mathbf{u}} \cdot \hat{\mathbf{u}}) - \kappa\bar{p}(\bar{\mathbf{u}} \cdot \nabla)(\nabla \cdot \hat{\mathbf{u}}) \\ & - \kappa\bar{p}\nabla \cdot \hat{\mathbf{S}}_{\mathbf{u}}^{v,s,\nabla\hat{p}=0} + s(\kappa - 1)\hat{q} + (\kappa - 1)\bar{\mathbf{u}} \cdot \nabla \hat{q}, \end{aligned} \quad (4.6)$$

When applying the homogeneous convective wave equation to arbitrary mean flow fields, the overall source  $S_{iCHE}$  is neglected. The corresponding source terms can be used to quantify the errors resulting from this procedure.

Consistently exploiting the consideration of eq. (4.4) as an acoustic analogy allows for the derivation of a natural Neumann boundary condition from the flux terms. This is detailed in Appendix C also providing a universal weak form of the homogeneous convective Helmholtz equation (hCHE) for uniform mean flow fields and the Helmholtz equation (HE) for quiescent fluids. In the presence of flow inhomogeneities, this procedure requires the proper resolution of the source  $S_{iCHE}$ . However, this is not straightforward since some source terms depend on the velocity fluctuations. They are not solved for with the iCHE, which is thus unclosed. To prevent an extensive resolution of all source terms, a procedure to account for them via a boundary flux transformation is developed in the following.

### 4.3.2 Volume Source Treatment

The acoustically consistent inhomogeneous convective Helmholtz equation (4.2) was derived from the APE (2.9) in the FD. Consequently, those two sets of equations are physically equivalent although taking a different mathematical form. Specifying the same boundary conditions and properly resolving the source terms of the iCHE, the two sets of equations are thus expected to give the same solutions. Instead of resolving the unclosed source terms, the corresponding terms are compared to the boundary flux terms. This requires to

consider the source terms  $S_{iCHE}$  as an integral part of the wave propagation instead of sources for an acoustic analogy as in Appendix C. Then, a general formulation of the boundary flux is obtained by using the APE momentum equation (2.9a) in the FD leading to

$$\begin{aligned} \mathbf{F} &= s\bar{\mathbf{u}}\hat{p} + \bar{\mathbf{u}}(\bar{\mathbf{u}} \cdot \nabla \hat{p}) - \bar{c}^2 \nabla \hat{p} \\ &= s\bar{\mathbf{u}}\hat{p} + \bar{\mathbf{u}}(\bar{\mathbf{u}} \cdot \nabla \hat{p}) + s\kappa \bar{p} \hat{\mathbf{u}} + \kappa \bar{p} \nabla (\bar{\mathbf{u}} \cdot \hat{\mathbf{u}}) - \kappa \bar{p} \hat{\mathbf{S}}_{\mathbf{u}}^{v,s,\nabla \bar{p}=0}. \end{aligned} \quad (4.7)$$

Under the assumptions of a uniform mean flow and acoustically compact sub boundaries allowing for a 1D characterization, all terms but the third term vanish (cf. Appendix C). As all of those terms are functions of the mean flow velocity, they naturally vanish for stagnant fluids. This can be exploited by requiring the flux to comply with the boundary conditions of the Helmholtz equation for stagnant fluids

$$\mathbf{F}^{M=0} = s\kappa \bar{p} \hat{\mathbf{u}}^{M=0}, \quad (4.8)$$

which creates an erroneous flux for the iCHE with mean flow. The error denoted by  $\boldsymbol{\epsilon}_F^{M=0}$  becomes manifest in the four terms depending on the mean flow velocity:

$$\boldsymbol{\epsilon}_F^{M=0} = s\bar{\mathbf{u}}\hat{p} + \bar{\mathbf{u}}(\bar{\mathbf{u}} \cdot \nabla \hat{p}) + \kappa \bar{p} \nabla (\bar{\mathbf{u}} \cdot \hat{\mathbf{u}}) - \kappa \bar{p} \hat{\mathbf{S}}_{\mathbf{u}}^{v,s,\nabla \bar{p}=0}. \quad (4.9)$$

They can be related to the volume sources  $S_{iCHE}$  (4.6) by applying Gauss's theorem to the surface integral in eq. (4.10). This gives the overall volumetric RHS source  $S_{iCHE}^{M=0}$  when applying zero Mach number boundary conditions:

$$\begin{aligned} \iiint_V S_{iCHE}^{M=0} dV &= - \iint_{\partial V} \boldsymbol{\epsilon}_F^{M=0} \cdot \mathbf{n} dA + \iiint_V S_{iCHE} dV \\ &= - \iiint_V \left\{ s\kappa \hat{p} \nabla \cdot \bar{\mathbf{u}} + s\bar{\mathbf{u}} \cdot \nabla \hat{p} + \kappa \hat{p} \bar{\mathbf{u}} \cdot \nabla (\nabla \cdot \bar{\mathbf{u}}) + \kappa (\bar{\mathbf{u}} \cdot \nabla \hat{p}) (\nabla \cdot \bar{\mathbf{u}}) \right. \\ &\quad \left. + \bar{\mathbf{u}} \cdot \nabla (\bar{\mathbf{u}} \cdot \nabla \hat{p}) - s(\kappa - 1) \hat{q} - (\kappa - 1) \bar{\mathbf{u}} \cdot \nabla \hat{q} \right\} dV. \end{aligned} \quad (4.10)$$

Note that for the pursued energetic comparison of the erroneous flux terms and the volume sources, the test function introduced for the weak formulation common to FEM discretization schemes is dropped. The procedure above is depicted in Fig. 4.2 for the combustion chamber of Fig. 4.1: Solving the full iCHE with the overall boundary flux  $\mathbf{F} = \mathbf{F}^{M=0} + \boldsymbol{\epsilon}_F^{M=0}$  at the interfaces to the

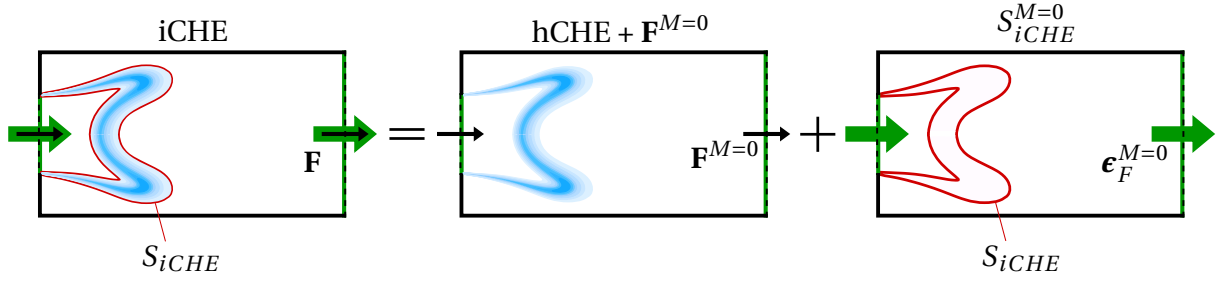


**Figure 4.2:** Left: full iCHE with flux  $\mathbf{F}$  and sources  $S_{iCHE}$ . Center: hCHE (without sources) and reduced flux  $\mathbf{F}^{M=0}$ . Right: resulting overall volumetric source  $S_{iCHE}^{M=0}$  from erroneous fluxes  $\epsilon_F^{M=0}$  and dropped sources  $S_{iCHE}$ .

burner and the turbine (highlighted in green) requires the resolution of the sources  $S_{iCHE}$  (Fig. 4.2 left). These are particularly dominant in the flame region outlined in red due to large gradients of the mean flow field. Instead, the hCHE can be solved without sources and only considering the fluxes corresponding to zero Mach number domains  $\mathbf{F}^{M=0}$  (Fig. 4.2 center). This yields an overall volumetric source  $S_{iCHE}^{M=0}$  formed by the dropped sources  $S_{iCHE}$  and the erroneous fluxes  $\epsilon_F^{M=0}$  (Fig. 4.2 right).

Taking a closer look on the overall volume source terms  $S_{iCHE}^{M=0}$  in eq. (4.10), they may be expressed in the following condensed form

$$S_{iCHE}^{M=0} = -\frac{\bar{D}}{D\hat{t}} \left\{ \bar{\mathbf{u}} \cdot \nabla \hat{p} + \kappa \hat{p} \nabla \cdot \bar{\mathbf{u}} - (\kappa - 1) \hat{q} \right\}. \quad (4.11)$$

The material derivative in the FD is denoted as  $\bar{D}/D\hat{t} = s + \bar{\mathbf{u}} \cdot \nabla$ . Employing the APE's energy equation (2.9b) in the FD, the remaining overall volume source term may also be expressed as

$$S_{iCHE}^{M=0} = \frac{\bar{D}}{D\hat{t}} \left\{ s\hat{p} + \kappa \bar{p} \nabla \cdot \bar{\mathbf{u}} \right\}, \quad (4.12)$$

which just represents the material derivative of the acoustic energy equation for stagnant fluids without heat release. Supposing that a low Mach number mean flow does not significantly affect the pressure field, the solution of the iCHE approximately satisfies the linearized energy conservation of the Helmholtz equation. As a result, the overall resulting source term  $S_{iCHE}^{M=0}$  (cf. right part of Fig. 4.2) vanishes. The assumption of source terms only having a marginal effect on the acoustic solution field was made before by Culick

[54] for investigating sources and their impact on the wave equation using Lighthill's analogy.

Under the common assumption of negligible impact of the mean flow on the mode shape it may indeed be concluded that the erroneous flux approximately compensates for the interaction mechanisms between acoustics and non-uniform mean flows. This may be interpreted with the help of the Gauss theorem: neglecting the interaction between acoustics and mean flow non-uniformity yields an erroneous excitation or attenuation of the waves. This energetic discrepancy is simply transported out of the domain advectively due to the inconsistent Helmholtz boundary conditions for stagnant fluids. This concept also works for a straight duct with uniform mean flow velocity, being the typical application of the homogeneous CHE: Due to the lack of acoustic sources, the spurious energy advectively introduced at the inlet boundary is advected through the domain ultimately leaving it via the outlet boundary.

Also the impact of a fluctuating heat release  $\hat{q}$  can be included using the corresponding source terms of eq. (4.6). With the errors due to the application of the Helmholtz boundary conditions, the overall remaining source term then becomes

$$S_{iCHE}^{M=0, \hat{q} \neq 0} = \frac{\bar{D}}{D\hat{t}} \left\{ s\hat{p} + \kappa \bar{p} \nabla \cdot \hat{\mathbf{u}} - (\kappa - 1) \hat{q} \right\}. \quad (4.13)$$

This is the energy equation for zero Mach number flows including heat release fluctuations. Again following the argument of eq. (4.12), this term is approximately satisfied for  $\hat{q} \neq 0$  when assuming that the mean flow does not significantly alter the solution field.

In conclusion, the convective Helmholtz equation may be consistently applied to arbitrary mean flow fields including heat release rate fluctuations by solving the following consistent weak form:

$$\begin{aligned} & \iiint_V \left\{ s^2 \hat{p} \tilde{p} + s \left( (\bar{\mathbf{u}} \cdot \nabla \hat{p}) \tilde{p} - \hat{p} \bar{\mathbf{u}} \cdot \nabla \tilde{p} \right) - (\bar{\mathbf{u}} \cdot \nabla \hat{p}) \bar{\mathbf{u}} \cdot \nabla \tilde{p} + \bar{c}^2 \nabla \hat{p} \cdot \nabla \tilde{p} \right\} dV \\ & + \iint_{\partial V} s \bar{\rho} \bar{c}^2 \hat{\mathbf{u}}^{M=0} \cdot \mathbf{n} \tilde{p} dA = \iiint_V (\kappa - 1) \frac{\bar{D} \hat{q}}{D\hat{t}} \tilde{p} dV. \end{aligned} \quad (4.14)$$

Similar to the explication in Appendix C, the boundary flux in eq. (4.14) corresponds to an acoustic Neumann boundary condition. However, this formulation requires the adequate and energetically consistent boundary conditions for zero Mach number domains as would be required for the Helmholtz equa-

tion. Before elaborating on energetically consistent Helmholtz boundary conditions in section 4.4, the Neumann boundary flux is first transformed into more useful acoustic boundary conditions subsequently.

### 4.3.3 Acoustic Boundary Conditions for the Weak Form

The boundary flux term of the iCHE (4.14) is a function of the velocity fluctuation, representing an acoustic Neumann boundary condition (cf. Appendix C). It can be further generalized for the application of frequency dependent acoustic boundary conditions. The most general representative of acoustic one-ports as discussed in section 2.6 is the specific impedance  $z$ . Using its definition of eq. (2.29), the boundary flux becomes a function of the state variable  $\hat{p}$  and the specific impedance

$$\mathbf{F} \cdot \mathbf{n} = s \bar{\rho} \bar{c}^2 \hat{\mathbf{u}} \cdot \mathbf{n} = s \bar{c} \frac{\hat{p}}{z}, \quad (4.15)$$

which represents a boundary condition of the third kind. Note that the superscript ( $M = 0$ ) has been dropped for this transformation of a general acoustic Neumann boundary condition.

For the coupling of two spatially disconnected domains like the plenum and the combustion chamber in Fig. 4.1, acoustic two-ports such as transfer matrices can be employed. They may be obtained from measurements or from 1D network models. The network elements presented in section 3.2 are derived from equations subject to restrictive assumptions like homentropic and irrotational flows. The consistent integration of the network models into the numeric model of the (convective) Helmholtz equation requires a consistent implementation of restrictions at the boundaries. Since the transfer matrix formulation is based on the assumption of 1D acoustic propagation, the coupling boundaries are required to be acoustically compact. This is also a prerequisite for the derivation of the natural Neumann boundary condition in Appendix C. Then, the native formulation of the transfer matrix (3.2) is very useful for the implementation of a coupling boundary condition. However, the discrepancy of the 1D formulation of the transfer matrix and its application to boundaries with arbitrary spatial orientation needs to be accounted for by only using the

boundary normal velocity component as per

$$\begin{pmatrix} \frac{\hat{p}}{\rho\bar{c}} \\ -\hat{\mathbf{u}} \cdot \mathbf{n} \end{pmatrix}_d = \mathbf{TM} \begin{pmatrix} \frac{\hat{p}}{\rho\bar{c}} \\ \hat{\mathbf{u}} \cdot \mathbf{n} \end{pmatrix}_u = \begin{pmatrix} \text{TM}_{11} & \text{TM}_{12} \\ \text{TM}_{21} & \text{TM}_{22} \end{pmatrix} \begin{pmatrix} \frac{\hat{p}}{\rho\bar{c}} \\ \hat{\mathbf{u}} \cdot \mathbf{n} \end{pmatrix}_u. \quad (4.16)$$

Note that the two opposite coupling boundaries have differently oriented normal vectors. Using the convention of the upstream boundary normal vector being oriented in positive velocity direction, a negative signum must be added to the downstream velocity. This equation explicitly provides the acoustic velocity to specify the flux at the downstream boundary  $\mathbf{F}_d$  as a function of the primitive variables at the upstream boundary. Additionally employing eq. (C.3), the velocity fluctuation at the upstream side can exclusively be expressed as a function of the solution variable  $\hat{p}$ . The weak form flux at the downstream coupling boundary  $\mathbf{F}_d$  then yields

$$\mathbf{F}_d \cdot \mathbf{n} = - \iint_{\partial V_u} \left\{ s\bar{c} \text{TM}_{21} \hat{p} + \text{TM}_{22} (s\bar{\mathbf{u}} \hat{p} + \bar{\mathbf{u}} (\bar{\mathbf{u}} \cdot \nabla \hat{p}) - \bar{c}^2 \nabla \hat{p}) \cdot \mathbf{n} \right\} \tilde{p} \, dA_u. \quad (4.17)$$

Recalling the modeling workflow of Fig. 4.1, the downstream boundary corresponds to the interface between burner and combustion chamber. To obtain an equivalent formulation for the upstream boundary, i.e. the interface between plenum and burner in Fig. 4.1, the transfer matrix definition (4.16) is inverted first:

$$\begin{pmatrix} \frac{\hat{p}}{\rho\bar{c}} \\ \hat{\mathbf{u}} \cdot \mathbf{n} \end{pmatrix}_u = \mathbf{TM}^{-1} \begin{pmatrix} \frac{\hat{p}}{\rho\bar{c}} \\ -\hat{\mathbf{u}} \cdot \mathbf{n} \end{pmatrix}_d = \frac{1}{|\mathbf{TM}|} \begin{pmatrix} \text{TM}_{22} & -\text{TM}_{12} \\ -\text{TM}_{21} & \text{TM}_{11} \end{pmatrix} \begin{pmatrix} \frac{\hat{p}}{\rho\bar{c}} \\ -\hat{\mathbf{u}} \cdot \mathbf{n} \end{pmatrix}_d. \quad (4.18)$$

Again, the second equation gives direct access to the required velocity fluctuation at the upstream coupling boundary. The corresponding weak form flux reads

$$\mathbf{F}_u \cdot \mathbf{n} = - \frac{1}{|\mathbf{TM}|} \iint_{\partial V_d} \left\{ s\bar{c} \text{TM}_{21} \hat{p} + \text{TM}_{11} (s\bar{\mathbf{u}} \hat{p} + \bar{\mathbf{u}} (\bar{\mathbf{u}} \cdot \nabla \hat{p}) - \bar{c}^2 \nabla \hat{p}) \cdot \mathbf{n} \right\} \tilde{p} \, dA_d, \quad (4.19)$$

which is an exclusive function of the solution variable at the downstream coupling boundary.

At this point, no distinction was made between boundary conditions for domains with moving media and the suitable counterparts employing the stagnant Helmholtz approximation. This is discussed in the next section.

## 4.4 Energetical Consistency

Reconsidering the acoustic energy flux equation for homentropic potential flows, eq. (2.22b), reveals an advective energy transport across the boundaries of a system with mean flow. At the boundaries of a substitute system neglecting the mean flow, also the advectively transported energy flux is dropped. This implies an energetic inconsistency between the system with mean flow and its quiescent substitute when presuming equal values of pressure and velocity fluctuations at the boundaries. Although not representing energetic fluxes, this is similarly indicated in Fig. 4.2: the energetic discrepancy at the boundaries between the iCHE (left image) and the hCHE (center image) manifests in the energy adherent to the advective flux terms represented by the green arrows (right image). The consistent use of the CHE with arbitrary mean flow fields requires the negligence of advective energy fluxes, just as in domains with quiescent flow fields. However, the identification of the energy flux components subject to advection is not straightforward for impedance boundary conditions or transfer matrix couplings. To still reestablish energetic consistency between a system with mean flow and its substitute system with a zero Mach number assumption, suitable transformation procedures are desired for such boundary conditions. While a simple energetic transformation rule for impedance boundary conditions has been presented in the literature (cf. e.g. [188]), an equivalent transformation is lacking for transfer matrix couplings. To overcome this issue, the impedance transformation is first analyzed in detail. Afterwards, the findings are used to derive a transformation procedure for transfer matrices to provide an energetically consistent coupling of zero Mach number domains. Regarding the overall modeling workflow in Fig. 4.1, this also allows to consistently connect the transfer matrix of the burner when using the CHE formulation for the plenum and the combustion chamber.

### 4.4.1 Impedance Transformation for Zero Mach Number Domains

Apart from the local Mach number, the amplitudes of the pressure and velocity fluctuations govern the acoustic energy flux, cf. section 2.5. The specific impedance  $z$  relates the local pressure and velocity fluctuations and is thus also a measure for the energy flux. Applying the same impedance boundary

condition to a system considering mean flow and the substitute system neglecting mean flow yields energetic discrepancies as demonstrated by Motheau et al. [188]. To compensate for the missing advective flux, they recommend to use a modified impedance  $z^{M=0}$  in the substitute system. Following the notation of section 4.3.2, quantities of an energetically consistent substitute system without mean flow are henceforth denoted by the superscript  $(\cdot)^{M=0}$ . The modified consistent specific impedance may be calculated according to

$$z^{M=0} = \frac{z + M}{Mz + 1}, \quad (4.20)$$

only being a function of the original specific impedance and the scalar Mach number  $M$ . Obviously, for a system without mean flow,  $M = 0$ , the substitute impedance is equal to the original impedance.

Further insight into the impedance transformation by Motheau et al. is gained by analyzing the temporal average of the flux eq. (2.22b), also referred to as acoustic intensity  $I$ . Making use of eq. (2.24), this intensity may be expressed in terms of the fluctuating variables in the FD as

$$I = \langle \mathbf{F} \cdot \mathbf{n} \rangle_t = \int_{t-T_s}^t \mathbf{F} \cdot \mathbf{n} dt \approx \frac{1}{2} \Re \left\{ \overline{\hat{B}} \hat{m} \right\}, \quad |\alpha| \ll f \quad (4.21)$$

For simplicity, the generally 3D intensity was reduced to one dimension in eq. (4.21), with the velocities pointing in the direction of the unit surface normal vector  $\mathbf{n}$ . To get a handle on the general problem, the primitive variables are now replaced by the acoustic characteristics, i.e. downstream and upstream traveling wave components  $\hat{f}$  and  $\hat{g}$ , which are related to the primitive acoustic variables through relation (2.30). Now the complex amplitudes of total enthalpy and mass flow fluctuations may be written as

$$\hat{B} = \frac{\hat{p}}{\bar{\rho}} + \bar{u} \cdot \hat{u} = \bar{c} \left( (1 + M) \hat{f} + (1 - M) \hat{g} \right) \quad (4.22)$$

$$\hat{m} = \bar{\rho} \hat{u} + \frac{\bar{u}}{\bar{c}^2} \hat{p} = \bar{\rho} \left( (1 + M) \hat{f} - (1 - M) \hat{g} \right). \quad (4.23)$$

Using the definition of the reflection coefficient  $R_d = \frac{\hat{g}}{\hat{f}}$  relating the complex amplitudes of upstream to downstream traveling waves at a given downstream boundary, eq. (4.21) becomes

$$I = \frac{1}{2} \bar{\rho} \bar{c} (1 + M)^2 |\hat{f}|^2 \left( 1 - \frac{(1 - M)^2}{(1 + M)^2} |R_d|^2 \right). \quad (4.24)$$

The equivalent intensity of the substitute system at rest ( $M = 0$ ) is

$$I^{M=0} = \frac{1}{2} \bar{\rho} \bar{c} |\hat{f}^{M=0}|^2 \left( 1 - |R_d^{M=0}|^2 \right). \quad (4.25)$$

Using the relation between the specific impedance and the reflection coefficient (2.31), eq. (4.20) can be written as

$$|R_d^{M=0}| = \frac{(1 - M)}{(1 + M)} |R_d|. \quad (4.26)$$

Substituting eq. (4.26) into eq. (4.25) and comparing with eq. (4.24) it becomes apparent that equal intensities of original and substitute system require an additional condition:

$$\frac{1}{2} \bar{\rho} \bar{c} (1 + M)^2 |\hat{f}|^2 \stackrel{!}{=} \frac{1}{2} \bar{\rho} \bar{c} |\hat{f}^{M=0}|^2. \quad (4.27)$$

Equation (4.27) results from the choice of  $R_d = \frac{\hat{g}}{\hat{f}}$ . Instead using  $R_u = \frac{\hat{f}}{\hat{g}}$  for an upstream boundary with the transformation

$$|R_u^{M=0}| = \frac{(1 + M)}{(1 - M)} |R_u| \quad (4.28)$$

equivalently yields

$$\frac{1}{2} \bar{\rho} \bar{c} (1 - M)^2 |\hat{g}|^2 \stackrel{!}{=} \frac{1}{2} \bar{\rho} \bar{c} |\hat{g}^{M=0}|^2. \quad (4.29)$$

Since both results stem from the same intensity eq. (4.21) it can be concluded that conditions (4.27) and (4.29) must be fulfilled simultaneously to maintain the correct intensity in the substitute  $M = 0$  system. Satisfying these conditions is more restrictive than the requirement of equal total intensity for the real and the substitute system: the two conditions also imply the same intensities of purely upstream and purely downstream traveling waves for both systems. It can be shown that the conditions stated in eqs. (4.27) and (4.29) equal a requirement for the mass flow fluctuation in a root mean square sense [180]:

$$\langle \dot{m}'^2 \rangle^{M=0} \stackrel{!}{=} \langle \dot{m}'^2 \rangle^{M \neq 0}. \quad (4.30)$$

This yields an additional requirement for energetically equivalent boundary conditions: equal intensities are established if the root mean square of the mass flow fluctuations is equal. In conjunction with eq. (4.21), also the root

mean square of the total enthalpy fluctuations must thus be equivalent for both systems.

The transformation rule (4.26) is an exclusive function of the absolute values of the reflection coefficients and the Mach number. The phase information of the reflection coefficient is eliminated during the time averaging of the flux and does not affect the intensities of eqs. (4.24) and (4.25). The phase of the reflection coefficient represents the phase difference between upstream and downstream traveling waves, which are propagating at different speeds due to mean flow (cf. the solution of the 1D convective Helmholtz equation in section 2.2.4). This discrepancy in propagation speeds of the acoustic characteristics reduce the eigenfrequency of a system proportional to  $M^2$  [105, p. 159].<sup>3</sup> When the reflection coefficient's phase of the system considering mean flow is retained for the substitute system at rest, i.e.

$$\angle R = \angle R^{M=0}, \quad (4.31)$$

also the characteristic's modified propagation speed within the subsystem represented by the reflection coefficient is preserved. The phase relation of eq. (4.31) conforms to the transformation eq. (4.20) and its effect can be illustrated by means of Fig. 4.1: The eigenfrequencies of the real system are lower than the corresponding eigenfrequencies of the system entirely computed with the zero Mach number assumption. Alternatively, the eigenvalue is calculated only resolving the combustion chamber comprising the zero Mach number assumption, while all other components are represented by a reflection coefficient transformed with eq. (4.26) and (4.31). The resulting eigenfrequency is expected to be much closer to the value of the real system as it is the case for the substitute system entirely neglecting mean flow.

#### 4.4.2 Transfer Matrix Transformation for Zero Mach Number Domains

The analysis of the energetically consistent transformation of acoustic one-ports in the preceding section revealed an explicit relation between the Riemann Invariants of a system with mean flow and its substitute system neglecting mean flow. For the derivation of an equivalent transformation procedure for acoustic two-ports, the consideration of the scattering matrix (3.3) is thus

<sup>3</sup>Note that [105, p. 159] contains typos in Tab. 6-1. The factor  $(1 - M^2)$  in the equations for the axial frequency belongs to the numerator instead of the denominator.

beneficial. In this way, two domains approximated by the zero Mach number assumption may be consistently coupled by a scattering matrix including mean flow as illustrated in Fig. 4.3 (a). Following the discussion related to Fig. 3.2, Fig. 4.3 highlights the scattered wave at the downstream port  $\hat{f}_d$  being composed of a reflected (Fig. 4.3 (b)) and a transmitted (Fig. 4.3 (c)) component of the incident waves. The linear time-invariant properties of the scat-

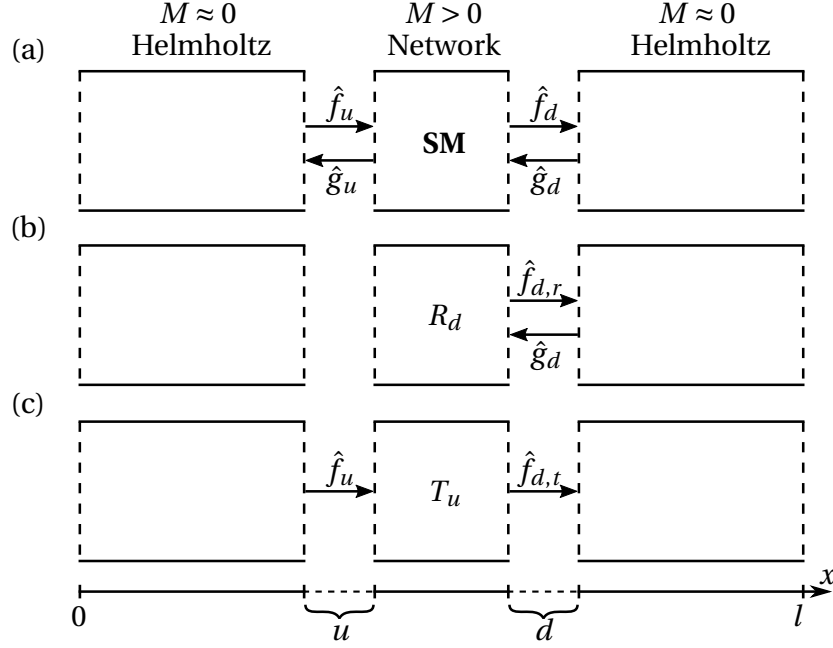


**Figure 4.3:** Schematic of a scattering matrix element connecting two low Mach number domains. (a) Complete scattering of characteristics. (b) Exclusive reflection of incident wave at downstream port. (c) Exclusive transmission of incident wave at upstream port.

tering matrix allow to derive its transformation to the  $M = 0$  substitute matrix by transforming the individual coefficients separately. This is done by requiring that the intensity transfer across the boundaries caused by the respective coefficient is preserved from the original to the substitute system.

The overall intensity at the two coupling interfaces from pure transmission of the incident wave  $f_u$ , cf. Fig. 4.3 (c), is given by:

$$\begin{aligned} \mathbf{I}_u^{g=0} \cdot \mathbf{n}_u + \mathbf{I}_d^{g=0} \cdot \mathbf{n}_d &= \frac{1}{2} \bar{\rho}_u \bar{c}_u (1 + M_u)^2 |\hat{f}_u|^2 - \frac{1}{2} \bar{\rho}_d \bar{c}_d (1 + M_d)^2 |\hat{f}_{d,t}|^2 \\ &= \frac{1}{2} \bar{\rho}_u \bar{c}_u (1 + M_u)^2 |\hat{f}_u|^2 \left( 1 - \frac{\bar{\rho}_d \bar{c}_d (1 + M_d)^2}{\bar{\rho}_u \bar{c}_u (1 + M_u)^2} |T_u|^2 \right). \end{aligned} \quad (4.32)$$

Equivalently, the intensity of the substitute system at rest becomes

$$\left(\mathbf{I}_u^{g=0} \cdot \mathbf{n}_u\right)^{M=0} + \left(\mathbf{I}_u^{g=0} \cdot \mathbf{n}_d\right)^{M=0} = \frac{1}{2} \bar{\rho}_u \bar{c}_u |\hat{f}_u^{M=0}|^2 \left(1 - \frac{\bar{\rho}_d \bar{c}_d}{\bar{\rho}_u \bar{c}_u} |T_u^{M=0}|^2\right). \quad (4.33)$$

For the real system transmitting an equal intensity as the substitute system, eq. (4.32) is equated with eq. (4.33). Comparing the prefactors of the equations immediately reveals the similarity to eq. (4.27). As discussed in the previous section, the equality of the prefactors constitute equal intensities of the waves exclusively traveling out of the upstream Helmholtz domain and an equal mass flow fluctuation in a mean square sense at the upstream port. With the same thermodynamic state of the real system and the substitute system at rest, the terms in the brackets of eqs. (4.32) and (4.33) are equal, if the transformation relation

$$|T_u^{M=0}| = \frac{(1 + M_d)}{(1 + M_u)} |T_u|, \quad (4.34)$$

between the transmission coefficients of the real system  $T_u$  and the substitute system  $T_u^{M=0}$  is satisfied. The transformation relation again only affects the absolute value of the transmission coefficients. The phase is kept constant

$$\angle T_u^{M=0} = \angle T_u. \quad (4.35)$$

The transformation of the other coefficients is carried out likewise, yielding

$$|T_d^{M=0}| = \frac{(1 - M_u)}{(1 - M_d)} |T_d|; \quad \angle T_d^{M=0} = \angle T_d, \quad (4.36)$$

$$|R_u^{M=0}| = \frac{(1 - M_u)}{(1 + M_u)} |R_u|; \quad \angle R_u^{M=0} = \angle R_u, \quad (4.37)$$

$$|R_d^{M=0}| = \frac{(1 + M_d)}{(1 - M_d)} |R_d|; \quad \angle R_d^{M=0} = \angle R_d. \quad (4.38)$$

Similar to the phase of the reflection coefficient discussed in the previous section, the phases of the scattering matrix coefficients determine the phase difference between incoming and scattered waves. Keeping the phase of the coefficients constant within the energetic transformation for the use in a consistent substitute system at rest causes an equal convection of the characteristics within the regions represented by the 1D network. This leads to the conclusion that the eigenfrequency reduction proportional to  $M^2$  due to the advection of 1D characteristics is captured in these regions, even if the adjacent systems

are subject to the zero Mach number assumption. Recall that the boundary condition transformations are also required for the consistent CHE framework (4.14), which additionally includes the wave advection in the 3D-CA domains discretized with FEM.

## 4.5 Linearization of the Nonlinear Eigenvalue Problem

A major drawback of the modal analysis based on the convective Helmholtz equation is its nonlinearity in terms of the Laplace variable  $s$ , cf. eq. (4.2). The most practical way to handle such a nonlinear eigenvalue problem is its linearization at a given linearization point. This procedure does not have an impact on the computational complexity. However, it comes with severe drawbacks:

1. The eigenvalues are only valid in the close vicinity of the linearization point.
2. The linearization point is normally specified as a pure function of the oscillation frequency.

The second drawback is related to the first drawback, as the eigenvalues are in general complex valued. Consequently, the errors of the modal analysis increase with increasing damping/growth rates. Computing eigenvalues for a large range of frequencies requires the adaption of the linearization point to obtain satisfying results.

A solution to these issues is provided by the conversion of the overall numerical setup into a linear state-space representation, which takes the following explicit form in the Laplace domain:

$$s \hat{\mathbf{x}}(s) = \mathbf{A} \hat{\mathbf{x}}(s) + \mathbf{B} \hat{\mathbf{u}}(s) \quad (4.39a)$$

$$\hat{\mathbf{y}}(s) = \mathbf{C} \hat{\mathbf{x}}(s) + \mathbf{D} \hat{\mathbf{u}}(s) . \quad (4.39b)$$

The first equation (4.39a) is referred to as state equation with the state vector  $\hat{\mathbf{x}}$ , the system matrix  $\mathbf{A}$ , the input matrix  $\mathbf{B}$  and the input vector  $\hat{\mathbf{u}}$ . In the output equation (4.39b), the system's output vector  $\hat{\mathbf{y}}$  depends on the output matrix  $\mathbf{C}$  and the feedthrough matrix  $\mathbf{D}$ .

In simple words, the state-space formalism may be used to transform a single differential equation of order  $m$  to a system of  $m$  differential equations of first

order. For the second order convective wave equation (4.2) this yields a linear state equation system of two equations:

$$s \begin{pmatrix} 0 & 1 \\ 1 & 0 \end{pmatrix} \begin{pmatrix} \hat{p} \\ \hat{\varphi} \end{pmatrix} = \begin{pmatrix} -\bar{\mathbf{u}} \cdot \nabla \tilde{p} (\bar{\mathbf{u}} \cdot \nabla) + \bar{\rho} \bar{c}^2 \nabla \cdot \left( \frac{1}{\bar{\rho}} \nabla \right) & -2\bar{\mathbf{u}} \cdot \nabla \\ 0 & 1 \end{pmatrix} \begin{pmatrix} \hat{p} \\ \hat{\varphi} \end{pmatrix} + \begin{pmatrix} S_V \\ 0 \end{pmatrix}, \quad (4.40)$$

with the substitution variable  $\varphi$  representing the first time-derivative of the pressure fluctuations. The RHS volumetric sources of eq. (4.2) are abbreviated with  $S_V$ . It needs to be highlighted that the spatial discretization of the system of equations (4.40) in the context of FEM simulations leads to a duplication of the degrees of freedom in comparison to the nonlinear eigenvalue problem. While eq. (4.40) exclusively represents the linearization of the convective wave equation, additional nonlinearities are introduced if frequency dependent boundary conditions and flame transfer functions are used.<sup>4</sup> Their linearization is discussed subsequently.

#### 4.5.1 Linearization of Frequency-Dependent Boundary Conditions

An output equation in the fashion of eq. (4.39b) for a state-space system is mainly required if the system is coupled to other independent state-space systems. This may be the case when employing frequency-dependent boundary conditions in the weak formulation of a linearized eigenvalue problem such as eq. (4.40). As described in section 4.3.3, the impedance boundary condition and the transfer matrix coupling are most suitable for the weak form of the (convective) Helmholtz equation. In general, those one- and two-ports are nonlinearly depending on the frequency and thus also require a suitable linearization procedure. Their characterization using measurements or 1D network models commonly results in discrete transfer function data for exclusively real valued frequencies. By linearizing the nonlinear system at a linearization point, the transfer functions are simply extruded to the complex frequency plane, cf. Fig. 4.4 (left). This extrusion, however, does not reflect the physics and the general conventions for the attenuation of the waves in time correctly. This may be illustrated by a duct element representing a time-lag

---

<sup>4</sup>The nonlinearities in terms of the Laplace variable discussed in the present section are not to be confused with the nonlinear mechanisms occurring at high acoustic amplitudes covered in chapter 5.

for a downstream traveling characteristic entering the duct at a given amplitude: for pure harmonic oscillations, the traveling wave exits the duct at the same amplitude. This is in contrast to a temporally damped or excited wave, which will exit the duct at a decreased or increased amplitude, respectively. With the basic assumption of exponential growth (or damping), also an exponential extrapolation to the complex plane as depicted in Fig. 4.4 (right) is required. Schmid et al. [1] discuss different extrapolation methods and refer to the exponential extrapolation as *filter*.

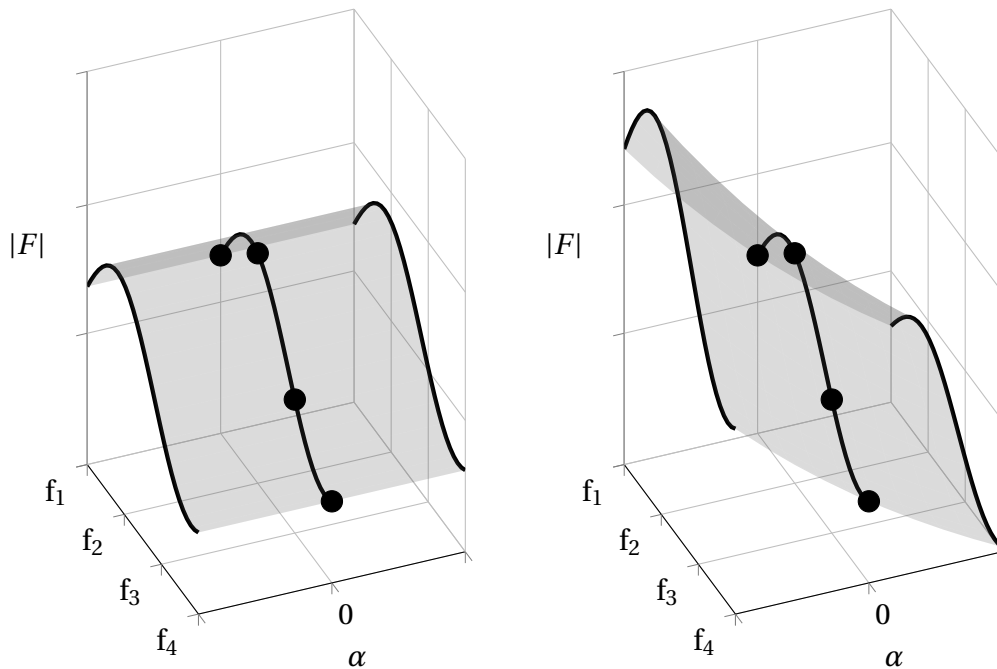


**Figure 4.4:** Schematic of different approaches for the extrapolation of transfer functions  $F$  specified for real valued frequencies  $f$  to the complex plane with growth rate  $\alpha$  following Schmid et al. [1]: extrusion (left) and filter (right).

A procedure to linearize frequency dependent boundary conditions has been presented by Jaensch et al. [189] for measured transfer functions. In particular, they consider a frequency dependent reflection coefficient as a function of the Laplace variable  $s$

$$R(s) = \frac{\hat{g}}{\hat{f}} \approx \frac{b_{n_o} s^{n_o} + \dots + b_1 s + b_0}{s^{n_i} + a_{n_i-1} s^{n_i-1} + \dots + a_1 s + a_0}. \quad (4.41)$$

The reflection coefficient is approximated by a rational function fit with an

output polynomial in the numerator and the input polynomial in the denominator. To satisfy the causality condition<sup>5</sup> of real systems, the order of the output polynomial has to be lower than that of the input polynomial  $n_o \leq n_i$ . Using the Laplace variable in the polynomials naturally expands the measured transfer function (here the reflection coefficient) from real valued frequencies to the complex plane. Therefore, the exponential extrapolation as depicted in Fig. 4.4 (right) is naturally included in this procedure. Reshaping eq. (4.41) and applying the inverse Laplace transform leads to

$$\mathbf{g}^{[n_i]} + a_{n_i-1} \mathbf{g}^{[n_i-1]} + \dots + a_1 \mathbf{g}^{[1]} + a_0 \hat{\mathbf{g}} = b_{n_o} f^{[n_o]} + \dots + b_1 f^{[1]} + b_0 f, \quad (4.42)$$

where the superscript in brackets  $(\cdot)^{[j]}$  denotes the  $j$ -th temporal derivative. This equation may directly be translated to a state-space system in the shape of eq. (4.39). This is explicated in more detail in Appendix D including the coupling of the linearized boundaries with the state-space representation of the convective Helmholtz equation's weak formulation.

### 4.5.2 Linearization of Flame Driving

After linearizing the boundary conditions, the only remaining nonlinear contribution may stem from the RHS volumetric sources  $S_V$  of the convective Helmholtz equation, cf. eq. (4.40). Since most of those terms are dropped when using the consistent weak formulation with Helmholtz boundary conditions, eq. (4.14), only the remaining heat release fluctuations need to be considered. It has been demonstrated with eq. (4.13) that the same driving mechanisms suitable for stagnant fluids must also be applied to the framework of the convective Helmholtz equation with Helmholtz boundary conditions. As explicated in section 2.8, flame driving mechanisms suitable for the Helmholtz equation are the flame displacement and deformation, which may thus also be applied to the convective Helmholtz equation. Then, the RHS source of eq. (4.14) becomes

$$(\kappa - 1) \frac{\bar{D}}{D\hat{t}} (\hat{q}_\rho + \hat{q}_\Delta) = (\kappa - 1) \left( \bar{q} \nabla \cdot \hat{\mathbf{u}} + \frac{1}{s} \bar{\mathbf{u}} \cdot \nabla (\bar{q} \nabla \cdot \hat{\mathbf{u}}) - \hat{\mathbf{u}} \cdot \nabla \bar{q} - \frac{1}{s} \bar{\mathbf{u}} \cdot \nabla (\hat{\mathbf{u}} \cdot \nabla \bar{q}) \right). \quad (4.43)$$

---

<sup>5</sup>The response of a causal system is only determined by past and present input signals. Regarding the reflection coefficient this means that any reflected wave is the result of a previously incident wave.

The source depends on the velocity fluctuations, which can only be expressed in terms of the pressure fluctuations under the very restrictive assumption of 1D wave propagation in uniform mean flows, cf. Appendix C. As those assumptions are not satisfied in the flame region, an alternative closure is required. A suitable closure may be obtained by identifying the pure acoustic velocity as the main driver for a coherent local flame displacement and the corresponding flame deformation. With the wave distortion due to the mean flow already included in the resolved pressure field, simply using the velocity fluctuations for stagnant flows, i.e.  $\hat{\mathbf{u}} = -\frac{1}{s\bar{\rho}}\nabla\hat{p}$ , accurately represents the pure acoustic velocity fluctuations. Then, the individual FRF source terms for the convective Helmholtz equation become

$$(\kappa - 1)\frac{\bar{D}}{D\hat{t}}\hat{q}_\rho \approx -(\kappa - 1)\left(\frac{1}{s}\bar{q}\nabla^2\hat{p} + \frac{1}{s^2}\bar{\mathbf{u}}\cdot\nabla(\bar{q}\nabla^2\hat{p})\right), \quad (4.44a)$$

$$(\kappa - 1)\frac{\bar{D}}{D\hat{t}}\hat{q}_\Delta \approx (\kappa - 1)\left(\frac{1}{s}\nabla\hat{p}\cdot\nabla\bar{q} + \frac{1}{s^2}\bar{\mathbf{u}}\cdot\nabla(\nabla\hat{p}\cdot\nabla\bar{q})\right). \quad (4.44b)$$

Again, these sources are nonlinear in terms of the Laplace variable  $s$ . Its incorporation into the state-space representation of the convective Helmholtz equation, eq. (4.40), would yield another duplication of degrees of freedom. However, this contradicts the desired low-cost numerical approach. Furthermore, the flame region normally only represents a small zone of the entire computational domain. Duplicating the number of solved equations at every spatial location is therefore not reasonable. Instead, the volumetric FRF source is linearized using a Taylor approximation at a linearization point  $s_0$ . This yields the final linearized sources, exemplarily shown for the displacement FRF

$$(\kappa - 1)\frac{\bar{D}}{D\hat{t}}\hat{q}_\Delta\Big|_{s_0} \approx (\kappa - 1)\left(\left(\frac{2}{s_0} - \frac{1}{s_0^2}s\right)\nabla\hat{p}\cdot\nabla\bar{q} + \left(\frac{3}{s_0^2} - \frac{2}{s_0^3}s\right)\bar{\mathbf{u}}\cdot\nabla(\nabla\hat{p}\cdot\nabla\bar{q})\right). \quad (4.45)$$

Equivalently, the Taylor linearized deformation FRF is obtained. For small mean flow velocities and high frequencies, the convection term is expected to vanish and may thus be neglected. As a linearization point, the frequency shift for the numerical eigenvalue solver may be used. The solver uses this shift value to transform the eigenvalue problem to find only eigenvalues closest to this frequency. As the linearized flame displacement source eq. (4.45) is a function of the state variable  $\hat{p}$ , it can be directly incorporated into the system matrix  $\mathbf{A}$  of eq. (4.40).

## 4.6 Simple Test Case

To validate the linearized weak formulation framework of the convective Helmholtz equation including the coupling boundary conditions, a comparative modal analysis of a simple test case is performed. The test case should also be suitable to investigate the energetically transformed Helmholtz boundary conditions in combination with the convective Helmholtz equation and the Helmholtz equation for stagnant mean flow fields. A test case satisfying these requirements is sketched in Fig. 4.5 and consists of two connected straight ducts of increasing cross-section with a mean flow from left to right, normally forming a jet downstream of the backward facing step. Such a setup has al-

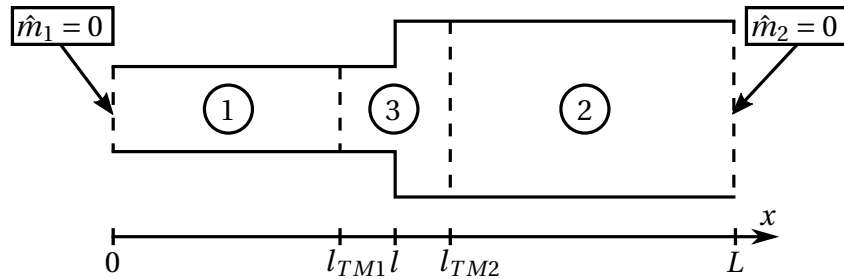


**Figure 4.5:** Cross-sectional sketch of the simple test case.

ready been widely investigated in the 1980's [31] regarding the interactions between acoustic waves and free shear layers of turbulent flows. The geometric and thermodynamic specifications of the present setup are listed in Tab. 4.1.

**Table 4.1:** Geometric and thermodynamic properties of the simple test case.

$A_1$ [m <sup>2</sup> ]	$A_2$ [m <sup>2</sup> ]	$l$ [m]	$l_{TM1}$ [m]	$l_{TM2}$ [m]	$L$ [m]								
0.01	0.02	0.5	0.45	0.55	1.1								
<table border="1"> <thead> <tr> <th><math>T</math> [K]</th> <th><math>p</math> [Pa]</th> <th><math>\gamma</math></th> <th><math>R</math> <math>\left[ \frac{\text{J}}{\text{kg K}} \right]</math></th> </tr> </thead> <tbody> <tr> <td>300</td> <td>101,325</td> <td>1.4</td> <td>287</td> </tr> </tbody> </table>						$T$ [K]	$p$ [Pa]	$\gamma$	$R$ $\left[ \frac{\text{J}}{\text{kg K}} \right]$	300	101,325	1.4	287
$T$ [K]	$p$ [Pa]	$\gamma$	$R$ $\left[ \frac{\text{J}}{\text{kg K}} \right]$										
300	101,325	1.4	287										

### 4.6.1 Numerical Model

The geometry is split in three parts as indicated in Fig. 4.5. First, part 3 representing the area change is replaced by a transfer matrix  $\mathbf{TM}$  resulting from 1D network modelling with mean flow. Then, this transfer matrix is used to couple parts 1 and 2, which are resolved as FEM domains.

Characterizing the intermediate part 3 of Fig. 4.5 in terms of a 1D network model has the advantage that the exact interaction mechanisms between acoustics and the mean flow shear layers do not need to be resolved. Instead, the network accounts for the losses and phase shifts associated with these interactions. An appropriate representation of this part consists of a duct of constant cross section and a subsequent sudden area change again followed by a duct. This sequence of basic network elements is depicted in Fig. 4.6. Us-

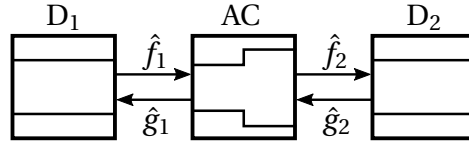


**Figure 4.6:** Network model of the sudden area change connected to ducts of constant cross-sectional areas on both sides.

ing the network modeling procedure as elaborated in section 3.1, the overall transfer matrix of part 3 can be characterized with the transfer matrices of the three individual elements. The ducts are represented by eq. (3.5) whereas a low Mach number approximation for the area change transfer matrix (3.14) is employed according to:

$$\mathbf{TM}_{pu,AC} = \begin{pmatrix} 1 & M_u \left( 1 - \left( \frac{A_u}{A_d} \right)^2 \right) - M_u \zeta \\ 0 & \frac{A_u}{A_d} \end{pmatrix}. \quad (4.46)$$

The overall transfer matrix  $\mathbf{TM}$  depends on the mean flow Mach number and the pressure loss at the sudden area change. These parameters are varied for the individual setups as described in the subsequent section 4.6.2. An energetically consistent counterpart of the transfer matrix for Helmholtz domains with stagnant mean flows  $\mathbf{TM}^{M=0}$  can be calculated using the transformation rules derived in section 4.4.

The remaining cylindrical parts 1 and 2 are resolved in three dimensions using the commercial FEM software COMSOL MULTIPHYSICS<sup>®</sup>. Figure 4.7 displays

the mesh of the two cylindrical parts consisting of approximately 14500 tetrahedral Lagrangian elements. The coupling between the state-space represen-

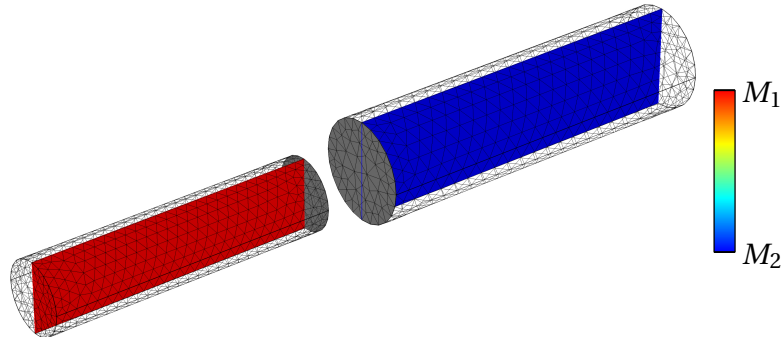


**Figure 4.7:** Mesh, axial Mach number field and coupled surfaces (grey) of the FEM setup.

tations of the two FEM domains and the transfer matrix of part 3 is implemented in accordance with section 4.5 and Appendix D employing a COMSOL MULTIPHYSICS<sup>®</sup> feature called *Average Operator* at the grey surfaces. At the left end of part 1 and the right end of part 2 energetically neutral zero mass flow fluctuations are imposed (cf. Fig. 4.5). This may be expressed in terms of a specific impedance according to eq. (2.34). The remaining surfaces are specified as sound hard wall boundaries. Since the jet and therefore the flow inhomogeneities are covered by part 3, a uniform and purely axial mean flow is employed in the parts 1 and 2. A modal analysis of the resulting model is performed using the eigenvalue solver of COMSOL MULTIPHYSICS<sup>®</sup> for different configurations and equations as explicated subsequently.

#### 4.6.2 Investigated Configurations

Four different setups are investigated, summarized in Tab. 4.2. As a reference configuration with mean flow, the APE (2.9) are solved in the FD constituting setup I. With the acoustic velocity being a solution variable of the APE, transfer matrix couplings are straightforward to implement for these equations. Due to the inclusion of mean flow in the two FEM domains, the original transfer matrix **TM** from the network model also incorporating mean flow must be applied to couple them. For setup II and III the Helmholtz equation for stagnant flows according to eq. (C.6) is solved. To prove the necessity of energetically consistent boundary conditions, the two FEM domains of setup II are coupled with

**Table 4.2:** Setups for eigenfrequency computations of the simple test case.

Setup	Equation	Mean flow assumption	Transfer Matrix formulation	Legend
I	APE ((2.9), FD)	$\bar{\mathbf{u}} = (\bar{u}, 0, 0)^T$	<b>TM</b>	—
II	HE (C.6)	$\bar{\mathbf{u}} = \mathbf{0}$	<b>TM</b>	--
III	HE (C.6)	$\bar{\mathbf{u}} = \mathbf{0}$	<b>TM</b> <sup><i>M=0</i></sup>	◇
IV	CHE (4.14)	$\bar{\mathbf{u}} = (\bar{u}, 0, 0)^T$	<b>TM</b> <sup><i>M=0</i></sup>	○

the original transfer matrix **TM**. Due to the inconsistent assumptions in the FEM domains and the network model, this configuration is expected to give erroneous results. In contrast, the results of setup III using the energetically consistent transfer matrix for zero Mach number flows **TM**<sup>*M=0*</sup> are expected to reproduce the results of the reference setup I. Finally, in setup IV the consistent convective Helmholtz equation for arbitrary mean flow fields (4.14) is solved in the FEM domains with mean flow. For the sake of consistency, the transfer matrix for zero Mach number domains **TM**<sup>*M=0*</sup> must be utilized. This configuration is expected to deliver the highest accuracy in the reproduction of both, oscillation frequencies and damping rates of the reference setup I.

The mean flow Mach number  $M_1$  in part 1 of the setups I and IV as well as for the calculation of the transfer matrices is varied between 0.05 and 0.3. The mean flow in part 2 is adjusted according to the area ratio. The pressure loss at the area change of the network model  $\Delta p_L$  takes values of 0 and 2% of the incompressible stagnation pressure in part 1:

$$\Delta p_L = \beta \left( p_1 + \frac{\bar{\rho}}{2} \bar{u}_1^2 \right), \quad \beta \in \{0, 0.02\}. \quad (4.47)$$

While the wall boundaries as well as the zero mass flux inlet and outlet boundary conditions are energetically neutral for all considered setups, this is not the case for the transfer matrix **TM**. It may incorporate acoustic dissipation due to the pressure loss and is thus the only physical mechanism contributing to the energy balance of the reference setup I. The eigenfrequencies resulting from the four different setups as described above are discussed in the following section, using the legend as provided in Tab. 4.2.

### 4.6.3 Results

Within the spectrum between 0 and 1000Hz, six eigenfrequencies are identified for all configurations and parameters. For the selected cross sectional areas and thermodynamic properties, this range is below the cut-on frequency and only longitudinal waves propagate. Selected spatial fluctuation distributions, also referred to as mode shapes, are presented for setup I in Fig. 4.8 in terms of velocity fluctuation magnitudes. Figure 4.9 displays the frequency  $f$

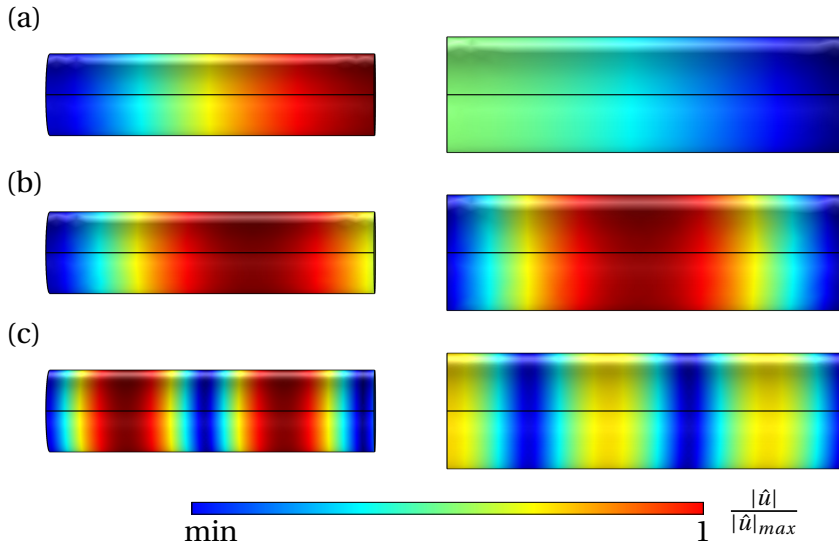


**Figure 4.8:** Mode shapes in terms of velocity fluctuations of the first (a), second (b) and sixth (c) eigenmode of setup I for  $M = 0.1$ ,  $\beta = 0.02$ .

and the damping rate  $\delta = -\alpha$  (i.e. the negative growth rate) of the first eigenmode over the Mach number in part 1 ( $M_1$ ) for zero pressure loss. As can be seen in the left graph, the frequency of the reference setup I is decreasing proportionally to  $M^2$  as expected. The frequencies of setups II and III remain almost constant at the zero Mach number frequency. The oscillation frequency seems not to be affected by the transfer matrix transformation, as the frequencies of setup II and III closely match. While the zero Mach number assumption of setups II and III can not reproduce the frequency drop of the reference setup, the CHE of setup IV excellently agrees with the reference. As expected, the damping rate is zero in the reference setup I for  $\beta = 0$  for all Mach numbers. This result is reproduced with the consistent transformation of the transfer matrix in setups III and IV. Using the original transfer matrix with the zero Mach number assumption (setup II), however, introduces linearly in-

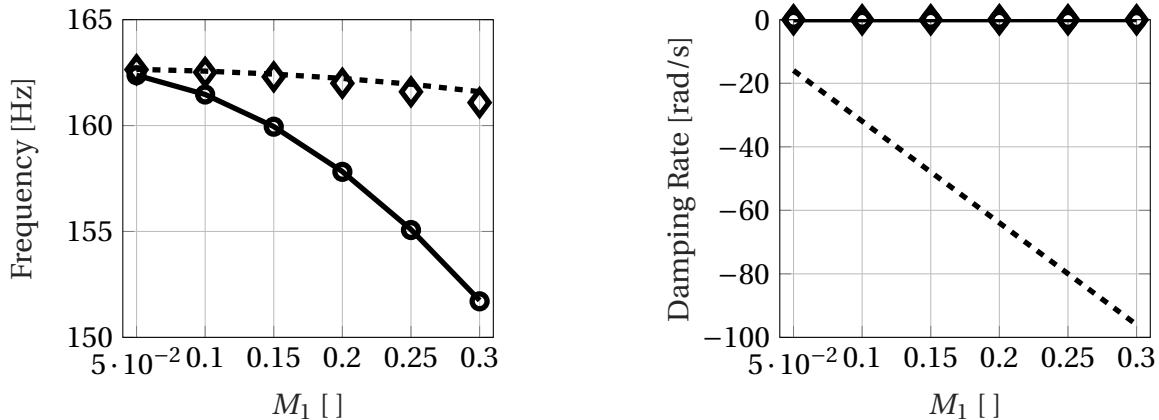


**Figure 4.9:** Frequency and damping rate of the first eigenfrequency over the Mach number for  $\beta = 0$  (cf. Tab. 4.2 for the legend).

creasing excitation to the system. This excitation reaches values up to  $100 \frac{\text{rad}}{\text{s}}$  at  $M_1 = 0.3$ . Only for  $M = 0$ , all four setups yield identical values of frequency and damping rate. Introducing a pressure loss of 2% at the area change as addressed in Fig. 4.10 still results in a slight frequency drop of the reference setup I over the Mach number. Again, only the consistent CHE setup IV correctly captures this frequency drop of setup I. Due to the pressure loss, high damping rates are obtained for all four setups. They start at approximately  $300 \frac{\text{rad}}{\text{s}}$  for  $M_1 = 0.05$  and are then monotonically decreasing. The deviation between the reference setup I and the energetically inconsistent setup II again increases with increasing Mach number. While the reference setup gives a damping rate of  $50 \frac{\text{rad}}{\text{s}}$  for  $M_1 = 0.3$  the inconsistent substitute setup predicts excitation of the same absolute value. The consistent configurations III and IV are again capable of accurately reproducing the reference setup's damping rates.

The second eigenfrequency for a vanishing pressure drop is shown in Fig. 4.11. The frequency qualitatively resembles the results of the first eigenfrequency, but the damping rate is equally increasing for the reference setup and for the consistent setups III and IV. Although this result is physically questionable, it may be explained by the low Mach number assumption within the transfer matrix derivation of the sudden area change, eq. (4.46). The energetically inconsistent setup II falsely predicts excitation for the considered Mach number range. The damping rate of the consistent Helmholtz setup III deviates slightly from the reference setup for the second eigenfrequency when introducing 2% pressure drop, cf. Fig. 4.12. The absolute deviation is still very small

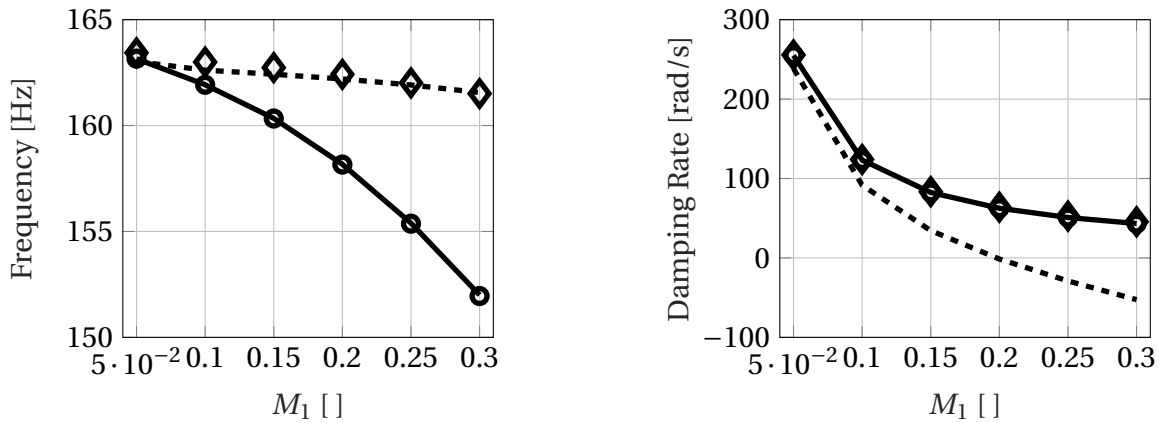


**Figure 4.10:** Frequency and damping rate of the first eigenfrequency over the Mach number for  $\beta = 0.02$ .

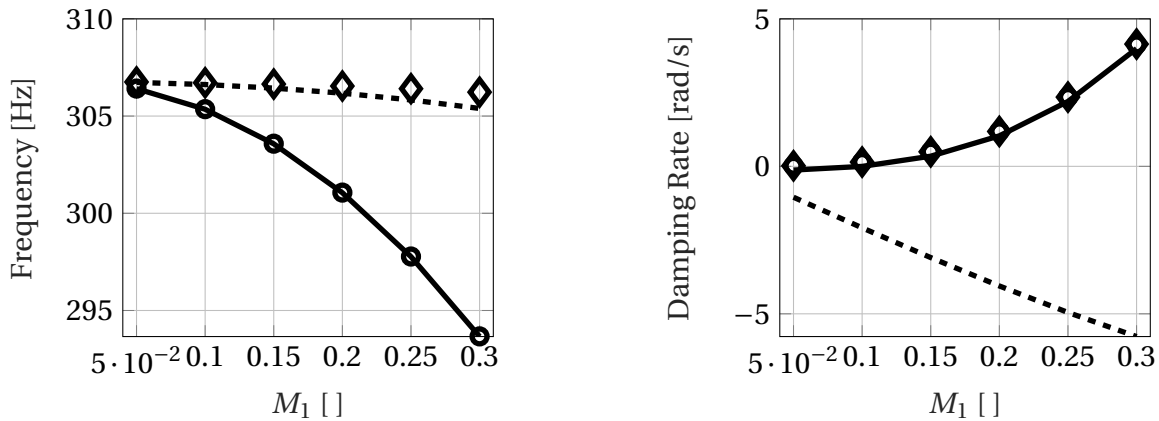


**Figure 4.11:** Frequency and damping rate of the second eigenfrequency over the Mach number for  $\beta = 0$ .

and comparable to the first eigenfrequency with 2% pressure drop (cf. Fig. 4.10). However, the relative deviation is increased due to the overall lower level of damping. Examining the mode shapes corresponding to the first and second eigenfrequencies of the reference setup in Fig. 4.8 reveals a velocity fluctuation antinode for the first and a velocity fluctuation node for the second eigenfrequency at the position of the area change. According to the transfer matrix representation of the area change in eq. (4.46), losses are introduced proportional to the absolute value of velocity fluctuations. At the same time, the gradients of fluctuation variables are largest at node locations. Small deviations in the mode shape and eigenfrequency due to the zero Mach number assumption may thus have high relative impact on the damping rate of the

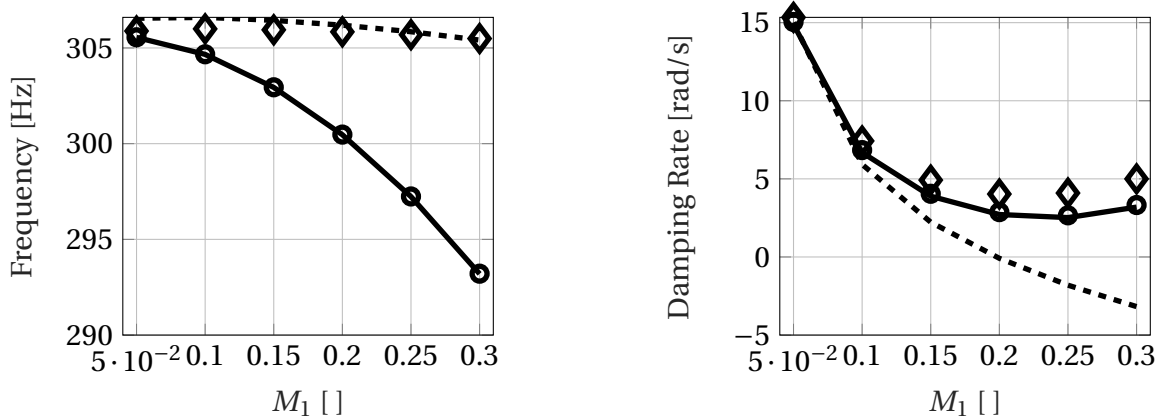


**Figure 4.12:** Frequency and damping rate of the second eigenfrequency over the Mach number for  $\beta = 0.02$ .

substitute system. This theory is confirmed by the CHE setup IV, which excellently reproduces the wave advection and thus the mode shape and eigenfrequency of the reference setup I. This manifests in an equal frequency drop of setups I and IV with matching damping rates. For the third eigenfrequency assessed in Fig. 4.13, an antinode of velocity fluctuations is situated close to the area change, again resulting in excellent agreement of damping rates between the reference setup I and the consistent setups III and IV.

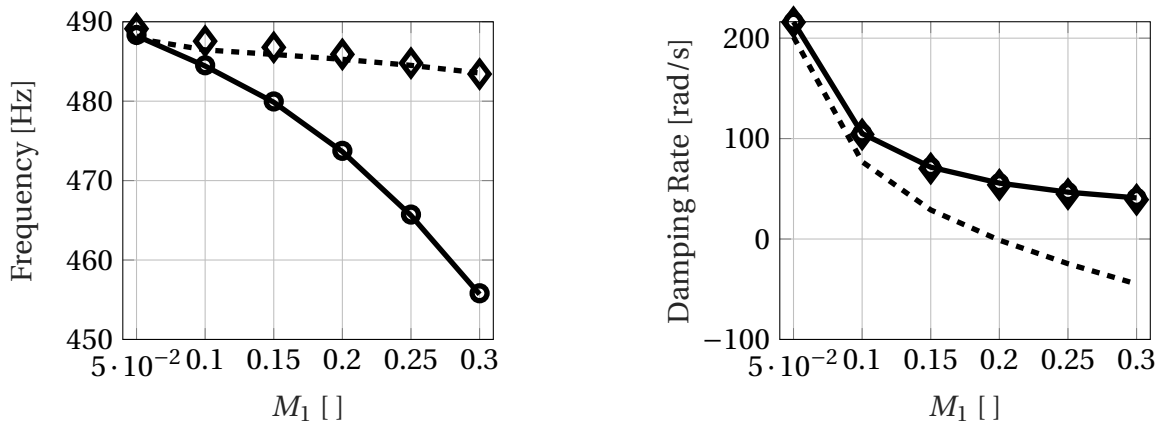


**Figure 4.13:** Frequency and damping rate of the third eigenfrequency over the Mach number for  $\beta = 0.02$ .

Finally, the validity of the transformation procedure is investigated for higher frequencies. Figure 4.14 exhibits the sixth eigenmode for  $\beta = 2\%$ . At higher Mach numbers the deviation in terms of damping rates between the consis-

tently transformed Helmholtz and the reference system again increases. However, the damping rates remain qualitatively correct in contrast to the inconsistent setup II. Again, setup IV excellently resembles the results of the APE.

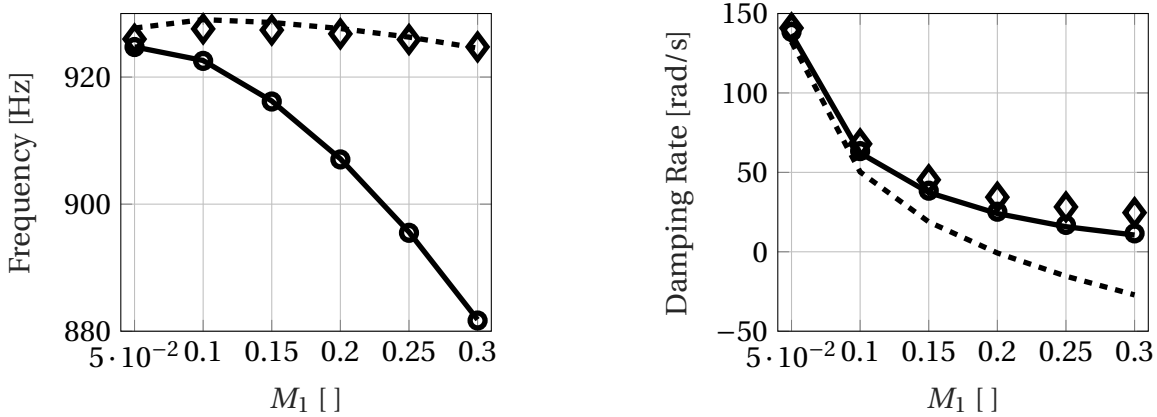


**Figure 4.14:** Frequency and damping rate of the sixth eigenfrequency over the Mach number for  $\beta = 0.02$ .

In conclusion, this simple test case demonstrates the significance of energetic consistency when performing stability analyses with the Helmholtz equation. This also proves the validity of the transformation procedure to obtain energetical consistency presented in section 4.4. In accordance with eq. (4.14), the same boundary conditions are also used for the consistent CHE. Since this setup involves a further increased accuracy of the stability predictions, the results above validate the corresponding mathematical framework of section 4.3. It may be observed that this increased accuracy only becomes relevant at larger Mach numbers. Since the overall Mach numbers in technically relevant combustors as investigated in chapter 6 are usually in the order of 0.1, the benefits of the CHE in terms of accuracy are thus expected to be marginal compared to the HE. Still, the slightly increased accuracy of the CHE comes at no additional computational cost. Therefore, the consistent convective Helmholtz equation presented in section 4.3.2 is a very cost-efficient and accurate approach to compute the acoustic stability in the presence of mean flow. Furthermore, its application with the well-established FEM framework is highly robust without the need of artificial damping. It does thus represent a promising alternative to more expensive and numerically less robust approaches like the APE or LEE.

## 5 Modal Model Order Reduction Methods

The linear hybrid numerical strategy presented in the previous chapter is perfectly suitable for a comprehensive modal stability analysis. Being based on linear acoustic equations, the methodology is by nature limited to the reproduction of linear processes. Growth rates obtained in that way are a measure of the exponential rise in pressure amplitudes at the onset of an instability. At elevated amplitudes, however, nonlinearities become relevant leading to limit cycle oscillations in real thermoacoustic systems.

For nonlinear thermoacoustic analyses, the chemical reaction and thus the flame is normally assumed to nonlinearly saturate [144, 190]. In these considerations, pure acoustic nonlinearities are normally disregarded. In the presence of mean flow, one may identify two different types of nonlinear acoustic mechanisms. Using the magnitude of velocity fluctuations as an indicator, they may be distinguished according to

1.  $\mathcal{O}(|\mathbf{u}'|) \approx \mathcal{O}(\bar{c})$  and
2.  $|\mathbf{u}'| \geq |\bar{\mathbf{u}}|$ .

At considerably high acoustic velocity amplitudes in the order of the mean speed of sound, the general linearity assumption fails. This is expressed by the first type of nonlinearities. As a consequence, the wave propagation speed becomes a function of the spatial pressure field ultimately leading to a steepening of the originally harmonic wave (cf. e.g. [118, 191]). Even in the limit cycle, such high amplitude levels are normally not reached in thermoacoustic systems. Consequently, this effect is of minor relevance and will not be considered in the present thesis. The second mechanism can already be observed at much lower amplitude levels. If the acoustic velocity exceeds the local mean flow velocity, periodic flow reversal occurs. This is of particular significance for sound propagation along jet flows as it may appear across apertures and thus also in perforated liners [112, 192, 193]. In the framework of linearized acoustic equations, the relevance of the nonlinearity may be mathematically substantiated by the fact that terms of the order  $\mathcal{O}(\bar{\mathbf{u}} \phi')$  are included, whereas

terms of the order  $\mathcal{O}(\mathbf{u}' \phi')$  are dropped. However, this is only valid for  $\mathbf{u}' < \bar{\mathbf{u}}$ . Particularly in the vicinity of perforated liners with small purge air mass flows, this condition may be violated. This is further substantiated by the  $g$ -function (3.28) in Bellucci's nonlinear pressure drop, eq. (3.27): the transition from linear to nonlinear behavior occurs as soon as the acoustic velocity amplitude exceeds the mean flow velocity. It is easy to see that only the first nonlinear mechanism can emerge in quiescent fluids.

By nature, none of the nonlinear mechanisms discussed above can be reproduced by linear methodologies in the FD. Instead, nonlinear equations need to be solved in the TD. To circumvent the high computational cost of conventional nonlinear TD solvers for the full thermoacoustic system, Reduced Order Models (ROMs) are an attractive alternative. Making use of the results of a linear modal stability analysis, modal model order reduction is a highly efficient methodology to include nonlinear mechanisms in the TD. Using a *Direct Modal Reduction* (DMR) procedure as described in section 5.1, Hummel et al. [100–102] include an empirical, nonlinear volumetric flame saturation source to reproduce thermoacoustic limit-cycles. However, the corresponding saturation function is hard to physically justify. Therefore, the present thesis targets the consideration of nonlinear acoustic damping mechanisms instead. More specifically, a reduced order model to include the well-investigated nonlinear damping capabilities of perforated liner patches is pursued. Since the DMR does not provide an intuitive way of including the effect of nonlinear boundary patches, an alternative reduction method limited to the Helmholtz equation and referred to as *Modal Amplitude Equations* (MAE) is reviewed in section 5.2. Both established approaches, the DMR and the MAE are compared with each other in section 5.3 to identify synergies. This ultimately allows to develop a combined, universal reduced order approach, particularly suitable for the convective Helmholtz equation. The approach can be coupled with nonlinear volumetric flame driving models as well as with nonlinear damper models at the boundaries as demonstrated in section 5.4.

## 5.1 Direct Modal Reduction

In principle, the DMR (also known as modal truncation) is based on a similarity transformation of the state-space system matrices. More precisely, the

canonical normal form with a diagonal system matrix is desired. An in-depth explication of the methodology is provided in [194, 195].

The basis of the DMR is formed by linear state-space system, eqs. (4.39). In the TD it reads

$$\mathbf{E}\dot{\mathbf{x}} = \check{\mathbf{A}}\mathbf{x} + \check{\mathbf{B}}\mathbf{u} \quad (5.1a)$$

$$\mathbf{y} = \mathbf{C}\mathbf{x} + \mathbf{D}\mathbf{u} , \quad (5.1b)$$

which may be created for any thermoacoustic system according to the linearization procedure of section 4.5. In contrast to eq. (4.39a), a descriptor (or mass) matrix  $\mathbf{E}$  is included to form a more general implicit state-space system. As can be seen from the state-space representation of the convective Helmholtz equation (4.40), the descriptor matrix is generally not a unity matrix. If it is not singular, multiplying the state-equation (5.1a) by the inverse of the mass matrix again leads to an explicit state equation:

$$\dot{\mathbf{x}} = \mathbf{A}\mathbf{x} + \mathbf{B}\mathbf{u} , \quad (5.2)$$

with  $\mathbf{A} = \mathbf{E}^{-1}\check{\mathbf{A}}$  and  $\mathbf{B} = \mathbf{E}^{-1}\check{\mathbf{B}}$ . The basis of the system can be changed by transforming the state vector by any square transformation matrix  $\mathbf{V}$  according to  $\mathbf{x}(t) = \mathbf{V}\boldsymbol{\xi}(t)$ . Introducing this relation into the state equation (5.2) and multiplying it with  $\mathbf{V}^{-1}$  yields

$$\dot{\boldsymbol{\xi}} = \mathbf{V}^{-1}\mathbf{A}\mathbf{V}\boldsymbol{\xi} + \mathbf{V}^{-1}\mathbf{B}\mathbf{u} . \quad (5.3)$$

The canonical normal form is obtained, if the transformation matrix  $\mathbf{V}$  is a  $(N \times N)$  matrix with the columns being the right eigenvectors of the system matrix  $\mathbf{A}$ , also referred to as right eigenvector matrix. As a result, the state space system becomes

$$\dot{\boldsymbol{\xi}} = \boldsymbol{\Lambda}\boldsymbol{\xi} + \mathbf{V}^{-1}\mathbf{B}\mathbf{u} \quad (5.4a)$$

$$\mathbf{y} = \mathbf{C}\mathbf{V}\boldsymbol{\xi} , \quad (5.4b)$$

with the diagonal eigenvalue matrix  $\boldsymbol{\Lambda} = \text{diag}(s_n)$ . This result may simply be illustrated by the definition of a right eigenvalue problem:

$$\mathbf{A}\mathbf{v}_n = s_n\mathbf{v}_n . \quad (5.5)$$

This equation is satisfied for each eigenvalue  $s_n$  and its related eigenvector  $\mathbf{v}_n$ . Hence, a system of equations may be established for all eigenvalues in matrix notation leading to

$$\mathbf{A}\mathbf{V} = \mathbf{V}\boldsymbol{\Lambda} , \quad (5.6)$$

with the right eigenvector matrix  $\mathbf{V} = (\mathbf{v}_1 \ \mathbf{v}_2 \ \dots \ \mathbf{v}_N)$ . Multiplying this equation by the inverse of the right eigenvector matrix finally yields the identity  $\mathbf{V}^{-1}\mathbf{A}\mathbf{V} = \mathbf{\Lambda}$  exploited to obtain eq. (5.4a). Since its rows are the left eigenvectors of the system, the inverse matrix  $\mathbf{V}^{-1}$  is referred to as left eigenvector matrix.

From a system theory point of view, the state-space system in eq. (5.4) gives the same outputs  $\mathbf{y}$  for given input signals  $\mathbf{u}$  as the original state-space system (5.1). This makes both systems equivalent. However, the state vector  $\boldsymbol{\xi}$  does not represent a thermodynamic quantity anymore. A descriptive interpretation of the transformed state quantity is delivered in section 5.3.

The state-space system (5.4) still has full order  $N$  and does thus not involve an accelerated solution process. Considerable reduction of the system order may be achieved by projecting the system on a subspace spanned by a significantly reduced number of eigenvectors  $N_{red} \ll N$ . The reduced right and left eigenvector matrices as well as the eigenvalue matrix then become

$$\mathbf{V}(N \times N) \rightarrow \mathbf{V}_{red}(N \times N_{red}) \quad (5.7a)$$

$$\mathbf{V}^{-1}(N \times N) = \mathbf{W}(N \times N) \rightarrow \mathbf{W}_{red}(N_{red} \times N) \quad (5.7b)$$

$$\mathbf{\Lambda}(N \times N) \rightarrow \mathbf{\Lambda}_{red}(N_{red} \times N_{red}), \quad (5.7c)$$

with the dimensions of the corresponding matrices appended in parentheses. In order to avoid confusion with an inverted non-square reduced right eigenvector matrix, the left eigenvector matrix is now referred to as  $\mathbf{W} = \mathbf{V}^{-1}$ . Due to this reduction procedure, also the transformed state vector is reduced  $\boldsymbol{\xi} \rightarrow \boldsymbol{\xi}_{red}$ . For an accurate projection, the reduced system needs to capture the fundamental dynamics of the system. However, there is no universal guideline on an a priori determination of the most relevant oscillation states [194]. If the relevant spectrum with distinct instabilities is known from measurements, it is best practice to project the system on the eigenmodes in this spectrum.

For large-scale systems, the inversion of the mass matrix  $\mathbf{E}$  to obtain the explicit input matrix  $\mathbf{B}$  may be problematic. Based on restrictive assumptions, Hummel [102] proposes to replace the projected input matrix by the relation

$$\mathbf{W}\mathbf{E}^{-1}\check{\mathbf{B}} = (\mathbf{W}\mathbf{E}\mathbf{V})^{-1}\mathbf{W}\check{\mathbf{B}}, \quad (5.8)$$

and therefore massively simplify the inversion procedure for the reduced system. A universal confirmation of this relation is provided in Appendix E. The input matrix  $\mathbf{B}$  can be used to include sources or sinks of the PDE subject to the

state-space model (e.g. heat release fluctuations of the Helmholtz equation) in the DMR.<sup>1</sup> This allowed Hummel et al. [100–102] to include stochastic, linear and nonlinear volumetric flame driving models in DMR computations as summarized in section 5.4.1. However, it is not straightforward to express the nonlinearity of damper patches using the input matrix in terms of a boundary source. For this reason, an alternative modal reduction methodology naturally containing boundary terms is presented in the subsequent section.

## 5.2 Modal Amplitude Equations

Being based on a modal series expansion, the Green's function approach as described in section 2.7 is predestined for a modal reduction procedure. Furthermore, under certain conditions this methodology allows for the coupling of thermoacoustic systems with nonlinear boundaries. A similar approach was presented by Noiray and Schuermans [196] for the Helmholtz equation. In this section, their procedure is adapted for the Sturm-Liouville PDE and generalized for a non-orthogonal base and more general boundary conditions. Adopting the naming of Lieuwen [105], this procedure will finally result in the MAE.

To start with, the Sturm-Liouville BVP (2.25) is reformulated for a specific set of boundary conditions. Therefore, the overall boundary is divided into sub-boundaries of three types,  $\partial V = \partial V_1 \cup \partial V_2 \cup \partial V_3$ , whereas now only homogeneous boundary conditions are permitted:

$$s^2 \hat{p} - \nabla (\bar{c}^2 \nabla \hat{p}) = s(\kappa - 1) \hat{q} \quad \text{in } V, \quad (5.9a)$$

$$\hat{p} = 0 \quad \text{on } \partial V_1, \quad (5.9b)$$

$$\nabla \hat{p} \cdot \mathbf{n} = 0 \quad \text{on } \partial V_2, \quad (5.9c)$$

$$s \hat{p} + \bar{c} z(s) \nabla \hat{p} \cdot \mathbf{n} = 0 \quad \text{on } \partial V_3. \quad (5.9d)$$

Making use of the relation  $s \bar{\rho} \hat{\mathbf{u}} = -\nabla \hat{p}$  for quiescent fluids, the homogeneous Robin boundary condition, eq. (5.9d), has been expressed in terms of the specific impedance (2.31). This formulation is particularly useful at boundary

<sup>1</sup>Purely linear sources and sinks can alternatively be directly included in the modal analysis, cf. eq. (4.40). This yields modified eigenvalues and corresponding linear growth rates. The temporal evolution of the oscillation amplitudes is then expected to be equivalent to including the source terms in TD via the input matrix.

patches connected to acoustic liners or resonators. Hereinafter, Green's function is assumed to satisfy the same boundary conditions. This is opposed to the procedure of Noiray and Schuermans [196] who only consider homogeneous Neumann boundary conditions. Still, the treatment of the second integral on the RHS of eq. (2.49) remains similar: integration by parts regarding the source location  $\mathbf{x}_0$  yields

$$\begin{aligned} \hat{p}(\mathbf{x}) = & \iiint_V \hat{G}(\mathbf{x}|\mathbf{x}_0) s(\kappa - 1) \hat{q}(\mathbf{x}_0) dV_0 \\ & + \iint_{\partial V} \left\{ \hat{G}(\mathbf{x}|\mathbf{x}_{0,s}) \bar{c}^2 \nabla_0 \hat{p}(\mathbf{x}_{0,s}) - \hat{p}(\mathbf{x}_{0,s}) \bar{c}^2 \nabla_0 \hat{G}(\mathbf{x}|\mathbf{x}_{0,s}) \right\} \cdot \mathbf{n} dA_0. \end{aligned} \quad (5.10)$$

In addition to the first volume integral, an additional volume integral would normally emerge from the partial integration. Since this additional volume integral vanishes, only a surface integral remains, which is denoted by the coordinates  $\mathbf{x}_{0,s}$ . Making use of the homogeneous Dirichlet and Neumann boundary conditions, only contributions from the subdomains of the third boundary type contribute to the solution of the pressure as per

$$\begin{aligned} \hat{p}(\mathbf{x}) = & \iiint_V \hat{G}(\mathbf{x}|\mathbf{x}_0) s(\kappa - 1) \hat{q}(\mathbf{x}_0) dV_0 \\ & - \iint_{\partial V_3} \bar{c} \hat{G}(\mathbf{x}|\mathbf{x}_{0,s}) \frac{s \hat{p}(\mathbf{x}_{0,s})}{z(s)} dA_0 - \iint_{\partial V_3} \bar{c}^2 \hat{p}(\mathbf{x}_{0,s}) \nabla_0 \hat{G}(\mathbf{x}|\mathbf{x}_{0,s}) \cdot \mathbf{n} dA_0. \end{aligned} \quad (5.11)$$

Since Green's function also satisfies the boundary condition (5.9d), the third integral on the RHS of eq. (5.11) does not vanish as it does for homogeneous Neumann boundary conditions used in [196]. With the frequency-dependency of the impedance violating the self-adjointness of the BVP, the (right) eigenfunctions of the system are not orthogonal anymore. In the formulation of Green's function (2.46) this is accounted for by using the bi-orthogonal basis formed by the left and the right eigenfunctions. Inserting the corresponding expression into eq. (5.11) first yields

$$\begin{aligned} \hat{p}(\mathbf{x}) = & \iiint_V \left( \sum_{n=0}^{\infty} \frac{\overline{\hat{\chi}_n(\mathbf{x}_0)} \hat{\psi}_n(\mathbf{x})}{E_n (s^2 - s_n^2)} \right) s(\kappa - 1) \hat{q}(\mathbf{x}_0) dV_0 \\ & - \iint_{\partial V_3} \bar{c} \left( \sum_{n=0}^{\infty} \frac{\overline{\hat{\chi}_n(\mathbf{x}_{0,s})} \hat{\psi}_n(\mathbf{x})}{E_n (s^2 - s_n^2)} \right) \frac{s \hat{p}(\mathbf{x}_{0,s})}{z(s)} dA_0 \\ & - \iint_{\partial V_3} \bar{c}^2 \hat{p}(\mathbf{x}_{0,s}) \nabla_0 \left( \sum_{n=0}^{\infty} \frac{\overline{\hat{\chi}_n(\mathbf{x}_{0,s})} \hat{\psi}_n(\mathbf{x})}{E_n (s^2 - s_n^2)} \right) \cdot \mathbf{n} dA_0. \end{aligned} \quad (5.12)$$

Similar to Green's function, also the pressure can be expanded in a series as per

$$\hat{p}(\mathbf{x}) = \sum_{n=0}^{\infty} \mu_n(s) \hat{\psi}_n(\mathbf{x}), \quad (5.13)$$

with the coefficients  $\mu_n$  representing the amplitudes of the corresponding right eigenfunctions, also referred to as *modal amplitudes*. They can be determined by a comparison of coefficients with eq. (5.12) leading to

$$\begin{aligned} (s^2 - s_n^2) \mu_n(s) = \frac{1}{E_n} \left[ \iiint_V \overline{\hat{\chi}_n(\mathbf{x}_0)} s(\kappa - 1) \hat{q}(\mathbf{x}_0) dV_0 \right. \\ \left. - \iint_{\partial V_3} \bar{c} \overline{\hat{\chi}_n(\mathbf{x}_{0,s})} \frac{s \hat{p}(\mathbf{x}_{0,s})}{z(s)} dA_0 - \iint_{\partial V_3} \bar{c}^2 \hat{p}(\mathbf{x}_{0,s}) \nabla_0 \overline{\hat{\chi}_n(\mathbf{x}_{0,s})} \cdot \mathbf{n} dA_0 \right]. \end{aligned} \quad (5.14)$$

These are the MAE in the FD. Inverse Laplace transformation leads to the corresponding equations in the TD:

$$\begin{aligned} \frac{d^2}{dt^2} \mu_n(t) = s_n^2 \mu_n(t) + \frac{1}{E_n} \left[ \iiint_V \overline{\hat{\chi}_n(\mathbf{x}_0)} (\kappa - 1) \frac{\partial \hat{q}'(\mathbf{x}_0)}{\partial t} dV_0 \right. \\ \left. + \iint_{\partial V_3} \bar{c}^2 \bar{\rho} \overline{\hat{\chi}_n(\mathbf{x}_{0,s})} \frac{\partial u'(\mathbf{x}_{0,s})}{\partial t} dA_0 - \iint_{\partial V_3} \bar{c}^2 p'(\mathbf{x}_{0,s}) \nabla_0 \overline{\hat{\chi}_n(\mathbf{x}_{0,s})} \cdot \mathbf{n} dA_0 \right]. \end{aligned} \quad (5.15)$$

Note that the specific impedance has been replaced by the surface normal velocity fluctuation  $u' = \mathbf{u}' \cdot \mathbf{n}$  for the TD formulation. It may be obtained from the coupling with suitable damper models as discussed in section 5.4.

The volumetric source due to a potentially nonlinear heat release rate fluctuation is accounted for in the first integral. Other nonlinear volumetric sources such as an acoustic-vortex interaction mechanism could be additionally included. Boundary sources as expected from nonlinear damper patches can be incorporated via the two surface integrals. It may be noted that for self-adjoint problems, i.e.  $\psi_n = \chi_n$ , the temporal fluctuation of one boundary integral corresponds to the modal quantity of the other integral. Therefore, those two boundary terms compensate each other in the linear regime. This is not necessarily the case for the general bi-orthogonal basis.

Particularly in the HF regime, source fields are generally not covered by the compactness assumption. Hummel et al. [100, 101] tackle this issue by dividing the volumetric source region into  $M$  compact subvolumes. Similarly, the overall boundary portion of the third type can be split into  $K$  compact subboundaries. In both cases, the integration can then be replaced by domain-

averaged quantities multiplied with the volume or the surface area of the sub-domain, respectively:

$$\begin{aligned} \frac{d^2}{dt^2} \mu_n(t) = & s_n^2 \mu_n(t) + \frac{1}{E_n} \left[ \sum_{m=1}^M \frac{d\dot{q}'_m}{dt} V_m \left( \overline{\hat{\chi}_n(\mathbf{x}_0)} (\kappa - 1) \right)_{V,m} \right. \\ & \left. + \sum_{k=1}^K \frac{du'_k}{dt} A_k \left( \bar{c}^2 \bar{\rho} \overline{\hat{\chi}_n(\mathbf{x}_{0,s})} \right)_{S,k} - \sum_{k=1}^K p'_k A_k \left( \bar{c}^2 \nabla \overline{\hat{\chi}_n(\mathbf{x}_{0,s})} \cdot \mathbf{n} \right)_{S,k} \right], \end{aligned} \quad (5.16)$$

where the indexed parentheses denote domain-averaged quantities. In analogy to the DMR, a model order reduction with the MAE is ultimately achieved by limiting the series expansion (5.13) to a finite number of eigenfunctions.

The proposed MAE (5.14) to (5.16) have some major advantages over other established modal expansion approaches for the investigation of thermoacoustic stability. Most commonly, the modal expansion of the Green's function approach is based on orthonormal eigenfunctions obtained from self-adjoint problems with purely rigid-wall boundaries. This yields a discrepancy between the basis spanned by those eigenfunctions and the actual acoustic field obtained from the equivalent system with frequency dependent impedance boundaries [54]. Laurent et al. [197] tackle this issue by establishing an over-complete frame consisting of two sets of eigenmodes: similar to the common MAE approach the first set exclusively relies on rigid-wall boundaries whereas the actually frequency-dependent boundaries are replaced by open-end boundary conditions for the second set. The actual acoustic field is then assumed to be some intermediate, linearly interpolated state. While this interpolation is also just an approximation of the actually expected acoustic field, a more severe drawback is the ill-conditioned reduced system matrix  $\mathbf{\Lambda}$  due to the over-complete frame. This requires complex and computationally extensive inversion procedures. Unlike those approaches, the MAE with its bi-orthogonal basis introduced in this section does not involve such numerical difficulties. Furthermore, the bi-orthogonal basis spanned by the eigenfunctions  $\chi_n$  and  $\psi_n$  accurately reproduces the actual acoustic field at low acoustic amplitudes. Therefore, a slight misrepresentation of the actual acoustic field by the bi-orthogonal basis is only expected once the boundary characteristics change due to nonlinear mechanisms at high amplitude levels. Despite the advantages of the MAE, it still comes at some drawbacks such as its limitation to the Sturm-Liouville problem. To overcome these drawbacks, a more

universal approach is developed by combining the MAE with the DMR in the following section.

### 5.3 Comparison of the Two Modal Reduction Approaches

Although one may perceive certain analogies between the DMR and the MAE, they differ considerably as summarized in Tab. 5.1. The purpose of the present

**Table 5.1:** Comparison of the Direct Modal Reduction (DMR), the Modal Amplitude Equations (MAE) and the combined Generalized Discrete MAE.

	DMR	MAE	Generalized Discrete MAE
Temporal Order:	1st Order	2nd Order	1st Order
Spatial Resolution:	Discrete	Continuous	Discrete
Input Domains:	Unspecific	Volume & Boundary	Volume & Boundary
Applicability:	General linearized PDEs	Helmholtz/ Sturm-Liouville	General linearized PDEs

section is to investigate these differences for the development of a novel approach combining the benefits of DMR and MAE. For a universal applicability to general linearized PDEs, particularly the convective Helmholtz equation (4.40), the pursued approach should be equivalent to the DMR. More specifically, it should be of first temporal order with a discrete spatial resolution for the use with discretized numerical state-space models. Additionally, explicit nonlinear volume and boundary source input terms equivalent to the MAE are desired. For this purpose, the MAE are transformed into the shape of the DMR. The resulting approach is labeled *Generalized Discrete MAE*.

In a first step, the MAE (5.16) is expressed in vectorial form for a reduced set of  $N$  eigenfunctions:

$$\frac{d^2}{dt^2} \boldsymbol{\mu}(t) = \text{diag}(s_n^2) \boldsymbol{\mu}(t) + \text{diag} \left( \frac{\overline{\chi}_n}{E_n} \right) \left\{ \mathbf{B}_V \frac{\partial \dot{\mathbf{q}}'}{\partial t} + \mathbf{B}_{S1} \frac{\partial \mathbf{u}'}{\partial t} - \mathbf{B}_{S2} \mathbf{p}' \right\}, \quad (5.17)$$

where the length of the column vectors  $\boldsymbol{\mu} = (\mu_1, \dots, \mu_N)^T$ ,  $\dot{\mathbf{q}}' = (\dot{q}'_1, \dots, \dot{q}'_M)^T$ ,  $\mathbf{p}' = (p'_1, \dots, p'_K)^T$  and  $\mathbf{u}' = (u'_1, \dots, u'_K)^T$  equals the number of eigenfunc-

tions, subvolumes or sub-boundaries, respectively. Particularly the latter vector must not be confused with the directional velocity vector. The left eigenfunction  $\chi_n$  has been extracted from the subvolume and subdomain averaging as well as from the nabla operator. Instead, these operations are included in the  $\mathbf{B}$  matrices. In accordance with eq. (5.16), the  $(N \times M)$ -matrix  $\mathbf{B}_V$  can be used to include volumetric sources (e.g. due to acoustic-flame interactions) whereas the  $(N \times K)$ -matrices  $\mathbf{B}_{S1}$  and  $\mathbf{B}_{S2}$  account for temporally varying boundary impedances. Recall that the two boundary input terms compensate for damper patches in the linear amplitude regime, provided that the problem at hand is self-adjoint. Then, an effective boundary source is only established in the nonlinear amplitude regime.

Equation (5.17) facilitates the reduction of the MAE's temporal order by a linearization in terms of a state-space formalism as proposed by Schuermans [49] and discussed in section 4.5. This linearization is again obtained by introducing the temporal derivative of the state variable  $\dot{\mu}_n = d\mu_n/dt$  as an additional state variable. This yields the linear state-space representation

$$\begin{aligned} \frac{d}{dt} \begin{pmatrix} \mathbf{0} & \mathbf{I} \\ \mathbf{I} & \mathbf{0} \end{pmatrix} \begin{pmatrix} \boldsymbol{\mu} \\ \dot{\boldsymbol{\mu}} \end{pmatrix} &= \begin{pmatrix} \text{diag}(s_n^2) & \mathbf{0} \\ \mathbf{0} & \mathbf{I} \end{pmatrix} \begin{pmatrix} \boldsymbol{\mu} \\ \dot{\boldsymbol{\mu}} \end{pmatrix} + \mathbf{B}_\mu \mathbf{u}_\mu \\ \mathbf{B}_\mu &= \begin{pmatrix} \mathbf{0} & \text{diag}(\overline{\chi_n}/E_n) \mathbf{B}_V & \text{diag}(\overline{\chi_n}/E_n) \mathbf{B}_{S1} & -\text{diag}(\overline{\chi_n}/E_n) \mathbf{B}_{S2} \\ \mathbf{0} & \mathbf{0} & \mathbf{0} & \mathbf{0} \end{pmatrix} \quad (5.18) \\ \mathbf{u}_\mu &= \begin{pmatrix} \mathbf{0} & \frac{\partial \dot{\mathbf{q}}'}{\partial t} & \frac{\partial \mathbf{u}'}{\partial t} & \mathbf{p}' \end{pmatrix}^T. \end{aligned}$$

For the sake of a better comparability with the state-space formulation of the convective Helmholtz equation (4.40), the linearized MAE is used to express the local pressure fluctuations. This is massively simplified by firstly discretizing the bi-orthogonal base functions such that the left and right eigenfunctions become eigenvectors

$$\psi_n(\mathbf{x}) \rightarrow \boldsymbol{\psi}_n; \quad \chi_n(\mathbf{x}) \rightarrow \boldsymbol{\chi}_n$$

satisfying the inner product property similar to eq. (2.37):

$$\langle \boldsymbol{\psi}_n, \boldsymbol{\chi}_n \rangle = \boldsymbol{\psi}_n \cdot \boldsymbol{\chi}_n = \overline{\boldsymbol{\psi}_n \boldsymbol{\chi}_n} = E_n. \quad (5.19)$$

Then, the space-discrete pressure vector  $\mathbf{p}'$  can be written as

$$\mathbf{p}' = \sum_{n=1}^N \mu_n(t) \boldsymbol{\psi}_n \rightarrow \mathbf{p}' = \boldsymbol{\Psi} \boldsymbol{\mu} \quad (5.20)$$

and, making use of eq. (5.19), its inverse relation

$$\boldsymbol{\mu} = \text{diag}\left(\frac{1}{E_n}\right) \bar{\mathbf{X}} \mathbf{p}' . \quad (5.21)$$

The eigenvector matrices  $\boldsymbol{\Psi}$  and  $\mathbf{X}$  are spanned by the corresponding eigenvectors. Inserting eq. (5.21) into the linearized MAE (5.18) and multiplying with  $\boldsymbol{\Psi}$  yields the desired state-space representation of the discretized pressure fluctuations as per<sup>2</sup>

$$\begin{aligned} \frac{d}{dt} \begin{pmatrix} \mathbf{0} & \mathbf{I} \\ \mathbf{I} & \mathbf{0} \end{pmatrix} \begin{pmatrix} \mathbf{p}' \\ \dot{\mathbf{p}}' \end{pmatrix} &= \begin{pmatrix} \boldsymbol{\Psi} \text{diag}(s_n^2/E_n) \bar{\mathbf{X}} & \mathbf{0} \\ \mathbf{0} & \mathbf{I} \end{pmatrix} \begin{pmatrix} \mathbf{p}' \\ \dot{\mathbf{p}}' \end{pmatrix} + \mathbf{B}_p \mathbf{u}_p \\ \mathbf{B}_p &= \begin{pmatrix} \mathbf{0} & \mathbf{B}_V & \mathbf{B}_{S1} & -\mathbf{B}_{S2} \\ \mathbf{0} & \mathbf{0} & \mathbf{0} & \mathbf{0} \end{pmatrix} \\ \mathbf{u}_p &= \begin{pmatrix} \mathbf{0} & \frac{\partial \dot{\mathbf{q}}'}{\partial t} & \frac{\partial \mathbf{u}'}{\partial t} & \mathbf{p}' \end{pmatrix}^T . \end{aligned} \quad (5.22)$$

The Laplace transform of eq. (5.22) is the discretized counterpart of the convective Helmholtz equation in state-space formulation (4.40) with additional boundary source terms. One can observe that the state variable  $\mathbf{p}'$  is also part of the input vector. It may thus be included into the state matrix. However, this input is a result of the eigenvector matrices containing the linear contribution of potentially nonlinear boundary impedances and must remain part of the sources. Then, dropping all sources yields the desired eigenvalue problem with linearized impedances as discussed in section 4.5. With the results of a modal analysis, eq. (5.22) can be retransformed into a reduced order model by means of the DMR methodology discussed in section 5.1. The reduced state equation then yields the Generalized Discrete MAE:

$$\dot{\boldsymbol{\xi}}_{red} = \boldsymbol{\Lambda}_{red} \boldsymbol{\xi}_{red} + (\mathbf{W}_{red} \mathbf{E} \mathbf{V}_{red})^{-1} \mathbf{W}_{red} \mathbf{B}_p \mathbf{u}_p . \quad (5.23)$$

Apparently, the state variables of the approaches DMR ( $\boldsymbol{\xi}$ ) and MAE ( $\boldsymbol{\mu}$ ) equivalently represent modal amplitudes, i.e. the amplitudes of the eigenmodes spanning the basis of the ROM. This is by virtue of the transformation  $\mathbf{x}(t) = \mathbf{V} \boldsymbol{\xi}(t)$  being equivalent to the series expansion of the reduced, discretized MAE (5.20).

<sup>2</sup>An easier approach in terms of algebra is to first form the second order PDE for the discretized pressure and then transform it into a linear state-space system.

The overall input matrix  $\mathbf{B}_p$  and vector  $\mathbf{u}_p$  of eq. (5.23) equal those specified in eq. (5.22). As mentioned above, the single input matrices forming the overall input matrix are assumed to contain the averaging and nabla operations regarding the original continuous eigenfunctions. For the discretized and reduced system (5.23), these operations now need to be applied to the left eigenvector matrix  $\mathbf{W}_{red}$ . In practice, this allows to circumvent an elaborate construction of the  $\mathbf{B}_p$  matrix. Instead, the elements of the combined matrix  $\mathbf{W}_{red}\mathbf{B}_p$  may be directly obtained from the eigenvalue solver. These elements include the area or volume-integrated values of the left eigenvectors or its gradient together with mean field quantities. The resulting matrices are provided in Appendix F.

While the MAE are based on Green's function for self-adjoint BVPs, eqs. (5.22) and (5.23) imply a more general applicability of the Generalized Discrete MAE. This is due to the fact that Green's ansatz in terms of the eigenfunctions (or eigenvectors) is only found explicitly in the system matrix of eq. (5.22). Furthermore, the input matrix  $\mathbf{B}_p$  and vector  $\mathbf{u}_p$  are a result of Green's function for a Sturm-Liouville problem with boundary conditions suitable to quiescent fluids. Both aspects can be transferred to the convective Helmholtz equation: While the system matrix in eq. (5.22) may simply be replaced by the discretized system matrix of the convective Helmholtz equation (4.40), the consistent convective Helmholtz equation (4.14) already requires boundary conditions for stagnant fluids. Consequently, the Generalized Discrete MAE (5.23) form an ideal basis for ROM simulations in the TD with the consistent convective Helmholtz equation in chapter 6.

## 5.4 ROM Coupling with Source Models

The model order reduction as extensively discussed in the previous sections only concerns the linear acoustic part of a combustor. Potential nonlinearities can be included by means of volumetric or boundary sources. Within the derivation above, specific emphasis was put on the inclusion of nonlinear acoustics-flame interactions as well as the nonlinear damping behavior of acoustic resonators. The coupling of the combustor acoustics in terms of the Generalized Discrete MAE with the partitioned flame volume and the individual damper patches is schematically depicted in Fig. 5.1. While the flame is as-

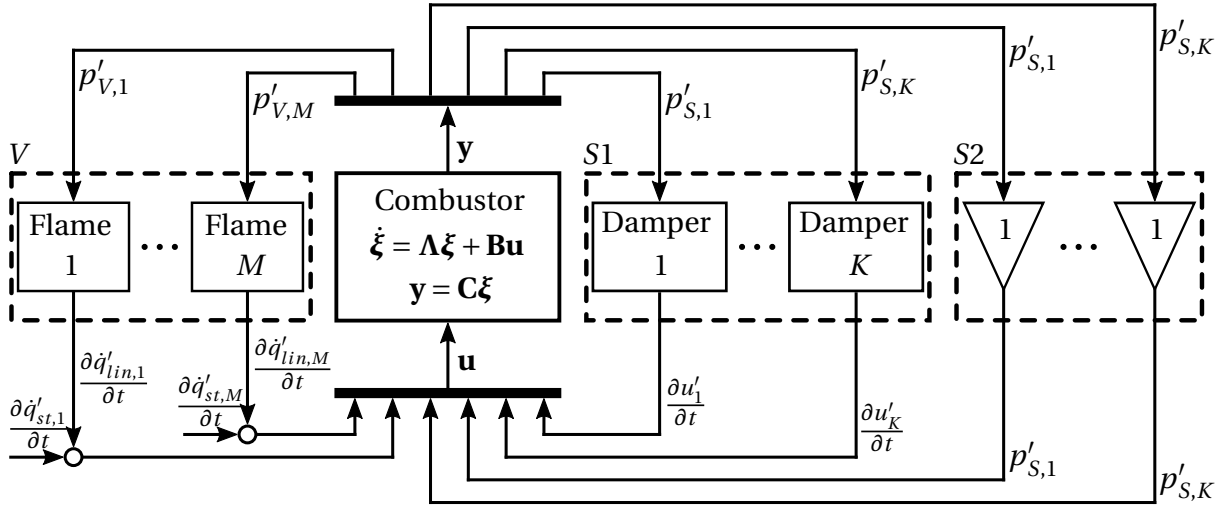


**Figure 5.1:** Schematic of the Generalized Discrete MAE coupled with the volumetric flame source model and the two boundary sources representing the damper models.

sumed to only feature stochastic (index  $st$  in Fig. 5.1) and linear (index  $lin$  in Fig. 5.1) components in the present thesis, a nonlinear amplitude saturation is exclusively ascribed to nonlinear dampers. Consequently, only a brief review of the implementation of flame sources in the TD is provided. A more elaborate discussion is reserved for the modeling of nonlinear damper patches and their coupling with the combustor acoustics.

#### 5.4.1 Flame Source

For the investigation of HF thermoacoustics using ROM simulations, Hummel et al. [100–102] provided a detailed framework to include heat release fluctuations as a driving and saturation mechanism. For HF analysis with non-compact flames, they propose to split the mean heat release field into compact subvolumes. Each of those subvolumes is considered an independent volumetric source. Due to the compactness of the individual flame partitions, subvolume-averaged quantities may be used to create the input and output matrices (cf. section 5.2).

As discussed in section 2.8.1, the overall heat release fluctuations may be split into stochastic, linear and nonlinear contributions, irrespective of the frequency regime. Considered an initiator of thermoacoustic instabilities, the stochastic part  $\dot{q}'_{st}$  is essential for ROM computations. Generally, the turbu-

lence induced combustion noise is colored [143], which may have significant impact on the overall dynamics of a thermoacoustic system [198, 199]. Still, this effect is considered negligible when limiting to a narrow spectrum of eigenfrequencies as done in the test configuration of chapter 6. In this case, white noise can be used to mimic the turbulence-driven stochastic heat release fluctuations. Regarding the linear acoustics-flame interactions  $\dot{q}'_{lin}$ , all types of models discussed in section 2.8.2 can generally be incorporated into the ROM, including global FRFs from measurements or CFD computations as well as from analytical models. Since the application of conventional global FRFs is limited to the LF regime, the linearized flame displacement and deformation models according to eq. (4.44) are employed for the HF analysis pursued in chapter 6. As mentioned in section 5.1, such linear flame driving models do not necessarily need to be coupled with the ROM in the TD. Alternatively, the linearity in terms of the pressure fluctuations allows to include the corresponding mechanisms directly in the modal analysis. This yields modified growth rates directly affecting the system matrix of the ROM, substituting the closed feedback loops on the left side of Fig. 5.1. In general, also nonlinear contributions to the heat release oscillations  $\dot{q}'_{nl}$  can be included into the ROM by means of a closed-loop coupling. Hummel et al. [101, 102] used a cubic pressure term to model a flame saturation mechanism leading to limit-cycle oscillations. This resembles a stochastic Van der Pol oscillator [141, 200] but lacks a physical justification for perfectly premixed flames as discussed in section 2.8.1. In the framework of this thesis, nonlinear saturation is thus exclusively investigated for nonlinear damper patches being subject of the subsequent section.

### 5.4.2 Nonlinear Resonator Patches

Perforated liners and multi-layer resonators can be acoustically characterized in terms of an impedance using the procedure presented in section 3.3. The highly sophisticated Bellucci model is suitable to accurately describe the transfer behavior of single perforated screens. It includes a nonlinear relation for the pressure drop in the TD, cf. eq. (3.26), which transforms to the  $g$ -function (3.28) in the FD. Other semi-empirical parameters depending on the oscillation frequencies were included, e.g. to account for hole-to-hole interactions [201]. For varying acoustic amplitude levels, the model is thus ca-

pable to predict different impedance curves. Similar to a FDE, the different impedance curves can then be used to investigate the system stability for virtually varying amplitude levels in a linear FD framework. The linearity in the FD still prevents for modal interactions though, which can only be realized in the TD. A self-evident approach would thus be to transform Bellucci's model back to the TD by means of an inverse Laplace transform. However, the various frequency-dependent parameters impedes such a procedure. Further difficulties arise for multi-layer perforated liners as the overall impedance becomes a complex function of the individual layer parameters.

To overcome this deficit, the analogy of the damped mechanical oscillator (cf. section 3.3.1) is exploited. Its impedance represents a rational transfer-function of second order. Now, instead of applying an inverse Laplace transform, the overall impedance of a (multi-layer) perforated liner can simply be approximated by a rational function fit. The corresponding procedure was explicated for a reflection coefficient in section 4.5.1. While the order of the fitted polynomials remained indefinite for general transfer functions, it is known a priori for the specific damper impedance as per

$$z_d(s) \approx \frac{b_2 s^2 + b_1 s + b_0}{a_1 s + a_0}. \quad (5.24)$$

By rewriting the rational function fit using a polynomial division according to

$$z_d(s) = \frac{\hat{p}}{\bar{\rho}\bar{c}\hat{u}} \approx \frac{b_2}{a_1} s + \frac{b_1 - \frac{b_2 a_0}{a_1}}{a_1} + \frac{b_0 - \frac{a_0}{a_1} \left( b_1 - \frac{b_2 a_0}{a_1} \right)}{a_1 s + a_0}, \quad (5.25)$$

the impedance can then be reshaped into a state equation for the velocity fluctuation:

$$s \hat{u} = - \left( \frac{b_1}{b_2} - \frac{a_0}{a_1} \right) \hat{u} - \frac{\frac{b_0}{b_2} - \frac{a_0}{a_1} \left( \frac{b_1}{b_2} - \frac{a_0}{a_1} \right)}{s + \frac{a_0}{a_1}} \hat{u} + \frac{a_1}{b_2} \frac{\hat{p}}{\bar{\rho}\bar{c}}, \quad (5.26)$$

still being a nonlinear function of the Laplace variable. Again introducing a substitute variable  $\hat{\phi} = \hat{u}/(s + \frac{a_0}{a_1})$  leads to the linear state-space system

$$s \begin{pmatrix} \hat{u} \\ \hat{\phi} \end{pmatrix} = \begin{pmatrix} \frac{a_0}{a_1} - \frac{b_1}{b_2} & \frac{a_0}{a_1} \left( \frac{b_1}{b_2} - \frac{a_0}{a_1} \right) - \frac{b_0}{b_2} \\ 1 & -\frac{a_0}{a_1} \end{pmatrix} \begin{pmatrix} \hat{u} \\ \hat{\phi} \end{pmatrix} + \begin{pmatrix} \frac{a_1}{b_2} \\ 0 \end{pmatrix} \frac{\hat{p}}{\bar{\rho}\bar{c}} \quad (5.27)$$

with the input quantity  $\hat{p}/(\bar{\rho}\bar{c})$ . This state-space system can now easily be transformed into the TD.

Since the rational function fit still poses a linear relation between pressure and velocity fluctuations it is generally not capable of reproducing amplitude-dependent, nonlinear damping characteristics. Still, the shape of eq. (5.25) and (5.26) now allow for a direct comparison of the individual fitting parameters with the acoustic analogy (3.20) by a comparison of coefficients. The first term on the RHS of eq. (5.26) is of zeroth order in the Laplace variable and can thus be attributed to the damping factor, also defining the mechanical resistance. For a single-layer resonator characterized with Bellucci's model, the resistance (3.33) and thus the damping factor is composed of two terms:

1. the nonlinear pressure loss due to acoustic-vortex interactions (index  $\nu$ ) exclusively contributing to the resistance and
2. the linear viscous losses (index  $\mu$ ) only contributing to the resistance in terms of the propagation constant's imaginary part.

If the acoustic velocity is lower than the bulk velocity, those two mechanisms may be summarized as (cf. section 3.3.4)

$$R_\nu = -\frac{\hat{\Phi}}{\sigma \hat{u}_0} = -\frac{\bar{\rho} \zeta_{lin} \bar{u}_0}{\sigma}, \quad (5.28)$$

$$R_\mu = \frac{\omega \bar{\rho}}{\sigma} t \mathcal{J}(\Gamma). \quad (5.29)$$

Both mechanisms are compared with each other in Fig. 5.2 for selected orifice radii, Mach numbers and liner thicknesses at ambient conditions. The parameters were selected in accordance with [179]. It may be seen that the acoustic-vortex interactions dominate the viscous losses for all considered parameters. Particularly for increasing orifice Mach numbers and increasing ratios between orifice radius to thickness, the viscous losses are negligible. Therefore, the entire resistance of the linearized damper may approximately be attributed to the linear part of the nonlinear acoustic-vortex interactions  $R_\nu$ . This corresponds to the linear part of the pressure drop in the FD, eq. (3.27). A comparison with the nonlinear form in the TD, eq. (3.26), reveals the equivalence of the terms  $2\bar{u}\hat{u}$  in the FD and  $(|\bar{u}_0 + u'_0|(\bar{u}_0 + u'_0) - |\bar{u}_0|\bar{u}_0)$  in the TD in the case of linear damping characteristics ( $|\hat{u}| < |\bar{u}|$ ). After transforming eq. (5.27) by means of an inverse Laplace transform, this can be exploited to convert the originally linear resistance into a nonlinear loss term yielding the

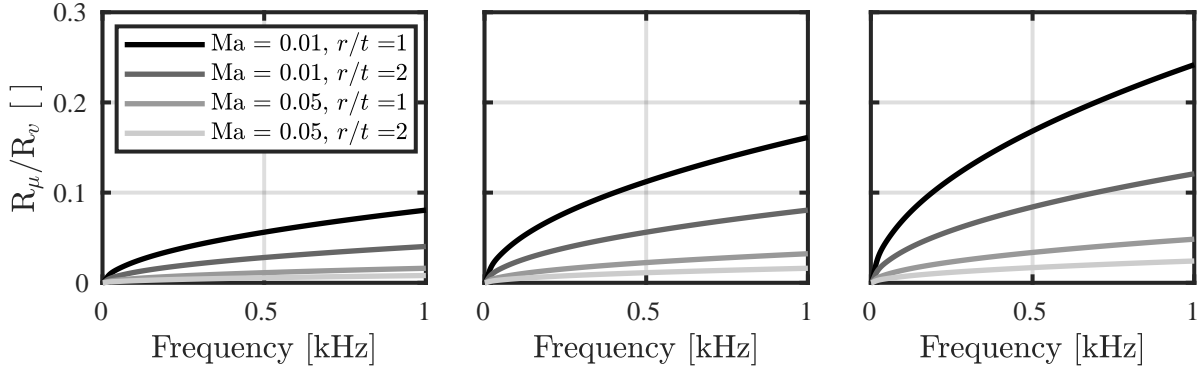


**Figure 5.2:** Ratio of the linear viscous ( $R_\mu$ ) and nonlinear vortical ( $R_\nu$ ) part of Bellucci's resistance at ambient conditions ( $p = 1$  bar,  $T = 300$  K). Left:  $r = 1$  mm, Center:  $r = 2$  mm, Right:  $r = 3$  mm.

following nonlinear state equation:

$$\begin{aligned} \frac{d}{dt} \begin{pmatrix} u' \\ \varphi' \end{pmatrix} = & \underbrace{\begin{pmatrix} 0 & \frac{a_0}{a_1} \left( \frac{b_1}{b_2} - \frac{a_0}{a_1} \right) - \frac{b_0}{b_2} \\ 1 & -\frac{a_0}{a_1} \end{pmatrix}}_{\mathbf{A}_d} \underbrace{\begin{pmatrix} u' \\ \varphi' \end{pmatrix}}_{\mathbf{x}_d} + \underbrace{\begin{pmatrix} \frac{a_1}{b_2} \\ 0 \end{pmatrix}}_{\mathbf{B}_d} \frac{p'}{\bar{\rho} \bar{c}} \\ & + \underbrace{\begin{pmatrix} \frac{a_0}{a_1} - \frac{b_1}{b_2} \\ \frac{2\bar{u}}{2\bar{u}} \\ 0 \end{pmatrix}}_{\mathbf{N}_d} [(\bar{u} + u') |\bar{u} + u'| - \bar{u} |\bar{u}|]. \end{aligned} \quad (5.30)$$

The resistance was extracted from the damper system matrix  $\mathbf{A}_d$  and now forms a nonlinearity matrix  $\mathbf{N}_d$ . It can be considered an input matrix for the nonlinear velocity fluctuations. The regular input matrix  $\mathbf{B}_d$  allows for a coupling with the Generalized Discrete MAE of the combustor. A block diagram of this nonlinear state-equation including the coupling with ROM in terms of the Generalized Discrete MAE is presented in Fig. 5.3. Selectors (black bars) were included to only extract the velocity or its temporal derivative from the state vector  $\mathbf{x}_d$ . At the same time, the selector connected to the combustor can also be interpreted as the output matrix of the damper, having only a unity flag at the (1,1) element to extract the velocity fluctuation's temporal derivative. Eventually, the nonlinear damper model in conjunction with the Generalized Discrete MAE and the consistent linear procedure presented in the previous chapter poses an elegant approach to investigate the effect of nonlinear damping mechanisms on limit-cycle oscillations.

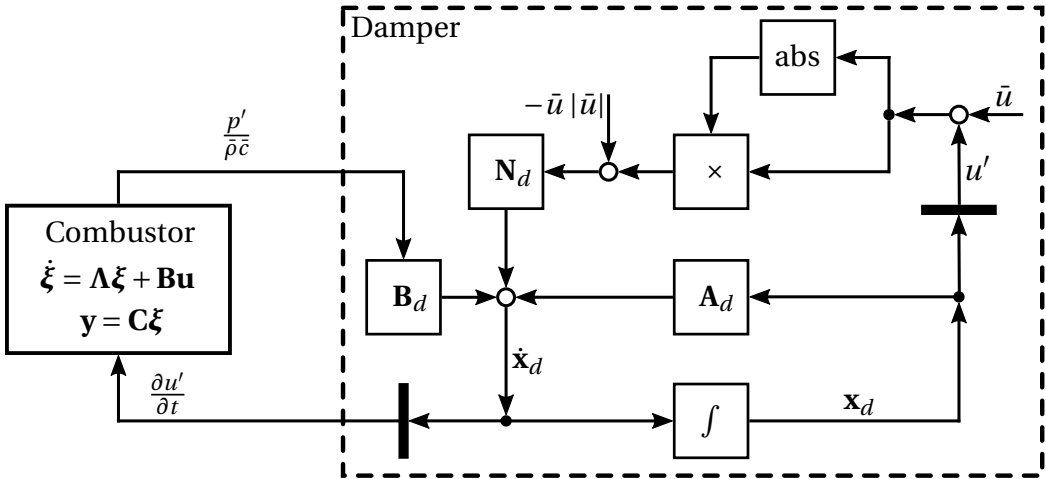


**Figure 5.3:** Signal flow diagram of the nonlinear damper model and its coupling with the ROM of the combustor.

## 6 Industrial-Scale Combustor

The methodology to predict the thermoacoustic stability proposed in the present thesis as summarized in Fig. 1.4 comprises multiple steps. All of those steps have been theoretically covered in the previous chapters with specific focus on the novelties presented in this work. A major asset of the entire procedure is the computational efficiency of each individual step. It is therefore predestined for the application to large-scale systems, which is demonstrated on the basis of a geometrically complex configuration representative for an industrial combustion chamber in this chapter. To begin with, a typical SIEMENS ENERGY combustor is introduced in section 6.1. A geometrically similar configuration is then used for the linear modeling procedure in section 6.2 including a suitable domain split as well as the characterization of the perforated liners and the burners. For the linear stability assessment, a modal stability analysis is performed with the results being presented in section 6.3. Using the modal data for a modal model order reduction in section 6.4 finally allows for the investigation of nonlinear modal interactions and limit-cycle oscillations. Due to a lack of validation data and the geometrical abstraction of confidential details, the corresponding studies may be considered a proof of concept for the proposed methodology to predict limit-cycle oscillations of large-scale systems based on nonlinear damping mechanisms.

### 6.1 Platform Combustion System

Meeting the high regulatory standards regarding  $NO_x$  and  $CO$  emissions at a wide load range and high efficiency, the products of the 8000H series of SIEMENS ENERGY are state-of-the-art gas turbines [202]. Depending on the specific machine, 12 (SGT6-8000H) or 16 (SGT5-8000H) can-annular combustion chambers based on an *Ultra Low  $NO_x$*  (ULN, [203]) *Platform Combustion System* (PCS, [204]) as schematically shown in Fig. 6.1 are installed. Compressed air is guided through the flow box into the flow sleeve, where it is directed into the plenum via an annular perforated liner to homogenize the

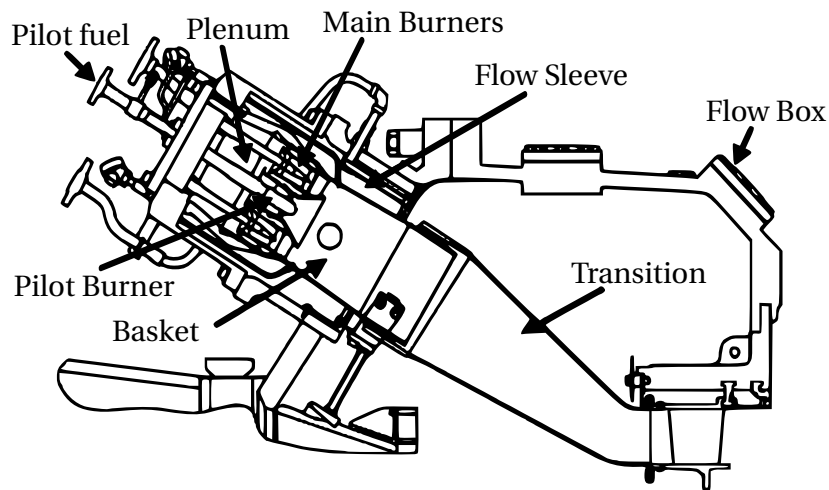


**Figure 6.1:** Sketch of a SIEMENS ENERGY H-Class can-annular combustion chamber based on Sattelmayer et al. [2].

flow. After a  $180^\circ$  flow turn across this flow conditioner, the air passes a central pilot burner and eight concentrically arranged main burners equipped with swirlers. The subsequent combustion chamber consists of a nearly cylindrical basket and a transition section guiding the hot gases to the annular turbine inlet. To control thermoacoustic oscillations mainly observed at part load, the basket is equipped with flush-mounted dual-layer perforated resonators. These are purged with air from the flow box to prevent damage from hot gas ingestion into the resonator cavities (cf. section 1.2.2). Fuel is added to the compressed air in five independently operating fuel stages [2, 202, 203]:

- PD: A pilot diffusion stage is realized via a central fuel lance and plays a crucial role for ignition.
- A/B: The concentric main burners are divided into two azimuthally alternating groups. The ratio of fuel between the main stages is referred to as A/B bias.
- C: For increased loads, fuel is added to the flow in the flow sleeve.
- D: A premixed pilot stage is realized via fuel addition through the pilot swirler vanes.

The specific operating conditions at part load considered in the subsequently presented numerical analysis are listed in Tab. 6.1.

**Table 6.1:** Operating conditions of the industrial-scale configuration.

Pressure [bar]	Load [%]	Active Stages	A/B bias [%]	Fuel
12.6	50	PD, A, B, C, D	70	Natural Gas

## 6.2 Hybrid Model of the Industrial-Scale Combustor

Representing the first three steps in the overall stability analysis procedure of Fig. 1.4, the present section covers the linear model creation of a configuration similar to the PCS.<sup>1</sup> Already at this point, the frequency range subject to the following stability analysis must be known. For the present demonstration of the developed analysis strategy, an investigation of HF thermoacoustic instabilities is pursued. Representative for HF oscillations, a target frequency  $f_{0,PCS}$  in the vicinity of the first transversal combustor mode is thus selected. This frequency will also be used as the linearization point for the employed linearized FTFs ( $s_{0,PCS} = i 2\pi f_{0,PCS}$ ) according to section 4.5.2.

### 6.2.1 Domain Split and FEM setup

Following the procedure presented in section 4.1, the PCS is first characterized using the local Helmholtz number and then split into subdomains. Downstream of the combustor, the turbine can be split from the transition right upstream of the first guide vane row, which features low Helmholtz numbers. On the upstream end, the perforated flow conditioner connecting the flow sleeve with the plenum is predestined to split the compressor side from the thermoacoustic computational domain. The perforation locally yields low Helmholtz numbers and considerable acoustic damping. In a simplistic way, the flow conditioner can then be considered as locally reacting. That is, the acoustic response of a boundary at a certain position exclusively depends on the local acoustic field independent of the acoustic field at neighboring positions. In the case of the flow conditioner, this precludes the coupling with the upstream components. This applies similarly to the dual-layer perforated resonators: the acoustic field transmitted into the flow box is considered suf-

<sup>1</sup>Due to the geometric similarity to the original PCS, the considered abstracted configuration is henceforth also simply referred to as PCS.

ficiently low to prevent a coupling between the individual resonators. Therefore, also the acoustically compact resonators are split from the basket at the liner mounting plane. Finally, also the burners are acoustically compact and can be split from the plenum and the basket at the corresponding face plates. Due to their overall large Helmholtz numbers, the plenum, basket and transition need to be resolved using 3D-FEM due to their overall large Helmholtz numbers. Figure 6.2 shows the corresponding disconnected computational domains including the mesh consisting of approximately 261k tetrahedral elements.

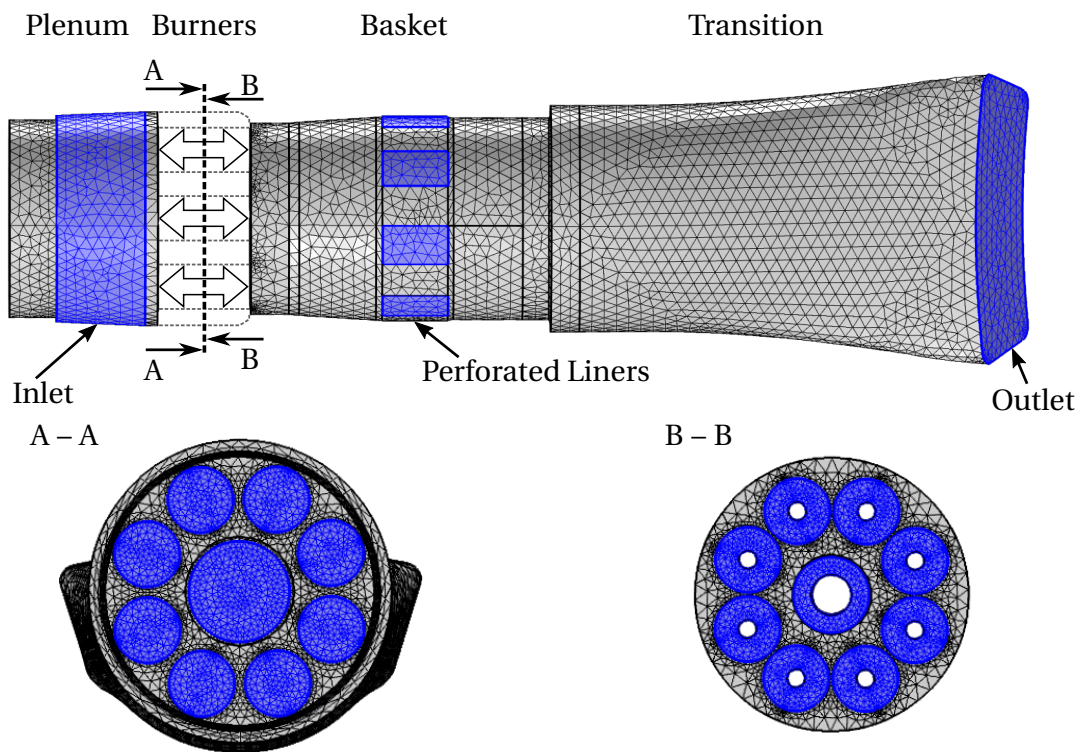


**Figure 6.2:** Disconnected FEM domains including the unstructured tetrahedral mesh of the investigated complex configuration. The burners connecting the two domains in terms of transfer matrices are indicated by double arrows. Top: Top view with the inlet, outlet and perforated liner patches highlighted in blue. Bottom left: View on the basket's face plate with the downstream coupling surfaces of the burners highlighted in blue. Bottom right: View on the plenum's face plate with the upstream coupling surfaces of the burners highlighted in blue.

A prerequisite for the 3D-CA simulations of the targeted hybrid CFD/CA approach is the mean flow field data for the operation point summarized in Tab. 6.1, which was provided by SIEMENS ENERGY. It stems from a reactive Unsteady Reynolds-Averaged Navier-Stokes (URANS) simulation using a Burning Velocity Model. For turbulent closure of the governing equations, a modified SST model was applied. Figure 6.3 shows cross-sections of the CA domains with the interpolated mean fields of the temperature and the volumetric heat release rate obtained from the time-averaged URANS results.

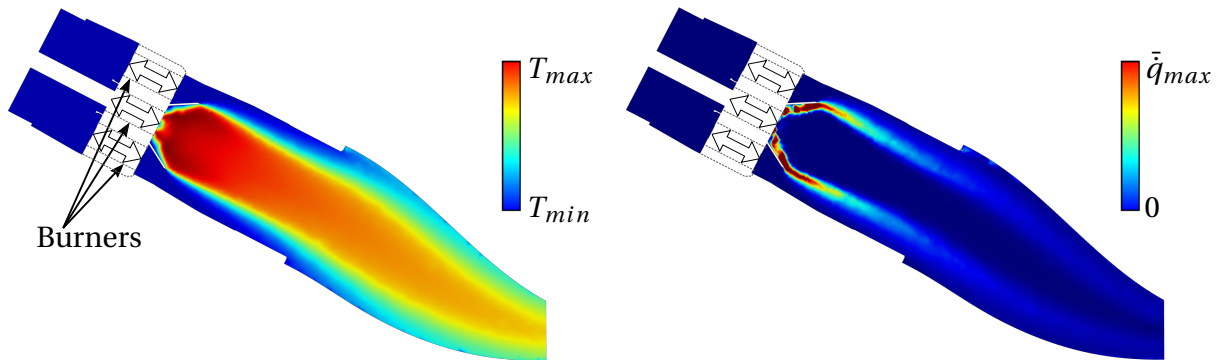


**Figure 6.3:** Mean temperature (left) and mean volumetric heat release rate (right) fields interpolated on the FEM mesh of the investigated complex configuration. The excluded burner geometries are indicated by double arrows.

The mean flow fields also contain essential information about the local Mach number, being the major indicator for the mean flow advection of acoustic waves. As demonstrated in section 4.6, this mean flow advection has a negligible impact on the results of a stability analysis for low mean flow Mach numbers ( $Ma \lesssim 0.1$ ). In this case, dropping the mean flow velocity by employing the energetically consistent Helmholtz equation is expected to accurately predict the system's eigenfrequencies and growth rates. In the considered configuration, the mean flow Mach number considerably exceeds values of 0.1 in the combustion chamber. Therefore, the consistent convective Helmholtz framework of eq. (4.14) yields more accurate results. Since it approximately comes at equal computational cost as the HE for quiescent fluids, the CHE is selected for the pursued modal stability analysis.

Using the consistent CHE framework for the 3D-CA part requires the specification of boundary conditions suitable for quiescent fluids. Most of the bound-

aries are walls, represented by the gray surfaces in Fig. 6.2. At wall boundaries, the normal mean flow velocity vanishes, corresponding to the zero mass flow impedance for quiescent fluids as discussed in section 2.6.4, which reads:

$$z^{\hat{m}, M=0} = -\infty. \quad (6.1)$$

The remaining boundaries of Fig. 6.2 are highlighted in blue and require a more detailed discussion. The turbine inlet resembles the outlet of the computational domain and features high Mach numbers. Making the simplified assumption of a choked turbine inlet corresponds to a wall boundary (6.1) for the outlet. To circumvent a complex characterization of the perforated flow conditioner, it is simply modeled as a sudden area change by means of the corresponding transfer matrix representation (4.46). Additionally assuming the apertures to be non-reflecting yields a suitable inlet impedance formulation as a function of the flow conditioner's porosity  $\sigma_{FC}$ . For quiescent fluids this impedance simplifies to

$$z_{inlet}^{M=0} = \frac{1}{\sigma_{FC}} = 20. \quad (6.2)$$

For the present investigation, eight dampers with equal azimuthal distance are applied to the basket as indicated in Fig. 6.2. Furthermore, the coupling surfaces for the burners are highlighted in cross-sectional views. Sophisticated models are required to characterize those elements in the subsequent sections.

### 6.2.2 Resonator Model

Multi-layer perforated resonators combine the benefits of Helmholtz resonators and perforated liners (cf. section 1.2.2). At the resonance frequency, predominantly determined by the cavity volume between the single layers, the acoustic amplitudes and thus the damping capabilities of the resonator are considerably amplified. Compared to Helmholtz resonators, multi-layer resonators exhibit more broadband damping characteristics [71] and provide uniform wall-cooling when being purged with compressed air [70]. This purge air is vital to prevent hot gases from entering the resonator cavities potentially damaging the dampers.

For practical applications, dual-layer perforated resonators are a great trade-off between the aforementioned benefits, production cost and space de-

mands. For this reason, such dual-layer resonators as schematically depicted in Fig. 6.4 are also employed to the PCS. The resonator cavity with solid side walls is terminated by a perforated plate on each side. One perforated plate is facing the cold section between flow box and flow sleeve while the second one is flush-mounted to the combustion chamber. A purge air flow is facili-

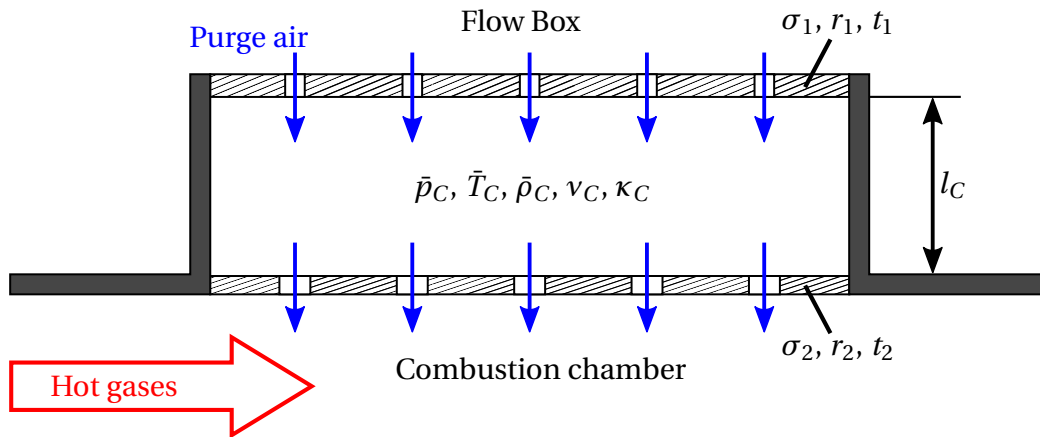


**Figure 6.4:** Schematic of a dual-layer resonator employed in the PCS.

tated by the pressure drop between flow box and combustion chamber. While the flush-mounted perforated plate is designed to obtain the desired damping characteristics, the upstream perforated plate facing the flow box may be used to meter the mass flow rate [70].

To determine the overall resonator impedance at the combustion chamber interface, the general framework to characterize multi-layer resonators in section 3.3 may be used. It requires the transfer impedances of the individual perforated plates, which are characterized using the Bellucci model as per section 3.3.4. Additionally, a termination boundary condition  $z_{BC}$  to represent the acoustic scattering at the interface between resonator and flow box is sought. Since the flow box represents a large volume, the transition from the upstream perforated plate to the flow box may be considered a sudden area change with a vast area ratio. This may conservatively be approximated by an open end boundary condition  $z_{BC,res} = 0$ .

While the geometric parameters of the resonator components may be chosen almost freely to obtain the desired damper characteristic, the thermodynamic properties are determined by the operating conditions. For low acoustic amplitudes, a normally damped resonator with a resonance frequency at  $f \approx 0.9f_{0,PCS}$  (cf. the results of the modal stability analysis in section 6.3) is

targeted for the present study. Recall from eqs. (3.27) and (3.33) that at high acoustic velocity amplitudes exceeding the mean flow velocity, the resonator's resistance becomes nonlinear. For a normally damped resonator, this nonlinearity leads to increased damping up to an optimally damped state as elaborated in section 3.3.1. The targeted damping characteristic of the employed dual-layer resonator is obtained by using the geometric and thermodynamic parameters as listed in Tab. 6.2.

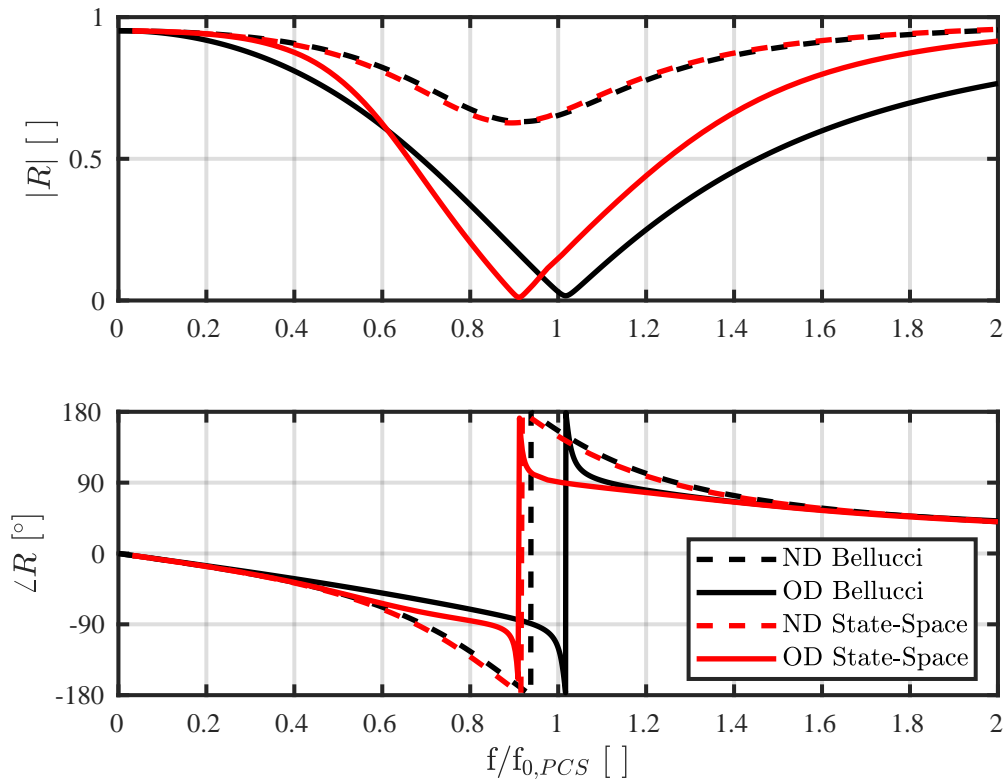
**Table 6.2:** Geometric and thermodynamic properties of the dual-layer perforated resonators.

Perforated plate	$\sigma$ [ ]	$r$ [m]	$t$ [m]	$\bar{u}_0$ [m/s]
1	$3.5 \times 10^{-3}$	$4 \times 10^{-4}$	$3.3 \times 10^{-4}$	35.54
2	$5.32 \times 10^{-2}$	$1.2 \times 10^{-3}$	$3.3 \times 10^{-3}$	2.37

$l_C$ [m]	$\bar{p}_C$ [bar]	$\bar{T}_C$ [K]	$\bar{\rho}_C$ [kg/m <sup>3</sup> ]	$\nu_C$ [m <sup>2</sup> /s]	$\kappa_C$ [ ]
0.046	12.6	650	6.72	$4.9 \times 10^{-6}$	1.37

The resulting end impedance at the interface to the combustion chamber may be transformed into a reflection coefficient using eq. (2.32). This is more meaningful, since the reflection coefficient directly correlates with the reflected acoustic energy. In Fig. 6.5, the reflection coefficient of the resonator design is plotted for different acoustic amplitude levels. While the normally damped (ND) characteristic (dashed curves) results for low acoustic amplitudes, the optimally damped (OD) characteristic (solid curves) is obtained due to nonlinear damping mechanisms at elevated amplitude levels. The black curves represent the characteristics of the procedure described in section 3.3 employing the Bellucci model. Based on a rational function fit of the ND Bellucci curve in the linear amplitude regime, a nonlinear state-space model has then been created according to the procedure developed in section 5.4.2. To recreate the frequency-dependent reflection coefficient, simulations for a wide range of frequencies have been performed with this model in the TD. Subsequently Fourier-transforming the harmonic TD signals for the two different amplitude levels then yields the red curves in Fig. 6.5. With the



**Figure 6.5:** Comparison of the resonator's reflection coefficients obtained from the original Bellucci model (black) and the state-space model based on a rational function fit of the ND Bellucci curve (red) at different acoustic amplitude levels (ND and OD).

state-space model being fitted to the ND Bellucci curve, it is not surprising that the reflection coefficients for both approaches are in excellent agreement at low amplitudes. At elevated acoustic amplitudes, the resonator reaches a nearly optimally damped state, with the entire incident acoustic energy being absorbed at the resonance frequency ( $|R| = 0$ ). In this nonlinear state, the reflection curves moderately deviate for the original multi-layer characterization and the fitted state-space model. While the resonance frequency remains constant for the state-space model, it shifts to higher frequencies for the Bellucci model. This is due to the nonlinearity of the empirical end-correction term  $\eta(Sr_{ac})$  in eq. (3.32), which can not be captured by the fit. Overall, the qualitative agreement between both setups is still acceptable. This is also confirmed by the amplitude levels at which the two models predict an optimally damped oscillator as listed in Tab. 6.3. The relative deviation is 13% and stems

from the inaccurate assumption of the generally linear viscous losses to also be of nonlinear character (cf. section 5.4.2).

**Table 6.3:** Acoustic velocity amplitudes for optimal damping of the dual-layer resonator using the multi-layer characterization and the fitted state-space model.

$ \hat{u}_{Bellucci} $ [m/s]	$ \hat{u}_{State-Space} $ [m/s]	Relative Deviation [%]
1.85	1.61	13

### 6.2.3 Burner Transfer Matrices

Although being complex and small-scale geometric elements, the burners including the swirlers of the PCS only slightly impact longitudinal waves passing those components. This impact is limited to a constriction of the cross-sectional area, an elongation of the propagation distance according to the swirler vane's chord length and a pressure loss due to viscous and turbulent losses in the swirling flow. These mechanisms can be reproduced by a series of duct elements and sudden area changes as presented in section 3.2. Regarding the burners of the PCS, the cross-sectional area is nearly constant upstream and downstream of the swirler section. Essentially, the abstracted network of the burners as depicted in Fig. 6.6 thus consists of three duct elements connected by sudden area changes. The central duct element  $D_2$  exhibits a smaller cross-sectional area than the remaining ducts. This mimics the constriction of the streamlines due to the burner's swirler vanes. The trailing area change  $AC_3$  is mainly added to include acoustic losses that are expected to be induced at the interface of burners and face plate due to flow separation.

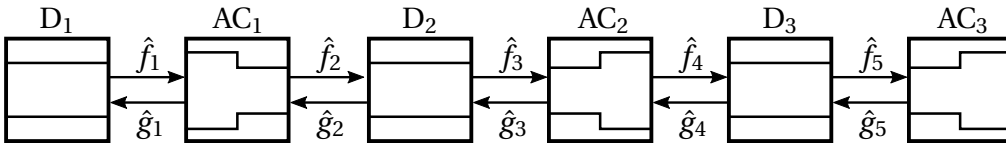


**Figure 6.6:** 1D network model of the PCS burners.

The specifications of the individual elements for both, the pilot as well as the

eight identical main burners, are listed in Tab. 6.4. The geometric parameters of the burners are normalized by the hydraulic diameter downstream of the trailing area change  $AC_3$ . This hydraulic diameter  $d_4$  corresponds to the coupling interface of the burners with the combustion chamber. Since the Mach

**Table 6.4:** Parameters of the 1D network to acoustically describe the pilot and main burners of the PCS. The naming is in accordance with Fig. 6.6.

Burner	Duct Element	$l/d_4$ [ ]	$d/d_4$ [ ]	AC Element	$M_u$ [ ]	$A_u/A_d$ [ ]	$\Delta p_l/p_t$ [%]
Pilot	D <sub>1</sub>	0.4138	0.6962	AC <sub>1</sub>	0.10	1.61	0
	D <sub>2</sub>	0.1153	0.5482	AC <sub>2</sub>	0.16	0.68	0.3
	D <sub>3</sub>	0.798	0.6665	AC <sub>3</sub>	0.11	0.44	0.7
Main	D <sub>1</sub>	0.165	1.042	AC <sub>1</sub>	0.10	1.29	0
	D <sub>2</sub>	0.420	0.919	AC <sub>2</sub>	0.13	0.84	0.3
	D <sub>3</sub>	1.454	1	AC <sub>3</sub>	0.11	1	0.7

number is reasonably low, the low Mach number approximation (4.46) for the sudden area change can be employed. In accordance with eq. (4.47), the pressure loss over the total pressure  $\Delta p_l/p_t$  corresponds to the total pressure loss coefficient  $\beta$ .

The 1D network model finally yields overall burner transfer matrices for the pilot and the main burners including the mean flow advection of sound waves. For an energetically consistent coupling of the FEM domains solving the CHE, the transfer matrices need to be energetically transformed by means of the procedure presented in section 4.4. In Fig. 6.7, the resulting scattering matrix coefficients are plotted for a single main burner. In addition to the SM coefficients, also the absolute value of a dissipation coefficient  $D$  is plotted. It originates from the idea that the entire incident acoustic energy is either reflected, transmitted or dissipated. For the upstream side, this may be expressed in terms of the upstream reflection and transmission coefficients as (cf. section 4.4 and [133, 205])

$$|D_u|^2 = 1 - |R_u|^2 - \frac{A_d}{A_u} |T_u|^2, \quad (6.3)$$

and equivalently for the downstream side. Plots of the scattering matrix coef-

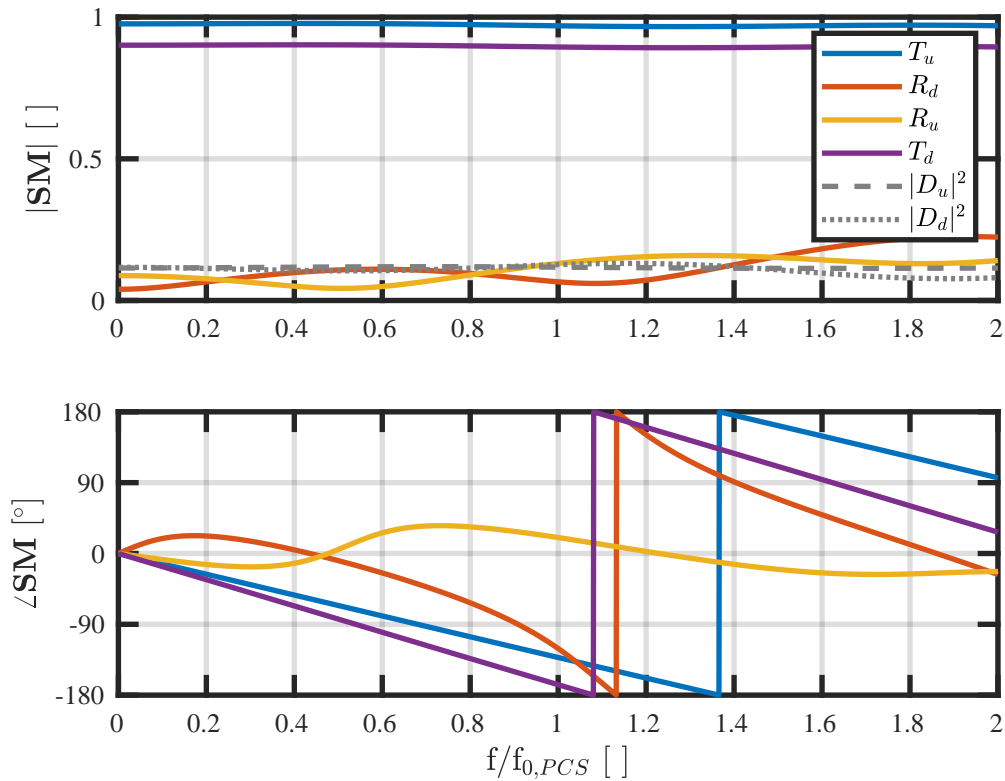


**Figure 6.7:** Energetically transformed scattering matrix coefficients of a single main burner obtained from a 1D network.

coefficients for the pilot burner are provided in Appendix G. Additionally, also the corresponding coefficients for the original scattering matrix without energetic transformation are plotted there.

### 6.3 Modal Analysis Results

After coupling the 3D-FEM domains with the 1D characteristics and interpolating the mean flow field, the model is ready for linear modal stability analysis. Three setups as listed in Tab. 6.5 are considered. All of them are computed on the basis of the CHE (4.14) and do thus incorporate the advection of acoustic waves along the 3D mean flow velocity. However, they differ by the boundary conditions applied to the perforated liner patches, cf. Fig. 6.2. Those damper patches are replaced by wall boundary conditions in the setup *No Dampers*. Instead, the frequency dependent boundary impedances corresponding to the liner characteristics ‘ND State-Space’ and ‘OD State-Space’

**Table 6.5:** Configurations for the modal stability analysis of the PCS.

Setup	Acoustic Equation	Damper Patch BC	FTF
No Dampers	CHE (4.14)	Wall	$\hat{q}_\rho + \hat{q}_\Delta$ (4.44)
ND Dampers	CHE (4.14)	ND State-Space (red dashed line in Fig. 6.5)	$\hat{q}_\rho + \hat{q}_\Delta$ (4.44)
OD Dampers	CHE (4.14)	OD State-Space (red solid line in Fig. 6.5)	$\hat{q}_\rho + \hat{q}_\Delta$ (4.44)

are used as boundary conditions in the setups *ND Dampers* and *OD Dampers*, respectively. In accordance with the consistent CHE framework, the boundary conditions of all three setups are transformed to comply with the zero Mach number assumption, cf. sections 4.3.2 and 4.4. Furthermore, the driving mechanisms of flame deformation and flame displacement represented by eqs. (4.44) are used to model the acoustics-flame interactions. In summary, four contributions to the acoustic energy balance can be distinguished: while the contributions from flame driving as well as from damping induced by the flow conditioner and the burner transfer matrices can be assumed to be equivalent for all three setups, only the contribution from the damper patches is notably varied. Due to its lowest system damping, the setup without dampers is expected to predict the least stable eigenmodes, whereas introducing additional damping via the perforated liner patches will supposedly increase the stability of the system.

The entire computational model is linearized by means of the state-space framework elaborated in section 4.5 yielding a duplication of degrees of freedom (DOF). In combination with the selected quadratic element order, the DOF add up to approx. 747k for all setups. The modal stability analysis is performed with the standard *Eigenvalue* solver of COMSOL MULTIPHYSICS® [206], which uses the MUMPS software [207]. To increase the solution's accuracy, the relative tolerance parameter to determine convergence is reduced to  $10^{-7}$ . For each of the setups, the ten eigenmodes closest to the target frequency  $f_{0,PCS}$  are computed. The resulting eigenvalues are plotted in the stability map of Fig. 6.8. It shows the growth rate  $\alpha$  over the normalized oscillation frequency of each eigenvalue with the stability limit being highlighted by a dashed line.

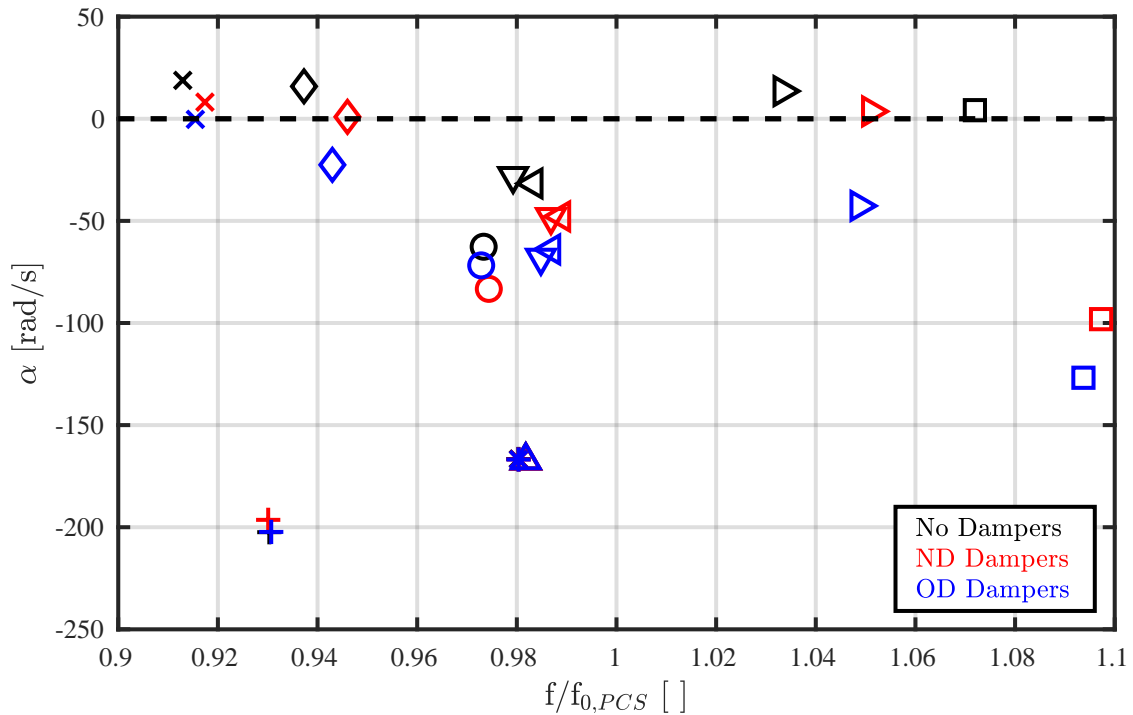


**Figure 6.8:** Stability map of eigenmodes computed in the vicinity of the target frequency  $f_{0,PCS}$ .

Each of the ten eigenmodes is assigned an individual symbol, whereas the different setups are distinguished by different colors. Figure 6.9 exhibits the mode shapes of all ten eigenmodes in terms of the pressure magnitude, corresponding to their right eigenvectors.

Even in the absence of perforated liners in the setup ‘No Dampers’, six stable modes with growth rates below zero are identified from the results (+, o, \*,  $\Delta$ ,  $\nabla$ ,  $\triangleleft$ ). As can be seen from Fig. 6.9, the corresponding mode shapes are mainly confined to the plenum, which does not enclose any heat release. For those modes, the losses at the flow conditioner and within the burners exceed the overall flame driving. The remaining four eigenmodes are unstable with positive growth rates ( $\times$ ,  $\diamond$ ,  $\triangleright$ ,  $\square$ ). All of the four modes show considerable oscillation amplitudes in the flame region within the combustion chamber (cf. the mean volumetric heat release field of Fig. 6.3 with the mode shapes of Fig. 6.9) and are thus excited by the flame response. The first of those eigenmodes ( $\times$ ) has the highest growth rate and is thus labeled most unstable. Its oscillation frequency was targeted as resonance frequency in the design of the

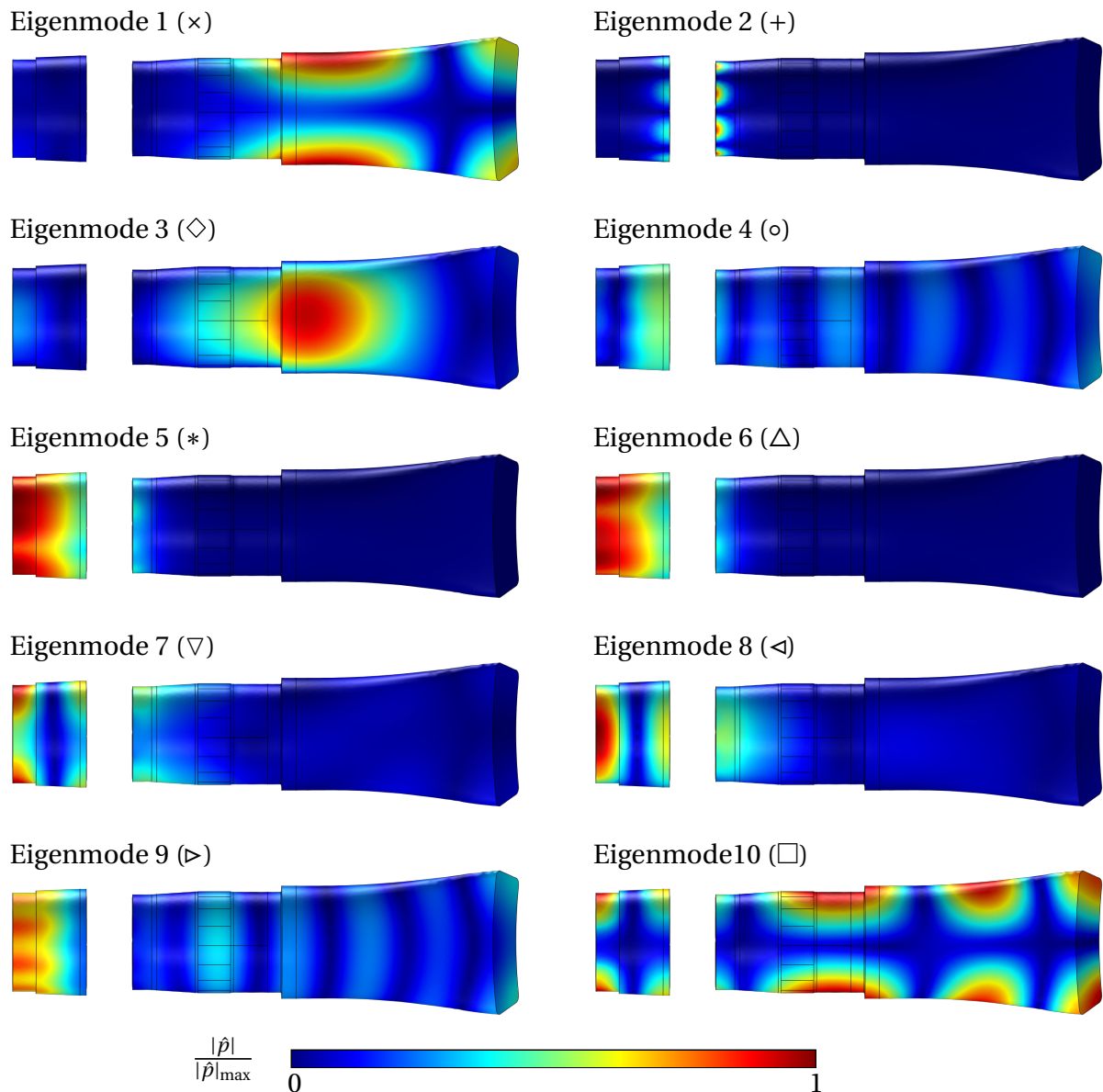


**Figure 6.9:** Mode shapes of the PCS without resonators in the vicinity of the target frequency  $f_{0,PCS}$  with the symbols in parentheses referring to the stability map in Fig. 6.8.

perforated resonator characteristics in section 6.2.2.

Employing the normally damped characteristic of the perforated liner characteristic to the eight damper patches of the PCS is supposed to introduce additional damping already at low acoustic amplitudes. Indeed, the setup ‘ND Dampers’ yields an increased stability. However, the first (×), third (◇) and ninth (▷) modes are still marginally unstable. Only the tenth mode (□) transitions from marginal instability to stability. In contrast to the other three

modes, the last mode shape has considerable pressure amplitudes at the liner patches and is thus severely impacted by the dampers.

Using a transfer function based on nonlinear mechanisms in a linear computational framework mimics the stability prediction at high acoustic amplitudes. This methodology is a common practice when employing an amplitude dependent flame describing function and was also exploited for the setup ‘OD Damper’. The corresponding liner characteristic for high amplitudes is optimally damped and has thus maximum damping capabilities. This is also reflected in the eigenvalues: all modes of the setup ‘OD Damper’ are predicted to have negative growth rates and are thus stable. With a value of  $\alpha = -0.29$  rad/s, the first eigenmode is only marginally stable, though.

Regarding the temporal amplitude evolution, the three unstable modes are thus supposed to exponentially grow in the linear amplitude regime. As soon as the acoustic velocity amplitude exceeds the perforated liners’ purge flow velocity, the damping increases nonlinearly. Therefore, the modes are expected to stabilize in terms of limit-cycle oscillations, which is investigated in the next section.

### **6.4 Nonlinear ROM Simulations of the Large-Scale Combustor**

Based on the linear modal stability analysis results of the previous section, a modal model order reduction followed by nonlinear ROM simulations are now performed with the following objectives:

1. Proving the concept of the Generalized Discrete MAE explicated in sections 5.3 and 5.4,
2. Demonstrating its applicability to large-scale systems on the basis of the PCS and
3. Highlighting the significance of nonlinear damping mechanisms for the limit-cycle oscillations.

Ultimately, the results obtained from the Generalized Discrete MAE are classified by comparing them to those of comparable studies available from literature.

### 6.4.1 ROM Creation

The centercore of the Generalized Discrete MAE is the bi-orthogonal basis spanned by the left and right eigenvectors. Recall that those eigenvectors must incorporate the linear damping mechanisms of potentially nonlinear boundary patches. The ROM is thus expected to accurately reproduce the dynamics of the combustor at low acoustic amplitudes. At high acoustic amplitudes, the nonlinear damper model subject to the boundary source  $S1$  (cf. Fig. 5.1) constitutes additional nonlinear losses.

In the case of the PCS, only the setup ‘ND Dampers’ (cf. Tab. 6.5) includes the required linear damping mechanisms of the resonators. Hence, it forms the basis for the modal model order reduction. The computation of the corresponding right eigenvectors as presented in the previous section is a fundamental feature of COMSOL MULTIPHYSICS<sup>®</sup>. However, an equivalent feature to compute the left eigenvectors does not natively exist. To circumvent this issue, the right eigenvalue problem (5.5) is reconsidered, which may also be written as  $(\mathbf{A} - s_n \mathbf{I}) \mathbf{v}_n = 0$ . The corresponding left eigenvalue problem may be transformed according to

$$\overline{\mathbf{w}_n} (\mathbf{A} - s_n \mathbf{I}) = \overline{(\mathbf{A} - s_n \mathbf{I})} \mathbf{w}_n = (\overline{\mathbf{A}} - \overline{s_n} \overline{\mathbf{I}}) \mathbf{w}_n = 0. \quad (6.4)$$

It becomes obvious that the left eigenvalue problem can be converted into a right eigenvalue problem by complex conjugation of the explicit system matrix  $\mathbf{A}$  (cf. eq. (5.2)) and the eigenvalue  $s_n$ . A straightforward procedure to achieve this is to extract the system matrices from COMSOL MULTIPHYSICS<sup>®</sup> using the LIVELINK<sup>™</sup>FOR MATLAB<sup>®</sup> [208]. After complex conjugation in MATLAB<sup>®</sup>, the matrices can be reimported into COMSOL MULTIPHYSICS<sup>®</sup> to perform a modal analysis resulting in the left eigenvectors and the complex conjugate eigenvalues.

Applying this procedure to the PCS results in the left eigenvectors corresponding to the right eigenvectors of the setup ‘ND Dampers’ discussed in the previous section. To check the orthogonality of the eigenvectors, the square Gram matrix  $\mathbf{G}^{m \times m}$  is of great use. It represents the elementwise inner product of a set of spatial functions. In the case of a set of eigenvectors  $\boldsymbol{\phi}$ , its elements may be expressed as

$$G_{i,j} = \langle \phi_i, \phi_j \rangle. \quad (6.5)$$

For the present study, this definition is expanded to also compare different

sets of eigenvectors, more precisely the right and left eigenvectors, with each other. The classic Gram matrices of the right and left eigenvectors exclusively as well as the pseudo Gram matrix of a combination of both eigenvectors are shown in Fig. 6.10 as heatmaps. Since the eigenvectors are normalized, the

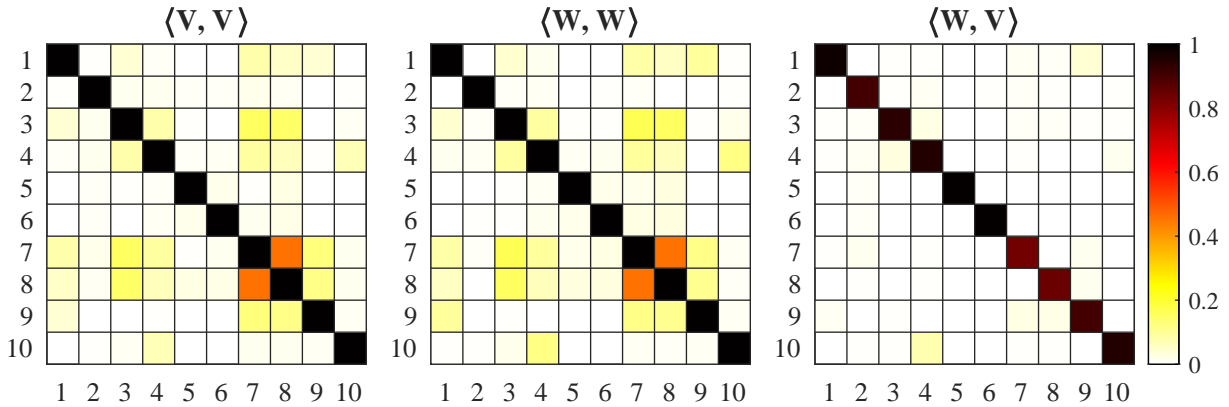


**Figure 6.10:** Eigenvector Gram matrices of the setup ‘ND Dampers’. Left: Inner product of right eigenvectors  $\mathbf{V}$ . Center: Inner product of left eigenvectors  $\mathbf{W}$ . Right: Inner product of left and right eigenvectors.

inner product with each other equals one by definition. Therefore, the diagonal elements of the Gram matrices  $\langle \mathbf{V}, \mathbf{V} \rangle$  and  $\langle \mathbf{W}, \mathbf{W} \rangle$  show unity flags. If the solved problem was self-adjoint, all other elements would be zero indicating the modes to be orthogonal. In this case, the left eigenvector matrix would equal the right eigenvector matrix. However, the mean flow field as well as the frequency-dependent boundary conditions break the self-adjointness in the PCS model. This is substantiated by the numerous non-zero elements apart from the main diagonal. In contrast to the Gram matrices  $\langle \mathbf{V}, \mathbf{V} \rangle$  and  $\langle \mathbf{W}, \mathbf{W} \rangle$ , the mixed Gram matrix  $\langle \mathbf{W}, \mathbf{V} \rangle$  exhibits the desired bi-orthogonality of left and right eigenvectors. Only slight deviations from the expected unity matrix shape are observed, which are a result of numerical inaccuracies.

After accomplishing the modal analysis, the reduced system matrix can be constructed as a diagonal matrix containing the eigenvalues.<sup>2</sup> Furthermore, the bi-orthogonal basis represented by the left and right eigenvector matrices may be used to reduce the input and output matrices of the Generalized

<sup>2</sup>Recall from eq. (6.4) that the eigenvalues of the right and left eigenvalue problem are identical.

Discrete MAE. As pointed out in section 5.4, these are required to couple the combustor acoustics with the flame and the resonator dynamics.

Regarding the flame source, the linear mechanisms of flame deformation and displacement have already been included in the modal analysis and are thus part of the system matrix. Since the nonlinear flame driving mechanisms are neglected, the closed-loop coupling between the Generalized Discrete MAE and the flame in Fig. 5.1 vanishes. Only a stochastic contribution  $\dot{q}'_{st}$  must be incorporated into the TD simulations to mimic the combustion noise as an initiator of the combustor dynamics. Despite representing an open-loop contribution, including a stochastic flame source for HF simulations requires similar steps as the closed-loop counterparts. First of all, the overall 3D-FEM domain is split into acoustically compact subdomains. Due to the geometry of the PCS, a split in cylindrical coordinates with the axial direction being in line with the pilot burner's axis is preferred. In the present configuration, the cylindrical bounding box is divided into  $10 \times 6 \times 30$  subdomains in radial, azimuthal and axial direction, respectively. Most of those 1800 subdomains have a negligible mean heat release rate and do thus not contribute to the overall flame driving. They may be removed when the ratio of the subvolume-integrated mean volumetric heat release to the overall mean heat release rate is below a threshold value. Here, an arbitrary threshold value of 0.14% was selected, giving a total of 206 remaining subvolumes. Figure 6.11 highlights the nodes of all 206 subdomains colored with their corresponding subdomain-averaged mean heat release rate. For closed-loop systems, the number of subvolumes essentially determines the computational cost of the nonlinear simulations. Therefore, the selection of the threshold value as well as the number of split bins is a trade-off between accuracy and computational cost. This is of minor relevance for the open-loop stochastic heat release fluctuations considered here. Independent of the loop-closure, each of the subvolumes is considered to have a uniform source strength. Regarding the combustion noise, this source strength is assumed to be proportional to the volume-averaged mean heat release rate in each subdomain. The input matrix is now constructed as per eq. (F.2) as a  $(10 \times 206)$  matrix. Additionally, every column is weighted by the corresponding subvolume-averaged heat release rate. A white noise signal with arbitrary but equal noise power for each of the subdomains is used as the open-loop input.

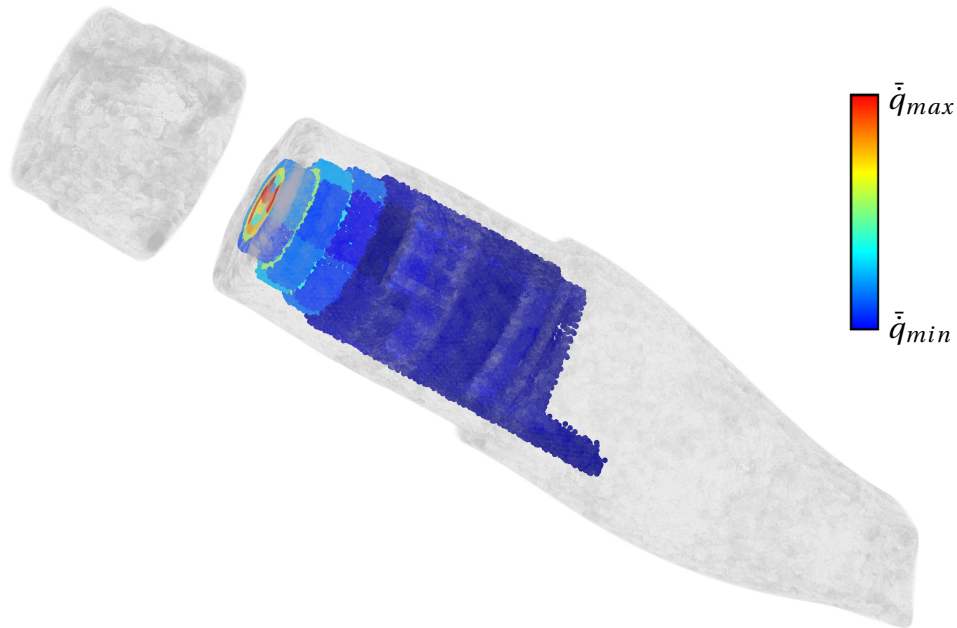


**Figure 6.11:** Compact subdomains with non-negligible heat release rate.

Each of the eight perforated liners is modeled as an individual and independent state-space system coupled to the combustion chamber. Both, the state-space modeling of the nonlinear dampers as well as the coupling with the combustor acoustics is established as explicated in section 5.4.2.

The finalized Generalized Discrete MAE of the PCS are implemented in MATLAB<sup>®</sup>. For this reason, MATLAB<sup>®</sup> SIMULINK<sup>®</sup> is an obvious choice for the temporal integration of the ROM discussed in the next section.

### 6.4.2 Time-Domain Results

For the analysis of the nonlinear TD simulations, first the pressure trace is evaluated. It is the most intuitive quantity since it is easily measurable in real systems. Depending on the output matrix of the Generalized Discrete MAE, the pressure can generally be extracted at any spatial location of the discretized PCS. Since it is already part of the closed-loop coupling between the combustor acoustics and the nonlinear dampers, the pressure is evaluated at the perforated liner patches. That comes at the additional advantage of gaining access to an assessment of the dominating oscillation frequencies at the damper locations. With the eigenmodes considered in the modal model order

reduction being nearly symmetric regarding to the center plane of the basket, it is sufficient to only consider four of the eight resonator patches. With reference to Fig. 6.2, these are the ones on the lower half of the top view, referring to the top-most resonator as D1. Figure 6.12 shows the temporal evolution of the pressure at the four dampers. Shortly after the start of the simulation, the signal is very noisy as can be observed in the left detail view for the normalized time interval  $100 \leq t \cdot f_{0,PCS} \leq 120$  and its FFT below. Despite the white noise excitation in the flame's subvolumes, the pressure signal is already slightly colored from the modal oscillations. It may be noted that the amplitude levels of the pressure oscillations are still nearly equal at all four damper locations. Until  $t \cdot f_{0,PCS} \approx 2000$ , the amplitude levels remain fairly low and begin to significantly increase afterwards. This is followed by a saturation phase leading to limit-cycle oscillations with a stagnating oscillation amplitude depending on the spatial location. Already in the exponential growth phase, significant amplitude discrepancies between the individual considered locations become obvious. Taking a closer look on the limit-cycle oscillations in the time interval  $6980 \leq t \cdot f_{0,PCS} \leq 7000$  shows pure harmonic oscillations. A FFT of the signals reveals the dominance of a single frequency being equal to the most unstable first eigenfrequency ( $\times$  in Fig. 6.8) for all four damper positions. The higher amplitude levels at the second and third resonator positions may now be explained by the pressure distribution of the corresponding mode shape of eigenmode 1 ( $\times$ ) in Fig. 6.9 taking maximum values at the positions of those patches.

Solely considering the overall pressure trace, one may assume that the exponential growth only starts after  $t \cdot f_{0,PCS} \gtrsim 2000$  of normalized simulation time. However, according to theory, the linearly unstable eigenmodes are expected to show such an amplitude gain immediately after being excited. A more detailed insight into the growth of the individual eigenmodes is attained by directly examining the temporal evolution of the modal amplitudes  $\xi_n$ , which are the states of the Generalized Discrete MAE. Recall that analogously to  $\mu_n$  in the series expansion of eq. (5.13), the states  $\xi_n$  quantify the contribution of the individual eigenmodes within the ROM to the overall pressure signal. In Fig. 6.13, the magnitudes of all ten modal amplitudes  $\xi_n$  are plotted on a logarithmic scale over time. Exponential growth can thus be identified from curves with constant positive slopes. Indeed, the most unstable first eigenmode ex-

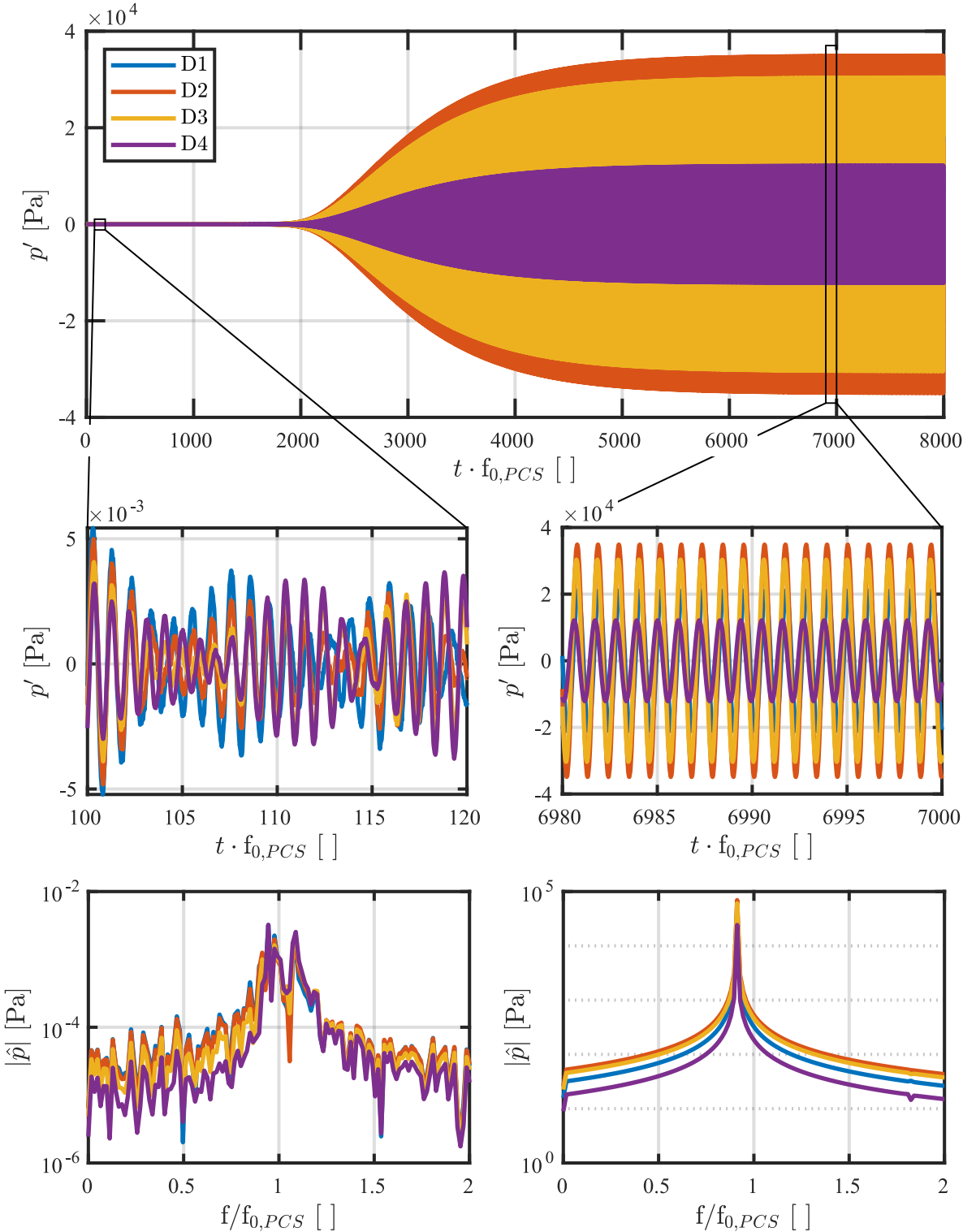


**Figure 6.12:** Temporal pressure evolution at four neighboring resonators including detailed views with corresponding FFTs.

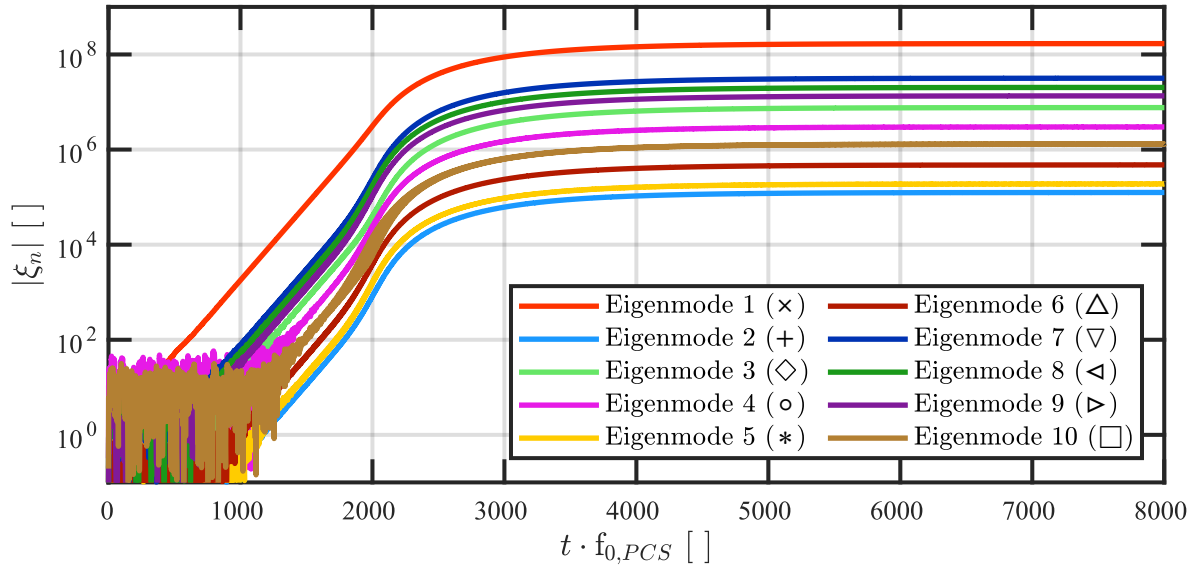


**Figure 6.13:** Temporal evolution of the modal amplitude's magnitudes  $|\xi_n(t)|$  over time.

hibits a distinct exponential growth only approximately  $t \cdot f_{0,PCS} \approx 500$  after the start of the simulation. Surprisingly, all other eigenmodes also start to exponentially grow after a short time delay. This is only expected for the three linearly unstable modes but is also observed for the linearly stable ones. Their amplitudes are much rather expected to remain at the level of the stochastic forcing due to their considerable damping rates. Such an exponential growth can only be caused by nonlinear modal interactions via the nonlinear resonator patches. However, the exponential growth of the linearly stable modes can already be observed some time before the nonlinear saturation comes into effect, flattening the modal amplitude curves at about  $t \cdot f_{0,PCS} \gtrsim 2100$ .

A better comprehension of the mechanisms leading to the nonlinear interactions can be obtained from the temporal evolution of the modal amplitudes' phases. For better visibility, Fig. 6.14 presents the unwrapped phase over time, which is not limited to the common range  $[-\pi, \pi]$ . Particularly at the start of the simulation, the slope of the individual modes is increasing for increasing mode numbers and thus increasing eigenfrequencies. This is highlighted in the left detail view of Fig. 6.14 and can be explained intuitively: a harmonic wave with a low frequency will exhibit a smaller integrated phase change when

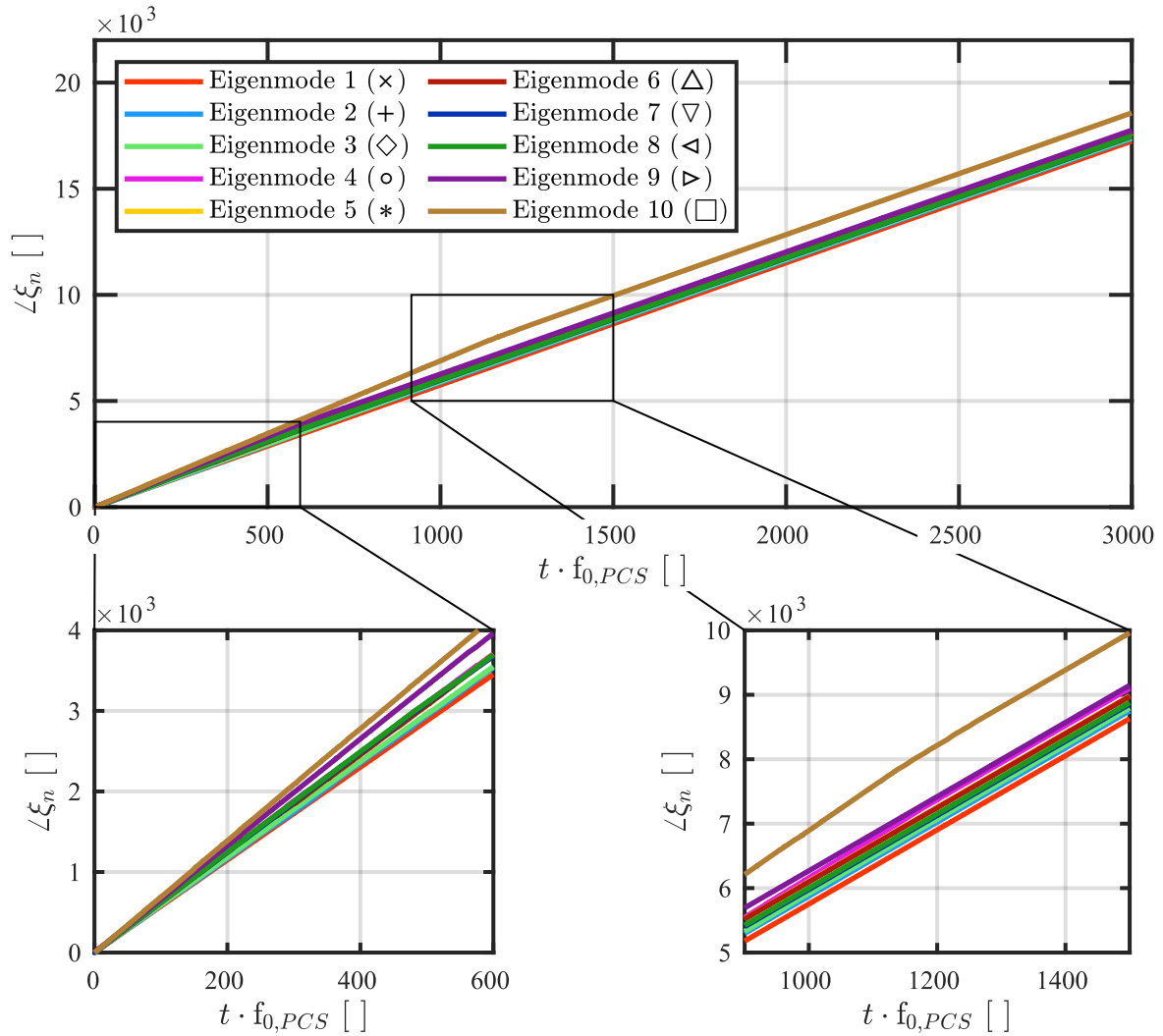


**Figure 6.14:** Temporal evolution of the modal amplitude's phase  $\angle\xi(t)$  over time with detailed views of the unsynchronized and the synchronized state.

traveling the same distance or time as a harmonic wave with higher frequency. Within the time interval  $900 \leq t \cdot f_{0,PCS} \leq 1500$ , however, the phase traces suddenly bend as may be seen from the right detail view of Fig. 6.14. Afterwards, the phases of all eigenmodes increase at an equal slope as the most unstable eigenmode 1. This may be interpreted as modal synchronization, which had been investigated by Bonciolini and Noiray [209] and by Moeck et al. [210] for only two interacting modes. Both use a generic cubic saturation term to account for nonlinear modal interactions. Moeck et al. [210] come to the con-

clusion, that a synchronization is only possible for eigenmodes with narrow differences in oscillation frequencies and growth rates. While the former condition is satisfied in the present case, the latter one does not apply here.

The key to understanding this unexpected synchronization lies in the boundary sources and their interaction with the combustor acoustics. Recall from section 5.3 in conjunction with Fig. 5.1 that two boundary sources are included in the Generalized Discrete MAE: While the boundary source  $S1$  represents the acoustic coupling between combustor and nonlinear damper model,  $S2$  can be interpreted as the purely linear damping part being subtracted from  $S1$ . Consequently, a net boundary source represented by the overall boundary input  $\mathbf{B}_S \mathbf{u}_S$  is mainly expected at high acoustic amplitudes. This is confirmed by Fig. 6.15, exhibiting the time trace of the two source terms for the linearly most unstable eigenmode 1 ( $\times$  in Fig. 6.8) as well as for the linearly stable eigenmodes 2 (+ in Fig. 6.8) and 7 ( $\nabla$  in Fig. 6.8). However, exclu-

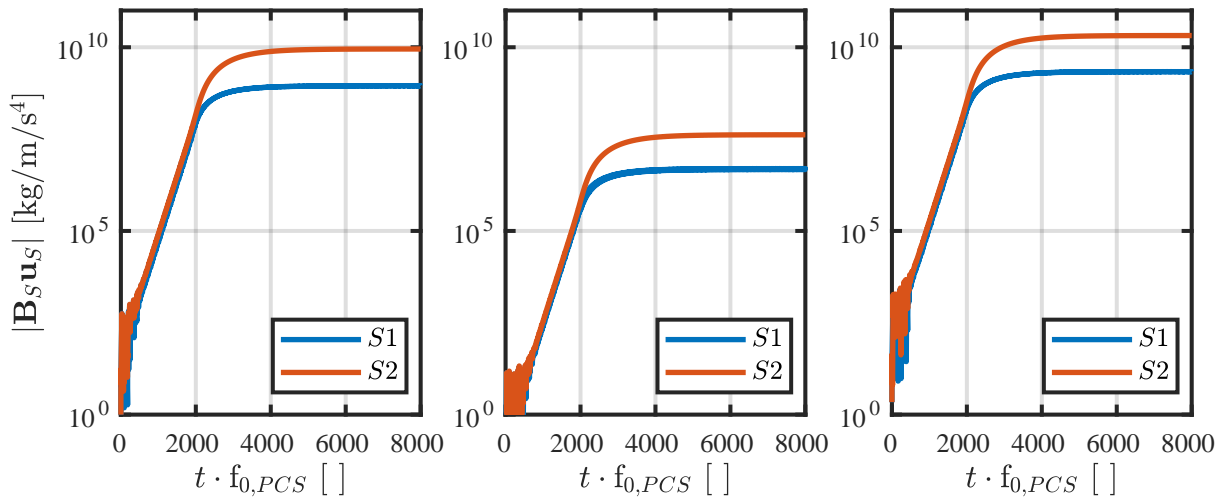


**Figure 6.15:** Comparison of the magnitude of boundary sources  $S1$  and  $S2$  for the linearly unstable eigenmode 1 (left) as well as the linearly stable eigenmodes 2 (center) and 7 (right).

sively assessing a source term is normally not adequate to determine its energetic driving capabilities as already indicated by Rayleigh's criterion, eq. (1.2), for the flame dynamics. Depending on the phase relation between source term and system dynamics, the source can be both driving or damping. Similar to the unsteady volumetric heat release rate  $\dot{q}'$  constituting a source term for the pressure fluctuations  $p'$  of the CHE's state-space representation, eq. (4.40), the

overall boundary source terms  $\mathbf{B}_S \mathbf{u}_S$  affect the modal amplitudes  $\xi$  of the Generalized Discrete MAE, eq. (5.23). In analogy to Rayleigh's criterion, the driving capabilities of the overall boundary source terms for an individual eigenmode  $n$  can thus be evaluated via

$$\langle S_S \rangle_{t,n} \propto \langle \xi \cdot \mathbf{B}_S \mathbf{u}_S \rangle_{t,n} \approx \frac{1}{2} \Re \left\{ \bar{\xi} \cdot \mathbf{B}_S \hat{\mathbf{u}}_S \right\}_n. \quad (6.6)$$

In eq. (6.6), the identity (2.24) is exploited to avoid an error-prone temporal signal integration. Instead, the period-averaged energetic source  $S_S$  can be evaluated in the FD. For this purpose, the total simulation time is first divided into windows of equal temporal length. Within each of the windows, the temporal signals of the modal amplitudes  $\xi$  and the boundary source terms  $\mathbf{B}_S \hat{\mathbf{u}}_S$  are then Fourier-transformed for each eigenmode. Finally, eq. (6.6) is evaluated in every window using the FFT values of the signals at the dominating frequency. The resulting temporal evolution of  $\langle \xi \cdot \mathbf{B}_S \mathbf{u}_S \rangle_{t,n}$  is plotted in Fig. 6.16 for three different eigenmodes with linear (top row) and logarithmic scale (bottom row). Equivalent to Rayleigh's criterion, the linearly most unstable eigenmode 1 ( $\times$ ) experiences an overall negative energetic source for its stabilization (Fig. 6.16 left). In contrast, the linearly stable eigenmodes 2 (+) and 7 ( $\nabla$ ) are subject to a positive energetic source as shown in the center and right plots of Fig. 6.16. It may be noted that the amplitude levels of the sources as highlighted with the logarithmic scale of the bottom row plots of Fig. 6.16 correspond to the modal amplitude levels reached at the limit cycle.

Contrary to expectations, the nonlinear resonator patches thus excite the linearly stable modes instead of further damping them. This phenomenon may be interpreted by means of a mechanical analogy, where the resonator exerts a force on the combustor acoustics: Already at an early instance in time ( $t \cdot f_{0,PCS} \gtrsim 800$ ), the combustor acoustics is dominated by the eigenfrequency of the most unstable first eigenmode ( $\times$ ), which coincides with the target frequency of the dampers. As a result, the damper cavity also exhibits high acoustic amplitudes at this resonance frequency. The associated quasi-harmonic pressure fluctuations of the resonator can be considered a force exerted on all eigenmodes included in the ROM. Individually considering the eigenmodes forced at a specific frequency is equivalent to a forced mechanical oscillator, which generally oscillates at the forcing frequency even if it deviates from the system's eigenfrequency. This leads to the conclusion that the resonator's high

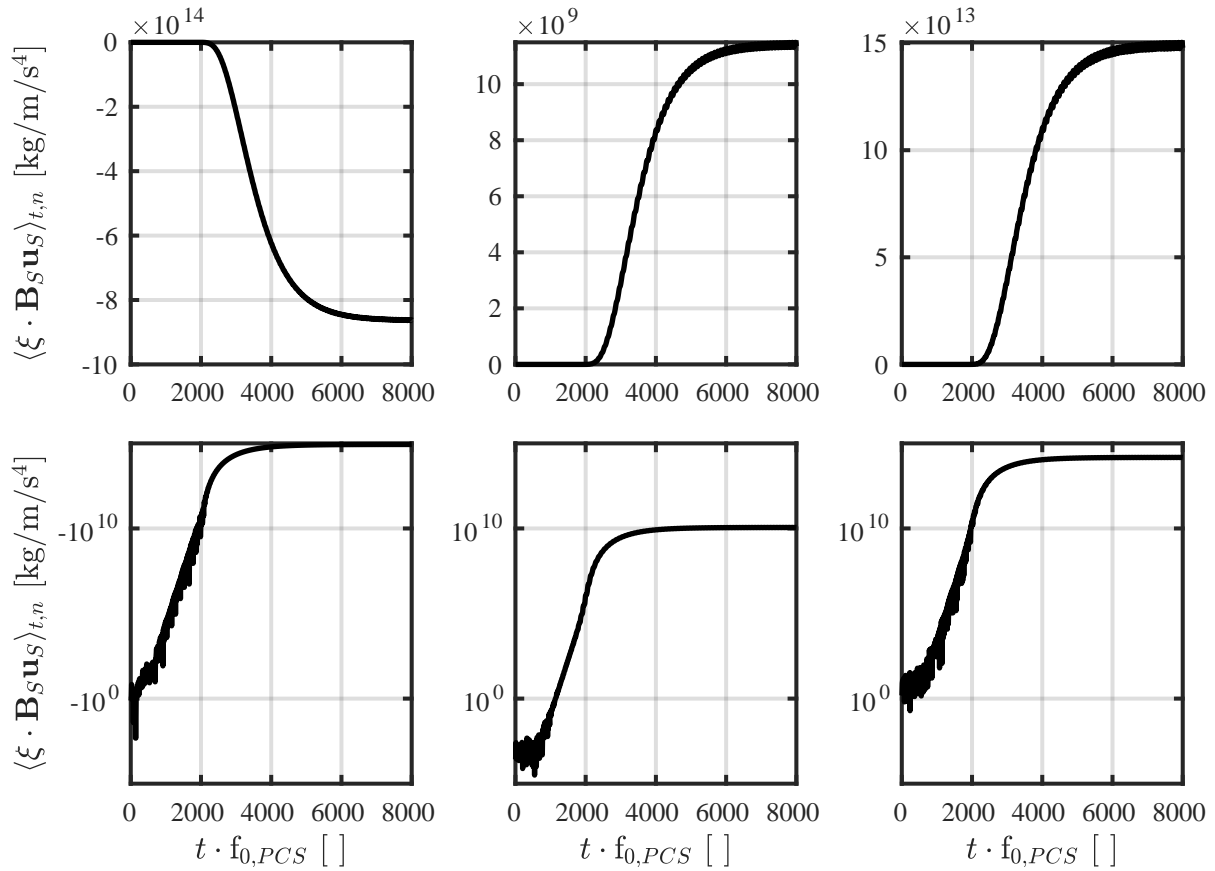


**Figure 6.16:** Comparison of the period-averaged sources  $\langle \xi \cdot \mathbf{B}_S \mathbf{u}_S \rangle_{t,n}$  for the linearly unstable eigenmode 1 (left) as well as the linearly stable eigenmodes 2 (center) and 7 (right). Top row: linear scale. Bottom row: logarithmic scale.

amplitude oscillations forces all eigenmodes of the ROM with the same frequency, resulting in a forced modal synchronization via the damper patches as observed in Fig. 6.14. Depending on the response of the individual eigenmodes to that forcing, their amplitudes increase to different levels. For the final limit-cycle oscillations, though, the identified synchronization is of minor relevance. This is due to the fact that the amplitude level of the linearly most unstable eigenmode 1 exceeds the amplitude levels of the other eigenmodes by approximately one order of magnitude as shown in Fig. 6.13.

To conclude this chapter, the nonlinear time-domain study with the associated results presented above are subsequently classified by means of comparable studies from literature.

### 6.4.3 Classification of the Time-Domain Results

Only few nonlinear thermoacoustic studies of technically relevant combustion systems based on modal reduction methods are available in the literature to classify the nonlinear TD results presented in the thesis at hand. Although Laurent et al. [197] investigate thermoacoustic instabilities in an annular combustor, their modeling procedure is entirely based on network models preventing their application to HF thermoacoustics in geometrically complex configurations. This is in contrast to the study based on a DMR performed by Hummel et al. [100–102] investigating nonlinear flame saturation mechanisms in a lab-scale combustor. The only work known to the author addressing the coupling between the ROM of a pseudo-thermoacoustic system and nonlinear resonators was conducted by Noiray and Schuermans [196]. However, the corresponding study is subject to strong limitations:

1. Since the orthonormal basis of the common Green's function approach is spanned by eigenfunctions of a self-adjoint problem (i.e. exclusively employing wall or open-end boundary conditions), the acoustic field is not correctly represented in the vicinity of the resonator patches.
2. To account for nonlinear saturation mechanisms, they implement an artificial amplitude limiter instead of using a universal damper model with a nonlinear resistance term.
3. The simplistic duct-like setup investigated in [196] is not representative for a large-scale industrial configuration.

Particularly the first two limitations are overcome by the Generalized Discrete MAE coupled to a nonlinear damper model developed in sections 5.3 and 5.4. Its application to the geometrically complex configuration above demonstrated that it is not limited to academic setups. The prediction of amplitude saturation as well as synchronization of multiple eigenmodes induced by the nonlinear damping characteristics of resonators with reduced order methodologies is a novelty of the present work. Providing the capability of predicting the maximum amplitude levels of unstable combustion systems, the Generalized Discrete MAE completes the efficient, accurate and robust numerical framework pursued in the thesis at hand.

## 7 Concluding Remarks and Future Work

In the present thesis, a sequential computational procedure for the analysis of the thermoacoustic stability in gas turbine combustors is developed. Thermoacoustic instabilities are governed by an imbalance between driving and damping mechanisms resulting in an exponential growth of oscillating pressure amplitudes. At considerably high amplitudes, nonlinear mechanisms eventually promote the balancing of the counteracting forces, which induces an amplitude saturation (limit-cycle). In the proposed procedure, specific emphasis is put on the consideration of linear and nonlinear contributions to the damping of a system.

Desired properties of the computational procedure are high efficiency and accuracy, completeness and numerical robustness. Essentially, the proposed procedure satisfying those requirements consists of three major and consecutive steps:

1. Creation of a combined 3D-CA and 1D network model.
2. Full order linear modal stability analysis.
3. Reduced order nonlinear time-domain simulations.

The combination of 3D-CA with 1D network models ensures a high computational efficiency. Using the popular Helmholtz equation to model the physics in the 3D-CA part does not only come at low computational cost, but is also highly robust. One drawback of describing the propagation of acoustic waves with the Helmholtz equation is the negligence of the mean flow advection. To account for the wave advection, a consistent, inhomogeneous convective wave equation is derived and transformed into the frequency-domain. In the fashion of an acoustic analogy, terms describing the interaction between acoustics and nonuniform mean flow fields are shifted to the RHS. For the use with FEM discretization, its weak form including suitable boundary flux expressions to implement general impedance boundary conditions and transfer matrix couplings is provided. It is proven that the volumetric RHS source

---

terms can be accounted for by using boundary conditions suitable for quiescent fluids, which are also required for the regular Helmholtz equation. However, using common 1D network models including mean flow mechanisms to characterize those boundary conditions yields an inconsistency with the zero Mach number requirement at the boundaries of the 3D-FEM setup. The corresponding discrepancies between the energetic fluxes at the interface of domains with and without mean flow may severely falsify the stability prediction. To reestablish consistency at the interface, an energetically consistent transformation procedure for the 1D characteristics is derived. Consequently, a novel framework consistently combining 3D-FEM based on the convective Helmholtz equation with 1D networks is obtained. This framework represents a nonlinear eigenvalue problem for the linear modal thermoacoustic stability analysis at low oscillation amplitudes. Solving for the eigenvalues of a system requires its transformation into a linear eigenvalue problem. For highest accuracy, a linearization procedure making use of a state-space formalism is applied to the framework.

The final linearized framework is investigated using a simple test case consisting of two straight ducts subject to mean flow and coupled via a sudden area change. The central part containing the area change is described by a transfer matrix obtained from a 1D network model. It is used to couple the remaining disconnected straight ducts resolved with 3D-FEM. As reference, the more elaborate Acoustic Perturbation Equations (APE) setup is compared to different Helmholtz setups. This allows to draw the following conclusions:

- The eigenvalues computed with the consistent convective Helmholtz equation with energetically transformed boundary conditions exhibits outstanding agreement with those of the reference APE setup.
- Using the Helmholtz equation instead, but also employing the energetically consistent boundary conditions still shows good agreement of the eigenvalues with the reference setup. For increasing mean flow Mach numbers, an increasing deviation of the eigenfrequencies is observed due to the neglected mean flow in the 3D-FEM part. This also leads to slight deviations in the predicted growth rates.
- Dropping the energetical consistency for the Helmholtz setup results in severe errors in the predicted stability of the system.

- Although showing an increased accuracy, the consistent convective Helmholtz equation comes at equal computational cost and robustness as the regular Helmholtz equation. Compared to the more elaborate APE, the consistent convective Helmholtz equation comes at decreased computational cost and is more robust while still showing the same level of accuracy.

The third major step of the proposed stability analysis comprises the investigation of nonlinear saturation mechanisms in the time-domain. A cost efficient methodology for this purpose is provided by reduced order models (ROM). They can be created using modal model order reduction methods, which make use of the previously computed linear eigenmodes of the combustion chamber. To consistently include the nonlinear damping mechanisms of acoustic resonators, a novel ROM framework suitable to the convective Helmholtz equation is developed. It is based on the Green function approach and the widespread direct modal reduction. The framework allows to include nonlinear volumetric and boundary sources. The latter are used to couple the combustor acoustics with nonlinear damper models. Suitable nonlinear damper models are proposed to be represented by a state-space system with parameters fitted to the impedances previously computed for the linear stability analysis.

Eventually, the developed sequential procedure is applied to an industrial-scale gas turbine combustion chamber. This test case serves as a proof of concept for the newly developed nonlinear ROM framework. For this purpose, a combined 3D-FEM and 1D network model is created first. Driving is provided by the linear mechanisms of flame deformation and displacement. They are suitable for the investigation of high-frequency thermoacoustics of perfectly premixed flames with the convective Helmholtz equation. Damping is exclusively introduced via the boundaries at the plenum inlet, the transfer matrix representation of the burners and the perforated resonators at the combustion chamber wall. This yields three linearly unstable modes in the vicinity of the first transversal mode. Due to their low purge flow velocities, only the resonators are expected to exhibit nonlinear damping effects. Since the acoustics-flame interactions are assumed to be exclusively linear, the dampers are also the only nonlinearity considered in the subsequent ROM simulations. From the corresponding results, the following conclusions are drawn:

- 
- The exponential amplitude growth initially observed for the most unstable eigenmode is indeed saturated by nonlinear damping mechanisms, leading to limit-cycle oscillations at a constant amplitude.
  - Unexpectedly, also linearly stable eigenmodes exhibited exponential growth once the most unstable mode reached a certain amplitude level. Investigating the phase of the modal amplitudes leads to the conclusion that those modes are synchronized with the dominating, most unstable mode. In this case, the resonant damper actually excites the linearly stable eigenmodes.
  - Both, the prediction of amplitude saturation as well as the modal synchronization on the basis of ROM coupled with nonlinear resonator models is a novelty of this thesis. It highlights the necessity of accurately capturing the linear and nonlinear contributions to system damping for a reliable stability prediction.

The development of the sequential computational procedure and its application to the geometrically complex combustor raises a number of open issues, which are not in the scope of the present thesis:

- Most notably, the procedure requires an extensive validation. A suitable validation case exhibits self-excited thermoacoustic instabilities from a perfectly premixed flame and can be equipped with dampers.
- The only nonlinearity considered in the present thesis stems from damper impedances. Generally, also the energy losses within the used transfer matrices can exhibit a nonlinear behavior. With the theoretical framework developed in this thesis, such a nonlinearity can be easily included in the future.
- Along the entire sequential procedure proposed in the present thesis, all contributions to the overall damping of the system have been included via boundary conditions described by 1D networks. Therefore, the losses are spatially concentrated, which is an oversimplification of spatially distributed source regions found in reality. Capturing this spatial distribution requires the development of volumetric energy sinks in the future.

- Ultimately, the considered linear acoustics-flame interaction mechanisms are limited to perfectly premixed combustion. To increase the technical significance, more elaborate linear and nonlinear models need to be developed, which also capture equivalence ratio fluctuations in high-frequency thermoacoustics.

Due to the modular character of the proposed sequential procedure, such future developments can be included in a straightforward manner. Having demonstrated its general applicability to large-scale systems might make this framework attractive for future developments in both, academic and industrial environments.



## Previous Publications

Significant parts of this Ph.D. thesis have been published by the author beforehand in conference proceedings and journal papers. All of these relevant prior printed publications are registered according to the valid doctoral regulations and are listed below. However, not all of them are quoted explicitly everywhere as they are part of this present work being official documents. Whether these personal prior printed publications were referenced, depended on maintaining comprehensibility and providing all necessary context.

1. Heilmann, G., Liu, T., Romero Vega, P., and Sattelmayer, T., 2022. “A Novel Decomposition Approach Preventing Spurious Entropy Generation in Hybrid Thermoacoustic Stability Computations”. *Journal of Engineering for Gas Turbines and Power*, **144**(9), p. 091013.
2. Heilmann, G., and Sattelmayer, T., 2022. “On the Convective Wave Equation for the Investigation of Combustor Stability Using FEM-Methods”. *International Journal of Spray and Combustion Dynamics*, **14**(1-2), pp. 55-71.
3. Heilmann, G., Hirsch, C., and Sattelmayer, T., 2021. “Energetically Consistent Computation of Combustor Stability with a Model Consisting of a Helmholtz Finite Element Method Domain and a Low-Order Network”. *Journal of Engineering for Gas Turbines and Power*, **143**(5), p. 051024.
4. Romero Vega, P., Hofmeister, T., Heilmann G., Hirsch, C., and Sattelmayer, T., 2021. “Isentropic Formulation of the Linearized Euler Equations for Perfectly Premixed Combustion Systems”. In Proceedings of ASME Turbo Expo 2021. GT2021-60055.
5. Mohammadzadeh Keleshtery, P., Heilmann, G., Hirsch, C., Panek, L., Huth, M., and Sattelmayer, T., 2020. “High-Frequency Instability Driving

---

Potential of Premixed Jet Flames in a Tubular Combustor Due to Dynamic Compression and Deflection”. In Proceedings of ASME Turbo Expo 2020. GT2020-15048.

## Supervised Student Theses

Associated with this Ph.D. thesis, a number of student theses were supervised by the author of the present work. These theses were created and written at the Lehrstuhl für Thermodynamik, Technische Universität München in the years 2017 to 2021 under the close supervision of the author. Parts of these supervised theses may be incorporated into the present thesis. The author would like to express his sincere gratitude to all formerly supervised students for their commitment and support of this research project.

---

Name	Thesis title, type, submission date
Alexander Mages	Characterization of Hydrogen Flames Using Equivalent Time-Averaged Natural Gas Flame Fields to Determine Thermoacoustic Growth Rates, Semester Thesis, February 1st, 2018.
Ángel Brito Gadeschi	Numerical Investigation of the Influence of Acoustic Amplitude Level on the Acoustic Scattering Behaviour of an In-Duct Orifice Using Nonlinear Computational Aeroacoustics, Bachelor's Thesis, June 19th, 2019.
Simon Wenzler	Implementierung und Anwendung von Multi-Frequenz-Anregung für Nichtlineare Numerische Aeroakustik-Simulationen, Bachelor's Thesis, August 5th, 2019.
Dominik König	Energetische Studie zum Einfluss Akustischer Randbedingungen auf Inkonsistente Mittlere Strömungsfelder, Bachelor's Thesis, September 29th, 2019.
Joachim Ottinger	Implementation of a Nonlinear Damper Model for Thermoacoustic Stability Analysis, Semester Thesis, October 30th, 2020.
Joachim Ottinger	Study on the Impact of Nonlinear Damping Devices on Thermoacoustic Limit Cycle Oscillations Using a Reduced Order Time-Domain Model, Master's Thesis, August 13th, 2021.

---



# Bibliography

- [1] Schmid, M., Blumenthal, R. S., Schulze, M., Polifke, W., and Sattelmayer, T., 2013. “Quantitative Stability Analysis Using Real-Valued Frequency Response Data”. In Volume 1B: Combustion, Fuels and Emissions, American Society of Mechanical Engineers, p. V01BT04A037. GT2013-95459.
- [2] Sattelmayer, T., Eroglu, A., König, M., Krebs, W., and Myers, G., 2013. “Industrial Combustors: Conventional, Non-premixed, and Dry Low Emissions (DLN)”. In *Gas Turbine Emissions*. Cambridge University Press, Cambridge, pp. 290–361.
- [3] Roser, M., Ritchie, H., and Ortiz-Ospina, E., 2013. “World Population Growth”. *Our World in Data*.
- [4] Wolfram, C., Shelef, O., and Gertler, P., 2012. “How Will Energy Demand Develop in the Developing World?”. *Journal of Economic Perspectives*, **26**(1), pp. 119–138.
- [5] Morales-Acevedo, A., 2014. “Forecasting Future Energy Demand: Electrical Energy in Mexico as an Example Case”. *Energy Procedia*, **57**, pp. 782–790.
- [6] Al-Badi, A., and AlMubarak, I., 2019. “Growing Energy Demand in the GCC Countries”. *Arab Journal of Basic and Applied Sciences*, **26**(1), pp. 488–496.
- [7] International Energy Agency, 2021. *World Energy Outlook 2021*. World Energy Outlook. OECD.
- [8] Kampa, M., and Castanas, E., 2008. “Human Health Effects of Air Pollution”. *Environmental Pollution*, **151**(2), pp. 362–367.

- [9] IPCC, 2021. *Climate Change 2021: The Physical Science Basis. Contribution of Working Group I to the Sixth Assessment Report of the Intergovernmental Panel on Climate Change*. Cambridge University Press, Cambridge, United Kingdom and New York, NY, USA.
- [10] Solomon, S., Plattner, G.-K., Knutti, R., and Friedlingstein, P., 2009. “Irreversible Climate Change Due to Carbon Dioxide Emissions”. *Proceedings of the National Academy of Sciences*, **106**(6), pp. 1704–1709.
- [11] United Nations, 2015. “Paris Agreement”. In Paris Climate Change Conference - November 2015, United Nations.
- [12] Fekete, H., Kuramochi, T., Roelfsema, M., den Elzen, M., Forsell, N., Höhne, N., Luna, L., Hans, F., Sterl, S., Olivier, J., van Soest, H., Frank, S., and Gusti, M., 2021. “A Review of Successful Climate Change Mitigation Policies in Major Emitting Economies and the Potential of Global Replication”. *Renewable and Sustainable Energy Reviews*, **137**, p. 110602.
- [13] IPCC, 2022. *Climate Change 2022: Mitigation of Climate Change. Contribution of Working Group III to the Sixth Assessment Report of the Intergovernmental Panel on Climate Change*. Cambridge University Press, Cambridge, UK and New York, NY, USA.
- [14] Kroposki, B., Johnson, B., Zhang, Y., Gevorgian, V., Denholm, P., Hodge, B.-M., and Hannegan, B., 2017. “Achieving a 100% Renewable Grid: Operating Electric Power Systems with Extremely High Levels of Variable Renewable Energy”. *IEEE Power and Energy Magazine*, **15**(2), pp. 61–73.
- [15] Al-Shetwi, A. Q., Hannan, M., Jern, K. P., Mansur, M., and Mahlia, T., 2020. “Grid-Connected Renewable Energy Sources: Review of the Recent Integration Requirements and Control Methods”. *Journal of Cleaner Production*, **253**, p. 119831.
- [16] Farhat, H., and Salvini, C., 2022. “Novel Gas Turbine Challenges to Support the Clean Energy Transition”. *Energies*, **15**(15), p. 5474.
- [17] de Gouw, J. A., Parrish, D. D., Frost, G. J., and Trainer, M., 2014. “Reduced Emissions of CO<sub>2</sub>, NO<sub>x</sub>, and SO<sub>2</sub> from U.S. Power Plants Owing to Switch from Coal to Natural Gas with Combined Cycle Technology”. *Earth's Future*, **2**(2), pp. 75–82.

- [18] Guandalini, G., Campanari, S., and Romano, M. C., 2015. “Power-to-Gas Plants and Gas Turbines for Improved Wind Energy Dispatchability: Energy and Economic Assessment”. *Applied Energy*, **147**, pp. 117–130.
- [19] Gulen, S. C., and Curtis, M., 2022. “Gas Turbine’s Role in Energy Transition”. In Proceedings of ASME Turbo Expo 2022, American Society of Mechanical Engineers. GT2022-81802.
- [20] Klein, M., 2013. “Overview of Worldwide Ground-Based Regulatory Framework”. In *Gas Turbine Emissions*. Cambridge University Press, Cambridge.
- [21] Bowman, C. T., 1992. “Control of Combustion-Generated Nitrogen Oxide Emissions: Technology Driven by Regulation”. *Symposium (International) on Combustion*, **24**(1), pp. 859–878.
- [22] Nemitallah, M. A., Rashwan, S. S., Mansir, I. B., Abdelhafez, A. A., and Habib, M. A., 2018. “Review of Novel Combustion Techniques for Clean Power Production in Gas Turbines”. *Energy & Fuels*, **32**(2), pp. 979–1004.
- [23] Lieuwen, T., Neumeier, Y., and Zinn, B. T., 1998. “The Role of Unmixedness and Chemical Kinetics in Driving Combustion Instabilities in Lean Premixed Combustors”. *Combustion Science and Technology*, **135**(1-6), pp. 193–211.
- [24] Yang, V., 2002. “Introductions – Stability Characteristics and Control Approach”. In *Active Control of Engine Dynamics*. RTO, Neuilly-sur-Seine.
- [25] Dowling, A. P., 2003. “The Challenges of Lean Premixed Combustion”. In Proceedings of the International Gas Turbine Congress.
- [26] Dowling, A. P., and Mahmoudi, Y., 2015. “Combustion Noise”. *Proceedings of the Combustion Institute*, **35**(1), pp. 65–100.
- [27] Morgans, A. S., and Duran, I., 2016. “Entropy Noise: A Review of Theory, Progress and Challenges”. *International Journal of Spray and Combustion Dynamics*, **8**(4), pp. 285–298.
- [28] Howe, M. S., 1979. “On the Theory of Unsteady High Reynolds Number Flow Through a Circular Aperture”. *Proceedings of the Royal Society of London. A. Mathematical and Physical Sciences*, **366**(1725), pp. 205–223.

- [29] Howe, M., 1980. “The Dissipation of Sound at an Edge”. *Journal of Sound and Vibration*, **70**(3), pp. 407–411.
- [30] Howe, M. S., 1984. “On the Absorption of Sound by Turbulence and Other Hydrodynamic Flows”. *IMA Journal of Applied Mathematics*, **32**(1-3), pp. 187–209.
- [31] Ronneberger, D., 1987. Theoretische und Experimentelle Untersuchung der Schallausbreitung durch Querschnittssprünge und Lochplatten in Strömungskanälen. Tech. rep., DFG, Göttingen.
- [32] Howe, M. S., 1995. “The Damping of Sound by Wall Turbulent Shear Layers”. *The Journal of the Acoustical Society of America*, **98**(3), pp. 1723–1730.
- [33] Rayleigh, 1878. “The Explanation of Certain Acoustical Phenomena”. *Nature*, **18**(455), pp. 319–321.
- [34] Polifke, W., 2004. “Combustion Instabilities”. In *Advances in Aeroacoustics and Applications*, no. 2004-03 in Lecture Series / Von Karman Institute for Fluid Dynamics. VKI, Rhode Saint Genèse, Belgium.
- [35] Krebs, W., Hellat, J., and Eroglu, A., 2003. “Technische Verbrennungssysteme”. In *Stationäre Gasturbinen*. Springer Berlin Heidelberg, Berlin, Heidelberg.
- [36] Campos-Delgado, D., Schuermans, B., Zhou, K., Paschereit, C., Galleste, E., and Poncet, A., 2003. “Thermoacoustic Instabilities: Modeling and Control”. *IEEE Transactions on Control Systems Technology*, **11**(4), pp. 429–447.
- [37] Zhao, D., Lu, Z., Zhao, H., Li, X., Wang, B., and Liu, P., 2018. “A Review of Active Control Approaches in Stabilizing Combustion Systems in Aerospace Industry”. *Progress in Aerospace Sciences*, **97**, pp. 35–60.
- [38] Betz, M., 2019. “Untersuchung Passiver Maßnahmen zur Erhöhung der Thermoakustischen Stabilität von Ringbrennkammern”. PhD thesis, Technical University of Munich.

- [39] Cohen, J., Hagen, G., Banaszuk, A., Becz, S., and Mehta, P., 2011. "Attenuation of Gas Turbine Combustor Pressure Oscillations Using Symmetry Breaking". In 49th AIAA Aerospace Sciences Meeting Including the New Horizons Forum and Aerospace Exposition, American Institute of Aeronautics and Astronautics. AIAA 2011-60.
- [40] Noiray, N., Bothien, M., and Schuermans, B., 2011. "Investigation of Azimuthal Staging Concepts in Annular Gas Turbines". *Combustion Theory and Modelling*, **15**(5), pp. 585–606.
- [41] Bothien, M. R., Noiray, N., and Schuermans, B., 2015. "Analysis of Azimuthal Thermo-acoustic Modes in Annular Gas Turbine Combustion Chambers". *Journal of Engineering for Gas Turbines and Power*, **137**(6), p. 061505.
- [42] Richards, G. A., Yip, M. J., Robey, E., Cowell, L., and Rawlins, D., 1997. "Combustion Oscillation Control by Cyclic Fuel Injection". *Journal of Engineering for Gas Turbines and Power*, **119**(2), pp. 340–343.
- [43] Prasanth, R. K., Annaswamy, A. M., Hathout, J. P., and Ghoniem, A. F., 2002. "When Do Open-Loop Strategies for Combustion Control Work?". *Journal of Propulsion and Power*, **18**(3), pp. 658–668.
- [44] Richards, G. A., Thornton, J. D., Robey, E. H., and Arellano, L., 2007. "Open-Loop Active Control of Combustion Dynamics on a Gas Turbine Engine". *Journal of Engineering for Gas Turbines and Power*, **129**(1), pp. 38–48.
- [45] Heckl, M. A., 1988. "Active Control of the Noise from a Rijke Tube". *Journal of Sound and Vibration*, **124**(1), pp. 117–133.
- [46] Poinso, T., Bourienne, F., Candel, S., Esposito, E., and Lang, W., 1989. "Suppression of Combustion Instabilities by Active Control". *Journal of Propulsion and Power*, **5**(1), pp. 14–20.
- [47] McManus, K., Poinso, T., and Candel, S., 1993. "A Review of Active Control of Combustion Instabilities". *Progress in Energy and Combustion Science*, **19**(1), pp. 1–29.

- [48] Annaswamy, A. M., and Ghoniem, A. F., 1995. “Active Control in Combustion Systems”. *IEEE Control Systems*, **15**(6), pp. 49–63.
- [49] Schuermans, B., 2003. “Modeling and Control of Thermoacoustic Instabilities”. PhD thesis, École Polytechnique Fédérale de Lausanne.
- [50] Krebs, W., Walz, G., Flohr, P., and Hoffmann, S., 2001. “Modal Analysis of Annular Combustors: Effect of Burner Impedance”. In Volume 2: Coal, Biomass and Alternative Fuels; Combustion and Fuels; Oil and Gas Applications; Cycle Innovations, American Society of Mechanical Engineers, p. V002T02A009. 2001-GT-0042.
- [51] Richards, G. A., Straub, D. L., and Robey, E. H., 2001. “Dynamic Response of a Premix Fuel Injector”. In Volume 2: Coal, Biomass and Alternative Fuels; Combustion and Fuels; Oil and Gas Applications; Cycle Innovations, American Society of Mechanical Engineers, p. V002T02A003. 2001-GT-0036.
- [52] Figura, L., Lee, J. G., Quay, B. D., and Santavicca, D. A., 2007. “The Effects of Fuel Composition on Flame Structure and Combustion Dynamics in a Lean Premixed Combustor”. In Volume 2: Turbo Expo 2007, American Society of Mechanical Engineers, pp. 181–187. GT2007-27298.
- [53] Lieuwen, T., McDonnell, V., Petersen, E., and Santavicca, D., 2008. “Fuel Flexibility Influences on Premixed Combustor Blowout, Flashback, Autoignition, and Stability”. *Journal of Engineering for Gas Turbines and Power*, **130**(1), p. 011506.
- [54] Culick, F. E. C., 2006. Unsteady Motions in Combustion Chambers for Propulsion Systems. Tech. rep., NATO Research & Technology Organisation, Neuilly-sur-Seine.
- [55] Zhao, D., and Li, X., 2015. “A Review of Acoustic Dampers Applied to Combustion Chambers in Aerospace Industry”. *Progress in Aerospace Sciences*, **74**, pp. 114–130.
- [56] Bellucci, V., Flohr, P., Paschereit, C. O., and Magni, F., 2004. “On the Use of Helmholtz Resonators for Damping Acoustic Pulsations in Industrial Gas Turbines”. *Journal of Engineering for Gas Turbines and Power*, **126**(2), pp. 271–275.

- [57] Dupère, I. D. J., and Dowling, A. P., 2005. “The Use of Helmholtz Resonators in a Practical Combustor”. *Journal of Engineering for Gas Turbines and Power*, **127**(2), pp. 268–275.
- [58] Sohn, C. H., and Park, J. H., 2011. “A Comparative Study on Acoustic Damping Induced by Half-Wave, Quarter-Wave, and Helmholtz Resonators”. *Aerospace Science and Technology*, **15**(8), pp. 606–614.
- [59] Zahn, M., Schulze, M., Hirsch, C., and Sattelmayer, T., 2016. “Impact of Quarter Wave Tube Arrangement on Damping of Azimuthal Modes”. In Volume 4A: Combustion, Fuels and Emissions, American Society of Mechanical Engineers, p. V04AT04A025. GT2016-56450.
- [60] Bourquard, C., and Noiray, N., 2016. “Criteria for Choosing Helmholtz or Quarter-Wave Dampers to Suppress Combustion Instabilities”. In International Symposium Thermoacoustic Instabilities in Gas Turbines and Rocket Engines, ETH Zurich.
- [61] Richards, G. A., Straub, D. L., and Robey, E. H., 2003. “Passive Control of Combustion Dynamics in Stationary Gas Turbines”. *Journal of Propulsion and Power*, **19**(5), pp. 795–810.
- [62] Zinn, B., 1970. “A Theoretical Study of Non-Linear Damping by Helmholtz Resonators”. *Journal of Sound and Vibration*, **13**(3), pp. 347–356.
- [63] Keller, J. J., and Zauner, E., 1995. “On the Use of Helmholtz Resonators as Sound Attenuators”. *ZAMP Zeitschrift für angewandte Mathematik und Physik*, **46**(3), pp. 297–327.
- [64] Förner, K., Tournadre, J., Martínez-Lera, P., and Polifke, W., 2017. “Scattering to Higher Harmonics for Quarter-Wave and Helmholtz Resonators”. *AIAA Journal*, **55**(4), pp. 1194–1204.
- [65] Schuermans, B., Bothien, M., Maurer, M., and Bunkute, B., 2015. “Combined Acoustic Damping-Cooling System for Operational Flexibility of GT26/GT24 Reheat Combustors”. In Volume 4A: Combustion, Fuels and Emissions, American Society of Mechanical Engineers, p. V04AT04A025. GT2015-42287.

- [66] Howe, M. S., 1979. “Attenuation of Sound in a Low Mach Number Nozzle Flow”. *Journal of Fluid Mechanics*, **91**(2), pp. 209–229.
- [67] Jones, M., Parrott, T., and Watson, W., 2003. “Comparison of Acoustic Impedance Education Techniques for Locally-Reacting Liners”. In 9th AIAA/CEAS Aeroacoustics Conference and Exhibit, American Institute of Aeronautics and Astronautics. AIAA 2003-3306.
- [68] Jones, M., Watson, W., Parrott, T., and Smith, C., 2004. “Design and Evaluation of Modifications to the NASA Langley Flow Impedance Tube”. In 10th AIAA/CEAS Aeroacoustics Conference, American Institute of Aeronautics and Astronautics. AIAA 2004-2837.
- [69] Scarpato, A., Ducruix, S., and Schuller, T., 2012. “A Novel Design Method for Robust Acoustic Dampers With Perforated Plates Backed by a Cavity Operating at Low and High Strouhal Numbers”. In Volume 2: Combustion, Fuels and Emissions, Parts A and B, American Society of Mechanical Engineers, pp. 885–895. GT2012-69249.
- [70] Rupp, J., Carrotte, J., and Macquisten, M., 2011. “The Use of Perforated Damping Liners in Aero Gas Turbine Combustion Systems”. In Volume 2: Combustion, Fuels and Emissions, Parts A and B, ASMEDC, pp. 495–506.
- [71] Kim, D., Jung, S., and Park, H., 2019. “Acoustic Damping Characterization of a Double-Perforated Liner in an Aero-Engine Combustor”. *Journal of Mechanical Science and Technology*, **33**(6), pp. 2957–2965.
- [72] McDonnell, V., and Klein, M., 2013. “Ground-Based Gas Turbine Combustion: Metrics, Constraints, and System Interaction”. In *Gas Turbine Emissions*. Cambridge University Press, Cambridge.
- [73] Poinso, T., 2013. Simulation Methodologies and Open Questions for Acoustic Combustion Instability Studies. Tech. rep., Center for Turbulence Research, Stanford.
- [74] Kornilov, V. N., and Rook, R., 2009. “Experimental and Numerical Investigation of the Acoustic Response of Multi-Slit Bunsen Burners”. *Combustion and Flame*, p. 14.

- [75] Courtine, E., Selle, L., and Poinso, T., 2015. “DNS of Intrinsic ThermoAcoustic Modes in Laminar Premixed Flames”. *Combustion and Flame*, **162**(11), pp. 4331–4341.
- [76] Gruber, A., Bothien, M. R., Ciani, A., Aditya, K., Chen, J. H., and Williams, F. A., 2021. “Direct Numerical Simulation of Hydrogen Combustion at Auto-Ignitive Conditions: Ignition, Stability and Turbulent Reaction-Front Velocity”. *Combustion and Flame*, **229**, p. 111385.
- [77] Wolf, P., Staffelbach, G., Roux, A., Gicquel, L., Poinso, T., and Moureau, V., 2009. “Massively Parallel LES of Azimuthal Thermo-Acoustic Instabilities in Annular Gas Turbines”. *Comptes Rendus Mécanique*, **337**(6-7), pp. 385–394.
- [78] Wolf, P., Balakrishnan, R., Staffelbach, G., Gicquel, L. Y. M., and Poinso, T., 2012. “Using LES to Study Reacting Flows and Instabilities in Annular Combustion Chambers”. *Flow, Turbulence and Combustion*, **88**(1-2), pp. 191–206.
- [79] Hernández, I., Staffelbach, G., Poinso, T., Román Casado, J. C., and Kok, J. B., 2013. “LES and Acoustic Analysis of Thermo-Acoustic Instabilities in a Partially Premixed Model Combustor”. *Comptes Rendus Mécanique*, **341**(1-2), pp. 121–130.
- [80] Sharifi, V., Kempf, A. M., and Beck, C., 2019. “Large-Eddy Simulation of Acoustic Flame Response to High-Frequency Transverse Excitations”. *AIAA Journal*, **57**(1), pp. 327–340.
- [81] Avdonin, A., Meindl, M., and Polifke, W., 2019. “Thermoacoustic Analysis of a Laminar Premixed Flame Using a Linearized Reactive Flow Solver”. *Proceedings of the Combustion Institute*, **37**(4), pp. 5307–5314.
- [82] Meindl, M., Silva, C. F., and Polifke, W., 2021. “On the Spurious Entropy Generation Encountered in Hybrid Linear Thermoacoustic Models”. *Combustion and Flame*, **223**, pp. 525–540.
- [83] Morris, P. J., Long, L. N., Bangalore, A., and Wang, Q., 1997. “A Parallel Three-Dimensional Computational Aeroacoustics Method Using Nonlinear Disturbance Equations”. *Journal of Computational Physics*, **133**(1), pp. 56–74.

- [84] Gikadi, J., 2014. “Prediction of Acoustic Modes in Combustors Using Linearized Navier-Stokes Equations in Frequency Space”. PhD thesis, Technical University of Munich.
- [85] Zahn, M., Schulze, M., Hirsch, C., Betz, M., and Sattelmayer, T., 2015. “Frequency Domain Predictions of Acoustic Wave Propagation and Losses in a Swirl Burner With Linearized Navier-Stokes Equations”. In Volume 4A: Combustion, Fuels and Emissions, American Society of Mechanical Engineers, p. V04AT04A055. GT2015-42723.
- [86] Ullrich, W. C., 2019. “Combustion Noise Prediction with Linearized Navier-Stokes Equations and Spectral Sound Sources”. PhD thesis, Technical University of Munich.
- [87] Long, L., 2000. “A Nonconservative Nonlinear Flowfield Splitting Method for 3-D Unsteady Fluid Dynamics”. In 6th Aeroacoustics Conference and Exhibit, American Institute of Aeronautics and Astronautics.
- [88] Koeglmeier, S., Kaess, R., and Sattelmayer, T., 2014. “Determination of Acoustic Scattering Matrices Using Nonlinear Disturbance Equations”. In 7th AIAA Theoretical Fluid Mechanics Conference, American Institute of Aeronautics and Astronautics. AIAA 2014-3338.
- [89] Bailly, C., and Juvé, D., 2000. “Numerical Solution of Acoustic Propagation Problems Using Linearized Euler Equations”. *AIAA Journal*, **38**(1), pp. 22–29.
- [90] Bogey, C., Bailly, C., and Juvé, D., 2002. “Computation of Flow Noise Using Source Terms in Linearized Euler’s Equations”. *AIAA Journal*, **40**(2), pp. 235–243.
- [91] Schulze, M., Wagner, M., and Sattelmayer, T., 2016. “Linearized Euler Equations for the Determination of Scattering Matrices for Orifice and Perforated Plate Configurations in the High Mach Number Regime”. *Aerospace*, **3**(4), p. 33.
- [92] Culick, F. E. C., 2002. *Dynamics of Combustion Systems: Fundamentals, Acoustics, And Control*. RTO, Neuilly-sur-Seine.

- [93] Bade, S., 2014. “Messung und Modellierung der Thermoakustischen Eigenschaften eines Modularen Brennersystems für Vorgemischte Drallflammen”. PhD thesis, Technical University of Munich.
- [94] Evesque, S., and Polifke, W., 2002. “Low-Order Acoustic Modelling for Annular Combustors: Validation and Inclusion of Modal Coupling”. In Volume 1: Turbo Expo 2002, American Society of Mechanical Engineers, pp. 321–331. GT-2002-30064.
- [95] Evesque, S., Polifke, W., and Pankiewitz, C., 2003. “Spinning and Azimuthally Standing Acoustic Modes in Annular Combustors”. In 9th AIAA/CEAS Aeroacoustics Conference and Exhibit, American Institute of Aeronautics and Astronautics. AIAA 2003-3182.
- [96] Campa, G., and Camporeale, S. M., 2010. “Influence of Flame and Burner Transfer Matrix on Thermoacoustic Combustion Instability Modes and Frequencies”. In Volume 2: Combustion, Fuels and Emissions, Parts A and B, ASMEDC, pp. 907–918. GT2010-23104.
- [97] Camporeale, S. M., Fortunato, B., and Campa, G., 2011. “A Finite Element Method for Three-Dimensional Analysis of Thermo-acoustic Combustion Instability”. *Journal of Engineering for Gas Turbines and Power*, **133**(1), p. 011506.
- [98] Ni, F., Miguel-Brebion, M., Nicoud, F., and Poinso, T., 2017. “Accounting for Acoustic Damping in a Helmholtz Solver”. *AIAA Journal*, **55**(4), pp. 1205–1220.
- [99] Ni, F., Nicoud, F., Méry, Y., and Staffelbach, G., 2018. “Including Flow–Acoustic Interactions in the Helmholtz Computations of Industrial Combustors”. *AIAA Journal*, **56**(12), pp. 4815–4829.
- [100] Hummel, T., Temmler, C., Schuermans, B., and Sattelmayer, T., 2016. “Reduced-Order Modeling of Aeroacoustic Systems for Stability Analyses of Thermoacoustically Noncompact Gas Turbine Combustors”. *Journal of Engineering for Gas Turbines and Power*, **138**(5), p. 051502.
- [101] Hummel, T., Hammer, K., Romero, P., Schuermans, B., and Sattelmayer, T., 2017. “Low-Order Modeling of Nonlinear High-Frequency Transver-

- sal Thermoacoustic Oscillations in Gas Turbine Combustors”. *Journal of Engineering for Gas Turbines and Power*, **139**(7), p. 071503.
- [102] Hummel, T., 2019. “Modeling and Analysis of High-Frequency Thermoacoustic Oscillations in Gas Turbine Combustion Chambers”. PhD thesis, Technical University of Munich, Munich, Germany.
- [103] Hofmeister, T., 2021. “Influence of Acoustically Induced Vorticity Perturbations on High-Frequency Thermoacoustic Instabilities in Gas Turbine Combustors”. PhD thesis, Technical University of Munich, Munich, Germany.
- [104] Poinso, T., and Veynante, D., 2011. *Theoretical and Numerical Combustion*, third ed. CNRS, Toulouse.
- [105] Lieuwen, T. C., 2012. *Unsteady Combustor Physics*. Cambridge University Press, Cambridge.
- [106] Zemansky, M. W., and Dittman, R., 1997. *Heat and Thermodynamics: An Intermediate Textbook*, 7. ed., internat. ed ed. International Series in Pure and Applied Physics. McGraw-Hill, New York, NY.
- [107] Baehr, H. D., and Kabelac, S., 2016. *Thermodynamik*. Springer Berlin Heidelberg, Berlin, Heidelberg.
- [108] Hofmeister, T., and Sattelmayer, T., 2021. “Amplitude-Dependent Damping and Driving Rates of High-Frequency Thermoacoustic Oscillations in a Lab-Scale Lean-Premixed Gas Turbine Combustor”. *Journal of Engineering for Gas Turbines and Power*, **143**(12), p. 121018.
- [109] Ewert, R., and Schröder, W., 2003. “Acoustic Perturbation Equations Based on Flow Decomposition via Source Filtering”. *Journal of Computational Physics*, **188**(2), pp. 365–398.
- [110] Marble, F., and Candel, S., 1977. “Acoustic Disturbance from Gas Non-Uniformities Convected Through a Nozzle”. *Journal of Sound and Vibration*, **55**(2), pp. 225–243.
- [111] Testud, P., Aurégan, Y., Moussou, P., and Hirschberg, A., 2009. “The Whistling Potentiality of an Orifice in a Confined Flow Using an Energetic Criterion”. *Journal of Sound and Vibration*, **325**(4-5), pp. 769–780.

- [112] Zhou, L., and Bodén, H., 2014. “Experimental Investigation of an In-Duct Orifice with Bias Flow under Medium and High Level Acoustic Excitation”. *International Journal of Spray and Combustion Dynamics*, **6**(3), pp. 267–292.
- [113] Kapur, A., Cummings, A., and Mungur, P., 1972. “Sound Propagation in a Combustion Can with Axial Temperature and Density Gradients”. *Journal of Sound and Vibration*, **25**(1), pp. 129–138.
- [114] Cummings, A., 1977. “Ducts with Axial Temperature Gradients: An Approximate Solution for Sound Transmission and Generation”. *Journal of Sound and Vibration*, **51**(1), pp. 55–67.
- [115] Lighthill, M. J., 1952. “On Sound Generated Aerodynamically I. General Theory”. *Proceedings of the Royal Society of London. Series A. Mathematical and Physical Sciences*, **211**(1107), pp. 564–587.
- [116] Delfs, J., 2016. Basics of Aeroacoustics.
- [117] Moehring, W., 1999. “A Well Posed Acoustic Analogy Based on a Moving Acoustic Medium”. In Aeroacoustic Workshop SWING, arXiv.
- [118] Rienstra, S. W., and Hirschberg, A., 2018. An Introduction to Acoustics.
- [119] Lele, S., 1997. “Computational Aeroacoustics - A Review”. In 35th Aerospace Sciences Meeting and Exhibit, American Institute of Aeronautics and Astronautics.
- [120] Agarwal, A., Morris, P. J., and Mani, R., 2004. “Calculation of Sound Propagation in Nonuniform Flows: Suppression of Instability Waves”. *AIAA Journal*, **42**(1), pp. 80–88.
- [121] Lahiri, C., and Bake, F., 2017. “A Review of Bias Flow Liners for Acoustic Damping in Gas Turbine Combustors”. *Journal of Sound and Vibration*, **400**, pp. 564–605.
- [122] Poinso, T., and Lele, S., 1992. “Boundary Conditions for Direct Simulations of Compressible Viscous Flows”. *Journal of Computational Physics*, **101**(1), pp. 104–129.

- [123] Baillot, F., Durox, D., and Prud'homme, R., 1992. "Experimental and Theoretical Study of a Premixed Vibrating Flame". *Combustion and Flame*, **88**(2), pp. 149–168.
- [124] Morgenweck, D., 2013. "Modellierung des Transferverhaltens im Zeitbereich zur Beschreibung Komplexer Randbedingungen in Raketenschubkammern". PhD thesis, Technical University of Munich.
- [125] Culick, F. E. C., and Yang, V., 1995. "Overview of Combustion Instabilities in Liquid-Propellant Rocket Engines". In *Liquid Rocket Engine Combustion Instability*. American Institute of Aeronautics and Astronautics, Washington DC.
- [126] Cantrell, R. H., and Hart, R. W., 1964. "Interaction Between Sound and Flow in Acoustic Cavities: Mass, Momentum, and Energy Considerations". *The Journal of the Acoustical Society of America*, **36**(4), pp. 697–706.
- [127] Morfey, C., 1971. "Acoustic Energy in Non-Uniform Flows". *Journal of Sound and Vibration*, **14**(2), pp. 159–170.
- [128] Myers, M. K., 1991. "Transport of Energy by Disturbances in Arbitrary Steady Flows". *Journal of Fluid Mechanics*, **226**, pp. 383–400.
- [129] Brear, M. J., Nicoud, F., Talei, M., Giauque, A., and Hawkes, E. R., 2012. "Disturbance Energy Transport and Sound Production in Gaseous Combustion". *Journal of Fluid Mechanics*, **707**, pp. 53–73.
- [130] Eriksson, K., Johnson, C., and Estep, D., 2004. *Applied Mathematics: Body and Soul*, Vol. 3. Springer Berlin Heidelberg, Berlin, Heidelberg.
- [131] Tam, C. K., and Webb, J. C., 1993. "Dispersion-Relation-Preserving Finite Difference Schemes for Computational Acoustics". *Journal of Computational Physics*, **107**(2), pp. 262–281.
- [132] Polifke, W., Verhaar, B., and van der Hoek, J., 1997. Everything You Always Wanted to Know About f and g. Tech. rep., Baden, Switzerland.
- [133] Karimi, N., Brear, M. J., and Moase, W. H., 2008. "Acoustic and Disturbance Energy Analysis of a Flow with Heat Communication". *Journal of Fluid Mechanics*, **597**, pp. 67–89.

- 
- [134] Morse, P. M., and Ingard, K. U., 1968. *Theoretical Acoustics*. Princeton University Press, Princeton, N.J.
- [135] Munjal, M. L., 2014. *Acoustics of Ducts and Mufflers*, second edition ed. Wiley, Chichester, West Sussex, United Kingdom.
- [136] Crighton, D. G., Dowling, A. P., Williams, J. E. F., Heckl, M., and Leppington, F. G., 1992. *Modern Methods in Analytical Acoustics*. Springer London, London.
- [137] Howe, M. S., 1998. *Acoustics of Fluid-Structure Interactions*, first ed. Cambridge University Press.
- [138] Howe, M. S., 2003. *Theory of Vortex Sound*. Cambridge Texts in Applied Mathematics. Cambridge University Press, New York.
- [139] Bleistein, N., Stockwell, J. W., and Cohen, J. K., 2001. *Mathematics of Multidimensional Seismic Imaging, Migration, and Inversion*, Vol. 13 of *Interdisciplinary Applied Mathematics*. Springer New York, New York, NY.
- [140] Estep, D. J., 2004. A Short Course on Duality, Adjoint Operators, Green's Functions, and A Posteriori Error Analysis.
- [141] Noiray, N., and Schuermans, B., 2013. "Deterministic Quantities Characterizing Noise Driven Hopf Bifurcations in Gas Turbine Combustors". *International Journal of Non-Linear Mechanics*, **50**, pp. 152–163.
- [142] Lieuwen, T., and Rajaram, R., 2002. "Acoustic Radiation from Premixed Flames Subjected to Convected Flow Disturbances". In 40th AIAA Aerospace Sciences Meeting & Exhibit, American Institute of Aeronautics and Astronautics. AIAA-02-0480.
- [143] Rajaram, R., and Lieuwen, T., 2009. "Acoustic Radiation from Turbulent Premixed Flames". *Journal of Fluid Mechanics*, **637**, pp. 357–385.
- [144] Dowling, A. P., 1997. "Nonlinear Self-Excited Oscillations of a Ducted Flame". *Journal of Fluid Mechanics*, **346**, pp. 271–290.

- [145] Crocco, L., 1951. "Aspects of Combustion Stability in Liquid Propellant Rocket Motors Part I: Fundamentals. Low Frequency Instability with Monopropellants". *Journal of the American Rocket Society*, **21**(6), pp. 163–178.
- [146] Crocco, L., 1952. "Aspects of Combustion Stability in Liquid Propellant Rocket Motors Part II: Low Frequency Instability with Bipropellants. High Frequency Instability". *Journal of the American Rocket Society*, **22**(1), pp. 7–16.
- [147] Bloxsidge, G. J., Dowling, A. P., and Langhorne, P. J., 1988. "Reheat Buzz: An Acoustically Coupled Combustion Instability. Part 2. Theory". *Journal of Fluid Mechanics*, **193**(-1), p. 445.
- [148] Schuller, T., Durox, D., and Candel, S., 2003. "A Unified Model for the Prediction of Laminar Flame Transfer Functions". *Combustion and Flame*, **134**(1-2), pp. 21–34.
- [149] Lieuwen, T., 2003. "Modeling Premixed Combustion-Acoustic Wave Interactions: A Review". *Journal of Propulsion and Power*, **19**(5), pp. 765–781.
- [150] Nicoud, F., and Wieczorek, K., 2009. "About the Zero Mach Number Assumption in the Calculation of Thermoacoustic Instabilities". *International Journal of Spray and Combustion Dynamics*, **1**(1), pp. 67–111.
- [151] Bellucci, V., Schuermans, B., Paschereit, C., and Flohr, P., 2001. "Thermoacoustic Simulation of Lean Premixed Flames Using an Enhanced Time-Lag Model". In 15th AIAA Computational Fluid Dynamics Conference, American Institute of Aeronautics and Astronautics. AIAA 2001-2794.
- [152] Polifke, W., Kopitz, J., and Serbanoviv, A., 2001. "Impact of the Fuel Time Lag Distribution in Elliptical Premix Nozzles on Combustion Stability". In 7th AIAA/CEAS Aeroacoustics Conference and Exhibit, American Institute of Aeronautics and Astronautics.
- [153] Chu, B.-T., 1953. "On the Generation of Pressure Waves at a Plane Flame Front". *Symposium (International) on Combustion*, **4**(1), pp. 603–612.

- [154] Polifke, W., Paschereit, C. O., and Paschereit, K., 2001. “Constructive and Destructive Interference of Acoustic and Entropy Waves in a Premixed Combustor with a Choked Exit”. *The International Journal of Acoustics and Vibration*, **6**(3).
- [155] Strobio Chen, L., Bomberg, S., and Polifke, W., 2016. “Propagation and Generation of Acoustic and Entropy Waves Across a Moving Flame Front”. *Combustion and Flame*, **166**, pp. 170–180.
- [156] Schulze, M., 2016. “Linear Stability Assessment of Cryogenic Rocket Engines”. PhD thesis, Technical University of Munich.
- [157] Sattelmayer, T., 2003. “Influence of the Combustor Aerodynamics on Combustion Instabilities From Equivalence Ratio Fluctuations”. *Journal of Engineering for Gas Turbines and Power*, **125**(1), pp. 11–19.
- [158] Donea, J., Giuliani, S., and Halleux, J., 1982. “An Arbitrary Lagrangian-Eulerian Finite Element Method for Transient Dynamic Fluid-Structure Interactions”. *Computer Methods in Applied Mechanics and Engineering*, **33**, pp. 689–723.
- [159] Donea, J., and Huerta, A., 2003. “Introduction and Preliminaries”. In *Finite Element Methods for Flow Problems*, first ed. Wiley.
- [160] Heilmann, G., Liu, T., Romero Vega, P., and Sattelmayer, T., 2022. “A Novel Decomposition Approach Preventing Spurious Entropy Generation in Hybrid Thermoacoustic Stability Computations”. *Journal of Engineering for Gas Turbines and Power*, **144**(9), p. 091013.
- [161] Schwing, J., Grimm, F., and Sattelmayer, T., 2012. “A Model for the Thermo-Acoustic Feedback of Transverse Acoustic Modes and Periodic Oscillations in Flame Position in Cylindrical Flame Tubes”. In Volume 2: Combustion, Fuels and Emissions, Parts A and B, American Society of Mechanical Engineers, pp. 553–566. GT2012-68775.
- [162] Schwing, J., and Sattelmayer, T., 2013. “High-Frequency Instabilities in Cylindrical Flame Tubes: Feedback Mechanism and Damping”. In Volume 1A: Combustion, Fuels and Emissions, American Society of Mechanical Engineers, p. V01AT04A003. GT2013-94064.

- [163] Zellhuber, M., Schwing, J., Schuermans, B., Sattelmayer, T., and Polifke, W., 2014. “Experimental and Numerical Investigation of Thermoacoustic Sources Related to High-Frequency Instabilities”. *International Journal of Spray and Combustion Dynamics*, **6**(1), pp. 1–34.
- [164] Hummel, T., Berger, F., Hertweck, M., Schuermans, B., and Sattelmayer, T., 2017. “High-Frequency Thermoacoustic Modulation Mechanisms in Swirl-Stabilized Gas Turbine Combustors—Part II: Modeling and Analysis”. *Journal of Engineering for Gas Turbines and Power*, **139**(7), p. 071502.
- [165] Olson, H. F., 1943. *Dynamical Analogies*. D. Van Nostrand, New York, NY.
- [166] Lenk, A., Pfeifer, G., and Werthschützky, R., 2001. *Elektromechanische Systeme*. Springer Berlin Heidelberg, Berlin, Heidelberg.
- [167] Fischer, A., 2004. “Hybride, Thermoakustische Charakterisierung von Drallbrennern”. PhD thesis, Technical University of Munich.
- [168] Fischer, A., Hirsch, C., and Sattelmayer, T., 2006. “Comparison of multi-microphone transfer matrix measurements with acoustic network models of swirl burners”. *Journal of Sound and Vibration*, **298**(1-2), pp. 73–83.
- [169] Evesque, S., 2003. Modelling of Combustion Instabilities in Annular Combustors. Tech. rep., Technical University of Munich.
- [170] Gentemann, A., Fischer, A., Evesque, S., and Polifke, W., 2003. “Acoustic Transfer Matrix Reconstruction and Analysis for Ducts with Sudden Change of Area”. In 9th AIAA/CEAS Aeroacoustics Conference and Exhibit, American Institute of Aeronautics and Astronautics. AIAA 2003-3142.
- [171] Howe, M. S., 1975. “Contributions to the Theory of Aerodynamic Sound, with Application to Excess Jet Noise and the Theory of the Flute”. *Journal of Fluid Mechanics*, **71**(4), pp. 625–673.

- [172] Hua, X., 2013. “Advanced Studies on Transfer Impedance with Application to After-Treatment Devices and Micro-Perforated Panel Absorbers”. PhD thesis, University of Kentucky, Lexington, Kentucky.
- [173] Lahiri, C., 2014. “Acoustic Performance of Bias Flow Liners in Gas Turbine Combustors”. PhD thesis, Technische Universität Berlin.
- [174] Kinsler, L. E., 2000. “Fundamentals of Vibration”. In *Fundamentals of Acoustics*. Wiley, New York.
- [175] Forner, K. H., 2017. “Nonlinear Aeroacoustic Characterization of Resonators”. PhD thesis, Technical University of Munich, Munich, Germany.
- [176] Jing, X., and Sun, X., 1999. “Experimental Investigations of Perforated Liners with Bias Flow”. *The Journal of the Acoustical Society of America*, **106**(5), pp. 2436–2441.
- [177] Jing, X., and Sun, X., 2000. “Effect of Plate Thickness on Impedance of Perforated Plates with Bias Flow”. *AIAA Journal*, **38**(9), pp. 1573–1578.
- [178] Bellucci, V., Paschereit, C. O., and Flohr, P., 2002. “Impedance of Perforated Screens with Bias Flow”. In 8th AIAA/CEAS Aeroacoustics Conference & Exhibit, American Institute of Aeronautics and Astronautics. AIAA 2002-2437.
- [179] Bellucci, V., Flohr, P., and Paschereit, C. O., 2004. “Numerical and Experimental Study of Acoustic Damping Generated by Perforated Screens.”. *AIAA Journal*, **42**(8), pp. 1543–1549.
- [180] Heilmann, G., Hirsch, C., and Sattelmayer, T., 2021. “Energetically Consistent Computation of Combustor Stability with a Model Consisting of a Helmholtz Finite Element Method Domain and a Low-Order Network”. *Journal of Engineering for Gas Turbines and Power*, **143**(5), p. 051024.
- [181] Heilmann, G., and Sattelmayer, T., 2022. “On the Convective Wave Equation for the Investigation of Combustor Stability Using FEM-Methods”. *International Journal of Spray and Combustion Dynamics*, **14**(1-2), pp. 55–71.

- [182] Leyko, M., Moreau, S., Nicoud, F., and Poinso, T., 2010. “Waves Transmission and Generation in Turbine Stages in a Combustion-Noise Framework”. In 16th AIAA/CEAS Aeroacoustics Conference, American Institute of Aeronautics and Astronautics.
- [183] Duran, I., and Moreau, S., 2012. “Study of the attenuation of waves propagating through fixed and rotating turbine blades”. In 18th AIAA/CEAS Aeroacoustics Conference (33rd AIAA Aeroacoustics Conference), American Institute of Aeronautics and Astronautics.
- [184] Silva, C. F., Durán, I., Nicoud, F., and Moreau, S., 2014. “Boundary Conditions for the Computation of Thermoacoustic Modes in Combustion Chambers”. *AIAA Journal*, **52**(6), pp. 1180–1193.
- [185] Kotake, S., 1975. “On Combustion Noise Related to Chemical Reactions”. *Journal of Sound and Vibration*, **42**(3), pp. 399–410.
- [186] Candel, S., Ducruix, S., Durox, D., and Veynante, D., 2002. “Combustion Dynamics: Analysis and Control - Modeling”. In *Active Control of Engine Dynamics*. RTO, Neuilly-sur-Seine.
- [187] Donea, J., and Huerta, A., 2003. “Steady Transport Problems”. In *Finite Element Methods for Flow Problems*, first ed. Wiley.
- [188] Motheau, E., Selle, L., and Nicoud, F., 2014. “Accounting for Convective Effects in Zero-Mach-Number Thermoacoustic Models”. *Journal of Sound and Vibration*, **333**(1), pp. 246–262.
- [189] Jaensch, S., Sovardi, C., and Polifke, W., 2016. “On the Robust, Flexible and Consistent Implementation of Time Domain Impedance Boundary Conditions for Compressible Flow Simulations”. *Journal of Computational Physics*, **314**, pp. 145–159.
- [190] Noiray, N., Durox, D., Schuller, T., and Candel, S., 2008. “A Unified Framework for Nonlinear Combustion Instability Analysis Based on the Flame Describing Function”. *Journal of Fluid Mechanics*, **615**, pp. 139–167.
- [191] Whitham, G. B., 1999. *Linear and Nonlinear Waves*. Pure and Applied Mathematics. Wiley, New York Chichester Weinheim.

- 
- [192] Ingard, U., and Ising, H., 1967. “Acoustic Nonlinearity of an Orifice”. *The Journal of the Acoustical Society of America*, **42**(1), pp. 6–17.
- [193] Melling, T., 1973. “The Acoustic Impedance of Perforates at Medium and High Sound Pressure Levels”. *Journal of Sound and Vibration*, **29**(1), pp. 1–65.
- [194] Antoulas, A. C., 2005. *Approximation of Large-Scale Dynamical Systems*. Society for Industrial and Applied Mathematics.
- [195] Lunze, P. D. J., 2020. *Regelungstechnik 1: Systemtheoretische Grundlagen, Analyse und Entwurf einschleifiger Regelungen*. Springer Berlin Heidelberg, Berlin, Heidelberg.
- [196] Noiray, N., and Schuermans, B., 2012. “Theoretical and Experimental Investigations on Damper Performance for Suppression of Thermoacoustic Oscillations”. *Journal of Sound and Vibration*, **331**(12), pp. 2753–2763.
- [197] Laurent, C., Bauerheim, M., Poinso, T., and Nicoud, F., 2019. “A Novel Modal Expansion Method for Low-Order Modeling of Thermoacoustic Instabilities in Complex Geometries”. *Combustion and Flame*, **206**, pp. 334–348.
- [198] Bonciolini, G., Boujo, E., and Noiray, N., 2016. “Effects of Turbulence-Induced Colored Noise on Thermoacoustic Instabilities in Combustion Chambers”. In *Thermoacoustic Instabilities in Gas Turbines and Rocket Engines: Industry Meets Academia*, ETH Zurich.
- [199] Bonciolini, G., Boujo, E., and Noiray, N., 2017. “Output-Only Parameter Identification of a Colored-Noise-Driven Van-Der-Pol Oscillator: Thermoacoustic Instabilities as an Example”. *Physical Review E*, **95**(6), p. 062217.
- [200] Noiray, N., and Schuermans, B., 2013. “On the Dynamic Nature of Azimuthal Thermoacoustic Modes in Annular Gas Turbine Combustion Chambers”. *Proceedings of the Royal Society A: Mathematical, Physical and Engineering Sciences*, **469**(2151), p. 20120535.

- [201] Javareshkian, A., 2022. “Modeling and Characterization of Acoustically Absorbing Liners”. PhD thesis, Technical University of Munich.
- [202] Janus, B., Bigalk, J., Helmers, L., Witzel, B., Ghermay, Y., Huth, M., Johnson, C., Landry, K., and Sunshine, R., 2014. “Successfully Validated Combustion System Upgrade for the SGT5/6-8000H Gas Turbines: Technical Features and Test Results”. In Volume 3A: Coal, Biomass and Alternative Fuels; Cycle Innovations; Electric Power; Industrial and Cogeneration, American Society of Mechanical Engineers, p. V03AT09A009. GT2014-27015.
- [203] Gruschka, U., Janus, B., Meisl, J., Huth, M., and Wasif, S., 2008. “ULN System for the New SGT5-8000H Gas Turbine: Design and High Pressure Rig Test Results”. In Volume 3: Combustion, Fuels and Emissions, Parts A and B, ASME DC, pp. 913–919. GT2008-51208.
- [204] Bohan, K., Klapdor, E. V., Prade, B., Haeggmark, A., Bulat, G., Prasad, N., Welch, M., Adamsson, P., and Johnke, T., 2020. Hydrogen Power with Siemens Gas Turbines. White Paper, Siemens Gas and Power GmbH & Co. KG.
- [205] Karimi, N., Brear, M. J., and Moase, W. H., 2010. “On the Interaction of Sound with Steady Heat Communicating Flows”. *Journal of Sound and Vibration*, **329**(22), pp. 4705–4718.
- [206] COMSOL Multiphysics®, 2017. Reference Manual. COMSOL AB.
- [207] Amestoy, P., Duff, I., and L’Excellent, J.-Y., 2000. “Multifrontal Parallel Distributed Symmetric and Unsymmetric Solvers”. *Computer Methods in Applied Mechanics and Engineering*, **184**(2), pp. 501–520.
- [208] COMSOL Multiphysics®, 2017. LiveLink™ for MATLAB® User’s Guide. COMSOL AB.
- [209] Bonciolini, G., and Noiray, N., 2019. “Synchronization of Thermoacoustic Modes in Sequential Combustors”. *Journal of Engineering for Gas Turbines and Power*, **141**(3), p. 031010.

- [210] Moeck, J. P., Durox, D., Schuller, T., and Candel, S., 2019. “Nonlinear Thermoacoustic Mode Synchronization in Annular Combustors”. *Proceedings of the Combustion Institute*, **37**(4), pp. 5343–5350.
- [211] Morinishi, Y., 2010. “Skew-Symmetric Form of Convective Terms and Fully Conservative Finite Difference Schemes for Variable Density Low-Mach Number Flows”. *Journal of Computational Physics*, **229**(2), pp. 276–300.
- [212] Kaltenbacher, M., 2018. “Advanced Finite Element Formulation for the Convective Wave Equation”. *Euronoise 2018*, pp. 291–296.



# Appendix

# A Acoustic Source Term Filtering for LEE

This appendix provides a detailed derivation of the APE discussed in section 2.2.3. It is based on the source term filtering according to [109] for the LEE, eqs. (2.8), which are reshaped in a first step. Only the purely acoustic terms remain on the left-hand side (LHS) while the remaining terms are shifted to the right-hand side (RHS), yielding

$$\frac{\partial \rho'}{\partial t} + \bar{\rho} \nabla \cdot \mathbf{u}' = -\bar{\mathbf{u}} \cdot \nabla \rho' - \mathbf{u}' \cdot \nabla \bar{\rho} - \rho' \nabla \cdot \bar{\mathbf{u}}, \quad (\text{A.1a})$$

$$\frac{\partial \mathbf{u}'}{\partial t} + \frac{1}{\bar{\rho}} \nabla p' = -\bar{\mathbf{u}} \cdot \nabla \mathbf{u}' - \mathbf{u}' \cdot \nabla \bar{\mathbf{u}} - \frac{\rho'}{\bar{\rho}} \bar{\mathbf{u}} \cdot \nabla \bar{\mathbf{u}}, \quad (\text{A.1b})$$

$$\frac{\partial p'}{\partial t} + \kappa \bar{p} \nabla \cdot \mathbf{u}' = -\bar{\mathbf{u}} \cdot \nabla p' - \mathbf{u}' \cdot \nabla \bar{p} - \kappa p' \nabla \cdot \bar{\mathbf{u}} + (\kappa - 1) \dot{q}'. \quad (\text{A.1c})$$

This system of equations may be written in the vectoral form

$$\frac{\partial \mathbf{U}}{\partial t} + \frac{\partial \mathbf{E}}{\partial x} + \frac{\partial \mathbf{F}}{\partial y} + \frac{\partial \mathbf{D}}{\partial z} = \mathbf{S}, \quad (\text{A.2})$$

with the state vector  $\mathbf{U} = (\rho', u', v', w', p')^T$  and the flux and source vectors  $\mathbf{E}$ ,  $\mathbf{F}$ ,  $\mathbf{D}$  and  $\mathbf{S}$ . Applying a combined Fourier and Laplace transform then leads to

$$\mathbf{A} \tilde{\mathbf{U}} = \tilde{\mathbf{G}}. \quad (\text{A.3})$$

Here,  $\tilde{\mathbf{U}}$  denotes the transformed state vector and  $\tilde{\mathbf{G}} = i(\tilde{\mathbf{S}} + \mathbf{U}_0^*/2\pi)$  is the transformed source vector, which incorporates the spatially transformed initial condition  $\mathbf{U}_0^*$ . The system matrix  $\mathbf{A}$  reads

$$\mathbf{A} = \begin{pmatrix} \omega & -\bar{\rho}\alpha & -\bar{\rho}\beta & -\bar{\rho}\gamma & 0 \\ 0 & \omega & 0 & 0 & -\frac{\alpha}{\bar{\rho}} \\ 0 & 0 & \omega & 0 & -\frac{\beta}{\bar{\rho}} \\ 0 & 0 & 0 & \omega & -\frac{\gamma}{\bar{\rho}} \\ 0 & -\kappa\bar{p}\alpha & -\kappa\bar{p}\beta & -\kappa\bar{p}\gamma & \omega \end{pmatrix}, \quad (\text{A.4})$$

which is a function of mean quantities, the complex angular frequency  $\omega$  and the spatial wave numbers in  $x$ ,  $y$  and  $z$  direction  $\alpha$ ,  $\beta$  and  $\gamma$ , respectively. The

eigenvalues of this system matrix are

$$\begin{aligned}\lambda_{1,2,3} &= \omega, \\ \lambda_{4,5} &= \omega \pm \bar{c}\xi,\end{aligned}$$

where  $\xi = \sqrt{\alpha^2 + \beta^2 + \gamma^2}$  represents the absolute value of the spatial wave number. The corresponding eigenvectors  $\mathbf{x}_{1-5}$  are combined to form the eigenvector matrix according to

$$\begin{aligned}\mathbf{X} &= (\mathbf{x}_1, \mathbf{x}_2, \mathbf{x}_3, \mathbf{x}_4, \mathbf{x}_5) \\ &= \begin{pmatrix} 1 & 0 & 0 & \bar{c}^{-2} & \bar{c}^{-2} \\ 0 & -\beta & -\gamma & -\frac{\alpha}{\bar{\rho}\bar{c}\xi} & \frac{\alpha}{\bar{\rho}\bar{c}\xi} \\ 0 & \alpha & 0 & -\frac{\beta}{\bar{\rho}\bar{c}\xi} & \frac{\beta}{\bar{\rho}\bar{c}\xi} \\ 0 & 0 & \alpha & -\frac{\gamma}{\bar{\rho}\bar{c}\xi} & \frac{\gamma}{\bar{\rho}\bar{c}\xi} \\ 0 & 0 & 0 & 1 & 1 \end{pmatrix}.\end{aligned}\quad (\text{A.5})$$

Note that these are the same eigenvectors that [124] found for the LEE with a constant mean flow in  $x$ -direction. The adjoint eigenvector matrix then reads

$$\begin{aligned}\mathbf{X}^{-1} &= \left( (\mathbf{x}_1^{-1})^T, (\mathbf{x}_2^{-1})^T, (\mathbf{x}_3^{-1})^T, (\mathbf{x}_4^{-1})^T, (\mathbf{x}_5^{-1})^T \right)^T \\ &= \begin{pmatrix} 1 & 0 & 0 & 0 & -\bar{c}^{-2} \\ 0 & -\frac{\beta}{\xi^2} & \frac{\alpha^2 + \gamma^2}{\alpha\xi^2} & -\frac{\beta\gamma}{\alpha\xi^2} & 0 \\ 0 & -\frac{\gamma}{\xi^2} & -\frac{\beta\gamma}{\alpha\xi^2} & \frac{\alpha^2 + \beta^2}{\alpha\xi^2} & 0 \\ 0 & -\frac{\bar{\rho}\bar{c}\alpha}{2\xi} & -\frac{\bar{\rho}\bar{c}\beta}{2\xi} & -\frac{\bar{\rho}\bar{c}\gamma}{2\xi} & \frac{1}{2} \\ 0 & \frac{\bar{\rho}\bar{c}\alpha}{2\xi} & \frac{\bar{\rho}\bar{c}\beta}{2\xi} & \frac{\bar{\rho}\bar{c}\gamma}{2\xi} & \frac{1}{2} \end{pmatrix}.\end{aligned}\quad (\text{A.6})$$

The source term components impacting the single mode types (i.e. acoustic, vortical or entropic modes) may now be identified by creating a source term filtering matrix  $\mathbf{T}$  using the eigenvectors and their corresponding adjoints as per

$$\mathbf{T} = \sum_i \mathbf{x}_i (\mathbf{x}_i^{-1})^T. \quad (\text{A.7})$$

---

Consequently, a matrix to filter the source terms purely impacting the acoustic field results from the acoustic eigenvectors and their adjoints

$$\begin{aligned}
\mathbf{T}^a &= x_4 (\mathbf{x}_4^{-1})^T + x_5 (\mathbf{x}_5^{-1})^T \\
&= \begin{pmatrix} 0 & 0 & 0 & 0 & \bar{c}^{-2} \\ 0 & \frac{\alpha^2}{\xi^2} & \frac{\alpha\beta}{\xi^2} & \frac{\alpha\gamma}{\xi^2} & 0 \\ 0 & \frac{\alpha\beta}{\xi^2} & \frac{\beta^2}{\xi^2} & \frac{\beta\gamma}{\xi^2} & 0 \\ 0 & \frac{\alpha\gamma}{\xi^2} & \frac{\beta\gamma}{\xi^2} & \frac{\gamma^2}{\xi^2} & 0 \\ 0 & 0 & 0 & 0 & 1 \end{pmatrix}, \tag{A.8}
\end{aligned}$$

whereas the pure vortical and entropic filter matrices, respectively, yield

$$\begin{aligned}
\mathbf{T}^v &= x_2 (\mathbf{x}_2^{-1})^T + x_3 (\mathbf{x}_3^{-1})^T \\
&= \begin{pmatrix} 0 & 0 & 0 & 0 & 0 \\ 0 & \frac{\beta^2 + \gamma^2}{\xi^2} & -\frac{\alpha\beta}{\xi^2} & -\frac{\alpha\gamma}{\xi^2} & 0 \\ 0 & -\frac{\alpha\beta}{\xi^2} & \frac{\alpha^2 + \gamma^2}{\xi^2} & -\frac{\beta\gamma}{\xi^2} & 0 \\ 0 & -\frac{\alpha\gamma}{\xi^2} & -\frac{\beta\gamma}{\xi^2} & \frac{\alpha^2 + \beta^2}{\xi^2} & 0 \\ 0 & 0 & 0 & 0 & 0 \end{pmatrix}, \tag{A.9}
\end{aligned}$$

$$\begin{aligned}
\mathbf{T}^s &= x_1 (\mathbf{x}_1^{-1})^T \\
&= \begin{pmatrix} 1 & 0 & 0 & 0 & -\bar{c}^{-2} \\ 0 & 0 & 0 & 0 & 0 \\ 0 & 0 & 0 & 0 & 0 \\ 0 & 0 & 0 & 0 & 0 \\ 0 & 0 & 0 & 0 & 0 \end{pmatrix}. \tag{A.10}
\end{aligned}$$

Note that the sum of the filter matrices results in a  $(5 \times 5)$  unity matrix. The filtered acoustic part of the transformed source vector  $\tilde{\mathbf{G}}^a = \mathbf{T}^a \cdot \mathbf{G}$  is then shifted to the LHS of the equation system (A.1). Subsequently applying the inverse

combined Fourier and Laplace transform then leads to the form

$$\begin{aligned} \bar{c}^2 \frac{\partial \rho'}{\partial t} + \bar{c}^2 \bar{\rho} \nabla \cdot \mathbf{u}' + \bar{\mathbf{u}} \cdot \nabla p' + \mathbf{u}' \cdot \nabla \bar{p} + \kappa p' \nabla \cdot \bar{\mathbf{u}} \\ - (\kappa - 1) \dot{q}' = S_{\rho}^{v,s}, \end{aligned} \quad (\text{A.11a})$$

$$\frac{\partial \mathbf{u}'}{\partial t} + \frac{1}{\bar{\rho}} \nabla p' + \nabla (\bar{\mathbf{u}} \cdot \mathbf{u}') = \mathbf{S}_{\mathbf{u}}^{v,s}, \quad (\text{A.11b})$$

$$\begin{aligned} \frac{\partial p'}{\partial t} + \kappa \bar{p} \nabla \cdot \mathbf{u}' + \bar{\mathbf{u}} \cdot \nabla p' + \mathbf{u}' \cdot \nabla \bar{p} + \kappa p' \nabla \cdot \bar{\mathbf{u}} \\ - (\kappa - 1) \dot{q}' = 0. \end{aligned} \quad (\text{A.11c})$$

The remaining source terms on the LHS of eq. (A.11) only excite the vortical and entropic modes and read

$$\begin{aligned} S_{\rho}^{v,s} = \bar{\mathbf{u}} \cdot \nabla p' + \mathbf{u}' \cdot \nabla \bar{p} + \kappa p' \nabla \cdot \bar{\mathbf{u}} \\ - \bar{c}^2 (\bar{\mathbf{u}} \cdot \nabla \rho' + \mathbf{u}' \cdot \nabla \bar{\rho} + \rho' \nabla \cdot \bar{\mathbf{u}}), \end{aligned} \quad (\text{A.12a})$$

$$\mathbf{S}_{\mathbf{u}}^{v,s} = -(\boldsymbol{\Omega}' \times \bar{\mathbf{u}}) - (\bar{\boldsymbol{\Omega}} \times \mathbf{u}') - \frac{\rho'}{\bar{\rho}} \bar{\mathbf{u}} \cdot \nabla \bar{\mathbf{u}}. \quad (\text{A.12b})$$

The acoustic part of the original source term of the linearized momentum equation (A.1b) conforms to the formulation of [109], who show that this part can be described by the gradient of a potential function. Hence, the sought part of the source exclusively exciting the acoustic modes is the purely irrotational part. It can be identified by exploiting the vector identity  $\bar{\mathbf{u}} \cdot \nabla \mathbf{u}' + \mathbf{u}' \cdot \nabla \bar{\mathbf{u}} = \nabla (\bar{\mathbf{u}} \cdot \mathbf{u}') + (\boldsymbol{\Omega}' \times \bar{\mathbf{u}}) + (\bar{\boldsymbol{\Omega}} \times \mathbf{u}')$  with the rotation of the mean and the fluctuating velocity  $\bar{\boldsymbol{\Omega}} = \nabla \times \bar{\mathbf{u}}$  and  $\boldsymbol{\Omega}' = \nabla \times \mathbf{u}'$ , respectively. Then, the only irrotational part in the momentum source term is the term  $\nabla (\bar{\mathbf{u}} \cdot \mathbf{u}')$ , which is considered the acoustic part and was thus shifted to the LHS of eq. (A.11b). The LHS of the momentum equation (A.11b) is slightly different as the formulation obtained from [109] as the second term does not include the gradient of the mean flow density. As a result, the acoustic velocity is not necessarily irrotational if density gradients are present. These may constitute baroclinic effects if the cross product of the density gradient and the acoustic velocity does not vanish, which is discussed by [103]. This effect may be considered a refraction of acoustic waves passing density gradients, which is not considered in classical acoustics but may play an important role in performing stability analyses of thermoacoustic systems.

---

The LHS of eq. (A.11b) and (A.11c) of the APE system are not depending on the density fluctuations. Therefore they form a closed set of acoustic equations if the source terms on the RHS are known a priori.

## B Partial Integration for the Weak Form of the Convective Helmholtz Equation

To discretize the inhomogeneous convective Helmholtz equation (4.2) with FE methods, its weak form is required in section 4.3.1. For this purpose, eq. (4.2) is multiplied by the weighting function  $\tilde{p}$  and integrated over the entire domain  $V$  first, yielding

$$\begin{aligned} & \iiint_V \left\{ s^2 \hat{p} + 2s\bar{\mathbf{u}} \cdot \nabla \hat{p} + \bar{\mathbf{u}} \cdot \nabla (\bar{\mathbf{u}} \cdot \nabla \hat{p}) - \bar{\rho} \bar{c}^2 \nabla \cdot \left( \frac{1}{\bar{\rho}} \nabla \hat{p} \right) \right\} \tilde{p} \, dV \\ = & \iiint_V \left\{ -s\kappa \hat{p} \nabla \cdot \bar{\mathbf{u}} - \bar{\mathbf{u}} \cdot \nabla (\kappa \hat{p} \nabla \cdot \bar{\mathbf{u}}) - \kappa \bar{p} \Delta (\bar{\mathbf{u}} \cdot \hat{\mathbf{u}}) + \kappa \bar{p} (\bar{\mathbf{u}} \cdot \nabla) (\nabla \cdot \hat{\mathbf{u}}) \right. \\ & \left. - \kappa \bar{p} \nabla \cdot \hat{\mathbf{S}}_{\mathbf{u}}^{v,s,\nabla \bar{p}=0} + s(\kappa - 1) \hat{q} + (\kappa - 1) \bar{\mathbf{u}} \cdot \nabla \hat{q} \right\} \tilde{p} \, dV, \end{aligned} \quad (\text{B.1})$$

Then, selected terms (particularly the ones with higher order spatial derivatives) need to be integrated by parts. The procedure of partial integration is only applied to terms on the LHS of eq. (B.1), which represents the propagation of acoustic waves subject to a mean flow advection. The RHS representing the interaction of the advected waves with a non-uniform mean flow remains unmodified. The corresponding procedure is demonstrated in the following for each individual term on the LHS, whereas the RHS remains as is. Finally, a weak formulation of the inhomogeneous Helmholtz equation is presented.

### 2nd term LHS

The skew symmetry of the second term in the volume integral on the LHS requires special treatment of the term to ensure energy conservation and numerical stability as initially discussed by Morinishi [211] and later applied and demonstrated by Kaltenbacher and Hüppe [212] for the homogeneous wave equation. The desired preservation of the skew symmetry can be ensured by integrating only half of the term by parts, which gives

$$\iiint_V 2s\tilde{p}\bar{\mathbf{u}} \cdot \nabla \hat{p} \, dV = \iint_{\partial V} s\hat{p}\tilde{p}\bar{\mathbf{u}} \cdot \mathbf{n} \, dA + \iiint_V \{s\tilde{p}\bar{\mathbf{u}} \cdot \nabla \hat{p} - s\hat{p}\nabla \cdot (\bar{\mathbf{u}}\tilde{p})\} \, dV. \quad (\text{B.2})$$

The vector  $\mathbf{n}$  denotes the outward pointing normal vector of the domain's boundary  $\partial V$ . Note that this result is slightly different as the one from Kaltenbacher and Hüppe [212] due to their limitation to constant and thus also solenoidal mean flow velocities. Applying those simplifications to eq. (B.2) resolves the discrepancies.

### 3rd and 4th terms LHS

The third and fourth terms on the LHS contain second order spatial derivatives of the state variable  $\hat{p}$  and do thus require regular integration by parts. This is for the third term

$$\iiint_V \bar{\mathbf{u}} \cdot \nabla (\bar{\mathbf{u}} \cdot \nabla \hat{p}) \tilde{p} \, dV = \iint_{\partial V} (\bar{\mathbf{u}} \cdot \nabla \hat{p}) \tilde{p} \bar{\mathbf{u}} \cdot \mathbf{n} \, dA - \iiint_V (\bar{\mathbf{u}} \cdot \nabla \hat{p}) \nabla \cdot (\bar{\mathbf{u}} \tilde{p}) \, dV, \quad (\text{B.3})$$

and for the fourth term

$$\begin{aligned} - \iiint_V \bar{\rho} \bar{c}^2 \nabla \cdot \left( \frac{1}{\bar{\rho}} \nabla \hat{p} \right) \tilde{p} \, dV &= - \iiint_V \left\{ \nabla \cdot (\bar{c}^2 \nabla \hat{p}) - \left( \frac{1}{\bar{\rho}} \nabla \hat{p} \right) \cdot \nabla (\bar{\rho} \bar{c}^2) \right\} \tilde{p} \, dV \\ &= - \iint_{\partial V} \bar{c}^2 \nabla \hat{p} \cdot \mathbf{n} \tilde{p} \, dA + \iiint_V \bar{c}^2 \nabla \hat{p} \cdot \nabla \tilde{p} \, dV. \end{aligned} \quad (\text{B.4})$$

Here, the afore met assumptions of a constant ratio of specific heats at isobaric flow conditions, i.e.  $\nabla (\bar{\rho} \bar{c}^2) = \nabla (\kappa \bar{p}) = 0$ , are exploited. It is worth noting that the weak formulation of the fourth term would look the same, if mean density gradients would have initially been precluded.

### Complete Weak Form of the Inhomogeneous Convective Helmholtz Equation

On the LHS all volume-integrated terms and all boundary-integrated terms are collected. Note that the product rule is applied to the expression  $\nabla \cdot (\bar{\mathbf{u}} \tilde{p}) = \bar{\mathbf{u}} \cdot \nabla \tilde{p} + \tilde{p} \nabla \cdot \bar{\mathbf{u}}$ . The emerging terms on the LHS incorporating the mean flow's divergence are shifted to the RHS. Ultimately, the quite lengthy weak formu-

lation of the inhomogeneous convective Helmholtz equation becomes

$$\begin{aligned}
 & \iiint_V \left\{ s^2 \hat{p} \tilde{p} + s (\bar{\mathbf{u}} \cdot \nabla \hat{p}) \tilde{p} - s \hat{p} \bar{\mathbf{u}} \cdot \nabla \tilde{p} - (\bar{\mathbf{u}} \cdot \nabla \hat{p}) \bar{\mathbf{u}} \cdot \nabla \tilde{p} + \bar{c}^2 \nabla \hat{p} \cdot \nabla \tilde{p} \right\} dV \\
 & + \iint_{\partial V} \left\{ s \bar{\mathbf{u}} \hat{p} + \bar{\mathbf{u}} (\bar{\mathbf{u}} \cdot \nabla \hat{p}) - \bar{c}^2 \nabla \hat{p} \right\} \cdot \mathbf{n} \tilde{p} dA \\
 = & \iiint_V \left\{ -s(\kappa - 1) \hat{p} \nabla \cdot \bar{\mathbf{u}} - \kappa \hat{p} (\bar{\mathbf{u}} \cdot \nabla) (\nabla \cdot \bar{\mathbf{u}}) - (\kappa - 1) (\bar{\mathbf{u}} \cdot \nabla \hat{p}) (\nabla \cdot \bar{\mathbf{u}}) + \kappa \bar{p} \Delta (\bar{\mathbf{u}} \cdot \hat{\mathbf{u}}) \right. \\
 & \left. - \kappa \bar{p} \nabla \cdot \hat{\mathbf{S}}_{\mathbf{u}}^{v,s,\nabla \bar{p}=0} - \kappa \bar{p} (\bar{\mathbf{u}} \cdot \nabla) (\nabla \cdot \hat{\mathbf{u}}) + s(\kappa - 1) \hat{q} + (\kappa - 1) \bar{\mathbf{u}} \cdot \nabla \hat{q} \right\} \tilde{p} dV .
 \end{aligned} \tag{B.5}$$

## C Natural Neumann Boundary Condition for the Convective Helmholtz Equation

The boundary flux terms of eq. (4.5) emerging from the partial integration within the derivation of the CHE's weak form in section 4.3.1 can be transformed into universal Neumann boundary conditions. For this purpose, a basic set of equations complying with the LHS assumption of a constant mean flow velocity is required. This set is provided by the APE (2.9) for a constant mean flow velocity with vanishing heat release. In frequency domain they read

$$s\hat{\mathbf{u}} + \frac{1}{\bar{\rho}}\nabla\hat{p} + \bar{\mathbf{u}} \cdot \nabla\hat{\mathbf{u}} = 0, \quad (\text{C.1a})$$

$$s\hat{p} + \kappa\bar{p}\nabla \cdot \hat{\mathbf{u}} + \bar{\mathbf{u}} \cdot \nabla\hat{p} = 0. \quad (\text{C.1b})$$

Combining this linearized momentum and energy equation according to  $\bar{\mathbf{u}}(\text{C.1b}) - \bar{\rho}\bar{c}^2(\text{C.1a})$  and exploiting the vector identity  $\nabla \times (\hat{\mathbf{u}} \times \bar{\mathbf{u}}) = \bar{\mathbf{u}} \cdot \nabla\hat{\mathbf{u}} - \bar{\mathbf{u}}(\nabla \cdot \hat{\mathbf{u}}) + \hat{\mathbf{u}}(\nabla \cdot \bar{\mathbf{u}}) - \hat{\mathbf{u}} \cdot \nabla\bar{\mathbf{u}}$ , the boundary flux  $\mathbf{F}$  can be transformed into

$$\mathbf{F} = s\bar{\rho}\bar{c}^2\hat{\mathbf{u}} + \kappa\bar{p}(\bar{\mathbf{u}} \cdot \nabla\hat{\mathbf{u}} - \bar{\mathbf{u}}(\nabla \cdot \hat{\mathbf{u}})) = s\bar{\rho}\bar{c}^2\hat{\mathbf{u}} + \kappa\bar{p}\nabla \times (\hat{\mathbf{u}} \times \bar{\mathbf{u}}). \quad (\text{C.2})$$

When introducing the above stated vector identity, consistent use was made of the constant mean flow velocity presumed for the entire LHS of eq. (4.4). The newly emerging term containing the rotation of the mean flow and perturbation velocity's vector product requires further explication. That term vanishes only if the velocity vectors of perturbation and mean flow are pointing in the same direction. This applies particularly for flow regimes which may be characterized as one-dimensional. In many practical applications, the assumption of one-dimensionality is an essential feature. It is for instance used in the well-established Multi-Microphone Method to measure acoustic characteristics of components. The same purpose is served by network models, which provide acoustic characterizations of components based on analytic expressions. Such network models for one dimensional acoustic propagation are discussed in

more detail below. Both approaches are only valid, if the investigated component is acoustically compact regarding its hydraulic diameter  $He \ll 1$ , forming the basis for one dimensional wave propagation.

Normally, an overall system boundary  $\partial V$  consists of different types of sub boundaries  $\partial V_j$ , which can be classified by their acoustic scattering characteristics. Common types have been discussed in section 2.6 and include boundaries open to the atmosphere and rigid wall boundaries. While the former boundary type exhibits a constant pressure, the latter type is characterized by a vanishing surface normal velocity ( $\bar{\mathbf{u}} \cdot \mathbf{n} = \hat{\mathbf{u}} \cdot \mathbf{n} = 0$ ). As a consequence, the weak form flux of eq. (C.2) also vanishes at wall boundaries. If the remaining sub boundaries  $\partial V_j$  are acoustically compact, one dimensional approaches may be applied and the boundary flux simplifies to

$$\mathbf{F} = s\bar{\mathbf{u}}\hat{p} + \bar{\mathbf{u}}(\bar{\mathbf{u}} \cdot \nabla \hat{p}) - \bar{c}^2 \nabla \hat{p} \approx s\bar{\rho}\bar{c}^2 \hat{\mathbf{u}}, \quad (\text{C.3})$$

which solely depends on the velocity fluctuations. In a pure acoustic sense, this result directly corresponds to the desired natural Neumann boundary condition.

To conclude this derivation, the final weak formulation of the acoustically consistent, inhomogeneous convective Helmholtz equation yields

$$\begin{aligned} & \iiint_V \left\{ s^2 \hat{p} \tilde{p} + s \left( (\bar{\mathbf{u}} \cdot \nabla \hat{p}) \tilde{p} - \hat{p} \bar{\mathbf{u}} \cdot \nabla \tilde{p} \right) - (\bar{\mathbf{u}} \cdot \nabla \hat{p}) \bar{\mathbf{u}} \cdot \nabla \tilde{p} + \bar{c}^2 \nabla \hat{p} \cdot \nabla \tilde{p} \right\} dV \\ & + \iint_{\partial V} s\bar{\rho}\bar{c}^2 \hat{\mathbf{u}} \cdot \mathbf{n} \tilde{p} dA = \iiint_V S_{iCHE} \tilde{p} dV. \end{aligned} \quad (\text{C.4})$$

With the assumptions of a uniform mean flow without heat release, the entire RHS of the former equation vanishes, leading to the weak formulation of the homogeneous convective Helmholtz equation (hCHE):

$$\begin{aligned} & \iiint_V \left\{ s^2 \hat{p} \tilde{p} + s \left( (\bar{\mathbf{u}} \cdot \nabla \hat{p}) \tilde{p} - \hat{p} \bar{\mathbf{u}} \cdot \nabla \tilde{p} \right) - (\bar{\mathbf{u}} \cdot \nabla \hat{p}) \bar{\mathbf{u}} \cdot \nabla \tilde{p} + \bar{c}^2 \nabla \hat{p} \cdot \nabla \tilde{p} \right\} dV \\ & + \iint_{\partial V} s\bar{\rho}\bar{c}^2 \hat{\mathbf{u}} \cdot \mathbf{n} \tilde{p} dA = 0. \end{aligned} \quad (\text{C.5})$$

For stagnant fluids, the iCHE (C.4) simplifies to the weak formulation of the Helmholtz equation (HE):

$$\iiint_V \left\{ s^2 \hat{p} \tilde{p} + \bar{c}^2 \nabla \hat{p} \cdot \nabla \tilde{p} \right\} dV + \iint_{\partial V} s\bar{\rho}\bar{c}^2 \hat{\mathbf{u}} \cdot \mathbf{n} \tilde{p} dA = \iiint_V s(\kappa - 1) \hat{q} \tilde{p} dV. \quad (\text{C.6})$$

---

Note that the second term within the volume integral on the LHS of eq. (C.6) is equally valid for mean flow fields with and without mean density gradients. Therefore, eq. (C.6) corresponds to the weak form of the inhomogeneous Helmholtz equation (2.21).

## D Linear Framework of the Convective Helmholtz Equation in Weak Form

In section 4.5, the state-space representation of the convective Helmholtz equation's strong form was introduced. For the implementation in FEM solvers, the state-space representation of the corresponding weak form counterpart, eq. (4.14), is of higher relevance though. It may be derived either by transforming the strong form's state-space representation into weak form or by linearizing the weak form using the state-space formalism. Both procedures lead to the following result:

$$\begin{aligned}
& \iiint_V s \begin{pmatrix} 0 & \tilde{p} \\ \tilde{\varphi} & 0 \end{pmatrix} \begin{pmatrix} \hat{p} \\ \hat{\varphi} \end{pmatrix} dV \\
& = \iiint_V \begin{pmatrix} \tilde{\mathbf{u}} \cdot \nabla \tilde{p} (\tilde{\mathbf{u}} \cdot \nabla) - \tilde{c}^2 \nabla \tilde{p} \cdot \nabla & -\tilde{p} (\tilde{\mathbf{u}} \cdot \nabla) + \tilde{\mathbf{u}} \cdot \nabla \tilde{p} \\ 0 & \tilde{\varphi} \end{pmatrix} \begin{pmatrix} \hat{p} \\ \hat{\varphi} \end{pmatrix} dV \\
& \quad + \iiint_V \begin{pmatrix} \tilde{p} (s(\kappa - 1) + (\kappa - 1) \tilde{\mathbf{u}} \cdot \nabla) \\ 0 \end{pmatrix} \hat{q} dV \\
& \quad + \iint_{\partial V} \begin{pmatrix} s \tilde{\rho} \tilde{c}^2 \tilde{p} \\ 0 \end{pmatrix} \hat{\mathbf{u}} \cdot \mathbf{n} dA.
\end{aligned} \tag{D.1}$$

In this general formulation, the heat release fluctuations and the velocity fluctuations in the last two terms are considered unknown and are treated as input quantities. When using the linearized flame displacement to model the volumetric heat release fluctuations as discussed in section 4.5, the third term can be directly incorporated into the descriptor and system matrices. The last term represents the boundary flux and must be treated differently on different portions of the overall system boundary. On partitions with a constant impedance, such as wall or energetically neutral boundary conditions, the boundary flux may also be directly included into the state-space framework as a function of the solution variables. In this case, the boundary flux may be transformed using relation (4.15). On the remaining partitions with more general frequency dependent characteristics, these characteristics are also lin-

earized using the state-space formalism (cf. section 4.5). To couple the state-space systems of the resolved domains and the linearized boundary patches, output equations for either of the systems must be specified. The output of one system is then the input of the other system.

The natural formulation of the boundary flux in terms of the velocity fluctuations can be exploited to find a suitable interconnection of the state-space representations of the convective Helmholtz domains and the frequency dependent boundary conditions. With the velocity fluctuations representing the input to the discretized domains, this quantity is the desired output quantity of the boundary condition model. To achieve this, the admittance may be transformed into state-space representation instead of the reflection coefficient as described in section 4.5. The admittance is the inverse of the impedance  $y = \frac{1}{z} = \frac{1-R}{1+R} = \frac{\hat{\rho}\hat{c}\hat{u}}{\hat{p}}$  and can be directly calculated from the reflection coefficient. In the context of transfer functions it relates the velocity fluctuations as output to the pressure fluctuations as input. Now the interconnection to the convective Helmholtz domains becomes obvious: the pressure at the boundaries of the discretized domains serves as input for the admittance state-space representation, which in turn provides the acoustic velocity at the boundaries required for the resolved domains.

To finalize the closure of the feedback loop between the Helmholtz equation (4.40) and the frequency-dependent boundary conditions, the linear state-space representation of the boundary condition according to eq. (4.39) must be provided first. To do so, different formulations may be used like the observable canonical form. A more straightforward form for the underlying ordinary differential equation of the admittance similar to eq. (4.42) is the controllable canonical form yielding the state vector  $\mathbf{x}$ , the output quantity  $\mathbf{y}$  and the system matrices  $\mathbf{A} - \mathbf{D}$

$$\mathbf{x} = \begin{pmatrix} \varphi_{(1)} \\ \varphi_{(2)} \\ \vdots \\ \varphi_{(n_i-2)} \\ \varphi_{(n_i-1)} \end{pmatrix}, \quad \mathbf{A} = \begin{pmatrix} 0 & 1 & & & \\ & 0 & 1 & & \\ & & \ddots & \ddots & \\ & & & 0 & 1 \\ -a_0 & -a_1 & \dots & -a_{n_i-2} & -a_{n_i-1} \end{pmatrix}, \quad \mathbf{B} = \begin{pmatrix} 0 \\ \vdots \\ 0 \\ 1 \end{pmatrix}$$

$$\mathbf{C} = (b_0, b_1, \dots, b_{n_i-1}), \quad \mathbf{D} = \mathbf{0}, \quad \mathbf{y} = \hat{u}, \quad \mathbf{u} = \hat{p},$$

for  $n_i = n_o + 1$ . In the controllable canonical form, the state variables  $\varphi_{(j)}$  do

not have any physical meaning. Ultimately, the output equation of the convective Helmholtz domain's state-space representation must be constructed. In the discretized form, the pressure is available at any mesh point. With the assumption of acoustically compact boundaries, the pressure is supposed to be nearly constant across that boundary. Therefore, this pressure may be extracted at a single node point on the discretized boundary or as a boundary average value. Either way, the output matrix has one row for each nonlinear boundary condition. In the first case, the output matrix is sparse with only a single unity flag per row at the position corresponding to the index of the mesh node. For the second case, an average operator involves multiple node points in each row.

The boundaries' output signals are the Helmholtz domain's input. Again exploiting the compactness of the boundary, the velocity signal is simply applied as input to all mesh points on the Helmholtz domain boundary. This yields an input matrix of the Helmholtz domain with a column per nonlinear boundary and normally multiple unity flags at each node position index of the individual boundaries.

## E Simplification of the Projected Input Matrix

To avoid an expensive inversion of the mass matrix  $\mathbf{E}$  when performing a modal model order reduction, the identity (5.8) was provided in section 5.1. This identity can be easily proven by starting from the implicit state equation (5.1a). Employing the base transformation and multiplying with the left eigenvector matrix yields

$$\mathbf{V}^{-1}\mathbf{E}\mathbf{V}\dot{\boldsymbol{\xi}} = \mathbf{V}^{-1}\check{\mathbf{A}}\mathbf{V}\dot{\boldsymbol{\xi}} + \mathbf{V}^{-1}\check{\mathbf{B}}\mathbf{u} . \quad (\text{E.1})$$

Left-multiply this equation by the inverse of  $\mathbf{V}^{-1}\mathbf{E}\mathbf{V}$  to get

$$\dot{\boldsymbol{\xi}} = (\mathbf{V}^{-1}\mathbf{E}\mathbf{V})^{-1}\mathbf{V}^{-1}\check{\mathbf{A}}\mathbf{V}\dot{\boldsymbol{\xi}} + (\mathbf{V}^{-1}\mathbf{E}\mathbf{V})^{-1}\mathbf{V}^{-1}\check{\mathbf{B}}\mathbf{u} . \quad (\text{E.2})$$

Making use of the inversion rule  $(\mathbf{ABC})^{-1} = \mathbf{C}^{-1}\mathbf{B}^{-1}\mathbf{A}^{-1}$ , the first term on the RHS can be written as

$$(\mathbf{V}^{-1}\mathbf{E}\mathbf{V})^{-1}\mathbf{V}^{-1}\check{\mathbf{A}}\mathbf{V}\dot{\boldsymbol{\xi}} = \mathbf{V}^{-1}\mathbf{E}^{-1}\underbrace{(\mathbf{V}^{-1})^{-1}\mathbf{V}^{-1}}_{=\mathbf{I}}\check{\mathbf{A}}\mathbf{V}\dot{\boldsymbol{\xi}} = \mathbf{V}^{-1}\underbrace{\mathbf{E}^{-1}\check{\mathbf{A}}\mathbf{V}}_{=\mathbf{A}}\dot{\boldsymbol{\xi}} = \text{diag}(s_n)\dot{\boldsymbol{\xi}} .$$

Finally, the state equation can be written as

$$\dot{\boldsymbol{\xi}} = \text{diag}(s_n)\dot{\boldsymbol{\xi}} + (\mathbf{V}^{-1}\mathbf{E}\mathbf{V})^{-1}\mathbf{V}^{-1}\check{\mathbf{B}}\mathbf{u} . \quad (\text{E.3})$$

Hummel [102] limits his derivation to self-adjoint problems. For systems which are not self-adjoint, the matrix  $(\mathbf{V}^{-1}\mathbf{E}\mathbf{V})$  is not diagonal. For the reduced system, inverting  $(\mathbf{W}_{red}\mathbf{E}\mathbf{V}_{red})$  instead of  $\mathbf{E}$  is still highly beneficial, since the dimension of the former is significantly reduced compared to the latter matrix.

## F Construction of the Input Matrices for the Generalized Discrete MAE

For the ROM creation based on the Generalized Discrete MAE, the input matrix  $\mathbf{B}_p$  needs to be thoroughly constructed. For brevity, a detailed representation of this matrix has been dropped within the derivation of the Generalized Discrete MAE in section 5.3. The input matrix has its origin in the discrete volumetric and boundary sources of the MAE, eq. (5.16). In fact, it is more reasonable to construct a combined matrix  $\mathbf{W}_{red}\mathbf{B}_p$ , since the source terms of eq. (5.16) also directly include the eigenvectors. For a better overview, the combined matrix  $\mathbf{W}_{red}\mathbf{B}_p$  is first split into the contributions from the single input matrices according to

$$\mathbf{W}_{red}\mathbf{B}_p = \begin{pmatrix} \mathbf{0} & \mathbf{W}_{red} \begin{pmatrix} \mathbf{B}_V \\ \mathbf{0} \end{pmatrix} & \mathbf{W}_{red} \begin{pmatrix} \mathbf{B}_{S1} \\ \mathbf{0} \end{pmatrix} & \mathbf{W}_{red} \begin{pmatrix} -\mathbf{B}_{S2} \\ \mathbf{0} \end{pmatrix} \end{pmatrix}. \quad (\text{E.1})$$

The elements of these individual contributions are then analogous to the source terms of eq. (5.16) and read

$$\mathbf{W}_{red} \begin{pmatrix} \mathbf{B}_V \\ \mathbf{0} \end{pmatrix} = \begin{pmatrix} V_1((\kappa-1)\mathbf{w}_1)_{V,1} & V_2((\kappa-1)\mathbf{w}_1)_{V,2} & \cdots & V_M((\kappa-1)\mathbf{w}_1)_{V,M} \\ V_1((\kappa-1)\mathbf{w}_2)_{V,1} & V_2((\kappa-1)\mathbf{w}_2)_{V,2} & \cdots & V_M((\kappa-1)\mathbf{w}_2)_{V,M} \\ \vdots & \vdots & \ddots & \vdots \\ V_1((\kappa-1)\mathbf{w}_R)_{V,1} & V_2((\kappa-1)\mathbf{w}_R)_{V,2} & \cdots & V_M((\kappa-1)\mathbf{w}_R)_{V,M} \end{pmatrix}, \quad (\text{E.2})$$

$$\mathbf{W}_{red} \begin{pmatrix} \mathbf{B}_{S1} \\ \mathbf{0} \end{pmatrix} = \begin{pmatrix} A_1(\bar{c}^2\bar{\rho}\mathbf{w}_1)_{S,1} & A_2(\bar{c}^2\bar{\rho}\mathbf{w}_1)_{S,2} & \cdots & A_K(\bar{c}^2\bar{\rho}\mathbf{w}_1)_{S,K} \\ A_1(\bar{c}^2\bar{\rho}\mathbf{w}_2)_{S,1} & A_2(\bar{c}^2\bar{\rho}\mathbf{w}_2)_{S,2} & \cdots & A_K(\bar{c}^2\bar{\rho}\mathbf{w}_2)_{S,K} \\ \vdots & \vdots & \ddots & \vdots \\ A_1(\bar{c}^2\bar{\rho}\mathbf{w}_R)_{S,1} & A_2(\bar{c}^2\bar{\rho}\mathbf{w}_R)_{S,2} & \cdots & A_K(\bar{c}^2\bar{\rho}\mathbf{w}_R)_{S,K} \end{pmatrix}, \quad (\text{E.3})$$

---


$$\mathbf{W}_{red} \begin{pmatrix} \mathbf{B}_{S2} \\ \mathbf{0} \end{pmatrix} = \begin{pmatrix} A_1 (\bar{c}^2 \nabla \mathbf{w}_1 \cdot \mathbf{n})_{S,1} & A_2 (\bar{c}^2 \nabla \mathbf{w}_1 \cdot \mathbf{n})_{S,2} & \cdots & A_K (\bar{c}^2 \nabla \mathbf{w}_1 \cdot \mathbf{n})_{S,K} \\ A_1 (\bar{c}^2 \nabla \mathbf{w}_2 \cdot \mathbf{n})_{S,1} & A_2 (\bar{c}^2 \nabla \mathbf{w}_2 \cdot \mathbf{n})_{S,2} & \cdots & A_K (\bar{c}^2 \nabla \mathbf{w}_2 \cdot \mathbf{n})_{S,K} \\ \vdots & \vdots & \ddots & \vdots \\ A_1 (\bar{c}^2 \nabla \mathbf{w}_R \cdot \mathbf{n})_{S,1} & A_2 (\bar{c}^2 \nabla \mathbf{w}_R \cdot \mathbf{n})_{S,2} & \cdots & A_K (\bar{c}^2 \nabla \mathbf{w}_R \cdot \mathbf{n})_{S,K} \end{pmatrix}. \quad (\text{E.4})$$

To attain a compact notation, the negative signum has been dropped in eq. (E.4). Each term in the combined input matrix still requires volume or area averaging denoted by the indexed round brackets as well as a gradient operation. Note that  $\nabla \mathbf{w}$  is a dyadic product and refers to the Jacobian containing the gradient of every element of  $\mathbf{w}$ . Both operations, i.e. averaging and spatial derivation, are easily achieved within the eigenvalue solver such as *COMSOL Multiphysics*. In a post-processing step after the left eigenvalue computation, the corresponding scalar quantities can be extracted. Lastly it may be noticed that the values of the left eigenvectors required for the input matrices correspond to the pressure of the right eigenvectors and not to their temporal derivatives. This is a result of the selected shape of the state-space representation of the MAE, eq. (5.18) and (5.22), with the non-diagonal descriptor matrices.

# G Scattering Matrix Coefficients of the PCS Burners

Complementary to the energetically transformed scattering matrix coefficients of a single main burner shown in section 6.2.3, further scattering matrix coefficients obtained from the 1D-network are plotted hereinafter. These include the energetically transformed scattering matrix coefficients of the pilot burner in Fig. G.1 as well as the original scattering matrix coefficients of a single main (Fig. G.2) and the pilot burner (Fig. G.3) without energetical transformation.

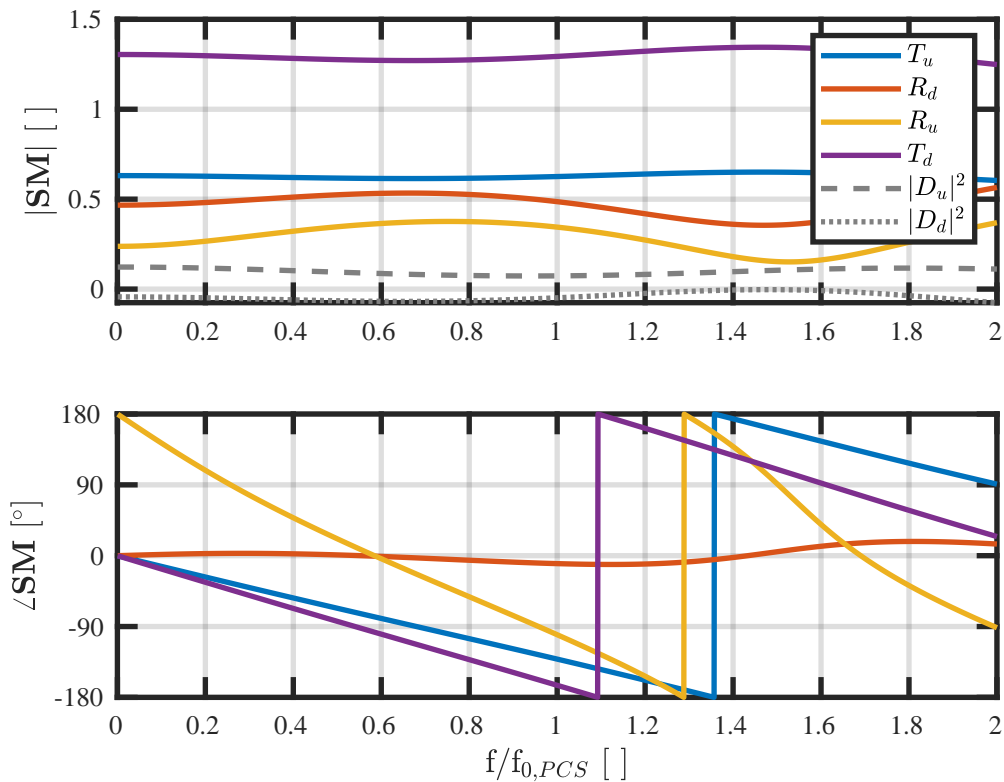


**Figure G.1:** Energetically transformed scattering matrix coefficients of the pilot burner obtained from a 1D network.

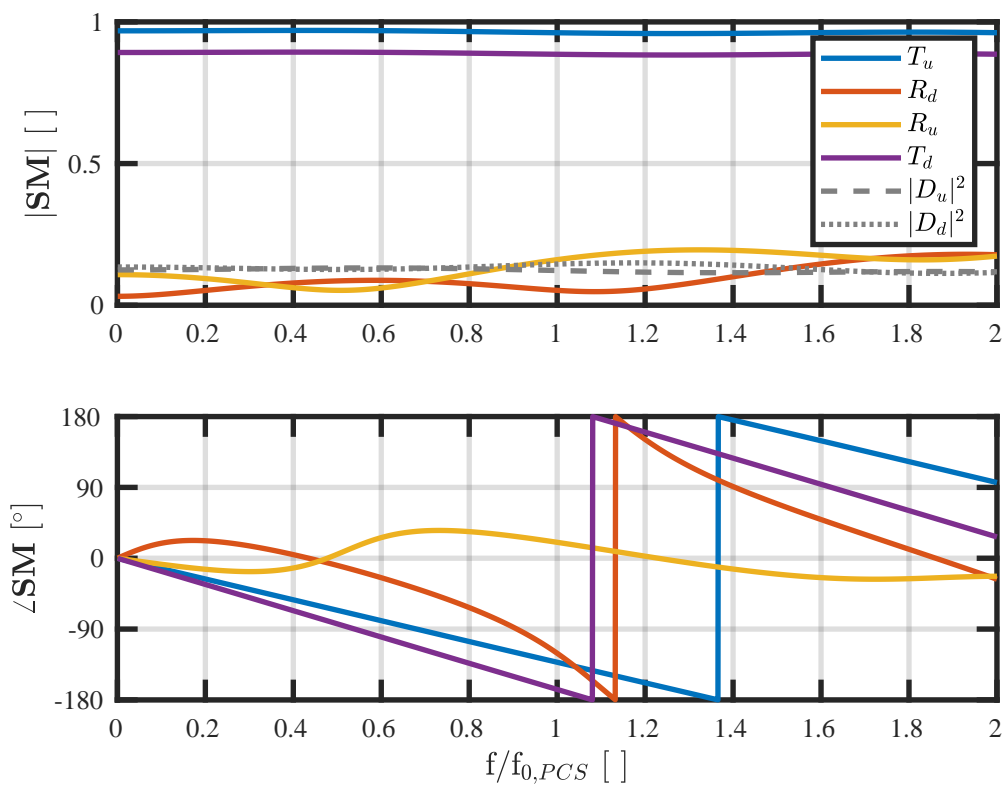


**Figure G.2:** Original scattering matrix coefficients of a single main burner obtained from a 1D network.

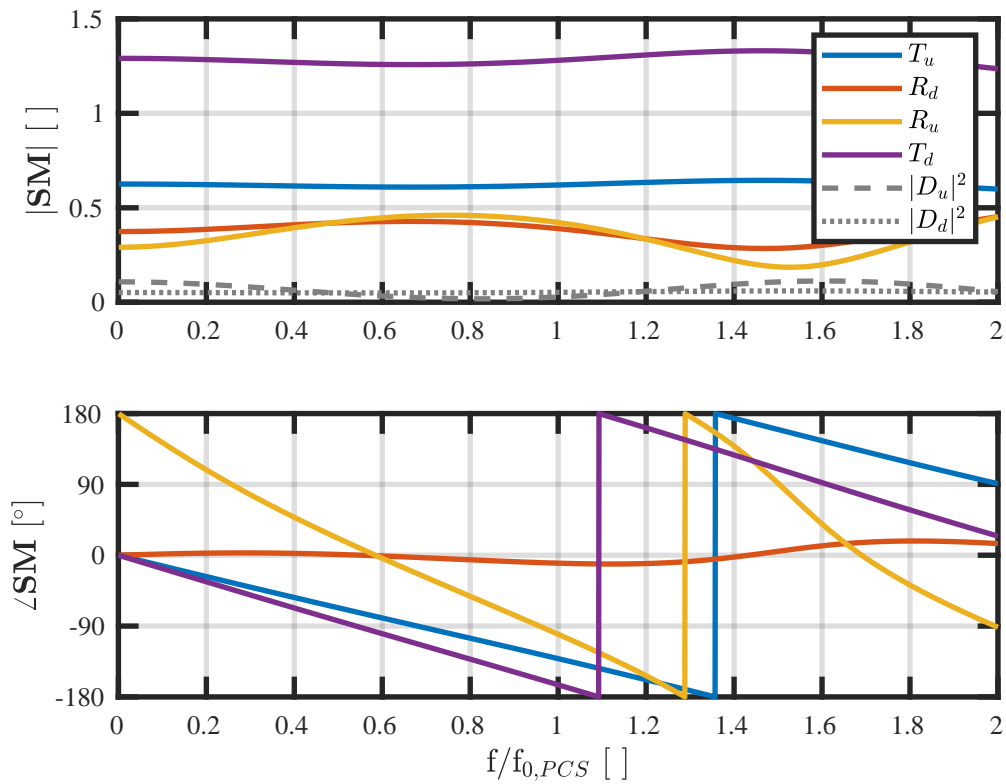


**Figure G.3:** Original scattering matrix coefficients of the pilot burner obtained from a 1D network.